Development of a Process and Toolset to Study UCAV Flight Mechanics using Computational Fluid Dynamics

Thesis submitted in accordance with the requirements of
the University of Liverpool for the degree of Doctor in Philosophy
by
David Vallespin

September 2011

Abstract

The work carried out during this project used a Computational Fluid Dynamics code to generate aerodynamic tabular models and aircraft manoeuvre simulations. As an outcome of this work, a validation of the aerodynamic prediction tools and an assessment of tabular models for aircraft flight dynamics applications was made. The Stability and Control Unmanned Combat Air Vehicle has been used as a demonstration case. Validation of computational fluid dynamics methods was carried out for highly nonlinear flow topologies using wind tunnel measurements. Integral data, pressure tap measurements and particle image velocimetry information was compared against the predictions over two configurations. Each one had a different leading edge shape distributed along the span of the model. One was sharp throughout with varying leading edge thickness and the other one was mainly rounded. Results showed a good agreement in longitudinal force and moment predictions for low angles of attack. High angles were dominated by a double vortex structure which was very sensitive to incidence angle and leading edge shape. Some wind tunnel effects were noticed in the measurements when predictions were made with and without sting. Overall the numerical predictive capabilities for low and high angles of attack were deemed good for the purpose of flight dynamics model generation.

Two methods for predicting manoeuvering flight aircraft loads are presented in this thesis. A tabular aerodynamic model based on numerical predictions was generated for the sharp configuration. Kriging interpolation was used to populate a model consisting of tables of lateral and longitudinal aerodynamic characteristics. Further to this, longitudinal dynamic derivatives were predicted for the test case in hand using forced oscillation numerical predictions. Aircraft geometric characteristics were approximated based on real aircraft data. A set of controls were designed and implemented for the purpose of manoeuvering flight predictions. A code was implemented to predict realistic aircraft manoeuvres based on an existing program. At the core of this method was a commercial optimisation Matlab code called DIDO. Using this and the nonlinear, six degree of freedom equations of motion, purposedly designed aircraft manoeuvres were predicted. The motions were then replayed using time-accurate simulations and the predicted loads were compared against the tabular predictions. In this manner, the validity of the tables of aerodynamic data were benchmarked against a more reliable

and expensive numerical method. The static based predictions showed good agreement with the replays for slow manoeuvres at low angles of attack. As manoeuvres became more aggressive, noticeable disagreement was present in the aircraft loads, particularly in the lateral characteristics during periods of large rates of change in attitudes. Hysteresis effects during manoeuvering flight were seen to produce large spreads in data in the angle of attack domain which the predicted dynamic derivatives were unable to capture.

Contents

List of Figures

Acknowledgement

Publications

Conference Papers

Vallespin D, Boelens O, Da Ronch and Badcock KJ. SACCON CFD Simulations Using Structured Grid Approaches, *Proceedings of the 28th AIAA Applied Aerodynamics Conference*, AIAA-2010-4560, June 2010.

Vallespin D and Badcock KJ. Assessment of the Limits of Tabular Aerodynamic Models for Flight Dynamics Analysis using the SACCON UCAV Configuration. *Proceedings of the RAeS Aerodynamics Conference 2010. Applied Aerodynamics: Capabilities and Future Requirements*, July 2010.

Journal Papers

Vallespin D, Da Ronch A, Badcock K and Boelens O. Vortical Flow Prediction Validation for an Unmanned Combar Air Vehicle Model. *Journal of Aircraft*, 48(6):1948-1959, 2011. doi: 10.2514/1.56673.

Vallespin D, Badcock KJ, Da Ronch A, White MD, Perfect P and Ghoreyshi M. Computational Fluid Dynamics Framework for Aerodynamic Model Assessment, *Progress in Aerospace Sciences*, 52:2-18, 2012.

Vallespin D, Boelens O and Badcock KJ. SACCON CFD Simulations Using Structured Grid Approaches. *NATO RTO AVT-161 Final Report*, Chapter 11, 2011.

Vallespin D, Cummings RM and Boelens O. Comparison of results for predicting highly non-linear vortical flow features of the UCAV SACCON configuration. *NATO RTO AVT-161 Final Report*, Chapter 19, 2011.

Da Ronch A, Vallespin D, Ghoreyshi M and Badcock KJ. Evaluation of Dynamic Derivatives Using Computational Fluid Dynamics, *Accepted in the AIAA Journal*, 2011.

Ghoreyshi M, Badcock KJ, Da Ronch, Vallespin D and Rizzi A. Automated CFD Analysis for the Investigation of Flight Handling Qualities. *Mathematical Modelling of Natural Phenomena*, 6(3):166-188, 2011.

Nomenclature

Variables

A	Amplitude of angle of attack [°]
C_D	Coefficient of drag, $\qquad\qquad C_D = \frac{2(Drag)}{\rho_\infty V_\infty^2 S}$
C_L	Coefficient of lift, $\qquad\qquad C_L = \frac{2(Lift)}{\rho_\infty V_\infty^2 S}$
C_{M_q}	Coefficient of pitching moment due to pitch rate
$C_{M_{\dot\alpha}}$	Coefficient of pitching moment due to rate of change of angle of attack
C_N	Coefficient of normal force
C_Y	Coefficient of side force
C_{Z_q}	Coefficient of normal force due to pitch rate
$C_{Z_{\dot\alpha}}$	Coefficient of normal force due to rate of change in angle of attack
C_j	Coefficient of force or moment
C_{j_q}	Coefficient of force or moment due to pitch rate
$C_{j_{\dot\alpha}}$	Coefficient of force or moment due to pitch rate
$\bar{C}_j$	Combined pitching dynamic derivative
$\bar{C}_{j_\alpha}$	In-phase component of force or moment coefficient
$\bar{C}_{j_q}$	Out-of-phase component of force or moment coefficient
C_l	Coefficient of rolling moment $\qquad C_l = \frac{2(Rolling\ Moment)}{\rho_\infty V_\infty^2 Sb_{ref}}$
C_m	Coefficient of pitching moment, $\quad C_m = \frac{2(Pitching\ Moment)}{\rho_\infty V_\infty^2 Sc_{ref}}$
C_n	Coefficient of yawing moment $\qquad C_n = \frac{2(Yawing\ Moment)}{\rho_\infty V_\infty^2 Sb_{ref}}$
C_p	Coefficient of pressure, $\qquad\qquad C_L = \frac{2(Lift)}{\rho_\infty V_\infty^2 S}$
$C_{p_{SS}}$	Coefficient of pressure from steady state solution
C_{p_R}	Coefficient of pressure from unsteady replay solution
$C_{p_{t_i}}$	Coefficient of pressure from solution at time t_i
$C_{X_{a_{dynamic}}}$	Coefficient of dynamic aerodynamic contribution
$C_{X_{a_{static}}}$	Coefficient of static aerodynamic contribution
$C_{X_{\delta_{ail}}}$	Coefficient of aileron aerodynamic contribution
E	Total energy
F	Running cost
$\mathbf{F^i}$	Inviscid flux vector along the x-axis
$\mathbf{\hat{F}^i}$	Inviscid flux vector along the x-axis in curvilinear form

$\mathbf{F^v}$	Viscous flux vector along the x-axis
$\hat{\mathbf{F}}^{\mathbf{v}}$	Viscous flux vector along the x-axis in curvilinear form
$\mathbf{G^i}$	Inviscid flux vector along the y-axis
$\hat{\mathbf{G}}^{\mathbf{i}}$	Inviscid flux vector along the y-axis in curvilinear form
$\mathbf{G^v}$	Viscous flux vector along the y-axis
$\hat{\mathbf{G}}^{\mathbf{v}}$	Viscous flux vector along the x-axis in curvilinear form
H	Total enthalpy
$\mathbf{H^i}$	Inviscid flux vector along the z-axis
$\hat{\mathbf{H}}^{\mathbf{i}}$	Inviscid flux vector along the z-axis in curvilinear form
$\mathbf{H^v}$	Viscous flux vector along the z-axis
$\hat{\mathbf{H}}^{\mathbf{v}}$	Viscous flux vector along the z-axis in curvilinear form
I_X	Moment of inertia about x-axis $[kg - m^2]$
I_Y	Moment of inertia about y-axis $[kg - m^2]$
I_Z	Moment of inertia about z-axis $[kg - m^2]$
J	Jacobian determinant
L	Characteristic length $[m]$
L	Lift force $[N]$
$\hat{L}$	Rolling moment $[Nm]$
$\hat{M}$	Pitching moment $[Nm]$
M	Mach number, $\qquad M = \frac{V_\infty}{a}$
$\hat{N}$	Yawing moment $[Nm]$
P_k	Turbulence kinetic energy production term
P_r	Prandtl number
$P_r t$	Turbulent Prandtl number
P_ω	Specific dissipation rate production term
$\mathbf{R}(\mathbf{W}_{i,j,k})$	Flux residuals
Re	Reynolds number, $\qquad Re = \frac{\rho_\infty V_\infty c_{ref}}{\mu}$
S	Reference surface area $[m^2]$
S_{ref}	Reference surface area $[m^2]$
T	Temperature $[K]$
T_0	Reference temperature $[T_0 = 288.16K]$
U	Velocity along the x-axis in body frame of reference $[m/s]$
U_∞	Freestream velocity $[m/s]$
V	Velocity along the y-axis in body frame of reference $[m/s]$
V_∞	Freestream velocity $[m/s]$
$\mathbf{V}$	Velocity vector $[m/s]$
$V_{i,j,k}$	Cell volume
$\mathbf{W}$	Column matrix of conserved variables
$\hat{\mathbf{W}}$	Column matrix of conserved variables in curvilinear form

$\mathbf{W}_{i,j,k}$	Flux variables
W	Velocity along the z-axis in body frame of reference $[m/s]$
W_a	Aircraft weight $[N]$
X	Force along the x-axis $[N]$
a	Speed of sound $[m/s]$
b_{ref}	Reference span $[m]$
c_{ref}	Reference chord length $[m]$
c_{root}	Root chord length $[m]$
d	Moment arm length $[m]$
e	Specific internal energy
f	Frequency of oscillation $[Hz]$
f_i	Body forces
k	Non-dimensional frequency
$\hat{k}$	Thermal conductivity
k'	Turbulence kinetic energy per unit mass
l_{thrust}	Distance from thrust force to CG $[m]$
p	Pressure $[N/m^2]$
p_i	Instantaneous pressure $[N/m^2]$
$\bar{p}_i$	Mean pressure component $[N/m^2]$
p'_i	Turbulent fluctuating pressure component $[N/m^2]$
$\hat{p}$	Roll rate $[°/s]$
$\dot{\hat{p}}$	First derivative of roll rate $[°/s^2]$
$\dot{q}$	Rate of volumetric heat addition per unit mass
$\bar{q}$	Dynamic pressure $[N/m^2]$
$\hat{q}$	Pitch rate $[°/s]$
$\dot{\hat{q}}$	First derivative of pitch rate $[°/s^2]$
$\hat{r}$	Yaw Rate $[°/s]$
$\dot{\hat{r}}$	First derivative of yaw rate $[°/s^2]$
t	Time $[s]$
t_0	Initial time $[s]$
t_f	Final time $[s]$
$\hat{t}$	Non-dimensional time
$\mathbf{u}(\cdot)$	Control vector
u	Velocity component along the x-axis
u_i	Instantaneous velocity component along the x-axis
$\bar{u}_i$	Mean velocity component along the x-axis
u'_i	Turbulent fluctuating velocity component along the x-axis
v	Velocity component along the y-axis
v_i	Instantaneous velocity component along the y-axis

$\bar{v}_i$	Mean velocity component along the y-axis
v'_i	Turbulent fluctuating velocity component along the y-axis
w	Velocity component along the z-axis
w_i	Instantaneous velocity component along the z-axis
$\bar{w}_i$	Mean velocity component along the z-axis
w'_i	Turbulent fluctuating velocity component along the z-axis
x	x-coordinate $[m]$
x_j	Coordinate axis, where $x_j = x$, y or z $[m]$
$\mathbf{x}(\cdot)$	State vector
y	y-coordinate $[m]$
y^+	Non-dimensional distance of first cell from wall
z	z-coordinate $[m]$
Δ	Change in
ΔC_{L_1}	Change in C_L due to data fusion errors
ΔC_{L_2}	Difference in C_L between steady and unsteady simulation
ΔC_{L_3}	Change in C_L due to vortex transient effects
ΔC_{m_1}	Change in C_m due to data fusion errors
ΔC_{m_2}	Difference in C_m between steady and unsteady simulation
ΔC_{m_3}	Change in C_m due to vortex transient effects
Λ	Sweep angle $[°]$
α	Angle of attack $[°]$
α_{trim}	Angle of attack at trim $[°]$
$\hat{\alpha}$	Closure coefficient
$\dot{\alpha}$	First derivative of angle of attack
β	Angle of sideslip $[°]$
β_{trim}	Angle of sideslip at trim $[°]$
$\hat{\beta}, \hat{\beta}^*$	Closure coefficients
γ	Flight path angle $[°]$
$\hat{\gamma}$	Ratio of specific heats $[\hat{\gamma} = 1.4]$
δ_{ele}	Elevator deflection angle $[°]$
δ_{ail}	Aileron deflection angle $[°]$
δ_{rud}	Rudder deflection angle $[°]$
ζ	Local coordinate axis in curvilinear form
η	Local coordinate axis in curvilinear form
η_T	Throttle $[\%]$
η_θ	Pitch thrust vector angle $[°]$
η_ψ	Yaw thrust vector angle $[°]$
θ	Angle of pitch $[°]$
μ	Laminar viscosity $[kg/ms]$

μ_0	Reference laminar viscosity $[\mu_0 = 1.7894 \cdot 10^{-5} kg/ms]$
μ_t	Turbulent eddy viscosity $[kg/ms]$
ξ	Local coordinate axis in curvilinear form
ρ	Density of air $[kg/m^3]$
ρ_i	Instantaneous density $[kg/m^3]$
$\bar{\rho}_i$	Mean density component $[kg/m^3]$
ρ'_i	Turbulent fluctuating density component $[kg/m^3]$
$\hat{\sigma}, \hat{\sigma}^*$	Closure coefficients
τ	Pseudo time-step
τ_{ij}	Viscous stress tensor
ϕ	Angle of roll $[°]$
ψ	Angle of yaw $[°]$
ω	Frequency of oscillation $[rad/s]$
ω_x	Vorticity in the y-z plane
ω_y	Vorticity in the x-z plane
ω_z	Vorticity in the x-y plane
ω'	Specific dissipation rate
∞	Freestream condition

Abbreviations and Acronyms

AVT	Applied Vehicle Technology
CFD	Computational Fluid Dynamics
CG	Centre of gravity
DNW	German-Dutch Wind Tunnels
DPT	Dynamic Pressure Transducer
DLR	German Aerospace Center
DoF	Degrees of Freedom
DNW-NWB	German-Dutch Wind Tunnels
EADS MAS	European Aeronautic Defence and Space Company
ENFLOW	NLR Navier-Stokes flow simulation system
ENSOLV	NLR Navier-Stokes flow solver
EPSRC	Engineering and Physical Sciences Research Council
F&M	Forces and moments
IDVD	Inverse Dynamics Calculation in the Virtual Domain
ISS	International Space Station
LGL	Legendre-Gauss-Lobatto
MRP	Moment Reference Point
MTOM	Maximum Take-Off Mass $[kg]$

MUSCL	Monotone Upstream-centred Schemes for Conservation Laws
NATO	North Atlantic Treaty Organisation
NASA	National Aeronautics and Space Administration
NLP	Non-Linear Programming
ONERA	The French Aerospace Lab
PIV	Particle Image Velocimetry
PMB	Parallel Multiblock
PMP	Pontryagin Maximum Principle
PS	Pseudospectral Methods
RANS	Reynolds Averaged Navier-Stokes
RLE	Round Leading Edge
RTO	Research and Technology Organisation
SACCON	Stability And Control Configuration
SLE	Sharp Leading Edge
TVD	Total Variation Diminishing
TNT	Turbulent Non-turbulent
UCAV	Unmanned Combat Air Vehicle
UKAAC	United Kingdom Applied Aerodynamic Consortium
URANS	Unsteady Reynolds Averaged Navier-Stokes

Chapter 1

Introduction

An adequate understanding of the aerodynamics of an aircraft is of utmost importance in aircraft design. Despite this, in a traditional aircraft design process, it is at a relatively late stage that an accurate prediction of the aerodynamic loads becomes available, obtained from wind tunnel experiments or flight tests. Any major changes in the configuration late in the design can dramatically increase costs. For this reason since the 1960's, simulation methods have been adopted throughout the design stages as fundamental engineering tools [1]. Analytical engineering methods have been heavily relied on to provide estimates of aircraft force and moment characteristics. These mainly empirical methods can be insufficient, particularly when a configuration lacks any empirical support. More reliable first principles computational methods have been developed and implemented. The potential to use numerical methods has progressed since the start of the digital era and great strides have been made in the fields of structural analysis, flight simulation and fluid dynamics which have been widely documented in the literature. Numerical aerodynamic prediction tools are commonly referred to as Computational Fluid Dynamics (CFD). The challenge nowadays is to obtain the best performance out of these methods with the minimum amount of effort and cost and in a manner that integrates with other disciplines in the engineering design process.

The prediction of reliable aerodynamic data can also be of great value for purposes other than aircraft design. Loss of Control In-flight (LOC-I) is the number one cause for fatalities in the commercial jet sector as reflected in Boeing's Summary of Commercial Jet Airplane Accidents [2], accounting for 37% of the total recorded fatalities from 2001 to 2010. In an attempt to reduce this number two possible approaches are most promising, improved pilot training and technology development. Training has strongly benefited from the development of flight simulators over the past decades although these are only as good as the models which drive them. Currently, the aerodynamic data ends well before the extreme flight conditions an aircraft may encounter in real flight. The use of flight simulators for training past these limits could yield pilot response to an inappropriate simulator behaviour. Acquiring this data from flight tests is impractical

1

and dangerous for the commercial type of aircraft although it is vital for adequate pilot training [3]. Hence, it is clear that there is a demand for high fidelity aerodynamic data throughout the operational flight envelope and beyond. Technological developments such as Fly by Wire (FBW) systems can potentially reduce this type of occurrence, although it is the case that to design and improve these systems a good knowledge of the aerodynamic behaviour throughout the flight envelope is required. It is an important open question as to how much fidelity in aerodynamic prediction is enough for such applications.

In the military sector, a major development in recent years has been the establishment of Unmanned Air Vehicles (UAVs) for a wide range of military operations. These span from Surveillance, Reconnaissance and Intelligence (ISR) to "persistent strike" functions [4]. As the technology matures new designs will keep replacing traditional manned aircraft operations. From an engineering point of view, new challenges are present in aircraft design. The removal of human survivability constraints has widened operational envelopes allowing for new design concepts. In turn, this requires an extensive study of the aircraft's performance from the conceptual stages of the design process. The autonomous nature of these aircraft requires a good understanding of flight dynamics behaviour prior to adequate control law design. Moreover, the blunt leading edge and low angle wing sweep of typical Unmanned Combat Air Vehicles (UCAVs) has not been studied as extensively as traditional highly swept wings. These configurations have been adopted more recently for reasons other than aerodynamics, mainly signature. This type of configuration has proven to be a challenging case for CFD solvers, as will be seen in this study.

Aerodynamic method validation	Aerodynamic data base generation	Assessment of aerodynamic model
-CFD prediction	-Systematic static & dynamic simulations	-Manoeuvre prediction using DIDO
-Wind Tunnel prediction	-Kriging interpolation	-Evaluation of tabular load predictions
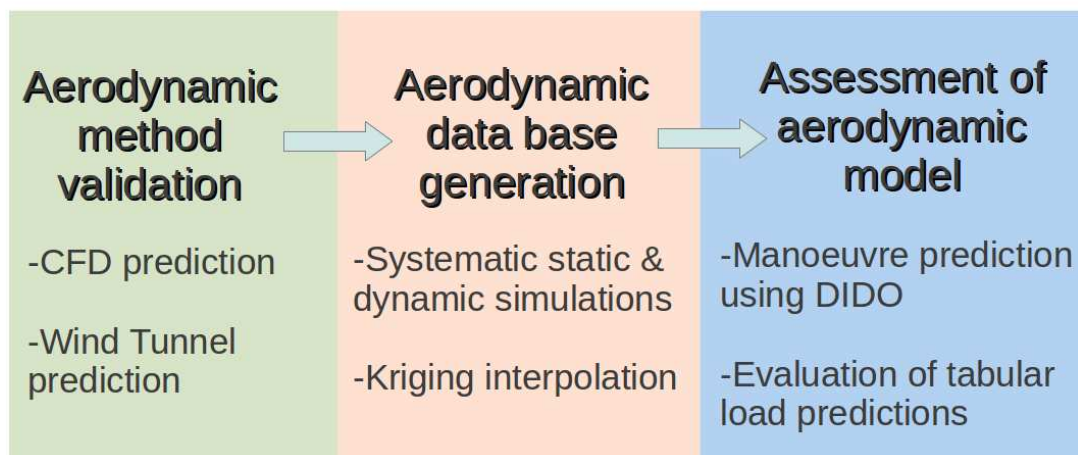
Figure 1.1: Flowchart of process described in this thesis.

The work presented here aims to demonstrate the application of CFD to flight

dynamics problems. Figure 1.1 shows the process that has been developed for the purpose of this study. This involves the efficient generation of flight dynamics models using CFD, the prediction of realistic time-optimised manoeuvres and the evaluation of tabular models for loads prediction in aircraft manoeuvering flight. The first step in the process was to validate the aerodynamic prediction tools available against wind tunnel measurements. Then, the efficient generation of a tabular aerodynamic database to be used for flight dynamics purposes. At this stage, systematic CFD simulations are carried out and the data is used to populate the data base using Kriging interpolation. The final step in the process is to evaluate the validity of the CFD based model by predicting realistic aircraft manoeuvres using an optimal control commercial tool called DIDO. Aircraft loads during manoeuvre trajectories can be predicted and compared using the tabular model and a time-accurate CFD simulation. This thesis first describes some of the previous work carried out in the field of delta wing aerodynamics and aircraft manoeuvre prediction methods. Then, an overview of the CFD solver used for this study is given. The thesis continues with a description of the UCAV test case and a validation of the CFD predictions using wind tunnel measurements. The selection of this test case was made because it is a very suitable configuration but also due to the large amount of valuable wind tunnel data available through the AVT-161 project in which the author participated. This is followed by a description of the generation methods for aerodynamic models and realistic manoeuvres. The predicted manoeuvres are then used to assess the validity of the generated model by comparing against a time-accurate forced motion simulation. Finally conclusions are given, together with possible future work.

Chapter 2

Literature Survey

The current understanding of vortical flow behaviour over delta wings is reviewed in Ref. [5] where a distinction is made between slender and non-slender wings, the latter being those with a leading edge sweep angle lower than 65°. Non-slender delta wings have recently become an important area of aerodynamic research due to their increasing use for UCAV configurations. Although much of the existing knowledge on vortical flow structures is related to slender delta wings, these flows make a relevant comparison with those of non-slender delta wings. One of the main differences between the two is that two primary vortices occur over the lower leading edge sweep wings at high angles of attack. These two vortices are distinct and have the same sense of rotation whereas a single primary vortex structure is present for the slender wing.

For a slender, sharp edged delta wing boundary layer separation is at the leading edge. As a result of this, a free, three-dimensional shear layer emanates from the wing's leading edge which initiates a primary vortex, as illustrated in Fig. 2.1. The regions of high vorticity at the core are surrounded and continuously fed by the shear layer. When the primary vortex interacts with the boundary layer on the upper surface of the wing it gives rise to boundary layer separation and the formation of a secondary vortex of the opposite sign of vorticity. A tertiary vortex may take place underneath the secondary one depending on the nature of the boundary layer and the viscosity of the flow. The flow through the symmetry plane of the body remains attached.

At the centre of the core the axial velocity reaches its maximum value and decreases radially. The vorticity and circulation values are associated with the vortex strength which varies with the angle of attack and sweep. Generally, increasing either of these angles produces stronger vortices. For sharp edged wings, Reynolds number is thought to have a noticeable effect on the secondary and tertiary structure formations but not on the primary vortex. This is because, for a sharp edged wing at a low angle of attack, a separated shear layer will always be produced at the leading edge yielding the primary vortex. The magnitude of the Reynolds number has a strong influence on the nature of the boundary layer and, hence, the formation of secondary and tertiary structures. Due

to the high rotation of the flow in the vortex core a region of low local static pressure is produced yielding a suction force on the upper surface called non-linear or vortex lift.
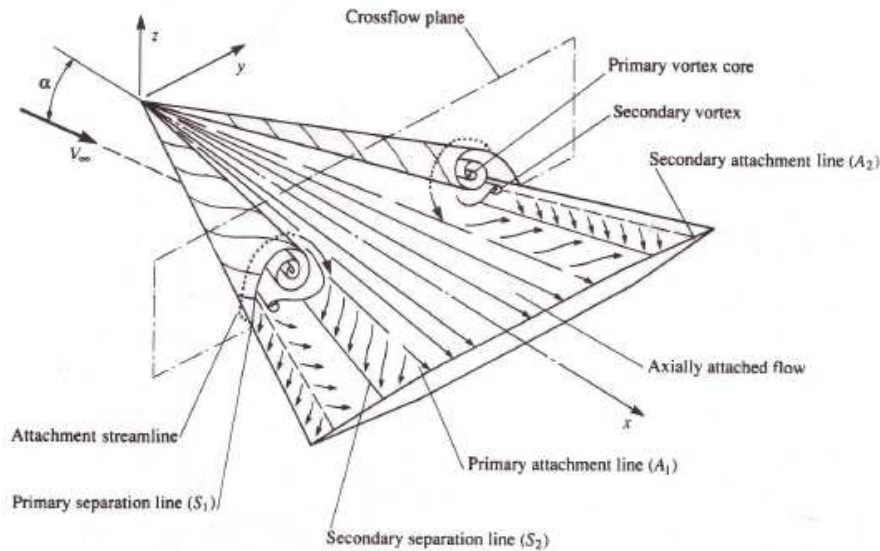
Figure 2.1: Illustration of the primary and secondary vortices formed over a slender wing [6].

The swirl has two peaks of opposite magnitude at a radial distance from the core and the region contained within them is called the viscous subcore. Immediately after this region is the inviscid rotational core which, at the same time, is surrounded by the free shear layer and its vortical substructures. The shear layer may exhibit instabilities which give rise to vortical substructures and progressively increase the thickness of the primary vortex as it extends downstream. A vortex which extends axially over the solid, may reach a point of dramatic flow disruption, termed vortex breakdown, at which the axial flow is known to stagnate. This takes place due to internal and external instabilities and its location travels upstream as the angle of attack is increased. The angle at which breakdown crosses the trailing edge of the wing is commonly known as the critical angle of attack and when it reaches the apex, the wing is known to be stalled. Downstream of the vortex breakdown the flow may take one of two forms: a spiral or a bubble vortical behaviour, as illustrated in Figure 2.2. The case for highly swept wings is for the vortex to transform into the latter which rotates in the swirl direction, winding opposite to the vortex swirl and around the stagnant flow region [7].

The time averaged representation of a spiral breakdown results in single-celled bubbles of reversed axial flow with both front and aft stagnation points. The bubble breakdown is an axisymmetric behaviour with a stagnation point on the vortex core and a region of reversed axial flow downstream from it. The remaining flow passes around this bubble as a bluff body. In both types, a further breakdown takes place into

6
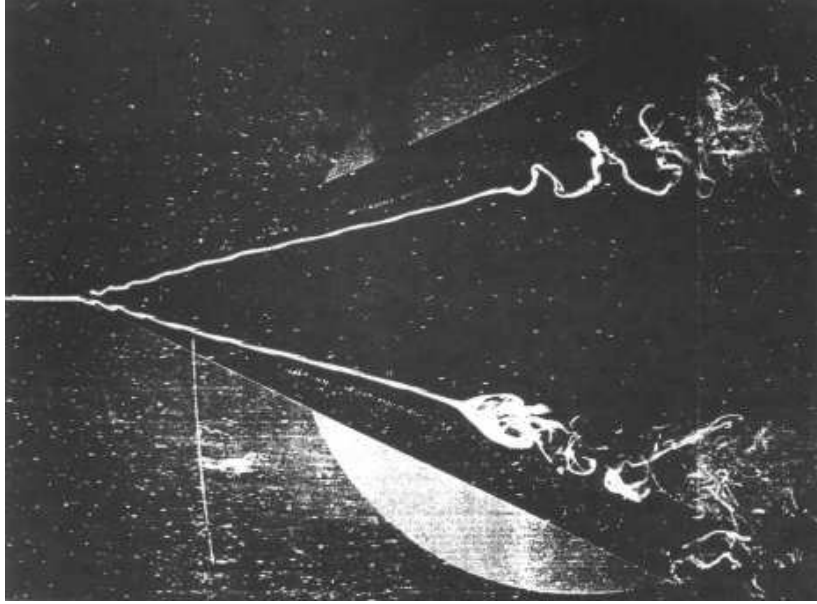
Figure 2.2: Visualisation of spiral and bubble forms of vortex breakdown [7].

large scale turbulent flow downstream.

Gursul et al. [5] describes the post-breakdown region as where the primary vortex core disintegrates into a large number of fine-scale, highly unsteady flow features. Only a large region of vortical flow made up of these small structures can be distinguished. In the case of highly swept wings, the secondary flow also follows the same pattern which is why pockets of opposite sign vorticity can still be seen in this unsteady region. It is also possible to find pockets of reversed axial flow in the breakdown region, as described later, with a large region of fluctuating kinetic energy.

Yaniktepe and Rockwell [8] identified three stages in the low sweep delta wing vortex breakdown process. First, small scale undulations, or spiralling, occur at the vortex core associated with the shear layer instabilities and the onset of breakdown. Secondly, the filament is seen to thicken and become small again at what is defined as the pinch off region, as described by Gursul [5]. Finally, breakdown occurs characterised by an abrupt expansion of the filament where the particles are diffused over a broad area. An increase in pressure accompanies this broken down flow region for which some examples are shown in Section 4.3.2.

An important characteristic describing the vortex stages is the axial flow velocity through the core. For the slender wing case, the axial flow decelerates downstream of the breakdown location, changing from a jet-like to wake-like type of flow. The onset of this is very abrupt and the core can expand by a factor of 3 of its original cross-sectional area. It can be defined as the point of maximum upstream penetration of the reversed axial flow [9]. According to Gursul et al. [5], for his non-slender wing ($\Lambda = 50°$) at

angles of attack above 10° the vortex core upstream from breakdown has a jet-like flow. After breakdown, the flow slows down and becomes wake-like. At lower angles of attack the jet-like region is no longer present, although the flow in the core upstream from the vortex breakdown has a higher velocity than that downstream from it, as shown in Fig. 2.3. The switching point pinpoints the location of vortex breakdown. Nonetheless, the breakdown of high sweep configurations is more abrupt. The experiments carried out by Ol and Gharib [10] at a Reynolds number of $1.54 \cdot 10^4$ on a 65° swept back wing demonstrate a nearly linear increase in peak vortex core velocity as the angle of attack is increased, which is not the case for a non-slender wing. Their results prove the jet-like and wake-like behaviours of the slender and non-slender configurations with slight discrepancies at the angles of attack at which they occur. These could be attributed to the influence of the Reynolds number. Reducing this number drives the flowfield toward a state of unperturbed freestream. It was shown that as the Reynolds number decreases lower variations and smaller gradients are seen for the axial and azimuthal velocities throughout a given flow structure.
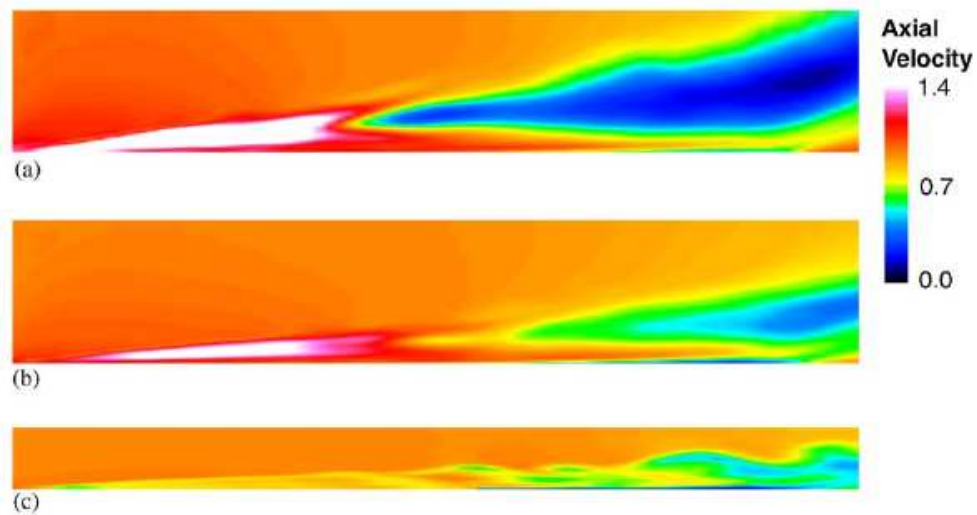
Figure 2.3: Mean axial velocity contours in a plane through the vortex core: (a) $\alpha = 15°$, (b) $\alpha = 10°$ and (c) $\alpha = 5°$, I. Gursul et al. [5].

Taylor et al. [9] concluded from an experimental study with a 50° sweep delta wing at a freestream Reynolds number around $3 \cdot 10^4$ that an elongated region of separated flow transforms into a dual vortex structure. This occurs further downstream from the formation of the primary vortex. Here, as the secondary flow separates from the body surface, it impinges on the separated shear layer emanating from the leading edge splitting it into two vortices of the same sign, as shown in Fig. 2.4 (a). This gives rise to the second primary vortex which is slightly weaker and smaller than the first vortex. Experiments carried out on a sharp 2% thick delta wing with a sweep of 50° at

Reynolds numbers of 10^4 [9] demonstrated that dual vortical flows may occur at angles of attack as low as 5°. As the incidence was further increased to 15° the clear dual vortex structure disappeared to form a structure that resembles those of highly swept wings, with primary, secondary and tertiary vortices. Therefore, it can be said that the splitting of the primary vortex into two by the boundary layer vorticity disappears as the angle of attack is increased. Ol and Gharib [10] performed a similar experiment and came to the same conclusion. Their results can be seen in Figure 2.4 (b).

(a) Computed illustration of a dual vortex structure over a 50° leading edge sweep, delta wing at $\alpha = 5°$ [5].

(b) Crossflow vorticity field at a section across the vortices for a 50° leading edge sweep, delta wing at $\alpha = 7.5°$ [9]
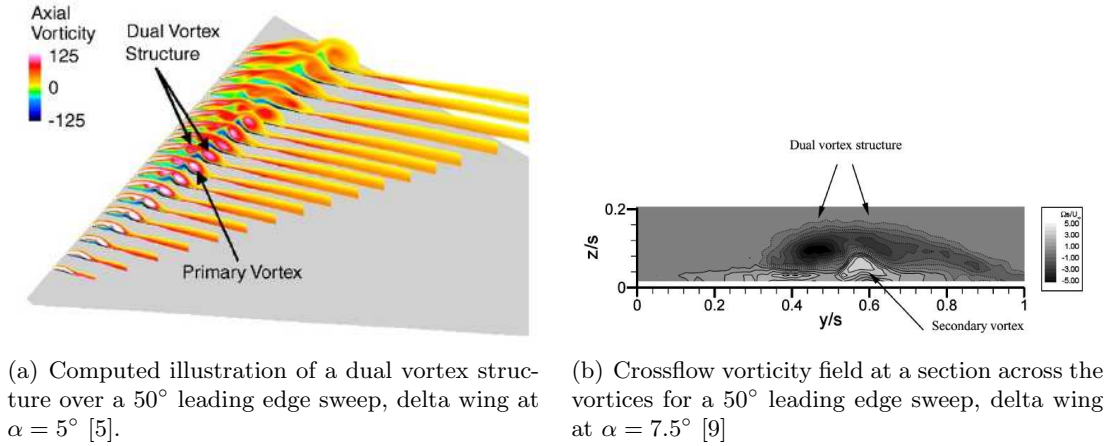
Figure 2.4: Illustration of dual vortex structures.

Figure 2.5 shows an experimentally obtained streamline pattern for the sharp edged, 50° sweep delta wing at 15° angle of attack [5]. The positions of the primary, secondary and tertiary attachment and separation lines can be seen for that case as PA, SA, TA and PS, SS, TS, respectively. This shows that secondary and tertiary vortices can occur over non-slender configurations, as shown in Section 4.3.2 in this thesis.

With increasing incidence, the attachment boundary moves inboard towards the wing's centre line until this line is no longer visible, corresponding to wing stall. It is interesting to follow the development of these regions as the angle of attack is varied from 0° to 25°, illustrated by Taylor et al. [9] in Figure 2.6. For the case of an angle of attack as low as $\alpha = 2.5°$, coherent leading edge vortices can be seen. These are recognised by the spanwise dyed flow patterns ranging from the primary attachment to the secondary separation lines.

When $\alpha = 10°$ is reached, the initial primary vortex becomes much more prominent than the second and gets shifted away from the surface and inboard on the wing. The flow patterns at $\alpha = 15°$ show a primary reattachment line downstream from the apex which then soon fades away, meaning that the vortex has broken down with its consequent expansion. At $\alpha = 21.25°$ breakdown shows an effect on the secondary separation line which is seen to kink and move away from the leading edge downstream of this point. Beyond this angle of incidence, the location of the kink moves rapidly
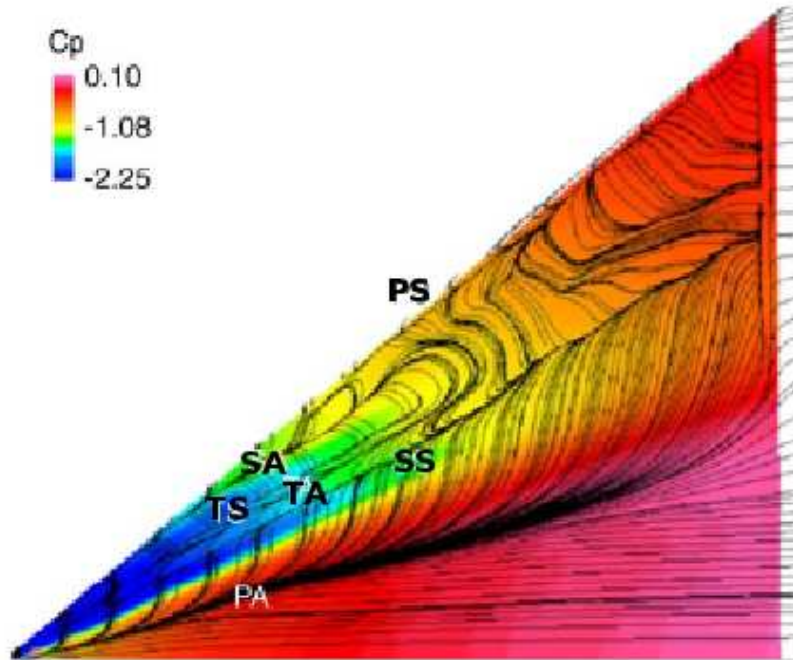
Figure 2.5: Experimentally obtained surface streamline patterns and pressure coefficients for a 50° leading edge sweep, delta wing at $\alpha = 15°$ [5].

upstream and stalled flow covers the wing surface. This evolution of the vortex structure as the angle of attack increases demonstrates the increasing similarity with the structure seen for slender bodies in terms of growth of the main vortex structure and upstream movement of the breakdown location with increasing angle of attack.

A direct comparison was made by Woods [11] between a slender (60° sweep) and a non-slender (40° sweep) lambda wing using wind tunnel experiments at a Reynolds number of $2 \cdot 10^6$. His results agree with the vortex behaviour seen by Gursul et al. [12], Taylor et al. [9] and Ol and Gharib [10] which suggests a similarity between delta and lambda wing flow behaviour, shown in Figure 2.7. Over the non-slender wing a dual vortex structure was present at $\alpha = 10°$. The second primary vortex was seen to reduce in size as the first primary vortex became dominant at $\alpha = 15°$ and an enlarged single primary vortex was present at $\alpha = 20°$ with reversed flow occurring over most of the top surface. The highly swept wing images show the path of the primary vortex at $\alpha = 10°$ and $15°$ where it is clear that the core does not move inboard as rapidly as the lower swept case.

As happens with slender wings, as the angle of attack is increased, the flow over the non-slender wing tends to become unsteady. Upstream from the vortex breakdown location, the shear layer manifests instabilities in its outer part that surrounds the rolled up vortex core. These instabilities are seen as smaller vortices that are shed from the shear layer and convected downstream and around the primary vortex core. It was
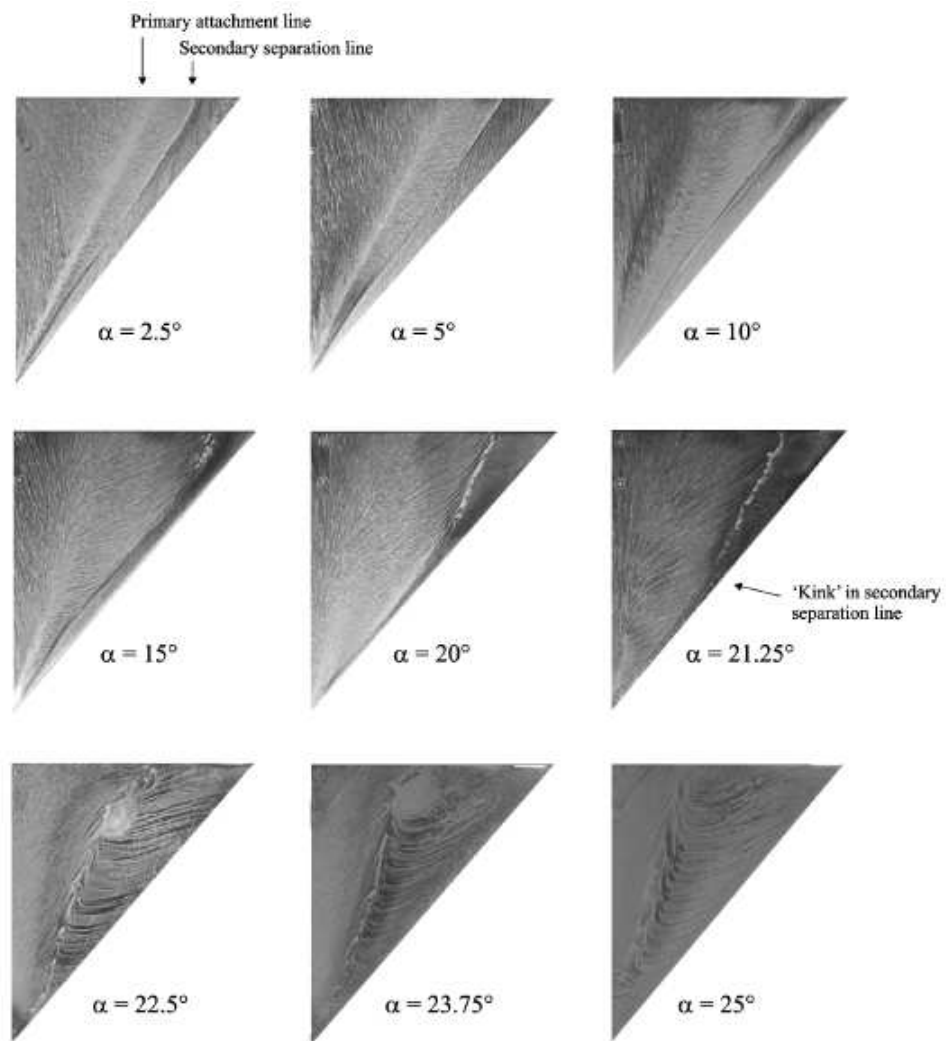
Figure 2.6: Surface oil visualisation of the flow over a sharp edged, $50°$ leading edge sweep, delta wing at $\alpha = 0° - 25°$ [9].
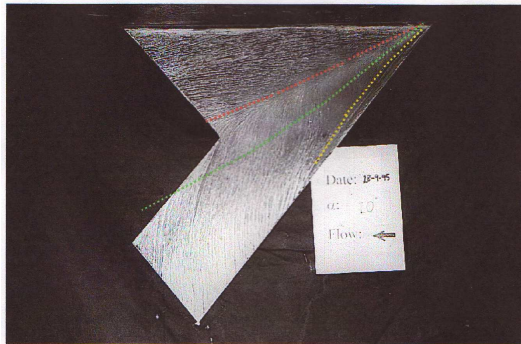
(a) $\Lambda = 40°$ at $\alpha = 10°$
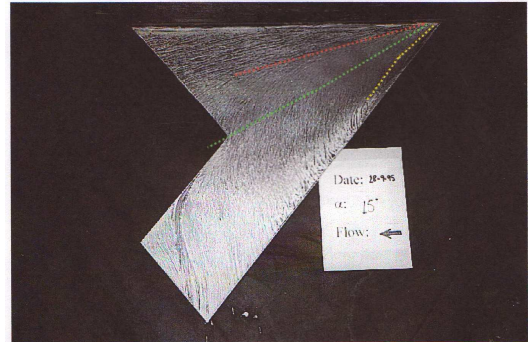
(b) $\Lambda = 40°$ at $\alpha = 15°$
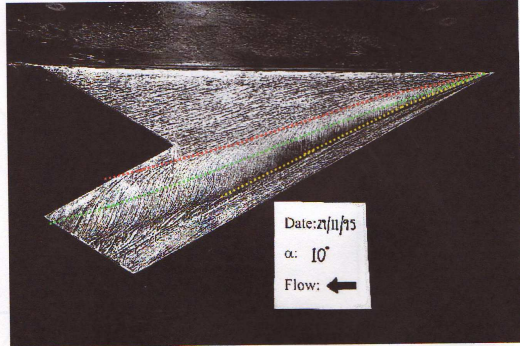
(c) $\Lambda = 60°$ at $\alpha = 10°$
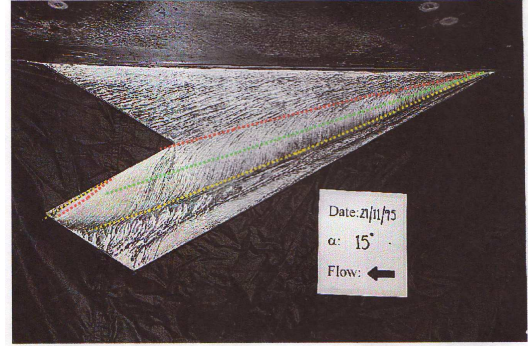
(d) $\Lambda = 60°$ at $\alpha = 15°$

Figure 2.7: Experimental flow visualisations of two different lambda wings at $Re = 2 \cdot 10^6$ [11].

noticed by Gad-el-Hak and Blackwelder [13] that this vortex sheet rolls up periodically into these vortical substructures. Another effect of this flow instability leads to vortex wandering around the mean core location in the y-z plane. This leads to the vortex core moving in an oval pattern in the same sense of rotation as the vortex swirl.

It is seen that for non-slender wings the post-breakdown behaviour is similar to that of slender wings, in the sense that a spiral mode can be recognised as shown by Gursul et al. [5] although not as abrupt. It is relevant to notice that the instabilities do not necessarily occur symmetrically over full wing configurations experimentally or in computations. The variation of streamwise vortex breakdown location on each side of the configuration can affect the lateral characteristics of the aircraft. The resulting asymmetric load distribution can yield significant lateral activity. The frequency of the breakdown oscillation and the magnitude of the resulting loads will determine how much impact these have on the overall performance. For slender wings, fluctuations of up to 10% of the chord length have been observed [5], whereas for non-slender wings, up to 50% variation along the chord has been registered [10]. Taylor et al. [9] showed that the vortices disintegrate and reform on a quasi-alternating basis in the range of $12.5° − 17.5°$ where oscillating motions reached an amplitude of 40% of the chord.

Experiments carried out by Miau et al. [14] on a $50°$ sweep delta wing at a free stream Reynolds number of $7 \cdot 10^3$ investigated the role of the leading edge shape in the overall flow behaviour. They looked at the flow over several different types of sharp, round and blunt leading edges and noticed differences in the streamlines and the vortex paths. More specifically, the shapes with bevelling on the windward surface had a leading edge vortex at $10°$ angle of attack whereas those with blunt shape or bevelling on the leeward surface did not. Figure 2.8 shows a schematic of the two types of sharp leading edge shape and the flow around it. Also, the rounded geometry developed a leading edge vortex further downstream than the sharp one, at 20% of the chord. It was concluded that the initial trajectory of the separated shear layer is what determines the overall vortex behaviour on the upper surface.
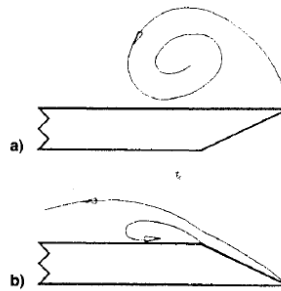
Figure 2.8: Illustration of the windward (a) and leeward (b) surface bevelling [14].

Previous references in this text referred to studies performed at relatively low

Reynolds numbers. Gordnier et al. [15] carried out a study on a 50° sweep delta wing looking at the influence of the Reynolds number on the resulting vortical flow. Their computations and experiments focused on the unsteady behaviour of the flow at three Reynolds numbers: 2 x 10^5, 6.2 x 10^5 and 2 x 10^6. They concluded that the vortex breakdown location moved upstream and then downstream again with helical substructures becoming more numerous in the shear layer and developing further upstream as the Reynolds number increased. It is important to mention that studies with varying leading edge geometry are rare.

According to Gursul et al. [5] non-slender delta wings have lower maximum lift coefficients and steeper lift curve slopes than slender delta wings, which agrees with experimental results shown in Fig. 2.9. This could be caused by a lower lift contribution from vortex suction over the the non-slender wing since these produce weaker vortices and, therefore, lower suction peaks. The fact that the primary vortex breakdown travels upstream over the low sweep wing at a faster rate causes the early stall and subsequently a lower maximum lift coefficient. The drag coefficient patterns show a better behaviour for the non-slender wing which reaches a lower value at stall than the slender wing.

(a) C_L vs α (b) C_D vs α
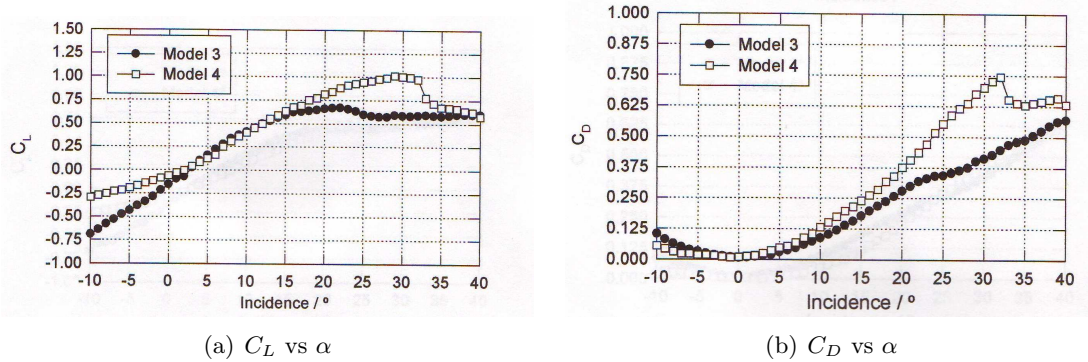
Figure 2.9: Experimental values for two lambda configurations of $\Lambda = 40°$ (Model 3) and $\Lambda = 60°$ (Model 4), [11].

The leading edge shape has been demonstrated to have an important effect on the vortex formation over the top surface of a non-slender wing. Windward bevelled leading edges at an angle of attack are the shapes most likely to produce vortical flows over the wing's top surface. Separation takes place at the leading edge and the emerging shear layer will roll up into a vortex structure. On the other hand, the round shaped leading edge does not guarantee separation at this point which delays the formation of such structures downstream from the apex. It can therefore be concluded that the leading edge profile determines the initial state of the separated shear layer and, consequently, the trajectory above the delta wing. Although, Gursul et al. [5] provides evidence that at higher Reynolds numbers the effects of leading edge shape on the prestall region of the flow are smaller in terms of lift coefficient. It can be seen that there is a variation

in stall angle due to this geometric factor, as shown in Figure 2.10.
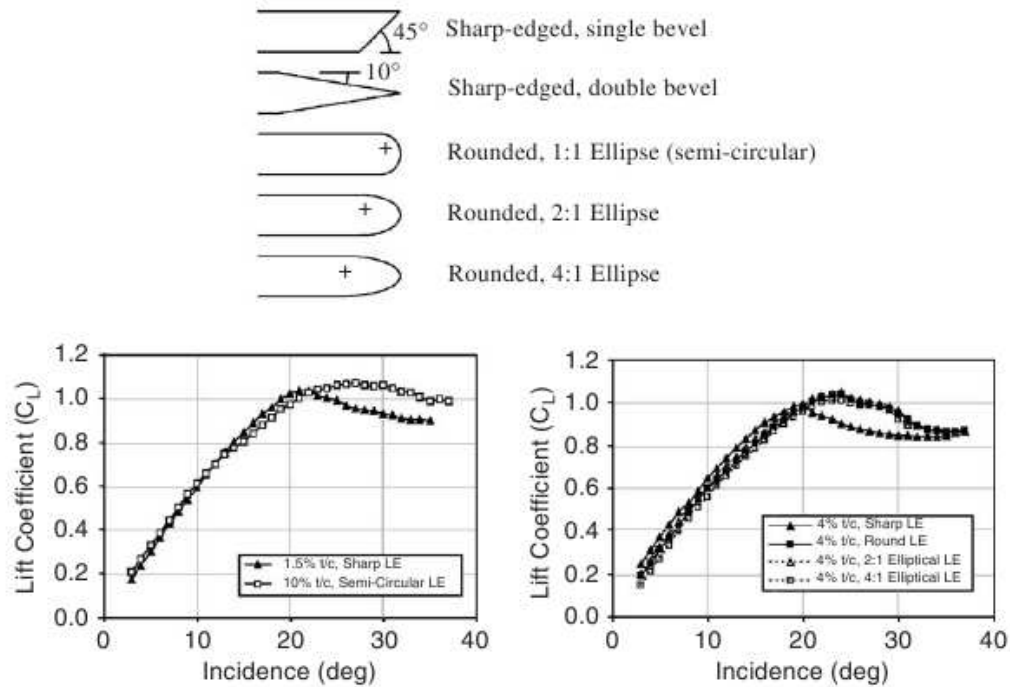
Figure 2.10: Variation of lift coefficient with angle of attack for various leading edge shapes and thicknesses, Gursul [5].

So far in this section we have seen that the leading edge sweep angle and profile distribution are two important characteristics determining the flow topology around delta wings. The literature has shown that weaker vortices occur as the sweep angle of a wing is reduced, although their influence on the overall aerodynamic loads is still predominant at high angles of attack. Non-slender wings show an interesting non-linear behaviour in the early post-stall region. It can arise as a dual vortex structure or as unsteady vortex wandering or vortex breakdown motion.

Understanding the aerodynamics of aircraft in motion has been the purpose of various wind tunnel campaigns since the late 1970s. Since that time, a wide range of test rigs has been designed to recreate simple oscillatory motions [16]. More recently, Rein et al. [17] modelled complex manoeuvres using novel rig designs for fighter configurations such as the X-31. Many details were included in the model geometry including moving control surfaces and motions based on previous flight tests. Issues such as Reynolds number similarities, ground effects and fluid-motion coupling are present, as described by Ericsson and Beyers [18].

More recently, with the introduction and development of CFD tools, accurate predictions of the aerodynamic behaviour have become available at an early stage in the design. Known non-linear effects such as flow surface separation, vortical flow and

shock wave formation can be predicted with confidence in the results. A recent study by Knight et al. [19] assessed the capabilities of a range of CFD codes to accurately predict shock wave formation over conical and cylindrical test cases. Results were compared with experimental measurements with good agreement overall with the exception of a low enthalpy, high Reynolds number test case in which the numerical methods disagreed. The use of CFD methods for flow separation and vortical flow prediction for a range of Reynolds and Mach numbers has been discussed previously in this chapter and good agreement has been seen with wind tunnel measurements. The CFD code used in this study, Parallel Multiblock (PMB), has been validated over the last twenty years for a wide range of flows. A detailed description of the numerical method is given in Chapter 3. Schiavetta et al. [20] investigated the effects of shock wave interaction with vortex breakdown for a slender delta wing configuration. The predictions from PMB were validated against wind tunnel measurements and other numerical methods with good agreement between the sources. The small scale turbulent structures occurring inside and donwstream from a UCAV weapons bay was investigated using PMB by Lawson et al. [21].

State of the art CFD simulations can be used for early detection of unwanted effects regarding structural integrity, noise or stability and control behaviour, amongst others. Extensive validation work has been carried out using PMB for a range of cases from fixed wing to rotorcraft aerodynamic simulations coupled with aeroelastic models [22, 23]. Marques et al. [24] studied the effects of ice over wing aerofoils and evaluated the detrimental effect of such occurence on the aerodynamic performance.

In an attempt to extend the use of computational methods, considerable effort has focused on predicting flight dynamics performance of aircraft based on a range of aerodynamic and flight dynamic models. Kruger [25] described a method which coupled linear aerodynamic strip theory with the equations of motion and a structural model based on a Multi Body System (MBS). Control over the motion was achieved by introducing changes to the local lift forces at the sections where the control surfaces were located. Important differences were noted between simulated pull-up manoeuvres for rigid and flexible aircraft. A more complex aerodynamic model was used by Costello and Sahu [26] in their study of projectile flight trajectories. Their aim was to validate a rigid body simulation of a projectile with spark range testing results. A full Reynolds Averaged Navier-Stokes (RANS) method was used in a time-accurate manner. The forces and moments computed by the CFD are transferred to the six degrees of freedom (DoF) equations of motion. Results show the free response behaviour of the projectile to control inputs.

A study by Koyuncu et al. [27] looked at the prediction of UCAV flight paths for real time simulation. In this case, the focus was flight in built up areas and collision avoidance. The path prediction was made in three steps, first the shortest, obstacle

free path from the start to finish is found. Using agility metrics, the manoeuvre is split into a sequence of elemental maneouvres in time, such as level flight, climb, descent, roll, etc. Finally, a feasibility study is made to determine whether it is dynamically possible for the aircraft to achieve the manoeuvre. The dynamics feasibility is assessed using the state boundaries of a flight envelope and maximum and minimum values for structural loads and control surface actuator saturation.

A recent study by McDaniel et al. [44] looked at the possibility of using System Identification (SID) [45] for the purpose of manoeuvring flight prediction. This approach relies on the aerodynamic characteristics of an aircraft in forced oscillatory motion. From this data, a set of polynomial equations relating the input variables to the output force and moment characteristics is obtained using a SID approach. In this study, a pitching motion was simulated and a model was identified for the C_L and C_m behaviour. Validation of this approach showed a good prediction of the dynamic terms but some discrepancies in the static aerodynamic coefficients due to the lack of static information. Extending this work, the same excitations could be simulated in the roll and yaw axes to produce a six degrees of freedom identified model.

Work carried out by Basset et al. [28] compared results from four direct methods for the solution of optimal aircraft manoeuvres. A basic problem is defined for a generic UAV. Simple state and control vectors are defined as well as dynamic functions which drive the motion. Solutions from two Pseudospectral Methods (PM), namely a Gauss PM [29] and a Legendre-Gauss-Lobatto (LGL) PM [30, 31, 32], are compared with classical Pontryagin Maximum Principle (PMP) [33] results and predictions from an Inverse Dynamics Calculation in the Virtual Domain (IDVD) method [34]. Overall the PMP is thought to be the most reliable and the IDVD the most cost effective for real-time calculations. The two PM methods produced good flight path predictions although the Gauss approach suffered from initialisation problems and the LGL from oscillations in the control prediction. These oscillations could lead to unfeasible control commands. The aerodynamic behaviour relied on the drag polar approximation for C_D and C_L as a function of the load factor.

A commercial tool known as DIDO, which makes use of the LGL PM method, has been successfully used for a range of optimisation problems. In March 2007, the International Space Station (ISS) was rotated by 180° without thrusters in a manoeuvre that would normally require $1,000,000$ worth of fuel [35]. This was accomplished by applying this optimisation method in order to minimise the use of the thrusters. Correct simulation results using this method required an adequate modelling of the environment and how this may effect the body dynamics. This included differential in the gravitational pull on different parts of the ISS due to its proximity to the Earth and aerodynamic drag forces causing moments about the centre of mass. Simulations were run on a typical desktop computer in a matter of hours and results obtained as a

sequence of discrete states and controls along the duration of the manoeuvre.

A similar application of this method was successfully demonstrated by Shekhavat et al. [36] to manoeuvre the NPSAT1 satellite built at the Naval Postrgraduate School in the United States. Control over the satellite motion is achieved using magnetic actuators and a pitch momentum wheel for attitude control. In this case, the computations are performed online and the control commands are constantly being updated as new simulations reach convergence. A more detailed description of the equations of motion and the numerical approach used for such satellite applications is given by McFarland [37].

Other documented applications of DIDO to engineering problems include onboard implementation for autonomous reusable launch vehicles [38] and optimisation of power output from large wind farms with varying throughput [39].

Kriging interpolation has been successfully used for a range of applications to obtain predictions of a certain variable distribution within a known domain. Zhu et al. [40] demonstrated its applicability to land moisture predictions for agricultural and forested landscapes. Paiva et al. [41] showed how Kriging can be successfully used as a surrogate model for aircraft wing design optimisation. A comparison was made between a quadratic interpolation based method, Kriging and artificial neural networks for the same test cases. Kriging and neural networks were found more appropriate for high dimensionality problems with a significant reduction in computational effort. Similarly, a surrogate model based on Kriging interpolation was used by Huanga et al. [42] for engine disc design based on a few finite element calculations. The objective in this case was to obtain a minimum mass design under high thermal and mechanical loads. Timme et al. [43] made a study on transonic aeroelastic instabilities using a Kriging approach. A transonic flight envelope was populated using CFD simulations for the Goland wing and a generic transport aircraft wing. In this case Kriging allowed to reduce the computational effort from a number of expensive time-dependent CFD simulations to around twenty, less expensive, steady state calculations. A significant amount of literature is available on the range of applications of this surrogate model method. One of the most valuable advantages of Kriging interpolation for the purpose of this work is its capability to handle large multidimensional variable spaces.

In this section, the aerodynamic behavoiur relevant to this work has been defined as documented in the literature. Some of the tools relevant to the process that has been developed have also been described as well as their capabilities. Figure 2.11 shows a detailed description of this process. Initially, sampling is carried out inside the aerodynamic model envelope and Kriging is performed to interpolate within this domain. This process is repeated until the desired fidelity of the model is obtained. This model consists of tables of aerodynamic data, such as coefficients of forces and moments, which depend on flow characteristics, such as Mach number and angle of attack. A flight
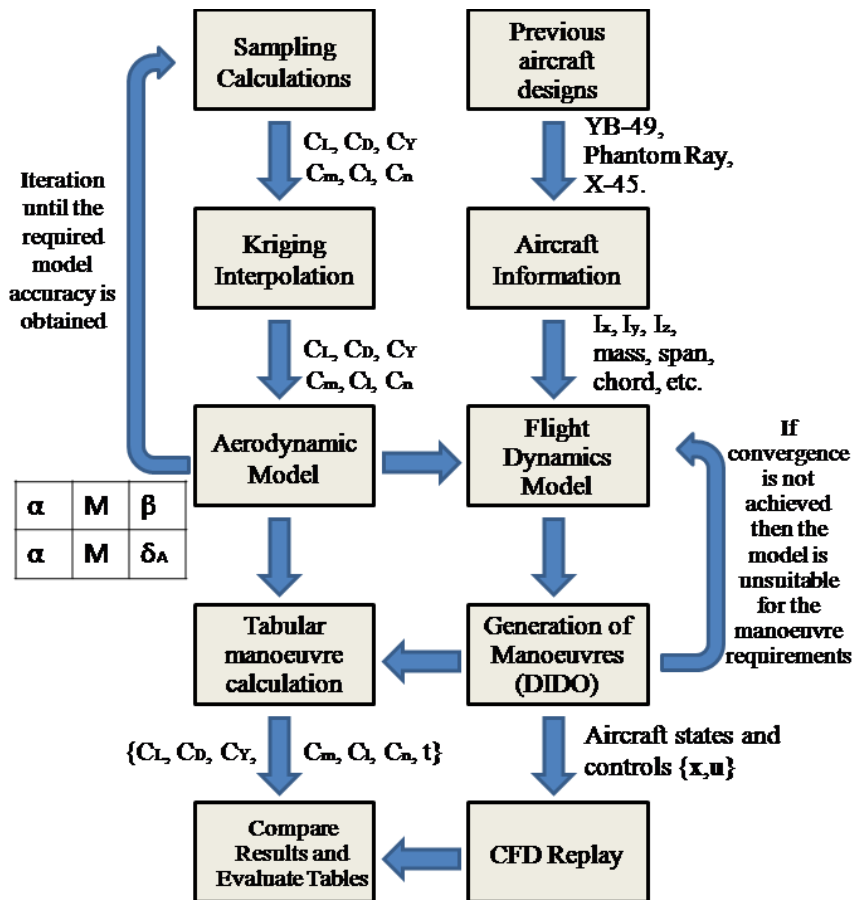
Figure 2.11: Flowchart of process described in this thesis.

dynamics model is generated using the aerodynamic data and geometry approximations based on similar aircraft designs. Manoeuvres are then designed and calculated based on this model. If convergence is not achieved either the model is unrealistic or the manoeuvre is over-demanding. A CFD simulation of the manoeuvre is performed and the resulting force and moment data is compared with tabular predictions. These comparisons allow the evaluation of the tabular model for aircraft manoeuvre load predictions.

Chapter 3

Formulation

3.1 CFD Method

The PMB solver is the primary CFD tool used throughout this thesis. It is a research based code developed over the past fifteen years at the Universities of Glasgow and Liverpool. This study makes use of this code and the RANS equations for both static, steady-state simulations and unsteady, forced-motion calculations. The current section highlights the key aspects of the code which are relevant to the current work.

3.1.1 Navier-Stokes Equations

The Navier-Stokes equations form the basis of the CFD formulation. Here, a brief description of the basic formulation is given. We start with the definition of the equations of mass, momentum and energy conservation.

Continuity equation

The continuity equation is obtained from the conservation of mass and is given as,

$$\frac{\partial \rho}{\partial t} + \frac{\partial (\rho u)}{\partial x} + \frac{\partial (\rho v)}{\partial y} + \frac{\partial (\rho w)}{\partial z} = 0 \tag{3.1}$$

where ρ is the density, t is time and $\mathbf{V}$ is the velocity vector composed of u, v and w components in Cartesian axes.

Momentum equations

The momentum equations are obtained from Newton's second law in the Cartesian x, y and z directions, as follows

$$\begin{aligned}
\frac{\partial (\rho u)}{\partial t} + \frac{\partial (\rho u u)}{\partial x} + \frac{\partial (\rho u v)}{\partial y} + \frac{\partial (\rho u w)}{\partial z} &= -\frac{\partial p}{\partial x} + \frac{\partial \tau_{xx}}{\partial x} + \frac{\partial \tau_{yx}}{\partial y} + \frac{\partial \tau_{zx}}{\partial z} + \rho f_x \\
\frac{\partial (\rho v)}{\partial t} + \frac{\partial (\rho v u)}{\partial x} + \frac{\partial (\rho v v)}{\partial y} + \frac{\partial (\rho v w)}{\partial z} &= -\frac{\partial p}{\partial y} + \frac{\partial \tau_{xy}}{\partial x} + \frac{\partial \tau_{yy}}{\partial y} + \frac{\partial \tau_{zy}}{\partial z} + \rho f_y \\
\frac{\partial (\rho w)}{\partial t} + \frac{\partial (\rho w u)}{\partial x} + \frac{\partial (\rho w v)}{\partial y} + \frac{\partial (\rho w w)}{\partial z} &= -\frac{\partial p}{\partial z} + \frac{\partial \tau_{xz}}{\partial x} + \frac{\partial \tau_{yz}}{\partial y} + \frac{\partial \tau_{zz}}{\partial z} + \rho f_z
\end{aligned} \tag{3.2}$$

where τ_{ij} are the components of the stress tensor, τ, and f_i are the body forces.

Energy equation

The energy equation is derived from the conservation of energy law as follows

$$\frac{\partial}{\partial t}\left[\rho\left(e + \frac{V^2}{2}\right)\right] + \nabla \cdot \left[\rho\left(e + \frac{V^2}{2}\right)\mathbf{V}\right] = \rho\dot{q} + \frac{\partial}{\partial x}\left(\hat{k}\frac{\partial T}{\partial x}\right) + \frac{\partial}{\partial y}\left(\hat{k}\frac{\partial T}{\partial y}\right) + \frac{\partial}{\partial z}\left(\hat{k}\frac{\partial T}{\partial z}\right)$$
$$- \frac{\partial(up)}{\partial x} - \frac{\partial(vp)}{\partial y} - \frac{\partial(wp)}{\partial z} - \frac{\partial(u\tau_{xx})}{\partial x} - \frac{\partial(u\tau_{yx})}{\partial y} - \frac{\partial(u\tau_{zx})}{\partial z} - \frac{\partial(v\tau_{xy})}{\partial x}$$
$$- \frac{\partial(v\tau_{yy})}{\partial y} - \frac{\partial(v\tau_{zy})}{\partial z} - \frac{\partial(w\tau_{xz})}{\partial x} - \frac{\partial(w\tau_{yz})}{\partial y} - \frac{\partial(w\tau_{zz})}{\partial z} + \rho\mathbf{f} \cdot \mathbf{V}$$

$$(3.3)$$

where $\dot{q}$ is the rate of volumetric heat addition per unit mass, $\hat{k}$ is the thermal conductivity, T is the temperature, E is the total energy given by

$$E = e + \frac{u^2 + v^2 + w^2}{2} \tag{3.4}$$

and H is the total enthalpy defined as

$$H = E + \frac{p}{\rho} \tag{3.5}$$

The components of the stress tensor are described for a Newtonian fluid by the following expressions,

$$\left.\begin{aligned}
\tau_{xx} &= -\mu\left(2\frac{\partial u}{\partial x} - \frac{2}{3}\left(\frac{\partial u}{\partial x} + \frac{\partial v}{\partial y} + \frac{\partial w}{\partial z}\right)\right) \\
\tau_{yy} &= -\mu\left(2\frac{\partial v}{\partial y} - \frac{2}{3}\left(\frac{\partial u}{\partial x} + \frac{\partial v}{\partial y} + \frac{\partial w}{\partial z}\right)\right) \\
\tau_{zz} &= -\mu\left(2\frac{\partial w}{\partial z} - \frac{2}{3}\left(\frac{\partial u}{\partial x} + \frac{\partial v}{\partial y} + \frac{\partial w}{\partial z}\right)\right) \\
\tau_{xy} &= \tau_{yx} = -\mu\left(\frac{\partial u}{\partial y} + \frac{\partial v}{\partial x}\right) \\
\tau_{xz} &= \tau_{zx} = -\mu\left(\frac{\partial u}{\partial z} + \frac{\partial w}{\partial x}\right) \\
\tau_{yz} &= \tau_{zy} = -\mu\left(\frac{\partial v}{\partial z} + \frac{\partial w}{\partial y}\right)
\end{aligned}\right\} \tag{3.6}$$

Here, μ represents the laminar viscosity which is determined using Sutherland's law as shown,

$$\frac{\mu}{\mu_0} = \left(\frac{T}{T_0}\right)^{\frac{3}{2}}\frac{T_0 + 110}{T + 110} \tag{3.7}$$

where the reference values are described with a subscript "0" and are specified as $\mu_0 = 1.7894 \cdot 10^{-5} kg/ms$ and $T_0 = 288.16K$.

The heat flux vector components are calculated using <u>Fourier's</u> Law and are given by the following expressions,

$$q_x = -\hat{k}\frac{\partial T}{\partial x} = -\frac{1}{(\hat{\gamma} - 1)M_\infty^2}\frac{\mu}{P_r}\frac{\partial T}{\partial x} \tag{3.8}$$

22

$$q_y = -\hat{k}\frac{\partial T}{\partial y} = -\frac{1}{(\hat{\gamma}-1)M_\infty^2}\frac{\mu}{P_r}\frac{\partial T}{\partial y} \tag{3.9}$$

$$q_z = -\hat{k}\frac{\partial T}{\partial z} = -\frac{1}{(\hat{\gamma}-1)M_\infty^2}\frac{\mu}{P_r}\frac{\partial T}{\partial z} \tag{3.10}$$

Here, P_r is the Prandtl number and M_∞ represents the freestream Mach number.

3.1.2 Vector Form

Equations 3.1, 3.2 and 3.3 can be combined and rewritten in vector form as

$$\frac{\partial \mathbf{W}}{\partial t} + \frac{\partial (\mathbf{F^i} + \mathbf{F^v})}{\partial x} + \frac{\partial (\mathbf{G^i} + \mathbf{G^v})}{\partial y} + \frac{\partial (\mathbf{H^i} + \mathbf{H^v})}{\partial z} = 0 \tag{3.11}$$

where $\mathbf{W}$ is a column matrix of conserved variables

$$\mathbf{W} = \{\rho, \rho u, \rho v, \rho w, \rho E\}^T \tag{3.12}$$

$\mathbf{F^i}$, $\mathbf{G^i}$ and $\mathbf{H^i}$ are the inviscid flux vectors

$$\begin{aligned}
\mathbf{F^i} &= \{\rho u, \rho u^2 + p, \rho uv, \rho uw, u(\rho E + p)\}^T \\
\mathbf{G^i} &= \{\rho v, \rho uv, \rho v^2 + p, \rho vw, v(\rho E + p)\}^T \\
\mathbf{H^i} &= \{\rho w, \rho uw, \rho vw, \rho w^2 + p, w(\rho E + p)\}^T
\end{aligned} \tag{3.13}$$

and $\mathbf{F^v}$, $\mathbf{G^v}$ and $\mathbf{H^v}$ are the viscous flux vectors

$$\begin{aligned}
\mathbf{F^v} &= \{0, \tau_{xx}, \tau_{xy}, \tau_{xz}, u\tau_{xx} + v\tau_{xy} + w\tau_{xz} + q_x\}^T \\
\mathbf{G^v} &= \{0, \tau_{xy}, \tau_{yy}, \tau_{yz}, u\tau_{xy} + v\tau_{yy} + w\tau_{yz} + q_y\}^T \\
\mathbf{H^v} &= \{0, \tau_{xz}, \tau_{yz}, \tau_{zz}, u\tau_{xz} + v\tau_{yz} + w\tau_{zz} + q_z\}^T
\end{aligned} \tag{3.14}$$

This form of the Navier-Stokes equations was implemented in the code in dimensionless form which allows for better numerical conditioning. The following equations are used to non-dimensionalise each variable

$$\begin{aligned}
x &= \frac{x^*}{L^*} & y &= \frac{y^*}{L^*} & z &= \frac{z^*}{L^*} \\
u &= \frac{u^*}{V_\infty^*} & v &= \frac{v^*}{V_\infty^*} & w &= \frac{w^*}{V_\infty^*} \\
t &= \frac{t^* V_\infty^*}{L^*} & \rho &= \frac{\rho^*}{\rho_\infty^*} & p &= \frac{p^*}{\rho_\infty^* V_\infty^{*2}} \\
& & T &= \frac{T^*}{T_\infty^*} & e &= \frac{e^*}{V_\infty^{*2}}
\end{aligned} \tag{3.15}$$

where the asterisk superscript, *, represents the non-dimensional variables. From the current section it can be seen that a set of unknown parameters are present, namely, p, ρ, u, v, w, and the Reynolds stress tensor components. Bearing in mind that only five equations have currently been noted, 3.1, 3.2 and 3.3, this creates an underdetermined problem with five equations and eleven unknowns, also known as the closure problem. To overcome this, the Boussinesq approximation is adopted. This states that the Reynolds stress tensor can be calculated using the turbulent viscosity and the strain-rate tensor of the mean flow, S_{ij} [46].

3.1.3 Reynolds Averaging

Direct numerical solution (DNS) of the Navier-Stokes equations is nowadays not feasible for realistic Reynolds numbers, requiring vast amounts of computer resources. For this reason, an approximation to the turbulent nature of the flow needs to be introduced. It is assumed that the instantaneous value of the different variables is made up of a mean and a turbulent fluctuating component as shown,

$$u_i = \overline{u_i} + u'_i \qquad v_i = \overline{v_i} + v'_i \qquad w_i = \overline{w_i} + w'_i$$
$$p_i = \overline{p_i} + p'_i \qquad \rho_i = \overline{\rho_i} + \rho'_i$$

(3.16)

The Reynolds-averaged form of the Navier-Stokes equations is identical to that presented previously, except for the Reynolds stress tensor and heat flux equations. Thus, after some algebraic manipulation of equation 3.6 we obtain the following expression for τ_{xx},

$$\tau_{xx} = -\left(\mu + \mu_t\right)\left(2\frac{\partial u}{\partial x} - \frac{2}{3}\left(\frac{\partial u}{\partial x} + \frac{\partial v}{\partial y} + \frac{\partial w}{\partial z}\right)\right)$$

(3.17)

where μ_t is the turbulent eddy viscosity and is calculated in the code using a turbulence model. Similarly, the other stress tensor components are rearranged to include this turbulent component. Rearranging equation in 3.8 we get the following expression for q_x,

$$q_x = -\frac{1}{(\hat{\gamma} - 1)M_\infty^2}\left(\frac{\mu}{P_r} + \frac{\mu_t}{P_{rt}}\right)\frac{\partial T}{\partial x}$$

(3.18)

where P_{rt} is the turbulent Prandtl number and the expression is equivalent to the those for q_y and q_z. A different approach is used for compressible flows, where a Favre averaging is required. This is described in detail in Refs. [7, 47].

3.1.4 Turbulence Models

$k - \omega$ Model

In this thesis two turbulence models were used, namely the baseline $k - \omega$ and the $k - \omega$ with vortex correction. These are two-equation models based on Wilcox's original $k - \omega$ formulation [48]. The turbulent eddy viscosity is given by

$$\mu_t = \frac{\rho k'}{\omega'}$$

(3.19)

where k' is the turbulence kinetic energy per unit mass and ω' is the specific dissipation rate. These are defined in this model as follows,

$$\underbrace{\rho\frac{\partial k'}{\partial t} + \rho\frac{\partial k'}{\partial x_j}}_{\textbf{Convection}} - \underbrace{\frac{1}{Re}\frac{\partial}{\partial x_j}\left[(\mu + \sigma^*\mu_t)\frac{\partial k'}{\partial x_j}\right]}_{\textbf{Diffusion}} = \underbrace{P_k}_{\textbf{Production}} - \underbrace{\beta^*\rho k'\omega'}_{\textbf{Destruction}}$$

(3.20)

$$\rho\underbrace{\frac{\partial \omega'}{\partial t} + \rho \cdot \frac{\partial \omega'}{\partial x_j}}_{\textbf{Convection}} - \underbrace{\frac{1}{Re}\frac{\partial}{\partial x_j}\left[(\mu + \sigma\mu_t)\frac{\partial \omega'}{\partial x_j}\right]}_{\textbf{Diffusion}} = \underbrace{P_\omega}_{\textbf{Production}} - \underbrace{\beta^*\rho\omega'^2}_{\textbf{Destruction}} \qquad (3.21)$$

where P_k and P_ω are the production terms of k' and ω', respectively, and are given as,

$$P_k = \mu_t P - \frac{2}{3}\rho k' S \qquad\qquad P_\omega = \alpha\frac{\omega'}{k'}P_k \qquad\qquad (3.22)$$

P and S are given by

$$P = \left[(\nabla\mathbf{V} + \nabla\mathbf{V}^T):\nabla\mathbf{V} - \frac{2}{3}(\nabla\cdot\mathbf{V})^2\right] \qquad\qquad S = \nabla\cdot\mathbf{V} \qquad (3.23)$$

The following closure coefficients are used,

$$\hat{\alpha} = \frac{5}{9} \qquad \hat{\beta} = \frac{3}{40} \qquad \hat{\beta}^* = \frac{9}{100} \qquad \hat{\sigma} = \frac{1}{2} \qquad \hat{\sigma}^* = \frac{1}{2} \qquad (3.24)$$

These differ slightly from the original formulation values due improvements in the PMB code over the years, Refs. [46, 47]. The same non-dimensional form of the flow variables are used in this formulation with the addition of the following normalised terms,

$$k' = \frac{k'^* Re}{U_\infty^{*2}} \qquad \omega' = \frac{\omega'^* L^*}{U_\infty^*} \qquad \mu_t = \frac{\mu_t^*}{\mu_\infty^*} \qquad\qquad (3.25)$$

$k - \omega$ with P_ω Enhancer Model

A modification to the original $k - \omega$ model was introduced by Brandsma et al. [49] in an attempt to correct the excessive amounts of turbulent kinetic energy produced within vortex cores. For this reason, two models were proposed which controlled the production of kinetic energy, and therefore the levels of turbulent eddy viscosity in the vortex region. The first method directly limits the production of k' whereas the second increases the production of the dissipation rate, ω', in the regions of high vortical flow. For this method to apply only in the regions where it is needed, a sensor was introduced which distinguished between shear layers and vortex cores. The second method is the one used in PMB and the resulting expression for the new dissipation production term is

$$P_{\omega_{new}} = \frac{\omega'^2}{k}max(\Omega^2, S^2) \qquad\qquad (3.26)$$

where Ω is the mean rotation tensor. The closure coefficients used in this model are the following

$$\begin{array}{cccc} \hat{\alpha} = \frac{1}{2} & \hat{\alpha}^* = 1 & \hat{\beta} = 0.075 & \hat{\beta}^* = 0.09 \\ \hat{\sigma} = 0.6 & \hat{\sigma}^* = 1 & \hat{\sigma}_d = 0.3 \end{array} \qquad (3.27)$$

Baseline $k - \omega$ Model

A model suggested by Menter [50] was introduced which exploited the robust formulation of the $k - \omega$ model in the regions near the wall and the lack of sensitivity to free-stream values of the $k - \epsilon$ in the regions away from the walls. This was achieved by transforming the $k - \epsilon$ model into a $k - \omega$ type of formulation which created an extra cross-diffusion term in the ω transport equation,

$$S = 2(1 - F_1)\rho\sigma_{\omega 2}\frac{1}{\omega'}\frac{\partial k'}{\partial x_j}\frac{\partial \omega'}{\partial x_j} \tag{3.28}$$

The closure coefficients, $\hat{\alpha}$, $\hat{\beta}$, $\hat{\sigma}_k$ and $\hat{\sigma}_\omega$, of the two models were blended using the following function

$$B\left\{\begin{array}{c} a \\ b \end{array}\right\} = F_1 a + (1 - F_1)b \tag{3.29}$$

and the following values were given to each coefficient,

$$\hat{\alpha} = B\left\{\begin{array}{c} 0.553 \\ 0.440 \end{array}\right\} \quad \hat{\beta} = B\left\{\begin{array}{c} 0.075 \\ 0.083 \end{array}\right\} \quad \hat{\beta}^* = \frac{9}{100}$$

$$\hat{\sigma}_k = B\left\{\begin{array}{c} 0.5 \\ 1.0 \end{array}\right\} \quad \hat{\sigma}_\omega = B\left\{\begin{array}{c} 0.5 \\ 0.856 \end{array}\right\} \tag{3.30}$$

3.1.5   Curvilinear Form

The equations describing the flow are written in curvilinear form. This is done to ease their use on grids of arbitrary local orientation and density. This transformation is carried out as follows

$$\xi = \xi(x, y, z) \tag{3.31}$$

$$\eta = \eta(x, y, z) \tag{3.32}$$

$$\zeta = \zeta(x, y, z) \tag{3.33}$$

$$t = t \tag{3.34}$$

The Jacobian determinant of the transformation is given by

$$J = \frac{\partial(\xi, \eta, \zeta)}{\partial(x, y, z)} \tag{3.35}$$

Equation 3.11 can then be rewritten as

$$\frac{\partial\hat{\mathbf{W}}}{t} + \frac{\partial(\hat{\mathbf{F}}_i - \hat{\mathbf{F}}_v)}{\partial\xi} + \frac{\partial(\hat{\mathbf{G}}_i - \hat{\mathbf{G}}_v)}{\partial\eta} + \frac{\partial(\hat{\mathbf{H}}_i - \hat{\mathbf{H}}_v)}{\partial\zeta} = 0 \tag{3.36}$$

where

$$\hat{\mathbf{W}} = \frac{1}{J}\mathbf{W}$$

$$\hat{\mathbf{F}}_i = \frac{1}{J}\left(\xi_x \mathbf{F}_i + \xi_y \mathbf{G}_i + \xi_z \mathbf{H}_i\right)$$

$$\hat{\mathbf{G}}_i = \frac{1}{J}\left(\eta_x \mathbf{F}_i + \eta_y \mathbf{G}_i + \eta_z \mathbf{H}_i\right)$$

$$\hat{\mathbf{H}}_i = \frac{1}{J}\left(\zeta_x \mathbf{F}_i + \zeta_y \mathbf{G}_i + \zeta_z \mathbf{H}_i\right) \qquad (3.37)$$

$$\hat{\mathbf{F}}_v = \frac{1}{J}\left(\xi_x \mathbf{F}_v + \xi_y \mathbf{G}_v + \xi_z \mathbf{H}_v\right)$$

$$\hat{\mathbf{G}}_v = \frac{1}{J}\left(\eta_x \mathbf{F}_v + \eta_y \mathbf{G}_v + \eta_z \mathbf{H}_v\right)$$

$$\hat{\mathbf{H}}_v = \frac{1}{J}\left(\zeta_x \mathbf{F}_v + \zeta_y \mathbf{G}_v + \zeta_z \mathbf{H}_v\right)$$

3.1.6 Steady State Solver

To solve the Navier-Stokes equations numerically it is necessary to divide the computational domain into a finite number of non-overlapping control volumes [51]. In the current study, this is done by means of structured grids generated using ANSYS ICEM [52] which are built using an array of hexahedral blocks. Each three-dimensional block is divided into a defined number of cells along the local x, y and z directions. PMB is a cell-centred method which solves the governing equations at the centre of each cell as opposed to cell-vertex which solves at the grid nodes. According to the finite volume approach the equations can discretised for each cell by

$$\frac{d}{dt}(\mathbf{W}_{i,j,k} V_{i,j,k}) + \mathbf{R}(\mathbf{W}_{i,j,k}) = 0 \qquad (3.38)$$

where $V_{i,j,k}$ is the cell volume, $\mathbf{W}_{i,j,k}$ the flux variables and $\mathbf{R}(\mathbf{W}_{i,j,k})$ the flux residuals. MUSCL interpolation [53] provides third order accuracy. The boundary conditions are specified by using the no-slip condition at solid walls and freestream conditions in the far field. For this reason, far fields are set far from the geometry of interest using streched grids. The following implicit time-marching scheme is used to integrate the solution in time to obtain a steady state solution,

$$\frac{\mathbf{W}_{i,j,k}^{n+1} - \mathbf{W}_{i,j,k}^{n}}{\Delta t} + \frac{1}{V_{i,j,k}}\mathbf{R}(\mathbf{W}_{i,j,k}^{n+1}) = 0 \qquad (3.39)$$

Equation 3.39 represents a system of non-linear algebraic equations. A description of how the flux residual is linearised to simplify the solution procedure is given in Ref. [46].

3.1.7 Unsteady Solver

An implicit dual-time method is used for time-accurate calculations [54]. In this manner, convergence is achieved by allowing the solution to march in pseudo-time for each real timestep. The residual is redefined to obtain a steady state equation which can be solved using acceleration techniques. Using a three-level discretisation of the time derivative, the updated flow solution is calculated by solving the following equation,

$$\frac{3\mathbf{W}_{i,j,k}^{n+1} - 4\mathbf{W}_{i,j,k}^{n} + \mathbf{W}_{i,j,k}^{n-1}}{2\Delta t} + \frac{1}{V_{i,j,k}}\mathbf{R}(w_{i,j,k}^{k_m}, q_{i,j,k}^{k_t}) = 0 \tag{3.40}$$

where $\mathbf{R}(w_{i,j,k}^{k_m}, q_{i,j,k}^{k_t})$ is the spatial discretisation as described above, with $w_{i,j,k}$ and $q_{i,j,k}$ being the vector form of the values of W and Q in the surrounding cells. Similarly, for the turbulence model

$$\frac{3\mathbf{Q}_{i,j,k}^{n+1} - 4\mathbf{Q}_{i,j,k}^{n} + \mathbf{Q}_{i,j,k}^{n-1}}{2\Delta t} + \frac{1}{V_{i,j,k}}\mathbf{Q}(w_{i,j,k}^{l_m}, q_{i,j,k}^{l_t}) = 0 \tag{3.41}$$

These equations represent a coupled non-linear system of equations. The superscripts, k_m, k_t, l_m and l_t determine the time levels of the variables used in the spatial discretisation and determine the behaviour of the coupling between the systems of equations. This non-linear system of equations can be solved by introducing an iteration through pseudo-time (τ) to the steady state given by,

$$\frac{\mathbf{W}_{i,j,k}^{n+1,k+1} - \mathbf{W}_{i,j,k}^{n+1,k}}{\Delta\tau} + \frac{1}{V_{i,j,k}}\left(\frac{3\mathbf{W}_{i,j,k}^{n+1} - 4\mathbf{W}_{i,j,k}^{n} + \mathbf{W}_{i,j,k}^{n-1}}{2\Delta t} + \frac{1}{V_{i,j,k}}\mathbf{R}(w_{i,j,k}^{k_m}, q_{i,j,k}^{k_t})\right) = 0$$
$$\tag{3.42}$$

with an equivalent form for the turbulent system of equations. Using this formulation the system of equations can again be linearised and iterated to a steady state solution in pseudo-time before being advanced in real time.

3.1.8 Grid Deformation

In this study control surface deflections are modelled using grid deformation. The grid is generated with a block topology accomodating the shape of the solid control surfaces to be deflected. Special boundary conditions are defined at these block faces and motions are prescribed prior to each simulation. Transfinite interpolation (TFI) is used to update the block topology to match the new solid surface geometry. The process is carried out in three steps by which the block edges, faces and volume points are displaced in turn. Initially the block vertices are moved as required. Assuming A_0 and B_0 are the original vertex locations and A and B the updated ones, the displacement of the edge vertices are given by

$$dA = A - A_0 \qquad dB = B - B_0 \tag{3.43}$$

where dA and dB correspond to the displacement of points A and B. From these displacements the rest of the points on the block edges are moved using the vertex displacements as shown below

$$d\mathbf{x}(\xi) = dA(1 - s(\xi)) + dBs(\xi) \tag{3.44}$$

where

$$s(\xi) = \frac{\text{Length from } A_0 \text{ to } x_0(\xi)}{\text{Length of the curve } A_0\text{-}B_0} \tag{3.45}$$

and the coordinates of the new grid points are given by

$$\boldsymbol{x}(\xi) = \boldsymbol{x_0}(\xi) + d\boldsymbol{x_0}(\xi) \tag{3.46}$$

This process is illustrated in Fig. 3.1. Once the edges of the block have been updated, the faces and the internal points are displaced in a similar manner. The method is described in more detail by Rampurawala [55, 56].
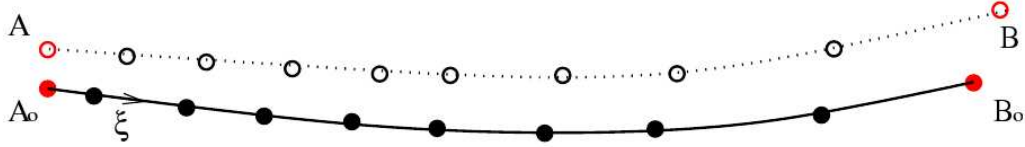
Figure 3.1: Grid point displacements along a block edge [55].

3.2 Tabular Model

Look up tables of aerodynamic forces and moments generally have a large number of entries due to dimensionality. One advantage of tables is that non-linear variations in the forces and moments with the aircraft states can be accurately represented. A typical model for a conventional aircraft would be dependent on Mach number (M), incidence angle (α), sideslip angle (β), and the pairs of control surface deflections, elevator (δ_{ele}), aileron (δ_{ail}) and rudder (δ_{rud}). A single table accounting for the influence of all six variables would result in an unmanageable size with the number of required data entries easy-reaching of the order of millions. Instead, by assuming that the coupled influence of β, ∂_{ele}, ∂_{ail} and ∂_{rud} is negligible, four three-dimensional tables can be used, namely [M, α, β], [M, α, δ_{ele}], [M, α, δ_{ail}] and [M, α, δ_{rud}]. The size is kept in the order of thousands of entries for each table. Thus, the aerodynamic model can be represented by the following non-linear equation,

$$C_j = C_j(\alpha, M, \beta) + C_j(\alpha, M, \delta_{ele}) + C_j(\alpha, M, \delta_{ail}) + C_j(\alpha, M, \delta_{rud}) \tag{3.47}$$

where $j = L, D, m, Y, l, n$. An assumption is made here by which a baseline table, based on the Mach number and angles of attack and sideslip, is used to describe the main aerodynamic trends and the control deflections represent increments from these values. This allows for savings in the sampling of the control surface tables. The format may change for unconventional aircraft with novel control effectors, as is the case for the SACCON UCAV. The table entries themselves consist of force and moment data required for the prediction of the aircraft motion. An example is shown in Table 3.1, where C_L, C_D, C_m, C_Y, C_l and C_n correspond to the wind axis coefficients of lift, drag, pitching moment, side force, rolling and yawing moment, respectively.

Table 3.1: Tabular Model Layout

α	M	β	∂_{ele}	∂_{ail}	∂_{rud}	C_L	C_D	C_m	C_Y	C_l	C_n
x	x	x	-	-	-	x	x	x	x	x	x
x	x	-	x	-	-	x	x	x	x	x	x
x	x	-	-	x	-	x	x	x	x	x	x
x	x	-	-	-	x	x	x	x	x	x	x

The flight envelope defines the limits of the aerodynamic tabular model. Within these limits, the table needs to be defined with a number of discrete entries in each dimension. The key is to define them with enough resolution to capture the variation in aerodynamic characteristics thoughtout the tabular domain without an unnecessarily large number of entries. A range of prediction methods can be used to generate the table entries, also called samples or design sites. Each can provide good data in certain regions of the Mach number and angle of attack domain. In the past, a range of sources has been used for populating tables, as described in Refs. [57, 58]. These made use of semi-empirical methods (DATCOM [59]), panel methods (Tornado) and Euler CFD calculations as required. The challenge here was to balance the validity of the predictions with the cost of the calculation itself. The lower order methods such as DATCOM and Tornado provide inexpensive and reliable predictions in the linear region at low angles of attack and for the increments due to control deflections. Euler based calculations come at a higher price but can be used for high Mach numbers and angles of attack up to stall. At the other end of the computational cost spectrum, RANS simulations provide the most reliable predictions at the extremes of the flight envelope. Note that methods such as Detached Eddy Simulations (DES) provide good insight about the time-varying flow topology but are not considered due to prohibitive costs for the purpose of static aerodynamic characteristic predictions.

Even with the range of prediction methods available the computation of all the cases in the tables would not be viable due to computational cost. To overcome this, an iterative method for the generation of tabular models was used. This is based on sampling and reconstruction using Kriging interpolation and data fusion [60]. Each iteration includes a new sample for the Kriging prediction, hence decreasing the uncertainty in the

predicted model. The end result is highly dependent on the number and distribution of samples. An effective scheme places samples in the regions of non-linear behaviour. With this in mind, two functions are used for this purpose, the mean square error (MSE) and the expected improvement function (EIF). The first is zero at the sampled entries and increases with distance from such points. The second function evaluates the location of global minimum and maximum points inside the predicted function. A combination of these two parameters allows for the determination of the best location for future samples as this iterative process is carried out. At the core of this process is a Matlab based code, Design and Analysis of Computer Experiments (DACE), produced by the Technical University of Denmark [61]. A choice of regression and a correlation functions can be made to find the approximate represention of the entire model. First and second order polynomials can be chosen for the regression model and a range of functions for the correlation, such as linear, exponential or Gaussian distribution.

Initially, sampling is carried out at the limits of the table. This gives an overview of the forces and moments in the extremes of the flight envelope. Kriging is then used to make an initial prediction for all the entries in the model. Further sampling is carried out to find the regions of non-linearity in the flow. In the case of SACCON, some experience had already been gained from the validation work as to where the sensitive areas of the aerodynamic characteristics were located. For this reason and to accelerate the process, the calculations performed for CFD benchmarking against wind tunnel measurements were used as table samples. The result was a set of aerodynamic tables describing the aerodynamic behaviour of the SACCON model within the defined flight envelope which is described in more detail in Section 5.2.

Chapter 4

Validation of CFD Results

In recent years there has been interest in understanding the flow behaviour around low sweep delta wings typical of UCAV configurations. The experimental data obtained from the Stability And Control Configuration (SACCON) UCAV wind tunnel tests [62, 63] is used in this study to validate the capabilities of two Reynolds Averaged Navier-Stokes (RANS) structured methods for predicting vortical flow, namely PMB and ENSOLV. This work was carried out within the framework of the NATO RTO AVT-161 technical group. The particular applications in mind are the generation of aerodynamic models for flight dynamics and the simulation of manoeuvres featuring aerodynamic history effects. In this chapter, a detailed description of the test case is given followed by the experimental and computational results.

4.1 Test Case

The SACCON is a UCAV configuration consisting of a lambda wing with a leading edge sweep angle of 53° and a wing washout of five degrees. This means that there is a negative twist in the wing leading to a five degree decrease in geometric angle of attack from root to tip. The design was a common effort by EADS, DLR and DNW-NWB for the purpose of the AVT collaboration. It was designed with the intention of validating CFD methods for complicated flow regimes with experimental measurements. For this reason, the considerations taken for this generic UCAV design were focussed on generating highly non-linear flows as opposed to optimising for certain flight regimes, as it is done in aircraft wing design. For the same reason, no engine intake or exhaust openings were considered. The engineering and manufacturing was carried out at NASA Langley Research Centre and it was made with an aluminium structure and a carbon fibre skin. An interchangeable leading edge was designed to allow two different geometries to be tested during the experimental campaigns. One was made with a partially round leading edge and another one which was sharp. These two will be referred to as the RLE and SLE models, respectively. An illustration of the leading edge profiles is shown in Fig. 4.1 (a). Different aerofoil sections are used across the span of the model, as

shown in Fig. 4.1 (b) for the RLE. A washout of 5° is used along the wing to off-load the wing tip region and delay the onset of vortical flow.
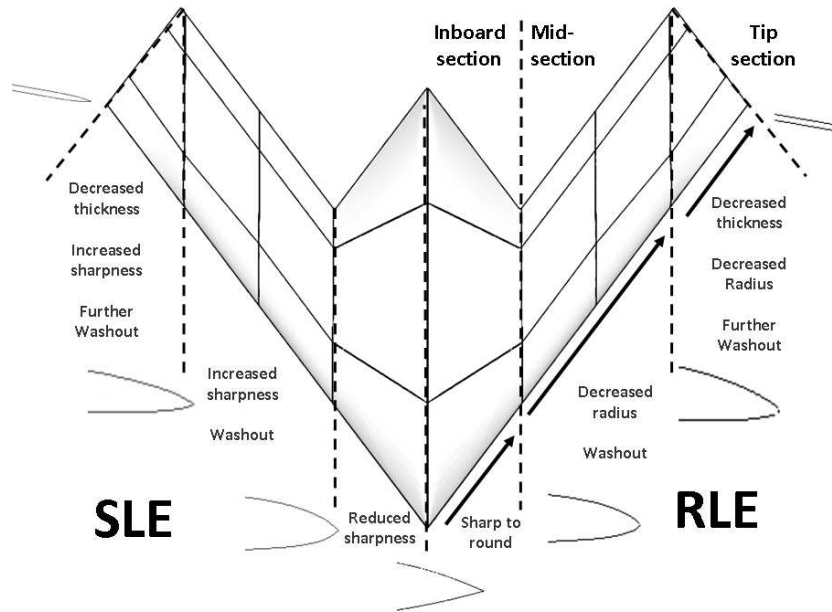
(a) Two different leading edge geometries.
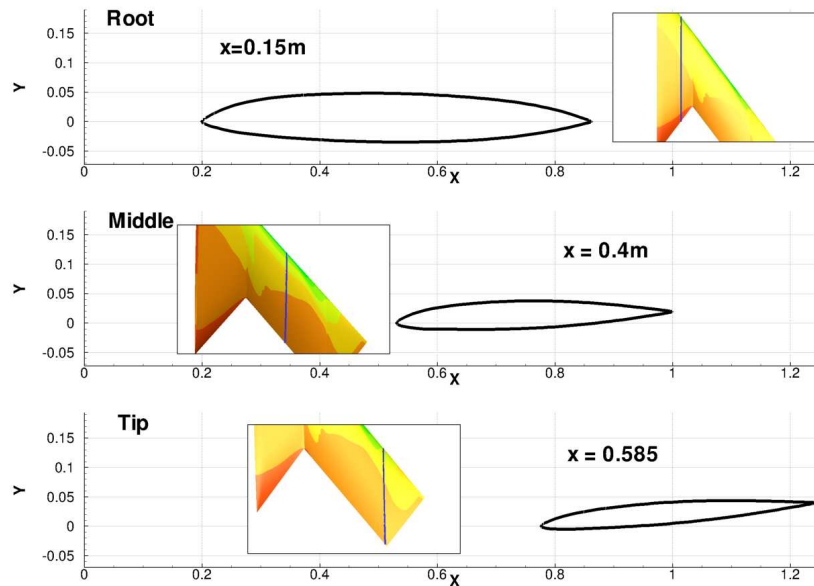
(b) RLE aerofoil sections.

Figure 4.1: SACCON geometrical description.

The gaps and screw heads shown in Fig. 4.2 (a) were filled using putty for the tests. For the RLE model, carborundum grit transition strips were used along the top and bottom parts of the leading edge to trip the boundary layer into a turbulent state. This was done to remove the influence of transition as a source of discrepancy between the measurements and the CFD predictions which were run in fully turbulent mode. The

result is shown in Fig. 4.2 (b) where the grit shown by the brown colour strip over the black carbon fibre skin.

(a) Before grit and gap filling.   (b) After grit and gap filling.
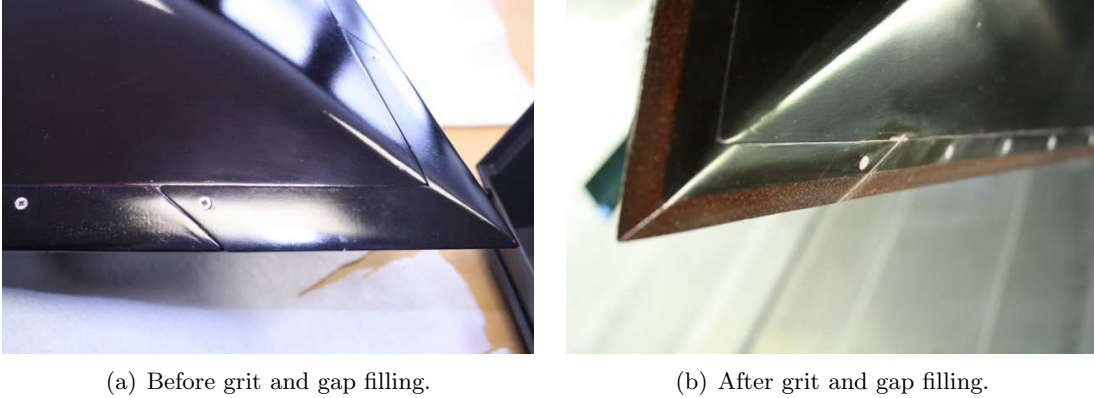
Figure 4.2: RLE model leading edge grit and gap filling.

The root chord of the model (c_{root}) is $1.061m$ long and the moment reference point (MRP) was located at $0.6m$ from the apex as shown in Fig. 4.3 (a). The force and moment coefficients were scaled using the reference surface area, $S_{ref} = 0.77m^2$, reference chord, $c_{ref} = 0.479m$, and reference span, $b_{ref} = 1.438m$. A six component strain gauge balance was used to measure the forces and moments of the complete model. 231 pressure ports connected to five electronically scanned pressure (ESP) modules were used to measure pressure variations on the surface. The ESP units were located inside the body of the model and the ports along longitudinal and transverse sections on the surface. An extra 8 high frequency dynamic pressure transducers (DPT), or kulites, were used to verify the unsteady pressure data recorded from the ESP modules. The instrumentation setup is represented in Fig. 4.3 by squares (pressure ports) and crosses (kulites). It is worth mentioning that the sections where the ports were located were not covered with grit strips.

Stereoscopic Particle Image Velocimetry (PIV) [64, 65] measurements were taken over the top surface of the model to gain insight into the flow topology. The cameras used allowed for a spatial resolution of $4mm$ and a time between measurements of $30-50\mu s$. 300 instantaneous images were taken for each run allowing for time averaged results to be calculated over a short time period. The incidence angles for which these measurements were taken were from $14°$ to $20°$ to look at the behaviour of the vortical structures. Measurements were taken at a number of sections along the chord of the wing, shown in Fig. 4.4 (a). A picture taken during the measurements shows the light sheet shone on the top surface of the model in Fig. 4.4 (b). These measurements were taken for both static and dynamic runs.

Three experimental campaigns took place in two wind tunnels, namely the atmospheric, closed circuit, closed section wind tunnels at DNW-NWB Braunschweig ($3.25m$

(a) Top   (b) Bottom
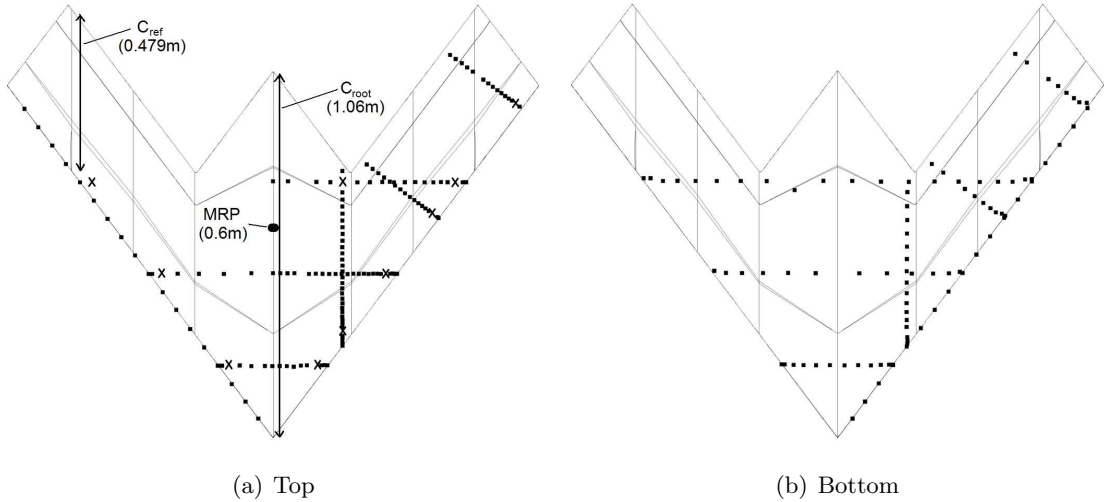
Figure 4.3: Pressure port and kulite arrangement on the SACCON wind tunnel model [63].

x 2.8m) and NASA Langley (14ft x 22ft). For the purpose of this study, the results from the first campaign at DNW-NWB are considered. This is because these were the first to become available and provided a broad set of static and dynamic cases. The model was mounted on a sting attached to the belly of the model which allowed for a motion of $\pm15°$ in pitch. The angle between the model's centreline and the sting can be set at $90°$ or $105°$ prior to each test run. During static experiments, this allowed for measurements to be taken by sweeping the angle of attack from $-5°$ to $30°$ and the sideslip angle from $-10°$ to $10°$.

Table 4.1 summarises the static cases which were run during the wind tunnel campaign relevant to the current work. Angle of attack and sideslip sweeps were carried out for angles ranging from $0°$ to $30°$ and $-10°$ to $10°$, respectively. The Mach number varied between 0.147 and 0.177 and the Reynolds number between $1.58 \cdot 10^6$ and $1.89 \cdot 10^6$. Pressure data was collected at the pressure tap positions as well as total balance force and moment data in wind and body axes. Modifications to the nominal values of angle of attack were made to correct for small sting deflections which were included in the data presented in this study. Further corrections were made to account for wind tunnel blockage effects, accounting for up to 4% balance measurement differences in the DNW-NWB facility at the highest angle of attack cases. A complete description of the corrections typically carried out at DNW-DWB can be found in Ref. [66].

Dynamic experiments were also carried out with motions in the pitch and yaw axes. For all these cases the mean sideslip angle remained at zero and the amplitudes at $A = \pm5°$. Table 4.2 outlines some of these cases and the conditions at which these were run. For further information on the wind tunnel campaigns, Refs. [62, 63] give
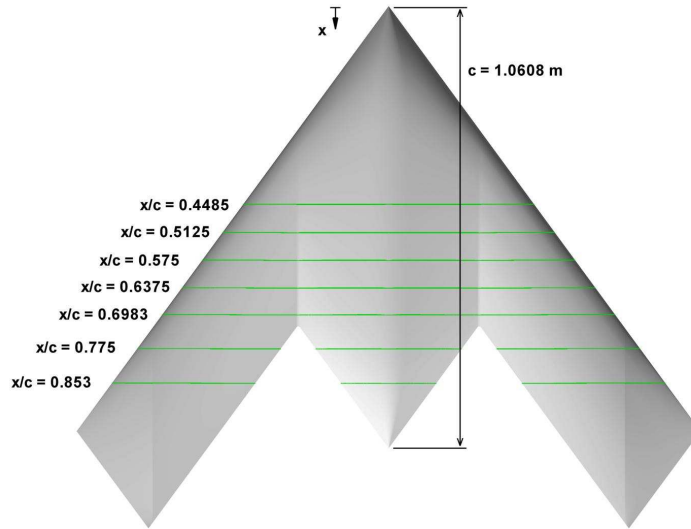
(a) Sections at which PIV measurements were taken.
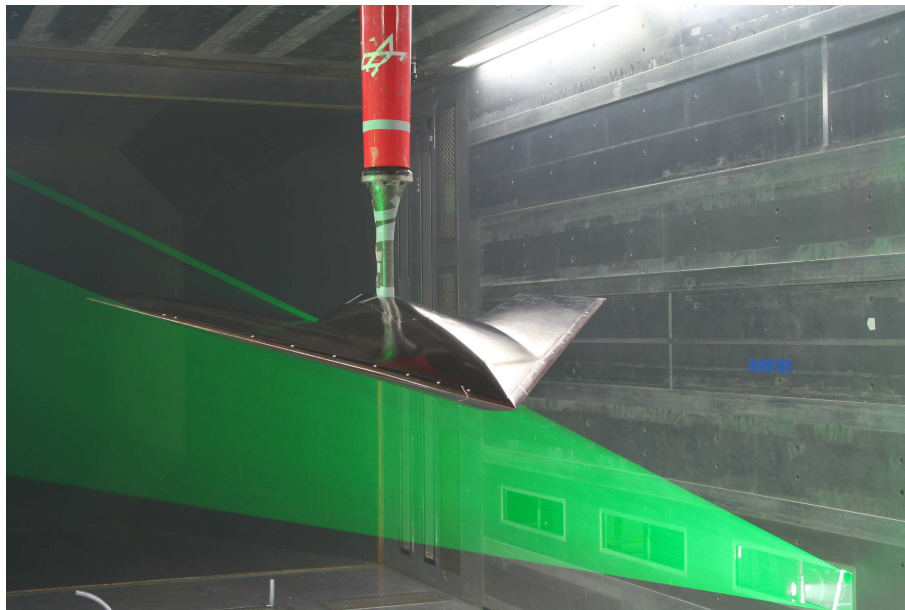
(b) Image during measurements using a light sheet.

Figure 4.4: SACCON PIV measurements.

full descriptions of the experiments carried out on SACCON.

4.2   Computational Setup

A grid refinement study was done at NLR to assess the grid size required to achieve grid convergence. To this end a family of structured multi-block grids was generated using the grid generation tools available in the flow simulation system ENFLOW. For

(a) Belly sting mounting at DLR wind tunnel.
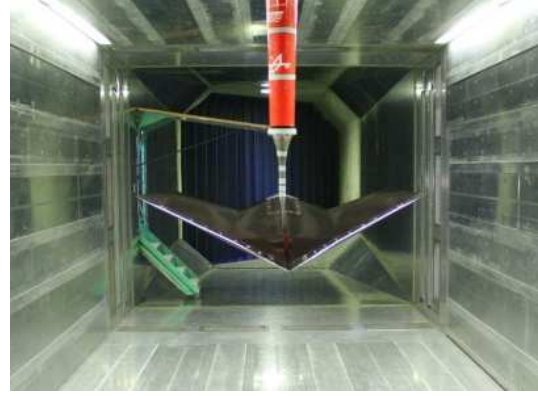
(b) Model in wind tunnel.

Figure 4.5: SACCON model setup in the wind tunnel.

Table 4.1: Wind Tunnel static runs measurements.

Config.	Mode	V_∞ $[\frac{m}{s}]$	α [°]	β [°]	M	Re $[\cdot 10^6]$	Measurements
SLE	α sweep	50,55,60	$0 \rightarrow 30$	0	$0.147, 0.162, 0.177$	$1.58, 1.73, 1.89$	F&M, p data
SLE	β sweep	50	$10, ...25$	$-10 \rightarrow 10$	0.147	1.58	F&M, p data
RLE	α sweep	50	$0 \rightarrow 30$	0	0.147	1.58	F&M, p data
RLE	β sweep	50	$10, ...25$	$-10 \rightarrow 10$	0.147	1.58	F&M, p data

this study, the grids all have the same topology consisting of 51 blocks. Each grid incorporates three multi-grid levels. The first cell spacing normal to the solid surface was around 1 x $10^{-5} c_{ref}$ on the coarsest multi-grid level, ensuring a suitable y^+ value of approximately one on this grid level. This non-dimensional parameter is used to ensure that the boundary layer is well resolved with the current grid density. Different codes and turbulent models may require different values for optimum performance. More details on the grids can be found in Table 4.3.

Steady-state flow simulations were performed by NLR for 10° angle of attack, a Mach number of 0.17 and a Reynolds number of $1.93 \cdot 10^6$ using the ENSOLV flow solver. The TNT k-ω turbulence model was used [67] in fully turbulent mode. On each grid level, calculations required 1500 iterations to ensure a fully converged solution.

The grid converged (asymptotic) value was computed. The difference between the actual value and the asymptotic value of the lift coefficient, the drag coefficient and the pitching moment coefficient were evaluated and the latter is shown in Fig. 4.6. This figure also shows the actual values on each grid level and the asymptotic values. The differences for each coefficient and grid are shown in Table 4.4. This study showed that as the grid size approaches 25 million grid cells, grid converged solutions are obtained with a difference with respect to the asymptotic value of approximately $2 \cdot 10^{-4}$ for the

Table 4.2: Wind Tunnel dynamic runs measurements.

Config.	Mode	V_∞ $[\frac{m}{s}]$	α_0 $[°]$	f [Hz]	M	Re $[\cdot 10^6]$	Measurements
SLE	yaw	60,50	10	1,2,3	0.147, 0.177	1.58, 1.89	F&M, p data
SLE	yaw	60	15	1,2	0.177	1.89	F&M, p data
SLE	yaw	50	15	1,2,3	0.147	1.58	F&M, p data
SLE	yaw	50	20, 25	1,3	0.147	1.58	F&M, p data
SLE	pitch	60	5, 10	1	0.177	1.89	F&M, p data
SLE	pitch	50	15, 20, 25	1	0.147	1.58	F&M, p data
RLE	yaw	50	10, 14, 15, 20, 25	1,2,3	0.147	1.58	F&M, p data
RLE	pitch	50	5, 10, 15, 20, 25	1,2,3	0.147	1.58	F&M, p data
RLE	plunge	50	10, 15, 20	1,2.5	0.147	1.58	F&M, p data

Table 4.3: Details of the grids used in the grid refinement study.

Grid	Characteristic edge dimension N on finest multi-grid level	Number of grid cells
Standard	80	9.088.000
Medium	96	15.704.604
Fine	112	24.937.472
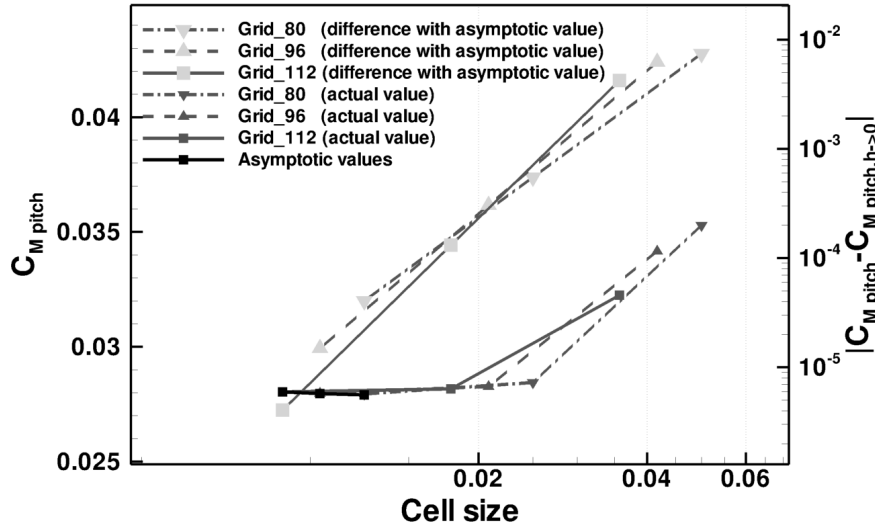
Figure 4.6: Results of the grid convergence study for the SACCON configuration.

lift coefficient, approximately $1.5 \cdot 10^{-5}$ for the drag coefficient and approximately $5 \cdot 10^{-6}$ for the pitching moment coefficient. The lift coefficient has the largest dependence on the grid used. However, on all grids the difference between the actual value and the

asymptotic value is for all force and moment coefficients smaller than 10^{-3}, which was considered to be sufficiently small for the present study. A similar study using unstructured grids carried out at DLR concluded with similar sized grids, around 7 million points, being used for their RANS calculations [68].

Table 4.4: Difference between the longitudinal characteristics and the assymptotic values for each grid size.

	Standard grid	Medium grid	Fine grid
C_L	$1.0 \cdot 10^{-3}$	$6.0 \cdot 10^{-4}$	$2.0 \cdot 10^{-4}$
C_D	$3.5 \cdot 10^{-4}$	$4.0 \cdot 10^{-5}$	$1.5 \cdot 10^{-5}$
C_m	$4.0 \cdot 10^{-4}$	$2.0 \cdot 10^{-5}$	$5.0 \cdot 10^{-6}$

Based on the lessons learnt from this study, grids with approximately 9 million points were generated at Liverpool for the SLE and RLE models using ANSYS ICEM Version 12. The same block topology was used for the RLE model and similar grid spacings and cell distributions as those generated at NLR. This allowed for comparison of the results from the two codes with reasonable confidence that the grids would not be the major source of discrepancy. The RLE model grid has a C-blocking around the leading edge and an O-grid at the blunt tip. The SLE, on the other hand, consists of an H-topology around the leading edge and a diamond shaped block sitting on the blunt tip. An illustration of the two topologies at a section $0.3m$ along the span from the symmetry plane is shown in Fig. 4.7. All of these grids were generated without modelling the sting present in the experiments. A high cell resolution was purposely used in the region near the leading edge in order to correctly capture the onset of vortical structures, as shown in Fig. 4.8. 5000 implicit iterations were used in each PMB calculation to reach a converged solution. Each calculation required 24 hours on 22 processors, using the computer cluster at the University of Liverpool CFD Laboratory. The boundary conditions in the farfield were set as freestream flow with a computational domain of approximately 15 times the chord length in all directions. Hence, the wind tunnel conditions were not reproduced in this simulation since the wind tunnel walls were not included.

Once the grids were generated, the first cases were run and the boundary layer solutions were plotted as shown in Fig. 4.9. Here, the velocity profile at point $(0.3m, 0.15m)$ over the wing is shown for both models. This point is depicted in the figures by a black square over the C_p distribution. The same case was computed for the RLE and SLE models at $\alpha = 15°$, $\beta = 0°$, $Re = 1.93 \cdot 10^6$ and $M = 0.17$. It can be seen from Fig. 4.9 (a) and (b) that the velocity profile has the typical shape for turbulent flow and that a large number of grid cells are contained within the boundary layer, 22 for the RLE
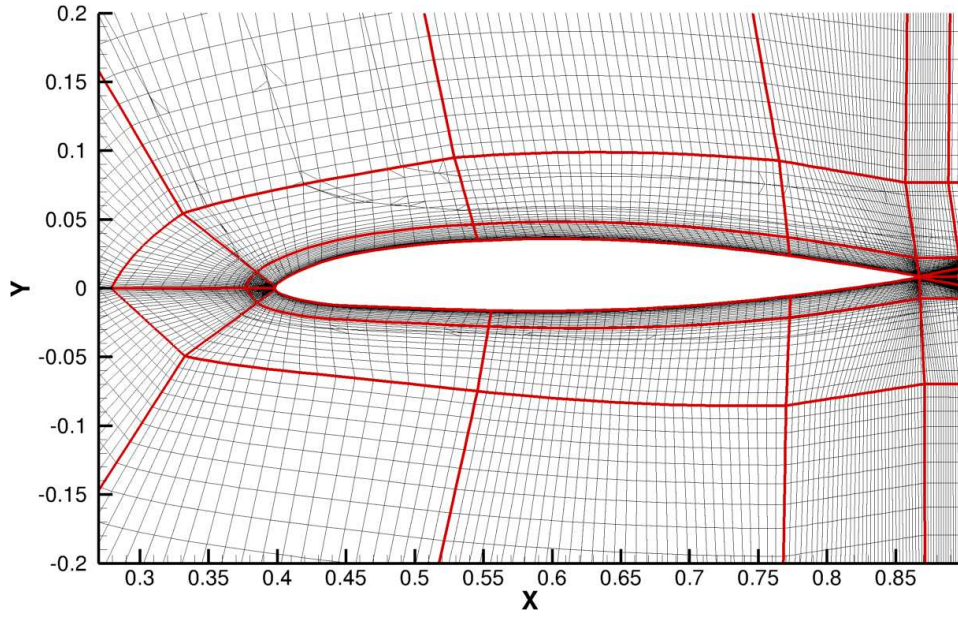
(a) RLE grid topology.
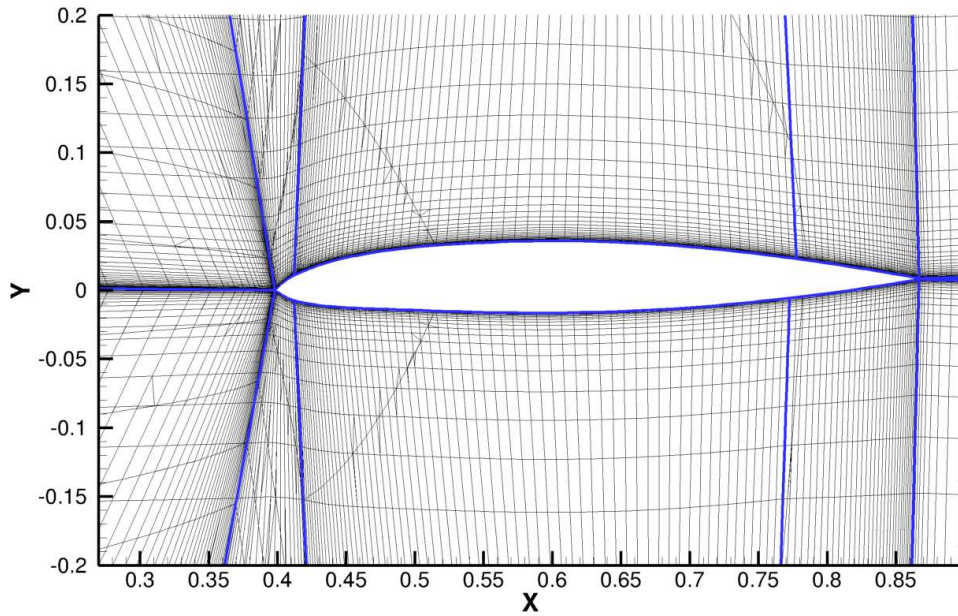
(b) SLE grid topology.

Figure 4.7: SACCON model grid topologies for PMB calculations.

and 14 for the SLE model. The reason for this difference is the shape of each plot. The SLE shows a flatter plot where the velocity reaches 99% of the freestream velocity, U_∞, closer to the surface. This means that the boundary layer at this point is thinner for the SLE model. This, in turn, has much to do with the vortex structures that form above the wing at these angles of attack which will be the topic of the rest of this chapter. Overall, the boundary layer behaviour is well captured which gave confidence on the suitability of the grids for further calculations.
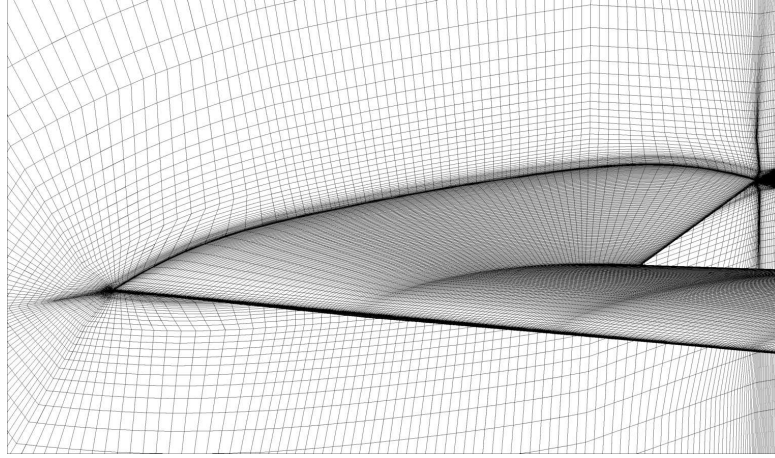
Figure 4.8: Structured grid for the RLE model.

(a) RLE.

(b) SLE.
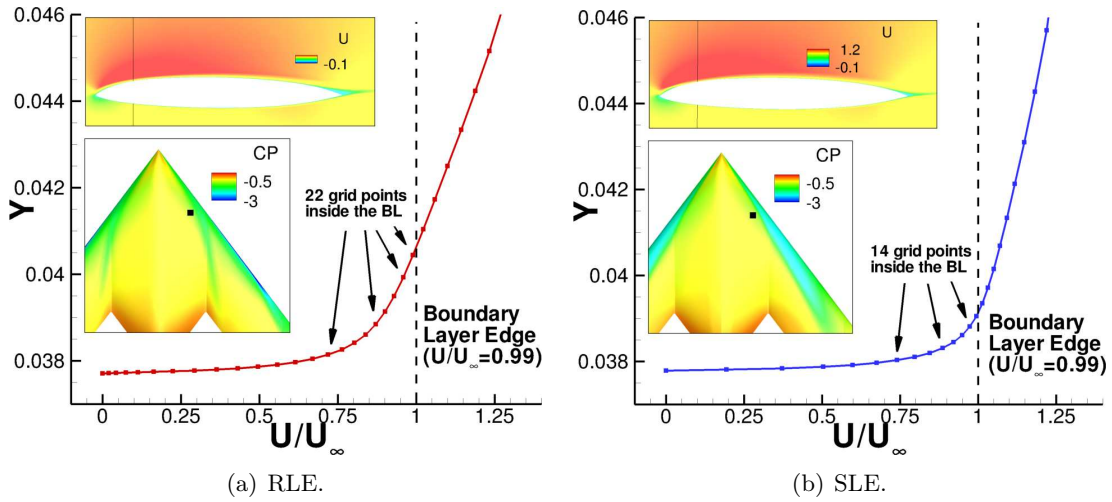
Figure 4.9: Boundary layer velocity profile at point $(0.3m, 0.15m)$ over the top surface of the wing for the RLE and SLE models.

There are some important differences in the flow topologies seen experimentally for the two configurations. To illustrate these differences the computed results for the flow over the configuration at $17°$ angle of incidence are shown in Fig. 4.10. The entire set of CFD results is described in detail in Section 4.3. According to these, both sharp and round leading edge models exhibit a two vortex structure for a range of angles of attack. The range of angles for which this behaviour happens is larger for the RLE case. As the incidence is increased the two vortices merge into one. This means that a single primary vortex structure is present over the top surface at high angles of attack.
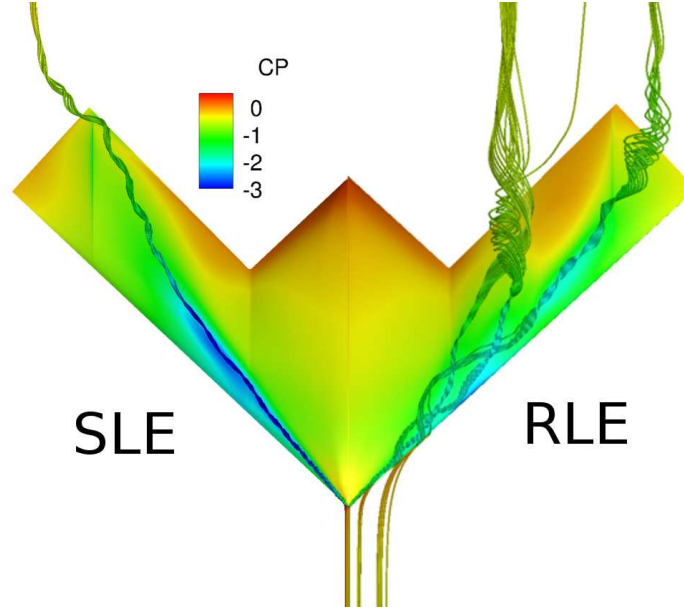
Figure 4.10: PMB k-ω flow solutions for the SACCON UCAV at $\alpha = 17°$ and $Re = 1.93 \cdot 10^6$.

4.3 Static Results

4.3.1 Evaluation of Simulation Options

This section presents a study of the different simulations that were carried out for the SACCON configuration CFD validation. A comparison is made between the two available CFD codes using the grid generated for the RLE model for a range of angles of attack. An example is shown in Fig. 4.11 based on integral data. The results cross-plotted here have been obtained from PMB with the k-ω model with a P_ω enhancer and the baseline k-ω model, and from ENSOLV using the TNT k-ω model. The lift coefficient plot in Fig. 4.11 (a) shows a good agreement between the codes in the linear region with a constant offset from the experiments. Frink [69] showed this offset was corrected when the sting mounting was included in the simulations. The three methods used show a scatter beyond 15° incidence. The break in linearity occurs earliest for the baseline k-ω model. The k-ω models with vortex correction stay in good agreement up to 17° incidence which suggests there is turbulence model dependence in the solution. A more obvious scatter between computational methods is present in the pitching moment coefficient plot shown in Fig. 4.11 (c). Both the PMB baseline and ENSOLV TNT k-ω predict a strong dip although the former does it at 16° incidence and the latter at 19° which disagrees with the experiment, at 17.5°. Figure 4.12 shows the difference in pressure coefficient distribution over the SACCON predicted with PMB baseline k-ω and ENSOLV TNT k-ω. For a low angle of attack the C_p distributions are very similar, as seen in Fig. 4.12 (a). An early inboard shift of the onset of the tip vortex occurs

in the PMB results, at 16° incidence, whereas in the ENSOLV solution this does not happen until the model reaches 19° of incidence, see Fig. 4.12 (b) and (c). It is clear that in the ENSOLV predictions the complex vortical structure remains up to a higher incidence.
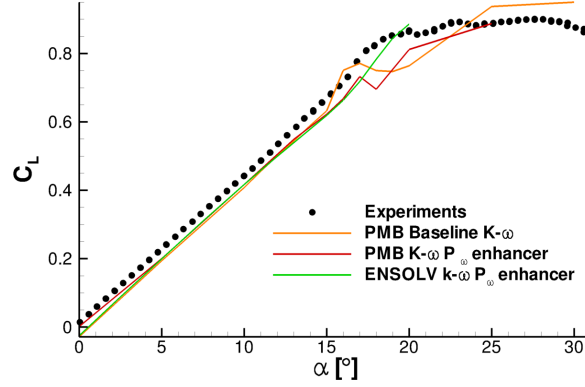
(a) C_L against angle of attack.
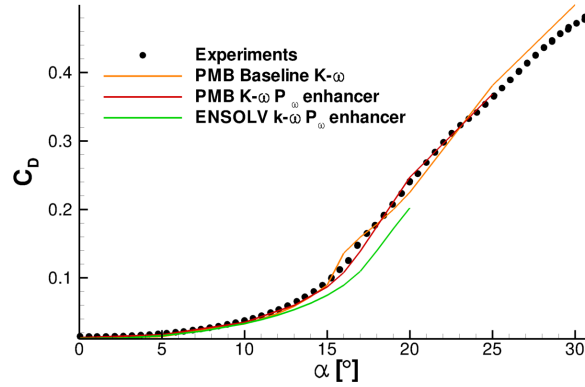
(b) C_D against angle of attack.
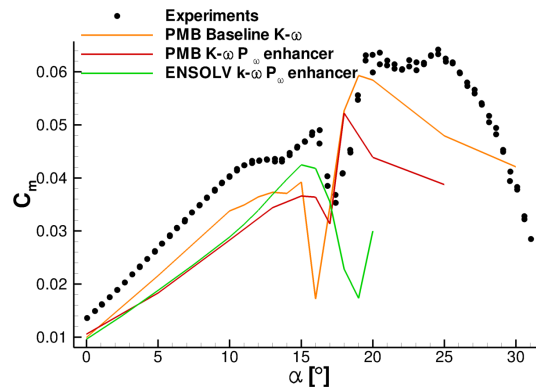
(c) C_m against angle of attack.

Figure 4.11: Integral data from experimental results and PMB computations for the round leading edge model.

Two sets of measurements were obtained for the RLE model at each incidence, starting from 0° up to 31° and vice versa. This was done to account for any repeatability

(a) C_P distribution at $\alpha = 10°$.

(b) C_P distribution at $\alpha = 16°$.

(c) C_P distribution at $\alpha = 19°$.
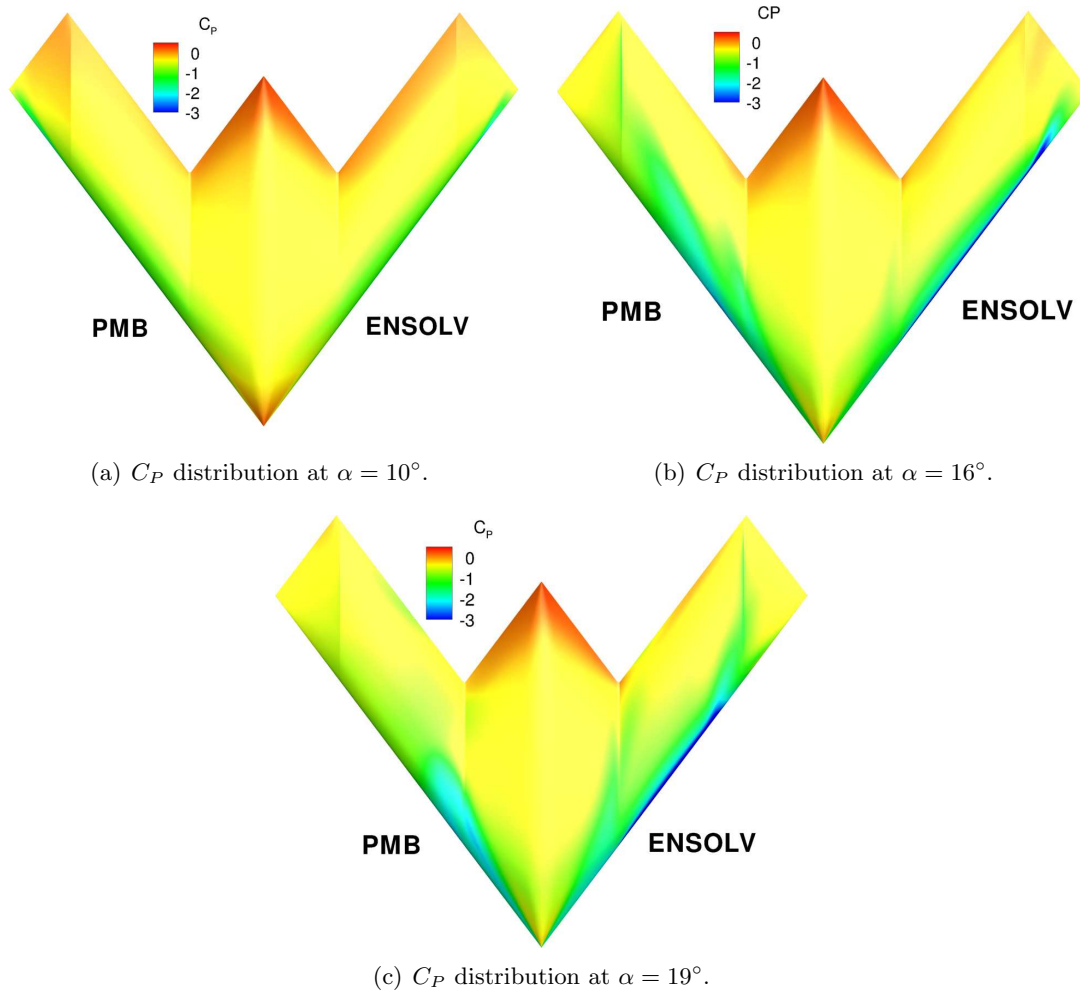
Figure 4.12: Difference in C_P distribution between PMB and ENSOLV solutions.

or hysteresis issues in the flow due to the up or down-stroke motion. The reason for reaching $31°$ is due to the deflection of the sting mounting and the subsequent correction to the angle of attack from the nominal value. Discrepancies are present in the C_m measurements beyond $16°$ angle of attack, shown by two black circles at the same incidence in Fig. 4.11 (c). This suggests that history effects due to vortex structures remaining from a previous angle of attack may be present. Another possibility is that the flow may become unsteady from this point onwards, which could be linked to vortex wandering or oscillation in vortex breakdown location as was seen from the literature review. Both these factors can play a big role in the pitching moment coefficient behaviour. Therefore it is not surprising that the steady RANS methods show high sensitivity to onset flow conditions in this region. Based on the integral RLE results it is not obvious which turbulence model is most realistic.

4.3.2   Flow Structure

The flow around the SACCON UCAV model is dominated by vortical flow which shows a strong sensitivity to changes in angle of attack and leading edge geometry. In this section, a description of the flow topology is given based on the steady state PMB calculations using the baseline k-ω model. Surface pressure coefficient and x-vorticity predictions are used to describe the flow around the SLE model at four angles of attack, 5°, 10°, 13° and 15°. The vorticity in body axes is calculated in Tecplot 2011 [70] using the velocity field information as follows,

$$
\left\{
\begin{array}{c}
\omega_x \\
\omega_y \\
\omega_z
\end{array}
\right\} =
\left\{
\begin{array}{c}
\frac{\partial w}{\partial y} - \frac{\partial v}{\partial z} \\
\frac{\partial u}{\partial z} - \frac{\partial w}{\partial x} \\
\frac{\partial v}{\partial x} - \frac{\partial u}{\partial y}
\end{array}
\right\}
\tag{4.1}
$$

Figure 4.13 shows the C_P distributions over the geometry with slices of flow field vorticity at three different streamwise locations. In addition to this, a plot at four sections over the wing, three perpendicular to the chord and one normal to the leading edge, are shown comparing experimental measurements (black squares) and CFD predictions (red lines). In this figure the chordwise direction is referred to as the x-axis, the upward as the y-axis and the spanwise as the z-axis. As the angle of attack is increased up to 10°, the suction over the top surface starts to build. Figure 4.13 (a) shows the C_P distribution at $\alpha = 5°$ with no indication of non-linear flow. Looking at the three slices to the right of the image a small scale vorticity pocket is shown in blue. Due to the thickness of the wing, these remain close to the leading edge causing no major influence on the overall flow which reattaches over the top surface. This is demonstrated by the velocity vectors in the middle frame showing an attached flow beyond the leading edge.

The first clear vortical structure can be seen at an incidence of 10° at the wing tip region, shown in Fig. 4.13 (b). Proof of this is the area of high vorticity seen in the top frame of Fig. 4.13 (b) and the low C_p footprint present along the leading edge in the tip area. This is also illustrated in Fig. 4.14 (a) by means of streamtraces. This is the term referred to in the software which, for a steady solution such as this one, has the same meaning as a streamlime or streakline. By inspecting this figure in detail, it can be seen that there is a pocket of vorticity above and along the entire leading edge. Looking at the cross-sectional flow at $x = 0.1m$ from the apex, the vortical flow structure has increased in size from the $\alpha = 5°$ case, shown by the large blue oval region. At section $x = 0.5m$ this structure remains present although it becomes flatter due to the thickening of the wing. Finally the aft section shows a large vortex structure which has moved away from the leading edge and lifted off the surface with lower values of vorticity. This implies that the vortex has become weaker as shown by the loss in suction shown in the pressure coefficient footprint. This flow slice clearly shows another high vorticity area forming in the tip region just above the leading edge

(a) $\alpha = 5°$

(b) $\alpha = 10°$

(c) $\alpha = 13°$

(d) $\alpha = 15°$
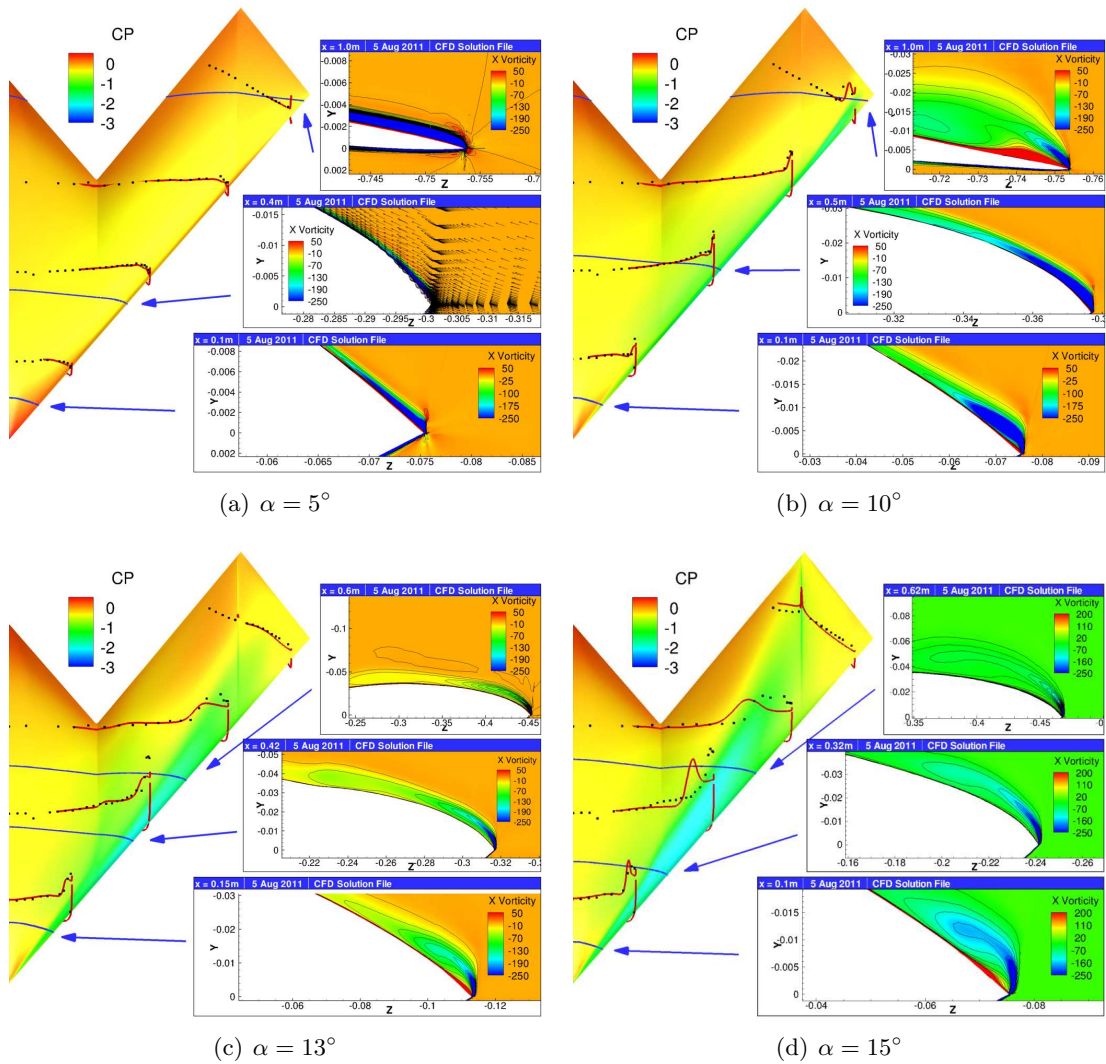
Figure 4.13: PMB predictions of pressure coefficient distribution (baseline k-ω) with plots of experimental measurements and computed results for the SLE model.

with the same sign vorticity as the one originating from the apex. This is caused by the shear layer separation ocurring over the thin section present at the wing which also feeds the apex vortex. It is important to notice the secondary structure that forms below this strong primary vortex. This can be clearly seen in the aft section from the red coloured area, which represents a positive vorticity. The vortex splitting which was discussed in the literature review is clear from this image. The primary vortex now has two cores with a reverse rotating secondary vortex between them. This vortex which rotates in the opposite direction to the primary vortex can be traced back all the way to the front section. It can be clearly seen from these results, that this is caused by the interaction of the reversed flow with the boundary layer and forcing it to rotate in the opposite direction. The favourable pressure gradients present in the main wing region yield a thin boundary layer and therefore the secondary structure is barely noticeable at $x = 0.5m$.

As the angle of attack is increased up to $13°$ the vortical structure changes significantly. Figure 4.13 (c) shows a pressure distribution over the wing with one vortex structure starting at the apex which then splits into two. The front slice taken at $x = 0.15m$ shows a vortex structure more detached from the surface than those seen at lower angles of attack. The secondary flow structure now has a more noticeable presence and is already splitting the vortex. As it extends downstream, the split becomes noticeable from the C_P distribution with one part remaining close to the leading edge and the other changing direction and causing a more downstream trajectory. The two vortex cores can be seen in the flow image at $x = 0.42m$ in Fig. 4.13 (c). The flow at section $x = 0.6m$ shows both vortices weakening with the leading edge vortex becoming flatter before it breaks down further downstream.

At $\alpha = 15°$ the vortex structure remains similar to that at $13°$ with vortices getting stronger at the onset and breaking down further upstream, as shown in part (d) of Fig. 4.13. It should be noted that the vorticity scales have been changed in this plot meaning that the secondary flow shown in red colour is now much stronger than in the previous cases. At angles of attack higher than $15°$ this behaviour remains until a full separated flow is reached at approximately $20°$ when the vortex breakdown occurs at the apex.

The flow from the apex along the vortex core is seen to expand and become weaker at angles of incidence above $15°$. This weakening is clear from the change from a low to a high pressure region further downstream along the vortex path, shown in Fig. 4.13 (c). The expansion in the vortex core can be seen from the increase in radius of the streamtrace's rotational path illustrated in Fig. 4.14 (b). As mentioned in Ref. [8] the breakdown of vortices over low sweep wings is a gradual one with a relatively elongated breakdown region. As a result of this, the surface pressure coefficient increases gradually below the vortex path. This breakdown location is seen to travel upstream as the angle

of attack is increased.

(a) Initial stages of vortex development

(b) Late stages of vortex with breakdown occurring over the top surface
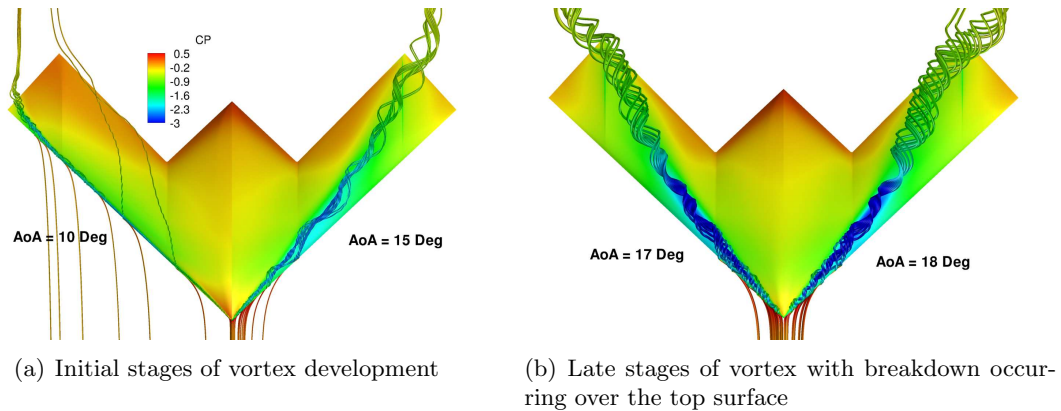
Figure 4.14: Liverpool's predicted flow topology (baseline k-ω) for the SLE.

As discussed previously in this study, the nature of broken down vortical flow is highly unsteady and for this matter, steady state solutions are not appropriate to evaluate the flow topology beyond this point. Nonetheless, these results allow us to determine the point at which the flow velocity inside the vortex core decreases suddenly, suggesting the vortex may be braking down. Figure 4.15 shows the distribution of normalised axial velocity across the vortex core at three different angles of attack, 15°, 18° and 20°. Note that the normalisation is done with respect to the freestream flow. It can be seen from these plots how the vortex core velocity reaches a point at which it decreases rapidly. This is the jet-like to wake-like behaviour which was noticed in previous non-slender wing studies. A minimum velocity is reached inside the wake-like region which becomes as low as approximately zero at 20° angle of attack. As expected, this point of change in core velocity is seen to move upstream as the angle of attack increases.

Plotted over the images of Fig. 4.13 is the measured and computed pressure coefficient, for the SLE model. The black symbols correspond to the experiments and the red lines to the simulations. In these plots the peaks represent the lowest, negative, values of pressure coefficient. The CFD results can be seen to be in good agreement with the experiments at low angles of attack, below 10°, whereas at higher angles some discrepancies occur. The second and third slices in Fig. 4.13 (d) show that the location of the vortex in the experiments is different from that of the CFD prediction, the latter showing the vortex further away from the leading edge. Although not shown here, a gradual improvement in the agreement occurs from 15° to 20° incidence. The region between 13° and 18° angle of attack is where the CFD predictions disagree the most with measurements. The rear section at 15° of incidence shows a strong spike caused by a chordwise discontinuity in the geometry, which is not caputured by the pressure tap measurements.
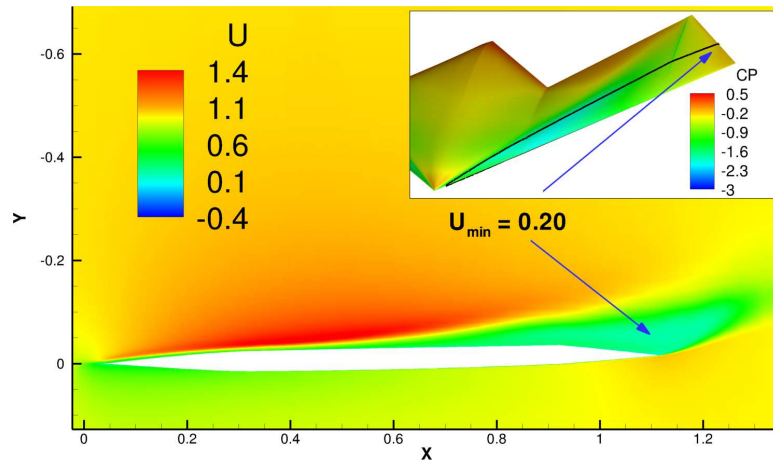
(a) $\alpha = 15°$
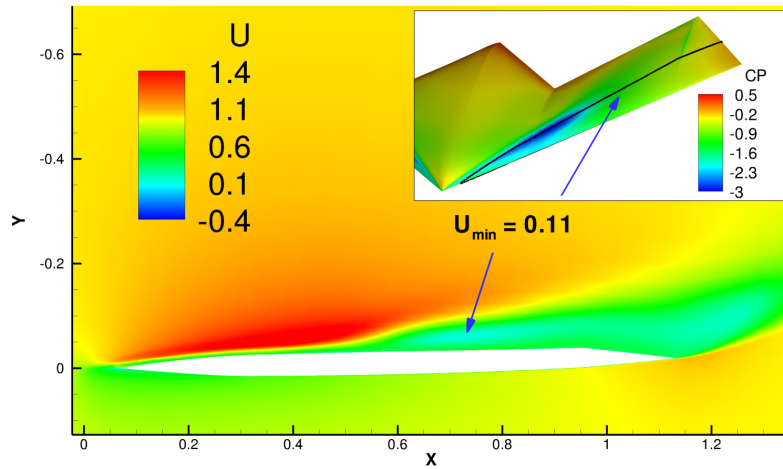
(b) $\alpha = 18°$
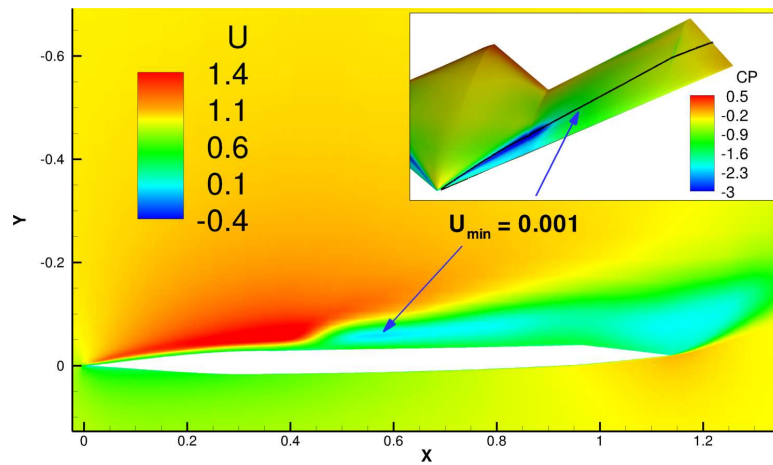
(c) $\alpha = 20°$

Figure 4.15: PMB predictions (baseline k-ω) of downstream velocity, U, across the vortex core.

The flow around the SACCON SLE model shows the existence of a vortex which is split into two by the effect of the boundary layer. This occurs over a small range of angles of attack, 10° to 15° approximately, as the vortex onset and breakdown locations move upstream. The variation in leading edge geometry and the wing washout are the main sources of this flow behaviour. The bluntness along the main wing flattens the vortex structure and forces the flow over them to reattach. Meanwhile, at the inner and outer sections of the model, the vorticity pockets become larger and secondary vortex flows develop. As the angle is increased, the flow over the midsection starts to separate more strongly, causing the vortex to move away from the leading edge.

The flow behaviour for the RLE configuration shows some differences from that seen for the SLE. In the same way as before, the surface pressure distributions at four angles of attack are shown in Fig. 4.16 from the range of angles computed, 10°, 15°, 17° and 18°.

At low angles of attack a similar behaviour to that present for the SLE model is seen. At 10° angle of attack a small pocket of vorticity occurs at the forward part of the leading edge, as shown in the slice at $x = 0.1m$ in Fig. 4.16 (a). Another such vortex structure occurs at the wing tip region, shown in the slice at $x = 1.0m$. The middle section of the wing shows attached flow, effectively giving rise to two distinct vortices, one emanating from the apex and another from the tip region. By 15° angle of attack, the apex vortex has become stronger as the onset of the outer vortex has started to move inboard along the leading edge, shown in Fig. 4.16 (b). Section $x = 0.5m$ shows the flow remaining attached at the leading edge and eventually separating due to the adverse pressure gradient along the top surface. This separated shear layer feeds the apex vortex with the consequent secondary vortical flow underneath, shown by the red region in this flow field slice. Results not shown here indicate that at 16° angle of attack the tip vortex onset is seen to displace quickly as it moves inboard. From here to around 19° incidence a slow merging of the two vortices occurs. At 17° angle of attack, in part (c) of this figure, the the flow over the entire leading edge is separated causing the onset of the outer vortex to move further inboards to start merging with the apex vortex. By section $x = 0.8m$ only the original outer vortex remains strong as it is fed by the shear layer separating from the leading edge. At 18°, the vortices get stronger and the breakdown position is thought to move forward, as seen from Fig. 4.17 (b).

The two vortex flow topology becomes clearer from the streamtraces shown in Fig. 4.17 (a) at 15° angle of attack. In Fig. 4.17 (b) at 17° of incidence, an image showing the beginning of the vortex merging process is presented. Vortex breakdown is present at 17° and 18° angles of attack where the streamtraces change in colour as the spiral increases in size.

Similarities are evident in the flow topologies of the SLE and RLE cases. The

(a) $\alpha = 10°$

(b) $\alpha = 15°$

(c) $\alpha = 17°$

(d) $\alpha = 18°$
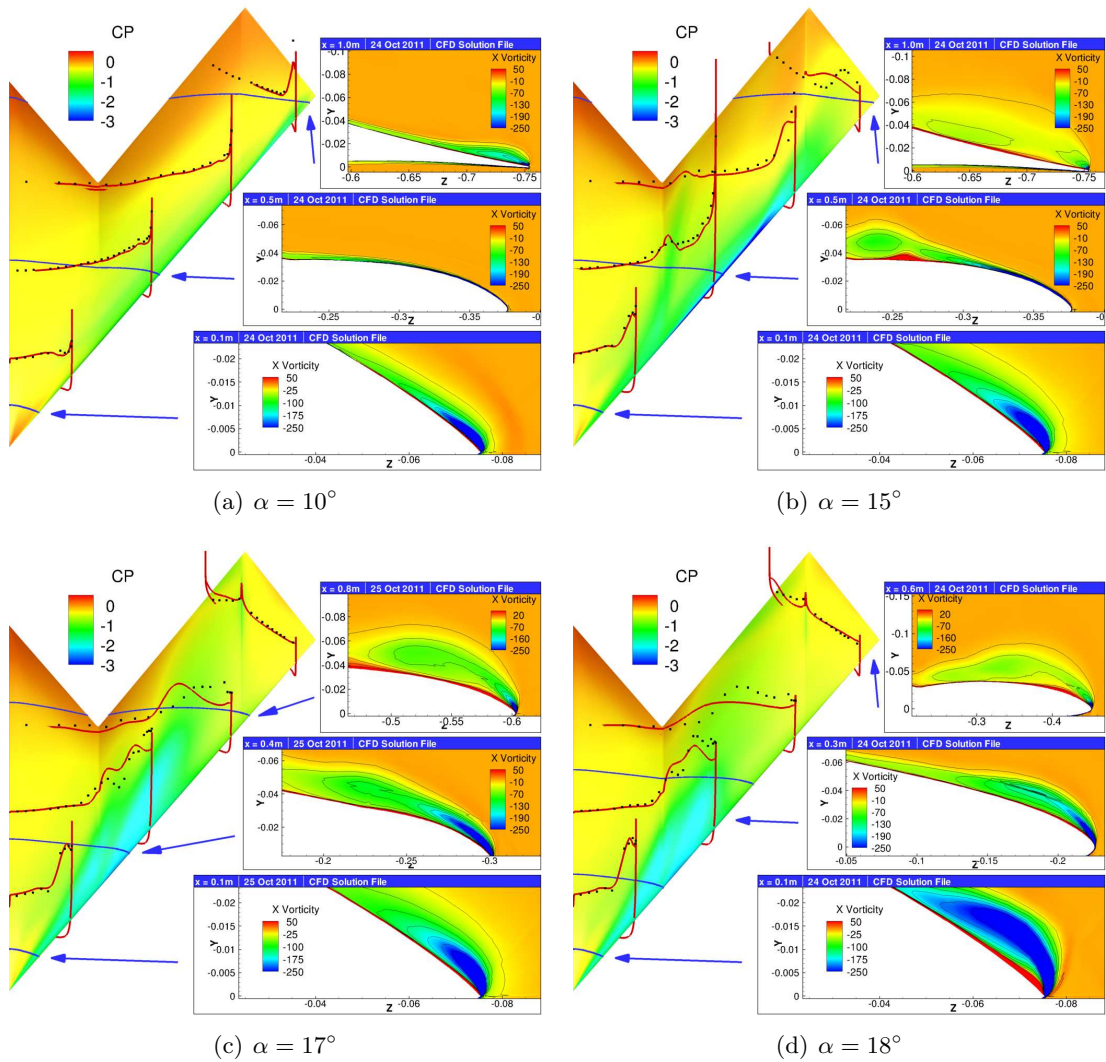
Figure 4.16: PMB predictions of pressure coefficient distribution (baseline k-ω) with plots of experimental measurements and computed results for the RLE model.

differences occur due to the way the flow separates over the leading edge of each model. Both models develop a complex flow structure with two primary vortices rotating in the same direction. Although the origin of this topology is different for the two cases. The sharp leading edge displays a single vortex along the leading edge from low angles of attack which eventually splits into two as the angle of attack is inceased due to a secondary vortex. Whereas the RLE model shows a topology with two different onset locations due to the attached flow occurring at the middle part of the wing. Therefore, as the angle of attack is increased separation starts to take over the entire wing as the two vortices get closer together and eventually merge. Generally, differences occur due to the angles of incidence at which separation occurs from each part of the wing and the way in which the flow separates. For the SLE model, separation always occurs at the leading edge. The RLE model separation occurs at higher angles but is not necessarily initiated at the leading edge. The flow over the SLE model shows what is called a dual vortex structure and the interesting flow behaviour occurring at lower angles of attack, from 10° to 15°, than for the RLE model.

Disagreement between experiments and simulations is present for both geometries. Both the strength and location of the vortices are seen to differ at high angles of attack. Inspection of the pressure coefficient plots in Figs. 4.13 and 4.16 shows that the predicted vortices are generally slightly weaker than the measured ones. In the case of the RLE wing, the noticeable disagreements start to occur at 16° incidence. This is when the outer vortex onset moves inboard and it is this same effect that starts to cause the disagreement in the SLE validation, at around 14°.

In order to look at the RLE flow separation in more detail, slices across the flow solutions were taken. Axial velocity field predictions were compared against PIV results. Angles of attack of 16° and 18° are shown in Figs. 4.18 and 4.19, respectively, since it is for these cases that comparisons disagree the most. Sections at $0.51c_{root}$ and $0.70c_{root}$ are investigated. It should be noted that the geometries from the PIV and CFD solutions appear different. This is because of the PIV grid not adjusting perfectly to the solid surface and focussing only in the regions of interest. This mainly occurs towards the right of the leading edge, where in the PIV measurements the solid blue area is larger than that seen for the CFD results. This did not cause a problem as the region of interest was the area immediately above the surface, where the vortices form. Vortices can be identified from the pockets of lower axial velocity above the surface. At 16° of incidence the PIV results at $0.51c_{root}$ show attached flow around the leading edge and a group of small vortices further inboard. In the aft section, the flow is seen to separate from the leading edge forming a vortex which increases in size as it extends downstream. This corresponds to the outer vortex described from the computations. The small vortices further inboard are seen to merge into a larger structure, thus, having two distinct vortices present with a region of reattached flow

between them. The merged larger structure corresponds to the apex vortex whereas the small scale structures were not seen in the CFD predictions. These smaller vortices are not originating at the leading edge but over the model's surface. This suggests that the cause of their formation is the adverse pressure gradient due to the thickness of the wing, which the CFD models do not capture correctly [71]. The PMB results show two flat vortices which have already started to merge into one at the $0.51c_{root}$ section and get larger as they extend downstream, hence disagreeing with the PIV measurements mostly in the $0.51c_{root}$ section. The ENSOLV solution shows a similar structure to that of the PIV measurements at $0.51c_{root}$ with a vortex above the wing-body intersection. At section $0.70c_{root}$, due to the lag in outer vortex displacement, the ENSOLV solution shows attached flow outboard where the outer vortex is seen to appear. For all cases, the vortex core axial velocity is seen to decrease downstream but no reversed flow is present and so vortex breakdown can be said to be absent.

Looking at the flow at 18° incidence in Fig. 4.19, section $0.51c_{root}$ has attached flow around the leading edge according to the PIV data. Again, a clear multiple small scale vortex structure is shown which then merges into two vortices further downstream. Pockets of broken down flow can be seen at section $0.70c_{root}$. The PMB solution shows the two vortices remaining flat above the surface and merging into one structure by the time they reach section $0.70c_{root}$. By this point, one large part of the flow at the core has reversed, meaning that breakdown is being predicted at an earlier stage. The flow shown in the ENSOLV solution remains similar to that at 16° angle of attack with flow attachment at the leading edge and no vortex breakdown.

Overall, the PIV data shows an image of the flow where large and small scale structures can be identified. The CFD solutions, on the other hand, do not predict the weaker smaller vortices. Advantages and disadvantages of the two CFD approaches can be seen at different sections across the flow but it is not obvious which one produces the best answer. This highlights the weaknesses of the k-ω turbulence models for this particular case. These crossplots provide some insight into the true complexity of the flow around the SACCON model and sets the ground for further work along the CFD validation path. The scope of this study did not allow for more detail than that provided in this section as the importance lain on the integral data predictions. This is the topic of the next section where the overall loads from the vortices which dominate the flow are shown to be in good agreement with the measurements.

4.3.3   Integral Data

An evaluation of the force and moment predictions is presented in this section. Where possible, an attempt is made to explain the non-linear characteristics of this data based on the flow behaviour shown in the previous section. The crossplots of lift, drag and moment coefficients are shown in Fig. 4.20.

(a) Initial stages of vortex development

(b) Late stages of vortex with breakdown occurring over the top surface
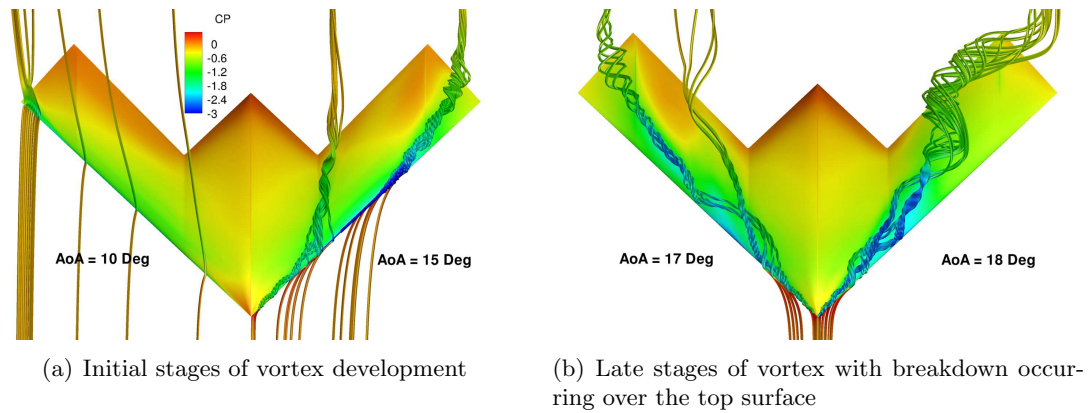
Figure 4.17: Liverpool's predicted flow topology (Baseline k-ω) for the RLE.

(a) PIV at section $c_{root} = 0.51$

(b) PIV at section $c_{root} = 0.70$

(c) PMB at section $c_{root} = 0.51$

(d) PMB at section $c_{root} = 0.70$

(e) ENSOLV at section $c_{root} = 0.51$

(f) ENSOLV at section $c_{root} = 0.70$
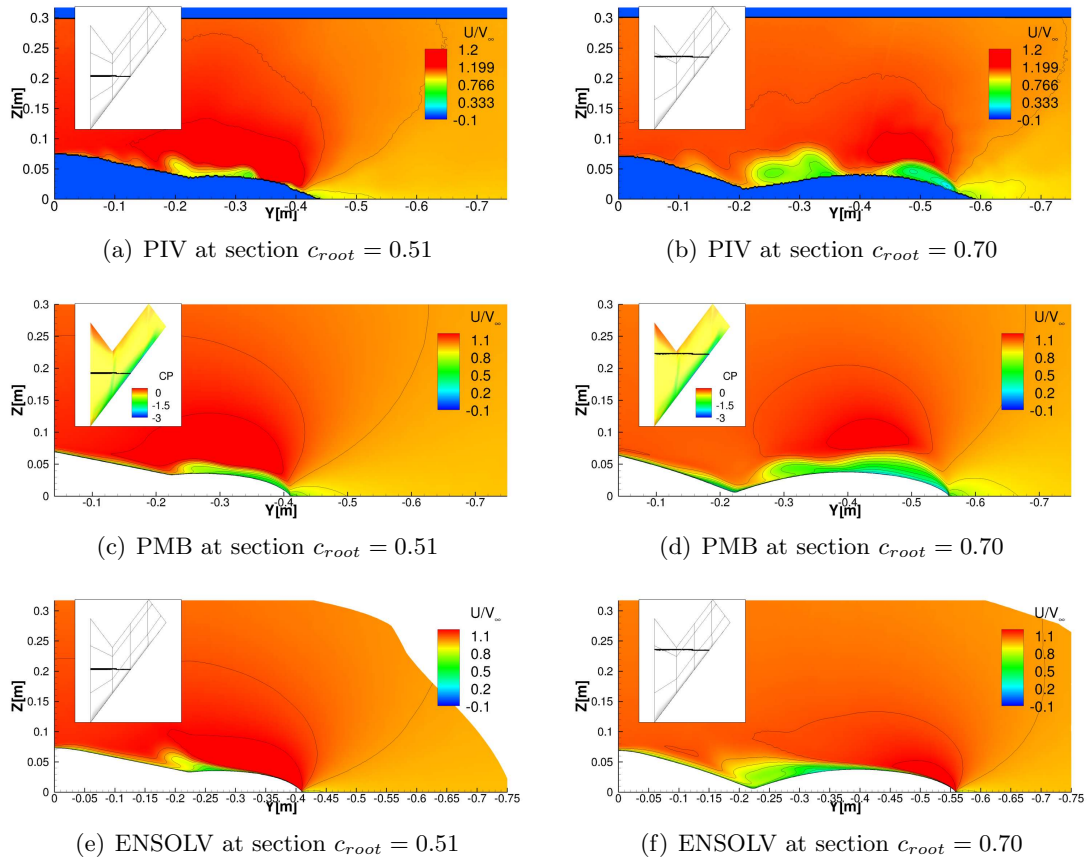
Figure 4.18: CFD data comparison with PIV measurements for the RLE model at $\alpha = 16°$.

(a) PIV at section $c_{root} = 0.51$

(b) PIV at section $c_{root} = 0.70$

(c) PMB at section $c_{root} = 0.51$

(d) PMB at section $c_{root} = 0.70$

(e) ENSOLV at section $c_{root} = 0.51$

(f) ENSOLV at section $c_{root} = 0.70$
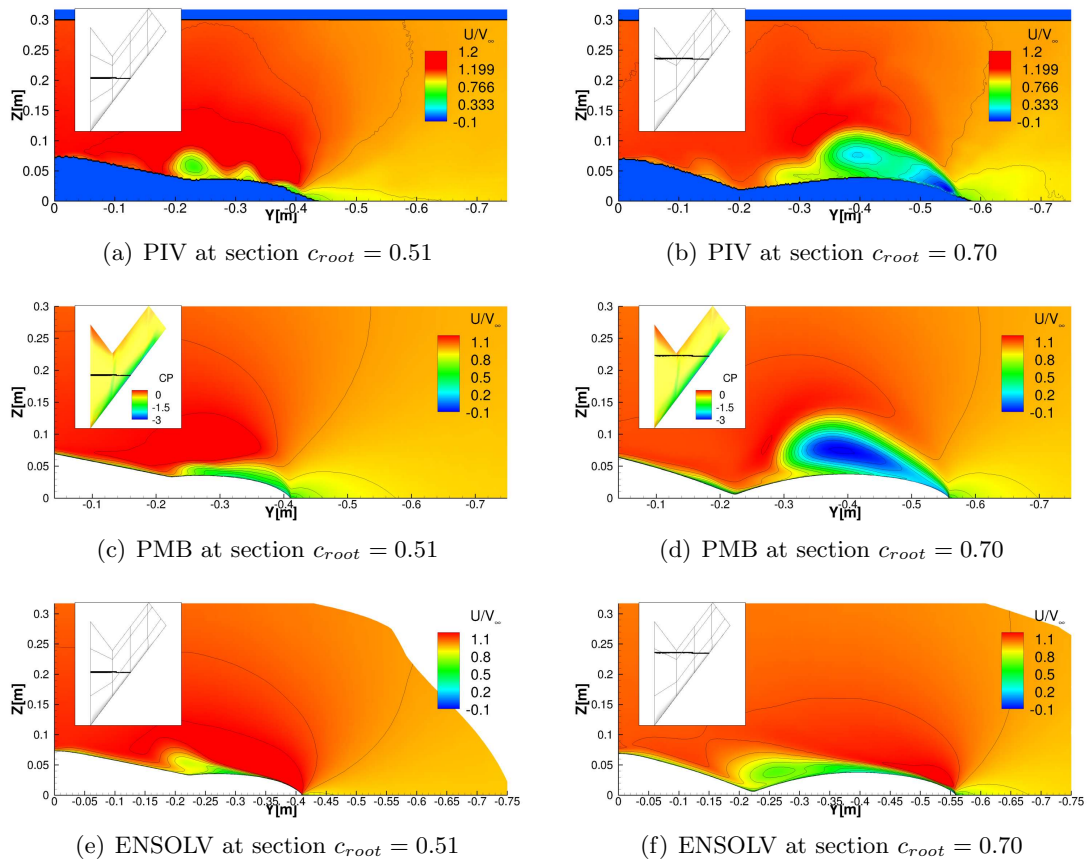
Figure 4.19: CFD data comparison with PIV measurements for the RLE model at $\alpha = 18°$.

Figure 4.20 (a) shows the lift coefficient values as a function of angle of attack for the SACCON SLE obtained from the experiments and a range of steady flow simulations. The plots follow a linear trend up to an angle of attack of 13° where they start to follow a shallower path. Beyond 20° incidence the plots become relatively flat due to a progressive wing stall. This occurs as the vortex breakdown position travels upstream towards the apex. This movement of breakdown position leads to a progressive reduction in the vortex-induced suction force which causes this deficit in lift. It can also be seen that the agreement between the two sets of data is good in the linear and non-linear regions with a slight offset throughout. As mentioned previously, this is due to the effect of the sting, as seen from other SACCON CFD studies [71, 72]. The drag predictions also show a good agreement with the experimental data, with a slight discrepancy beyond 20° angle of attack, see Fig. 4.20 (b).

The pitching moment behaviour is the most interesting of the three since it shows a more non-linear behaviour, Fig. 4.20 (c). The measurements show a change in gradient at 3° and a linear increase from there up to 12° angle of attack. A strong dip is present at 15° before the moment coefficient recovers up to a new maximum at 22°. The simulations predict the main characteristic drawn from the experiments. The computed coefficient increases linearly up to 10°. At this point the tip vortex starts to appear with a pitch down influence, causing the predictions to flatten up to 12.5°. The strength of the dip at 15° is overpredicted and so is the maximum value of C_m above 20° angle of attack.

The dip occurs because the onset of the tip vortex moves suddenly along the middle part of the wing and starts to merge with the apex vortex, at 13° angle of attack. This changes the force distribution over the wing very rapidly, to which the C_m is very sensitive. As the single vortex becomes stronger, due to the increasing incidence, a large region of high vortex-suction occurs at the forward section. For this reason and the fact that the vortex breakdown position moves gradually upstream, the pitching moment coefficient recovers again to a new maximum value. The overprediction in the dip does not result from an excess vortex strength, as the strengths were seen to be similar in Fig. 4.13 (c). The predicted vortex is seen to be located further inboard than the measured vortex, meaning that the onset is likely to be further forward. This suggests that the magnitude of the dip is overpredicted because the vortex onset is too far inboard between 12.5° and 15° incidence.

The SLE and RLE integral results show noticeable differences, as would be expected from the flow topologies seen in the previous section. Figure 4.11 (a) shows the measured and predicted lift curves. The linear slopes of the two curves are in good agreement apart from the previously mentioned sting offset. The drag coefficient results, Fig. 4.11 (b), also show a very good agreement between the predictions and the experiments for the RLE.
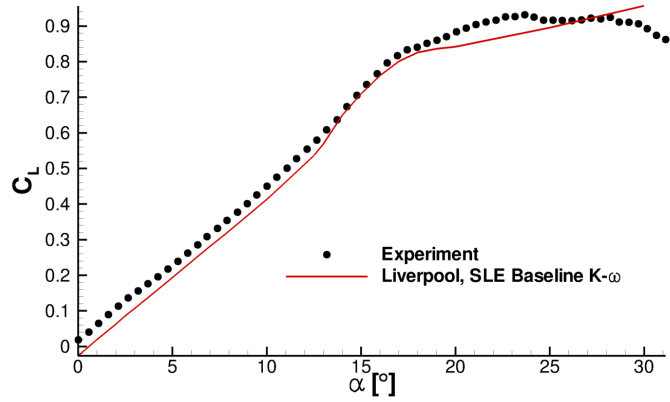
(a) C_L against angle of attack.
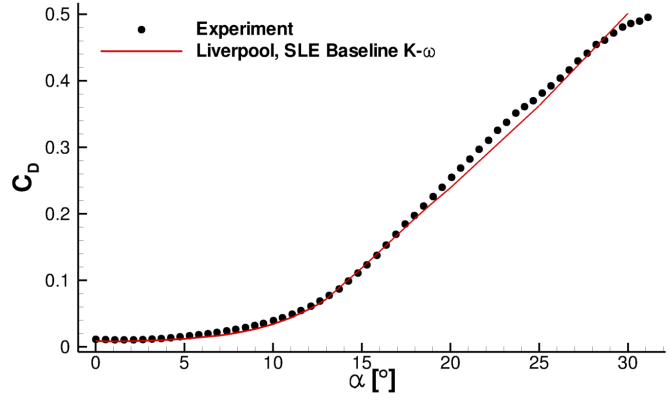
(b) C_D against angle of attack.
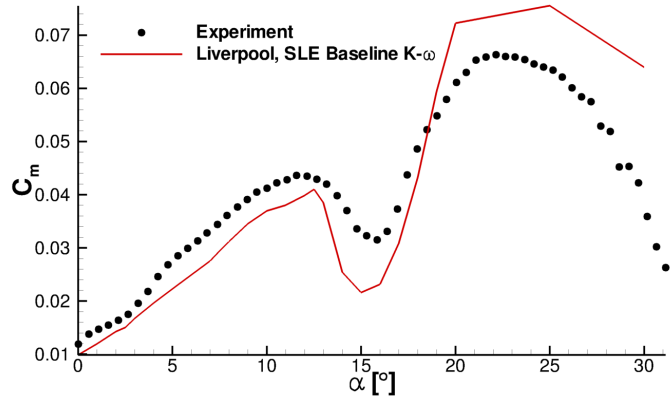
(c) C_m against angle of attack.

Figure 4.20: Integral data from experimental results and PMB computations for the sharp leading edge model.

The pitching moment plot for the RLE has some similarities with that of the SLE although generally the behaviour has more abrupt changes. The reason for the poor C_m agreement at lower angles of attack is not fully understood. Despite the good agreement in C_p shown by the pressure tap measurements there seems to be regions where the predicted flow is in disagreement. One suggestion points to vortices originating behind the sting not being predicted by the Unsteady RANS (URANS) methods. This could result in low pressure present on the aft bottom surface. In order to locate the regions of the flow around the body affecting the pitching moment plot, the differences in C_p distribution between the two solutions were calculated. Then the influence on the C_m was obtained by multiplying the C_p at each point by the moment arm. By subtracting the C_m distribution from solutions at two given incidences, the non-linearities in Fig. 4.11 (c) can be explained.

Figure 4.21 shows the ΔC_m distribution around the top and bottom of SACCON for different cases. The positive regions (red) show a pitch up moment contribution, and the negative (blue) represent a pitch down. The experiments show an initial linear part up to an incidence of 10°. In Fig. 4.21 (a) and (b) a positive increase in ΔC_m in the region near the apex can be seen. The negative influence of the outboard, aft section is not large enough to counteract the pitch up moment in this range of angles of attack. As the outer vortex starts to gain strength over the tip section from 10° onwards, the pitching moment plots are seen to flatten. Figure 4.21 (c) shows clearly the increase in pitch down effect from the tip section as the angle of incidence is increased from 10° to 14°. At the same time, the pitch up contribution from the apex region has decreased slightly compared to the lower angles of attack, hence the change in behaviour on the plot. Figure 4.21 (d) shows a pitch up area in the tip section due to the inboard displacement of the vortex between 14° and 15° incidence. This causes the small spike in pitching moment coefficient before the large drop at 16°. Up to this point the baseline k-ω predictions are in good agreement with the experiments with an offset throughout. The drop at 16° is similar to that seen for the SLE model and is caused by the sudden movement of the outboard vortex as it shifts inboard merging with the apex vortex. The same vortex behaviour causes this drop on the RLE wing, as shown in Fig. 4.21 (e). The large negative region in the aft part of the middle section of the geometry illustrates how the suction effect from the vortex causes the pitch down moment. The computed results from the baseline k-ω model predict an earlier dip than the measurements. This is due to the early movement of the outer vortex onset along the leading edge. Figure 4.21 (f) shows that the reason for the steep increase in moments from 16° to 20° is the strong vortex suction over a small elongated region near the apex. Furthermore, it can be seen here that separation from the trailing edge and the separated flow over the midsection also have an effect on the pitching moment.

(a) ΔC_m between $\alpha = 0°$ and $5°$

(b) ΔC_m between $\alpha = 5°$ and $10°$

(c) ΔC_m between $\alpha = 10°$ and $14°$

(d) ΔC_m between $\alpha = 14°$ and $15°$

(e) ΔC_m between $\alpha = 15°$ and $16°$

(f) ΔC_m between $\alpha = 16°$ and $20°$
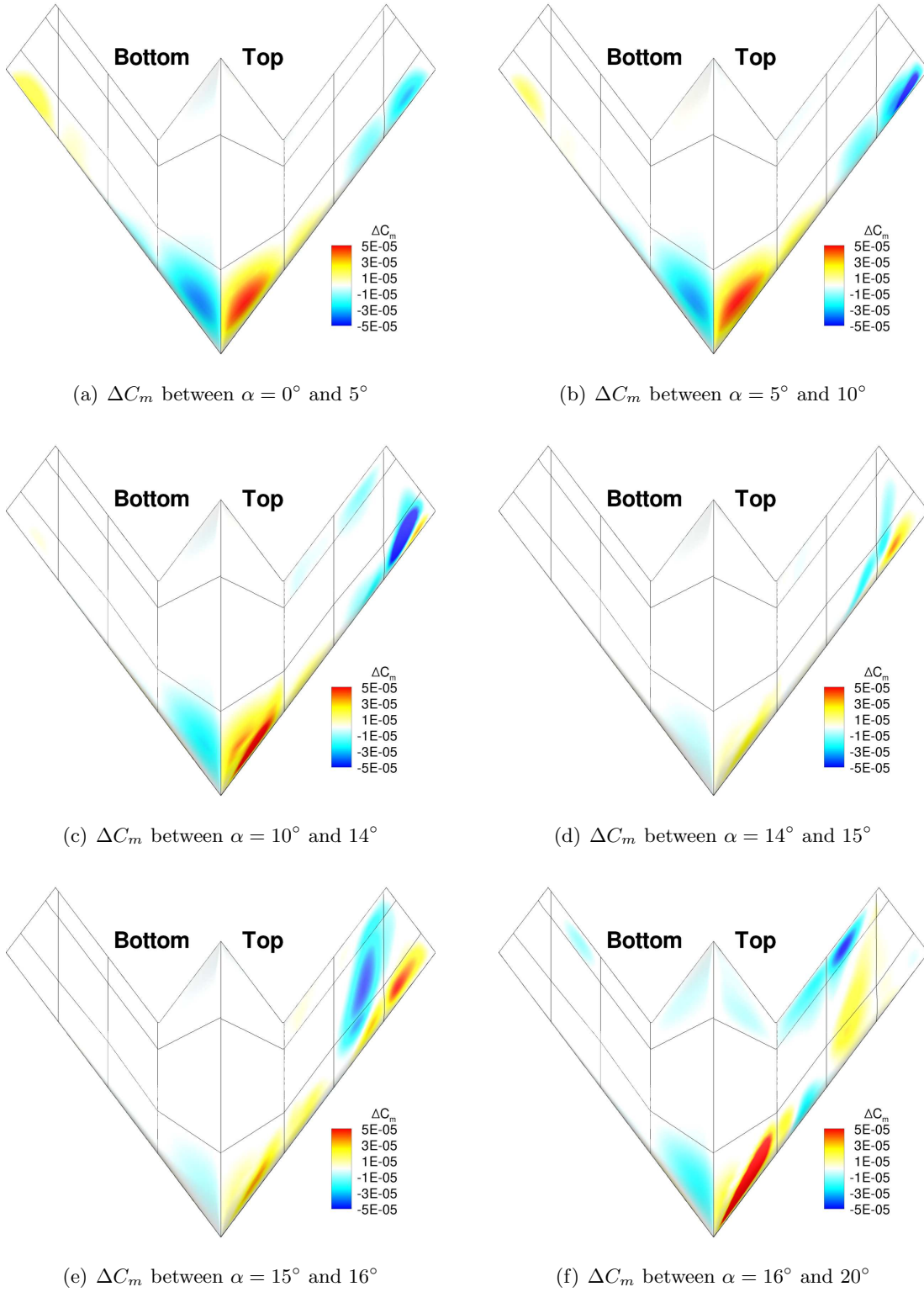
Figure 4.21: Distributions of change in moment over the top and bottom SACCON RLE surfaces.

4.4 Dynamic Results

SACCON forced oscillatory motions were simulated to evaluate the model's dynamic effects on the integrated forces and moments. These motions replicated those performed in the wind tunnel experiments to validate both the SLE and RLE model results. Table 4.5 outlines the cases that were selected for this study. Due to the computational cost of each simulation, two cases were selected from the range of frequencies, one for each model at the minimum and maximum frequencies tested during the experiments. During the experiments a set of "wind-off" measurements were taken with the model oscillating before turning on the wind tunnel. The mass and inertial forces obtained from the first run were used to process the data from the "wind-on" measurements. Low pass filtering was applied to the pressure tap and balance data to cut off all frequencies above $5Hz$. This was done to remove noise effects and capture frequencies which most affect the overall loads. It is important to highlight that no blockage corrections were made to the wind tunnel dynamic oscillation measurements. Only frequency effects were reviewed in this study, $f = 1, 3Hz$, whereas the effects of velocity and amplitude were not. Table 4.5 describes the conditions of the cases simulated for the SLE and RLE models. The results from each oscillation are shown here to see whether there is any unsteadyness influencing the flow. The scope of this project was for longitudinal pitch motions to be validated.

Table 4.5: Dynamic cases validated for SACCON.

Config.	Mode	α_0 [°]	f [Hz]	A [°]	M	Re [$\cdot 10^6$]	k	$\hat{t}$	T
SLE	pitch	10	1	5	0.1743	1.8763	0.025	0.07	$125.3\hat{t}$
RLE	pitch	10	3	5	0.1467	1.6167	0.09	0.25	$34.8\hat{t}$

To carry out the unsteady calculations it is important to understand how the time step is non-dimensionalised in PMB. A unit time step during an unsteady calculation is dependant on the length scale of the grid and the freestream velocity as follows,

$$\hat{t} = t\frac{V_\infty}{c_{ref}} \tag{4.2}$$

One non-dimensional time step, $\hat{t}$, is essentially how long it takes for a particle to travel the unit length of the grid in real time. For the SACCON case the grid was made to match the model size, a unit grid size being $1m$ which is approximately the length of the fuselage at the symmetry plane. This is particularly important when performing unsteady calculations in order to capture the desired frequency flow structures such as small vortices beyond breakdown. This study overlooks the effects of high frequency unsteady flow effects to focus on low frequency damping effects due to the oscillatory motion.

For this reason, time steps between 0.05 and 0.3 have been used in the calculation of forced oscillatory motions for SACCON. The frequency of oscillation of the motion, ω, was non-dimensionalised using the following equation,

$$k = \frac{c_{ref}}{2}\frac{\omega}{V_\infty} = \frac{\pi c_{ref} f}{V_\infty} \tag{4.3}$$

where k is the non-dimensional frequency. The period of oscillation of the $1Hz$ and $3Hz$ motions were $T = 125.3\hat{t}$ and $T = 34.8\hat{t}$, respectively.

(a) C_L.   (b) C_m.
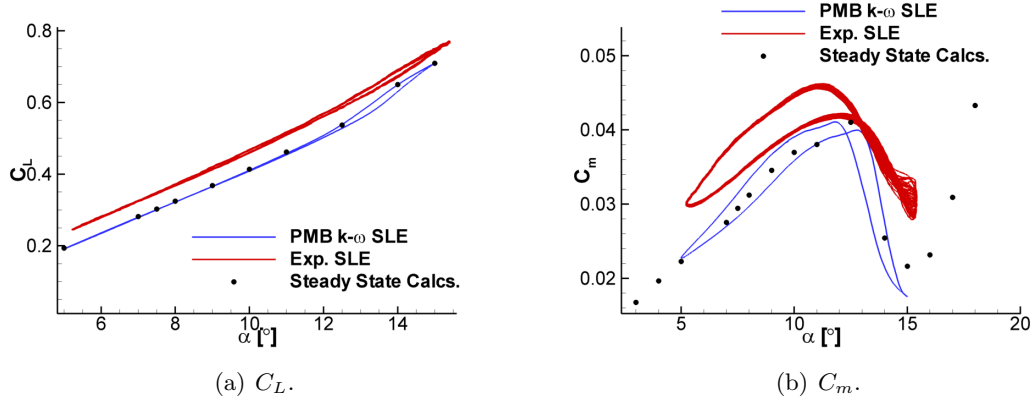
Figure 4.22: Pitch forced motion integral data from experiments and PMB computations for the sharp leading edge model at $\alpha_0 = 10°$ and an amplitude of $5°$.

Figures 4.22 shows the integral data computed for the SLE case. The red and blue lines denote the experimental measurements and the time-accurate simulation, respectively, whereas the black dots represent the steady state computations presented previously. It can be seen that the steady state data agrees well with the dynamic simulations for both C_L and C_m, Fig. 4.22 (a) and (b). In the case of the lift coefficient there is little hysteresis present except for at angles of attack above $13°$. The pitching moment shows more hysteresis than the lift coefficient. Also, the plot is seen to crossover at around $12.5°$ angle of attack. The static data generally lies at the mean of the upper and lower parts of the plot, denoting there is good agreement, except for at the top of the loop where the dynamic case reaches lower values. The measurements show very similar lift behaviour to the simulations with the discussed offset due to the sting mounting. The moments plot shows a noticeable spread at the higher angles of attack suggesting there is some unsteadiness in the flow in this region. The hysteresis seems to be larger than that seen from the simulations for the lower angles of attack. As expected from what was seen in the static measurements, the dip is not as strong as what is predicted.

The computed results for the RLE case are shown in Fig. 4.23. The lift shows little hysteresis in the simulations and good agreement with the static data. The experiments in this case do show some dynamic effects for the most part of the angle of attack range.

(a) C_L.   (b) C_m.
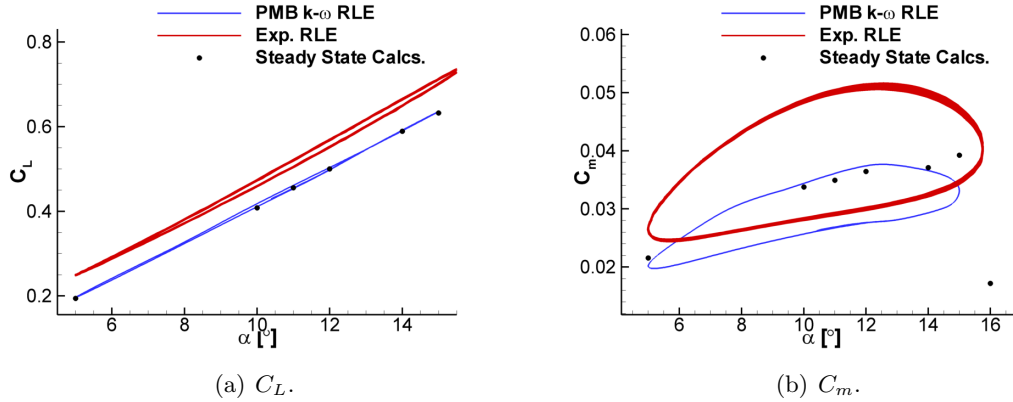
Figure 4.23: Pitch forced motion integral data from experiments and PMB computations for the round leading edge model at $\alpha_0 = 10°$ and an amplitude of $5°$.

The pitching moment here does not reach the angle of attack where the dip occurs so a relatively linear plot is shown from both measurements and predictions. This is the region in which the outer vortex starts to form, changing the shape of the typical linear behaviour elliptical plot. The hysteresis loops again are seen to be larger in the measurements. The static results in this case are slightly above the mean value of the predictions. Overall, it is clear that the model dynamics have a greater effect on the pitching moment than on the lift coefficient. A certain amount of unsteadiness seems to be associated with the pitching moment dip and the plots cross over.

4.5   Summary of Validation Work

Throughout this chapter a description of the flow behaviour and force and moment coefficients for the SACCON has been provided. Benchmarking the CFD results with experimental measurements has given confidence in the capability of the numerical methods to simulate the flow physics important for this particular test case. Differences between these methods have been highlighted and their influence on the comparisons discussed. Despite shortcomings such as walls, mountings and instrumentation interference effects, wind tunnel testing is still considered a more reliable source of aerodynamic data than CFD. Nonetheless, numerical methods are evolving to simulate the flow physics ever more realistically with all its advantages. These include the ability to model the geometry of interest alone, the availability of a complete data set across the entire flow field and the relatively low cost of simulation.

Balance, pressure tap and PIV results during static and dynamic experiments provided a good understanding of the nature of flow around the SACCON configurations. Pressure tap measurements showed the disparity in vortex locations at post stall angles of attack and the balance measurements showed the effect of this mainly on the pitching

moment curve. Forces remained in good agreement as the vortex strength predictions agreed well with the experimental measurements. Unsteady flow behaviour became evident from the spread in static and dynamic force and moment measurements beyond stall. Although not much insight can be gained from flow topologies from steady state computations in the unsteady vortical flow regions, these moderately expensive simulations demonstrated a good predictive capability of integral forces and moments at these conditions. Differences in overall load predictions were noticed between the two validated CFD codes which was found to come from differences in the turbulence models as opposed to a grid issue. The single most important source of discrepancy when benchmarking the CFD results was the sting mounting effect. An offset in the longitudinal forces and moments was seen throughout the linear flow region most likely due to the flow behaviour behind the sting. A more recent study using DDES at the U.S. Airforce Academy [73] has proven that the time dependent small scale eddies in this region are the cause for this disparity. Both the sting mounting and the wind tunnel walls were proven to have a noticeable effect on the integral data, the pitching moment coefficient in particular. Therefore the clean configuration RANS simulations can be thought to provide a more realistic prediction of the overall forces and moments acting on the SACCON model. Another source of disagreement is linked to the turbulence tripping which was used for the RLE model but not the SLE. It is reasonable to say that this was not as critical for the second case as high adverse pressure gradients develop at the leading edge causing separation and the onset of the vortex structures. For the round geometry on the other hand, it was imporant to ensure the fully turbulent CFD methods were being validated against comparable turbulent flows. Else, free transition effects would have to be accounted for, thus setting the foundations for a separate study, which although very interesting, is not the focus of the work presented here. Nonetheless, pressure gradients developing over the top surface of the RLE wing triggered multiple small vortical structures which were captured by the PIV measurements at low post stall incidence angles. These were not seen from the RANS simulations although their effect on the pressure distribution and the forces and moments was not evident. Wind tunnel corrections were made which account for blockage and wall effects on the balance measurement data, up to 4%, and corrections to the nominal angle of attack due to sting deflections. Finally, insight into the vast difference in flow behaviour arising from different leading edge shapes has been demonstrated. Both SLE and RLE models have a similar leading edge thickness distribution but the adverse pressure gradients caused by sharp surfaces trigger vortical structures which dictate the overall flow topology and subsequently the pressure distribution around the entire wing.

From the CFD validation point of view, the information on pressure distribution over the wing and flow field structures provided by the different measurement techniques

is very interesting. The comparisons presented in this chapter provide some insight as to how accurate the current aerodynamic simulation methods are and how the strengths of such techniques may be used for certain purposes. For this work, the goal was to predict aircraft loads for a manoeuvre prediction method and the results presented here provide confidence in the numerical capability. Therefore, it was concluded that CFD was suitable for the generation of aerodynamic data tables and flight dynamics predictions. Nonetheless, the understanding of the flow structure gained from this work provides a platform for the evaluation of the tabular methods in Chapter 6.

For the remainder of this thesis, focus is shifted towards the effect of the investigated flow on the flight dynamics of a UCAV configuration. As it has become evident from this and previous studies, vortical flow dominates the aerodynamic behaviour of UCAV delta wing configurations at moderate and high angles of attack. As such, the SACCON wing model has shown to be a valid generic test case for this type of wing and its aerodynamic characteristics make for a relevant and interesting test case for a flight dynamics representation. The performance of an aircraft in flight is dominated by its ability to alter the forces and moments acting on it at any given time to achieve a desired motion. As it will be shown in the next chapter, the motion of an aircraft in flight is dependant on a range of forces from which the aerodynamic one is important. In order to model flight motions, or manoeuvres, it is necessary to have an estimation of the aerodynamic characteristics of the vehicle. To do this, the CFD techniques described before can be used in different ways to predict the aerodynamic forces on the aircraft during a given manoeuvre. Purely from an aerodynamic point of view, the particular interest lies on the vortical flow at high angles of attack causing sudden changes in pitching moments and non-linear behaviour in every other aerodynamic characteristic. Another important factor is the hysteresis seen at relatively low frequencies of oscillation which can cause major differences in the forces and moments expected to occur during flight. These dynamic effects cause local induced angles of attack and sideslip as well as transient vortical structures which add complexity to the flow behaviour to be predicted.

Chapter 5

Generation of Manoeuvres

In this section a methodology is described which allows the generation of realistic aircraft manoeuvres based on CFD RANS computations [74]. The aim is to evaluate the advantages of different methods to predict aircraft loads during manoeuvring flight. The SACCON SLE model was chosen for the purpose of this study due to its highly non-linear flow behaviour and well validated CFD predictions. The process is divided in several stages involving aerodynamic and flight dynamics modelling. Figure 5.1 shows a flowchart describing the methodology used. At the core of this process is a tabular aerodynamic model. First, a data fusion method is used to populate a predefined set of aerodynamic tables. The tables are populated using a small number of static, steady state RANS calculations. In addition, the RANS equations are also used to determine control surface effectiveness and body dynamics effects which are implemented as increments to the method. Once the aerodynamic model is complete, a Matlab based commercial package, called DIDO [75], is used to predict realistic manoeuvres. To do this, the mass and inertial characteristics of the aircraft model need to be defined. The code is then run using the nonlinear equations of motion to predict the exact motion of a predifined manoeuvre. These manoeuvres are designed using time-based state and control constraints. The resulting aircraft motion can then be replayed using a time-accurate RANS simulation. The resulting force and moment characteristics through the manoeuvre replay can be crossplotted against the predictions from the tabular model. This chapter describes in detail the nature of the tabular model and the methods to predict the static and dynamic aerodynamics. This is followed by a detailed description of the manoeuvre prediction method.

5.1   Test Case

The SACCON model was designed purely as an aerodynamic validation test case. Hence, no consideration was given to common wing design issues such as wing tip offloading, centre of gravity location effects, engine intake and exhaust modelling or wing thickness considerations due to drivetrain and fuel tank constraints. Although
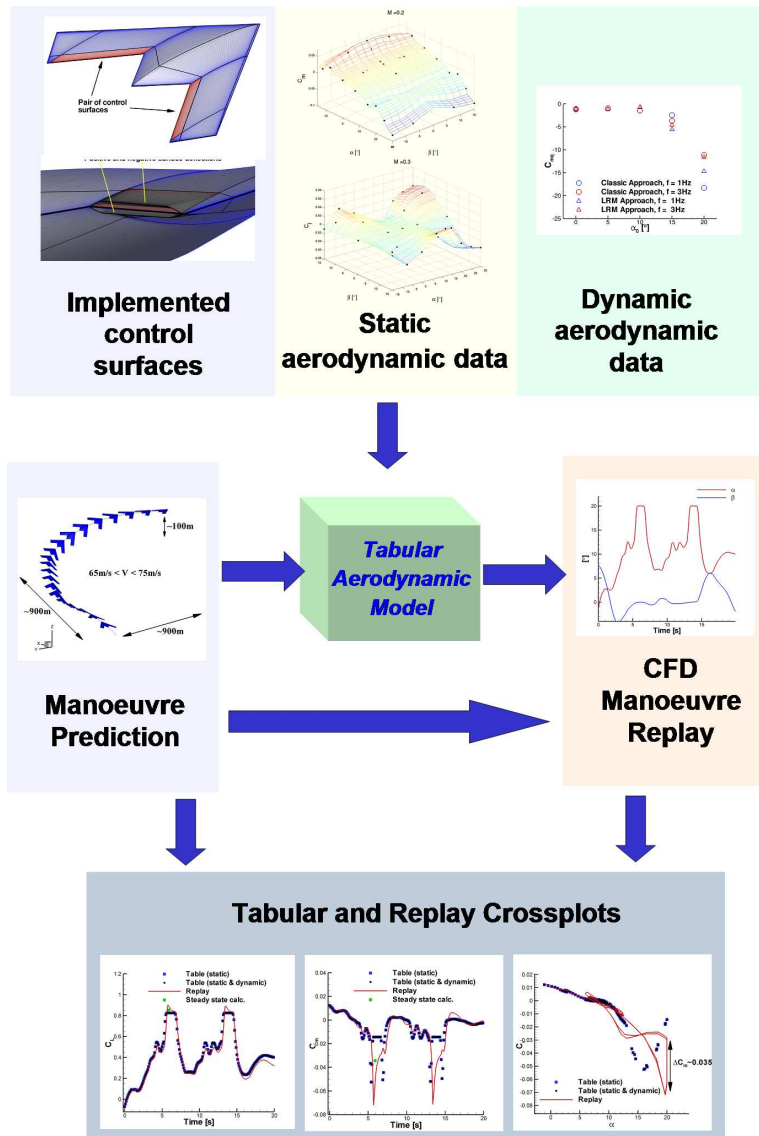
Figure 5.1: Flowchart describing the flight dynamics assessment methodology.

due to the interesting flow behaviour seen in Chapter 4, the SACCON SLE model was chosen as a test case for this methodology. In order to accurately capture the flow behaviour the RANS equations were used in PMB with the baseline $k - \omega$ turbulence model, as for the validation. For the purpose of this study, a full span grid was generated in order to compute lateral characteristics.

The SACCON is a wind tunnel model with no real data for a full scale aircraft based on that exact geometry. Therefore, the first step was to determine an appropriate location for the centre of gravity which was both realistic and provided static and dynamic stability. Not only this, but with high angle of attack manoeuvres in mind a high trim angle of attack was preferred. In order to allow for manoeuvres to be performed at high angles of attack for noticeable time periods ideally the gradient of the pitching moment curve would be small to allow for large changes in angle of attack without strong aerodynamic pitching moment reaction. The validation data provided a good starting point. All integral data had been computed about the MRP location at $0.6m$ from the apex on the symmetry plane. As shown in Chapter 4, the pitching moment shows a positive gradient as the angle of attack is increased, meaning that a centre of gravity located here would yield a statically unstable configuration. Different positions were tested and the resulting pitching moment behaviour with a Mach number of 0.17 is shown in Fig. 5.2. From this, it can be seen how at $0.6m$ the plot is positive for positive angles of attack and therefore the aircraft is unstable. If the CG is placed at $0.4m$ from the apex the system becomes stable although the pitch down moment is very strong at high angles of attack, meaning that the aircraft would require large control forces to rotate in the pitch axis. At $0.5m$ the C_m plot shows a nice decreasing trend with a trim point at approximately 2.1° angle of attack. At $0.55m$ the C_m plot becomes even flatter with a high angle of attack trim point at 6°. Both $0.5m$ and $0.55m$ locations seem appropriate, although the CG was finally located at $0.55m$ due to its low maximum and minimum values across the incidence angle range. Tests using the manoeuvre prediction software showed this location was more suited for high angle of attack manoeuvres due to the high angle trim points and relatively low C_m values at high α, allowing for small control forces to counteract the aerodynamic forces. In Section 5.3 it is shown how the aircraft is also dynamically stable when the CG is located at this point. From this analysis it is also evident that the centre of pressure for the range of angles of attack lay somewhere between $0.55m$ and $0.6m$ from the apex. This explains the sensitivity of the pitching moment plot to changes in the flow distribution.

The next step was to devise a set of controls to allow the UCAV to be steered through a given manoeuvre. Ideally, each one of these would provide completely decoupled control over each one of the aircraft states. In reality this is almost never the case and some compromise needs to be accepted. Control effectiveness was also taken into
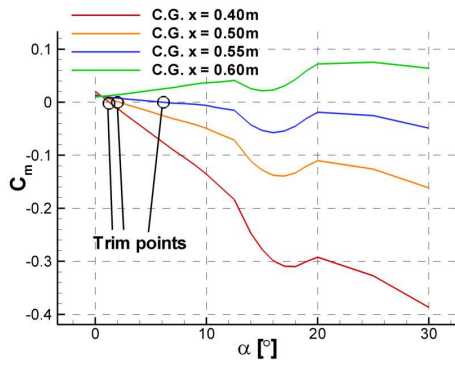
(a) C_m against α for different CG locations.
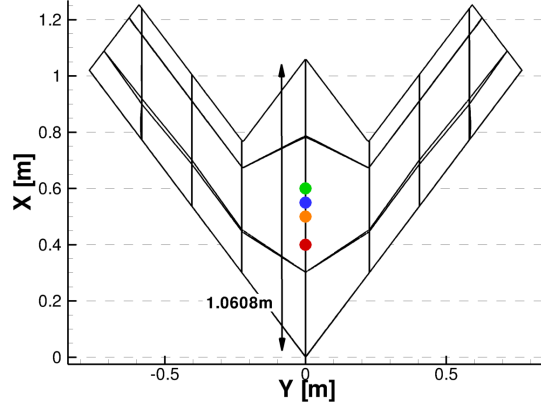
(b) Schematic representation of the CG positions on the symmetry plane of the configuration.

Figure 5.2: Influence of centre of gravity location on the pitching moment coefficient.

account to make sure that all forces and moments acting on the aircraft could be counteracted by control driven forces and moments. A pair of control surfaces was designed, one on either wing, which spanned almost the entire length of the wing's trailing edge. The dimension along the x-axis is 20% of the local chord and is shown by the green areas in Fig. 5.3 (a). These can be used as elevators if deflected in the same direction or ailerons if deflected differentially (one up, one down). It was decided that for this UCAV model the control surfaces would be used as ailerons for roll control and a thrust vectoring technique for pitch and yaw. This feature is not uncommon in modern day fighter aircraft where both fluidic and mechanical thrust vectoring techniques have been used. This has an added advantage over conventional aerodynamic surfaces where the effectiveness is seen to decrease for high angle of attack or low dynamic pressure conditions [76]. The point from which the thrust is modelled is at 1m from the apex and angular rotations about the Y and Z-planes of up to 45° are allowed. Figure 5.3 shows this in detail, where η_θ and η_ψ are the deflections about the Y and Z axes, respectively. The short body of the SACCON configuration meant that large thrust forces and vector deflections would be required to control the pitching moment during flight.

The control surfaces were implemented in the original full span grid as plain, trailing edge flaps which are shown in Fig. 5.4 (a). This was done by matching the block topology around these surfaces and deforming the solid surface as required. Transfinite interpolation is then used to displace the grid points in the blocks adjacent to the control surfaces. Thus, the result is a deflection of the solid boundary which approximates that from real flap configurations. The advantage is the simplicity of having the same block topology as opposed to dealing with a new free surface boundary everytime the controls are deflected. This is depicted in Fig. 5.4 (b) where positive and negative deflections

(a) Top view.　　　　　　　　　　　　　(b) Side view.
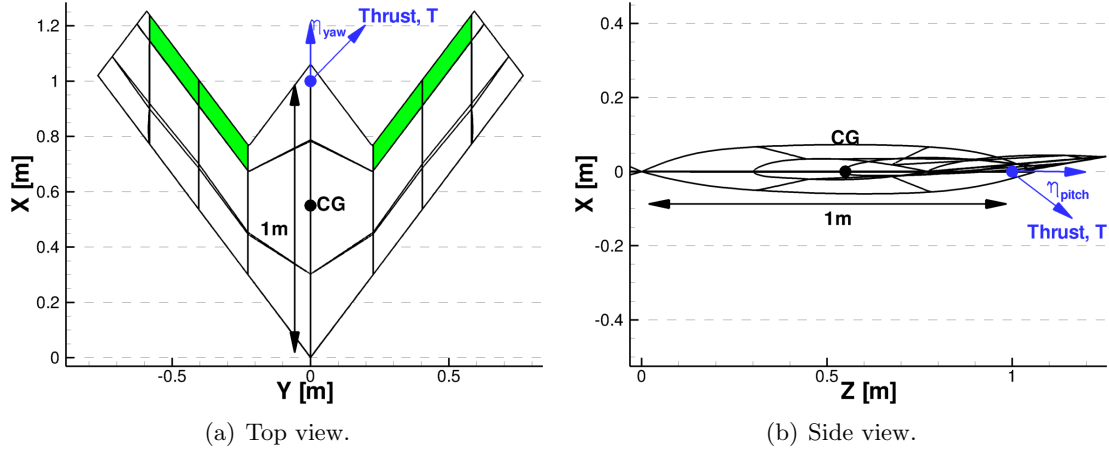
Figure 5.3: Thrust vectoring technique schematics.

of the surface are shown, in this case $\pm 15°$.
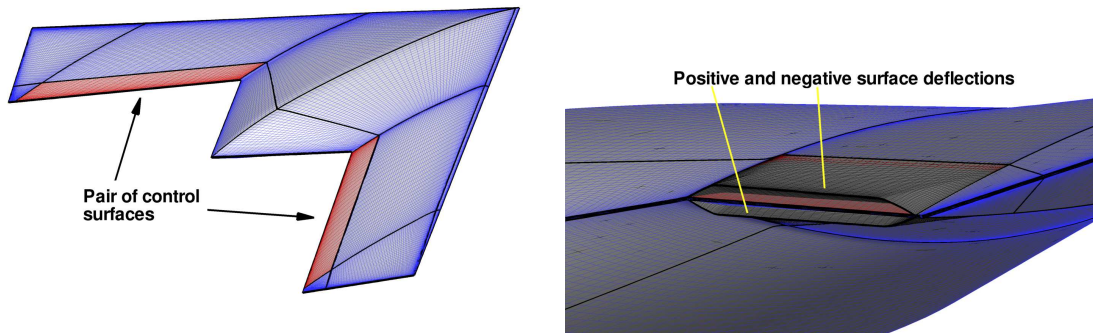
(a) Global view of the SACCON surface grid with control surfaces.

(b) Side view of the control surface deflections.

Figure 5.4: Control surface grid illustrations.

Computations at $M = 0.17$ with aileron controls deflected at $7.5°$ and $15°$ were carried out and compared to the baseline SACCON results with no deflections. The effect of the aileron on the lift and lateral force coefficients is negligible. The rest of the aerodynamic characteristics is shown in Fig. 5.5. Small increases in drag and pitching moment coefficient can be seen from Fig. 5.5 (a) and (b). The rolling moment in Fig. 5.5 (c) shows an approximately constant increment from the baseline values as the angle of attack is increased with a mean value of $\Delta C_{l_{mean}} = 0.15$ for a $15°$ aileron deflection. A slight deviation from this can be seen at $\pm 15°$ angle of attack. The effect on the yawing moment coefficient is negligible with values of the order of 10^{-3}, as shown in Fig. 5.5 (d).

Inertial and mass data approximations were made based on a similar aircraft, the Northrop Grumman YB-49, following the work carried out by the Garteur Group AG-47 which used SACCON for free-response manoeuvre simulations. An illustration of

(a) Drag coefficient.

(b) Pitching moment coefficient.

(c) Rolling moment coefficient.

(d) Yawing moment coefficient.
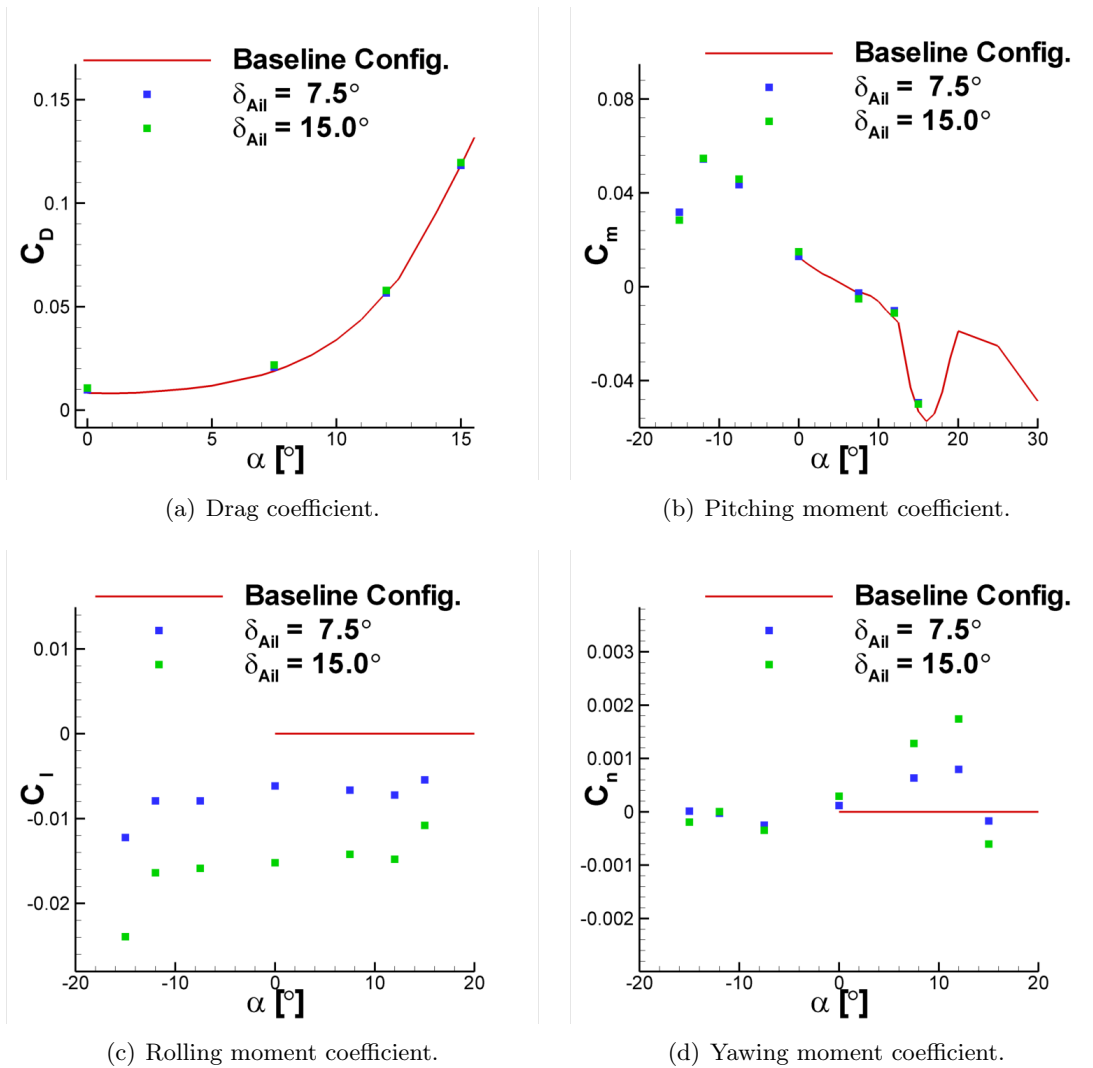
Figure 5.5: Aileron control surface aerodynamic characteristics.

which is shown in Fig. 5.6. A list of the estimated full size aircraft geometric characteristics is given in Table 5.1. These approximations were obtained by evaluating the geometries of similar UCAV configurations and estimating a set of realistic parameters that suited our needs. The aircraft has been increased in size by a factor of approximately ten times from the model dimensions, as seen from the chord length and the span length. This increase will incur an increase in the Reynolds number and subsequently in the flow behaviour. A study by Huber [68] into the influence of Mach and Reynolds numbers on the SACCON flow behaviour showed negligible differences when comparing pressure distributions at $Re = 1.3 \cdot 10^6$ up to $6, 0 \cdot 10^6$. For this reason, the tabular aerodynamic tables were generated using the validated grid and wind tunnel model conditions previously described. As for the Mach number variation, a noticeable influence was noted in these results, spanning from $M = 0.15$ up to 0.7. The tabu-
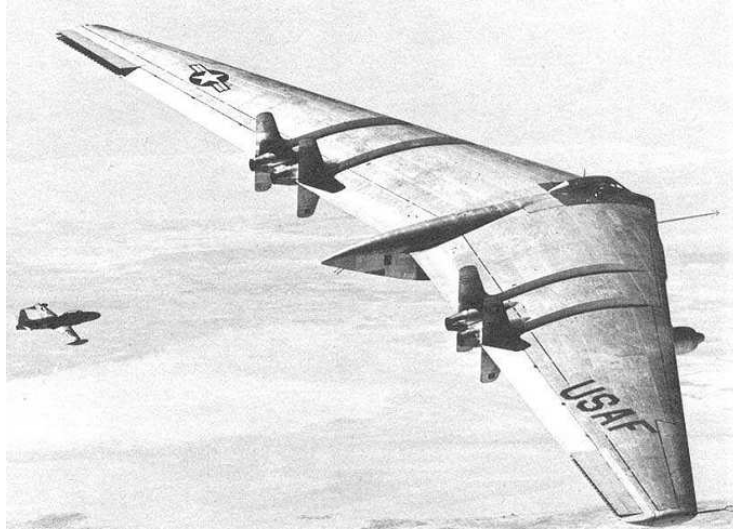
Figure 5.6: Image of the YB-49 Aircraft [77].

lar model takes this variable into account, as will be shown later on in this chapter. The position of the centre of gravity was placed in a location to suit our needs. As it will be seen in Chapter 6, this location was moved backward for the more aggressive manoeuvres.

To estimate the mass and thrust characteristics for our model, characteristics of real UCAV configurations were obtained. These are shown in Table 5.2, namely Boeing's X-45A and X-45C Phantom Ray and Northrop Grumman's X-47B Pegasus. All of these aircraft have similar geometric dimensions to the SACCON based flight dynamics model. Thrust to weight ratios from 0.36 to 0.53 are common for this type of configuration. The mass and thrust values were estimated empirically and resulted in smaller values than those seen for other real aircraft. A thrust to weight ratio of 0.71 was used for the model. In this case a slightly higher ratio was modelled for the purpose of this study to allow highly agile manoeuvering and high angle of attack aerodynamic effects to develop. The moments of inertia were extrtacted directly from the YB-49 and were divided by the same factor as the mass. These informal estimations were found suitable to calculate manoeuvres using DIDO.

The flight envelope of this UCAV model was defined under the assumption that it would fly at low Mach numbers, $0.1 < M < 0.3$, thus avoiding compressibility related aerodynamic effects. It is understood that the type of aircraft which this UCAV model represents would be expected to fly at Mach numbers well beyond 0.3, but for the purpose of this study the specified range provided sufficient interesting aerodynamic effects. Since interest was in the non-linear flow behaviour at high angles of attack, the full range of experimental measurements was used and extended, $-15° < \alpha < 30°$. The range of sideslip, aileron deflection and thrust vector deflection angles were specified as

Table 5.1: Aircraft Reference Data.

Parameter	SACCON
Span length (m)	13
Chord length (m)	5.01
Aspect ratio	2.6
Surface Area (m^2)	55.08
Centre of Gravity (m)	2.00
Mass (kg)	2000
Thrust at trim (kN)	14.0
Thrust/Weight ratio	0.71
I_X (kgm^2)	8015
I_Y (kgm^2)	6565
I_Z (kgm^2)	8937

Table 5.2: UCAVs Reference Data.

Aircraft	Length (m)	Span (m)	MTOM (kg)	Engine	T_{max} (kN)	T/W
X-45A [78, 79]	11.9	14.9	5,529	F124-GA-100	28.9	0.53
Phantom Ray [80, 81]	10.9	15.2	16,556	F404-GE-102D	78.7	0.49
X-47B Pegasus [82]	11.6	18.9	20,215	PW F100-220U	71.2	0.36

$-15° < \beta < 15°$, $-15° < \delta_{ail} < 15°$ and $-15° < \eta_{\theta,\psi} < 15°$, respectively.

The following section describes how the CFD predicted aerodynamic characteristics are generated and stored for subsequent use in a manoeuvre prediction code. The method consists of populating predetermined tables of data with limits defined by the boundaries of the given aircraft's flight envelope. In the case of the SACCON model two aerodynamic data tables are necessary, one representing $[M, \alpha, \beta]$ and another for $[M, \alpha, \delta_{ail}]$. The effects of the rotation of the thrust vector are directly linked to the equations of motion in the manoeuvre prediction algorithm omitting the need for extra tables.

5.2 Table Generation

Tabular based models usually suffer from dimensionality effects when large aerodynamic models are required. Aerodynamic forces and moments usually vary as a function of a number of variables, such as angle of attack, Mach number or control effects. To model all these variables in a single table would require a multidimensional array with a large number of entries. If the trends in the aerodynamic characteristics are expected to be highly non-linear, a large number of discrete entries will be required in each dimension. It is only in this way that the trends would be captured accurately throughout the table domain. For a model consisting of four dimensions, $[M, \alpha, \beta, \delta_{ail}]$ with 15 by 45 by 15 by 15 entries, respectively, the total number of entries required for a single table would be $151,875$, as shown in Table 5.3. It was found that each steady state simulation required 288 processor hours. Knowing this, it was possible to calculate the total computer time required to populate a table. Tables of this size are difficult to manage and to use as a look-up table for flight dynamics simulations due to computer memory limitations.

Table 5.3: Cost of aerodynamic data table generation for SACCON.

Type of model	Number of entries per table	Total number of entries	CPU time [processor-hour]
Single table	$151,875$	$151,875$	$43,740,000$
Two three-dimensional tables	$10,125$	$20,250$	$5,832,000$
Two three-dimensional tables using a sampling approach	$10,125$	$20,250$	$32,240$

Instead, a method based on sampling and data fusion is used to construct the aerodynamic model [83]. In order to reduce the tabular model to a size which can be easily handled by the manoeuvre prediction method, three-dimensional tables are generated. As shown in Table 5.3, this allows for a considerable reduction in number of

data entries, by a factor of 7.5, by assuming the cross-coupling between sideslip angle and aileron control are negligible. Nonetheless, 20, 250 entries is still a large number of entries to commit to CFD simulations as shown by the large amount of processor hours required. For this reason a sampling approach was used. Sampling consists of performing steady state computations at selected conditions inside the flight envelope and updating the aerodynamic database using Kriging interpolation. Everytime this is done a data fusion method is used to approximate the rest of the entries in the model. As always, a balance needs to be accepted between the amount of resources committed and the level of certainty required in the data. This method is performed in an online basis until there is enough confidence in the level of uncertainty within the dataset. For the SACCON case, the CFD validation provided good knowledge about the type of non-linearities present in the aerodynamic characteristics and where these may be found.

Initially, a first set of samples was generated at the extremes of the flight envelope. These CFD calculations were run in the HECToR supercomputer taking under six hours on 48 processors. As the sample results were computed the tables were populated. For the $[M, \alpha, \beta]$ table a balance between the computational effort required from sampling, and the level of accuracy, was reached at 80 samples. An extra 25 samples were required for the $[M, \alpha, \delta_{ail}]$ table. In total, 105 steady state simulations were required at this stage of the model generation process. It can be seen from Table 5.3, the required computational resources has been dropped dramatically from the first single table approach.

The results for the $[M, \alpha, \beta]$ table are shown in Figs. 5.7, 5.8, 5.9, 5.10, 5.12 and 5.13 using three dimensional surface representations of each one of the aerodynamic characteristics. Each plot represents a single sideslip or Mach number and the overlaying black dots represent the samples. Of course, there are more levels at which these forces and moments can be illustrated but for conciseness the upper, middle and lower values of the $Mach$ and β ranges have been illustrated. These give a good idea of the most important aerodynamic behaviour. Figure 5.7 (a) to (c) show C_L at different Mach numbers. The variation of C_L with respect to sideslip is very small. Similarly, in Fig. 5.7 (d) to (f) the variation with respect to Mach number at given sideslip angles is shown with little change. Note that Fig. 5.7 (e), showing the symmetric case, has a row of samples at $M = 0.17$ representing the validation computations which are used here as a high-density baseline for interpolation. The drag coefficient shown in Fig. 5.8 also shows little variation along the sideslip and Mach number range. The surface plots show a smooth interpolation between the samples. Gaussian correlation and a second order polynomial regression model were used for the reconstruction.

Figure 5.9 (a), (b) and (c) shows a non-symmetrical side force coefficient behaviour about $\beta = 0°$. In the low range of α the side force is negligible across the β range.

(a) C_L at $Mach = 0.1$

(b) C_L at $Mach = 0.2$

(c) C_L at $Mach = 0.3$

(d) C_L at $\beta = -15°$

(e) C_L at $\beta = 0°$

(f) C_L at $\beta = 15°$
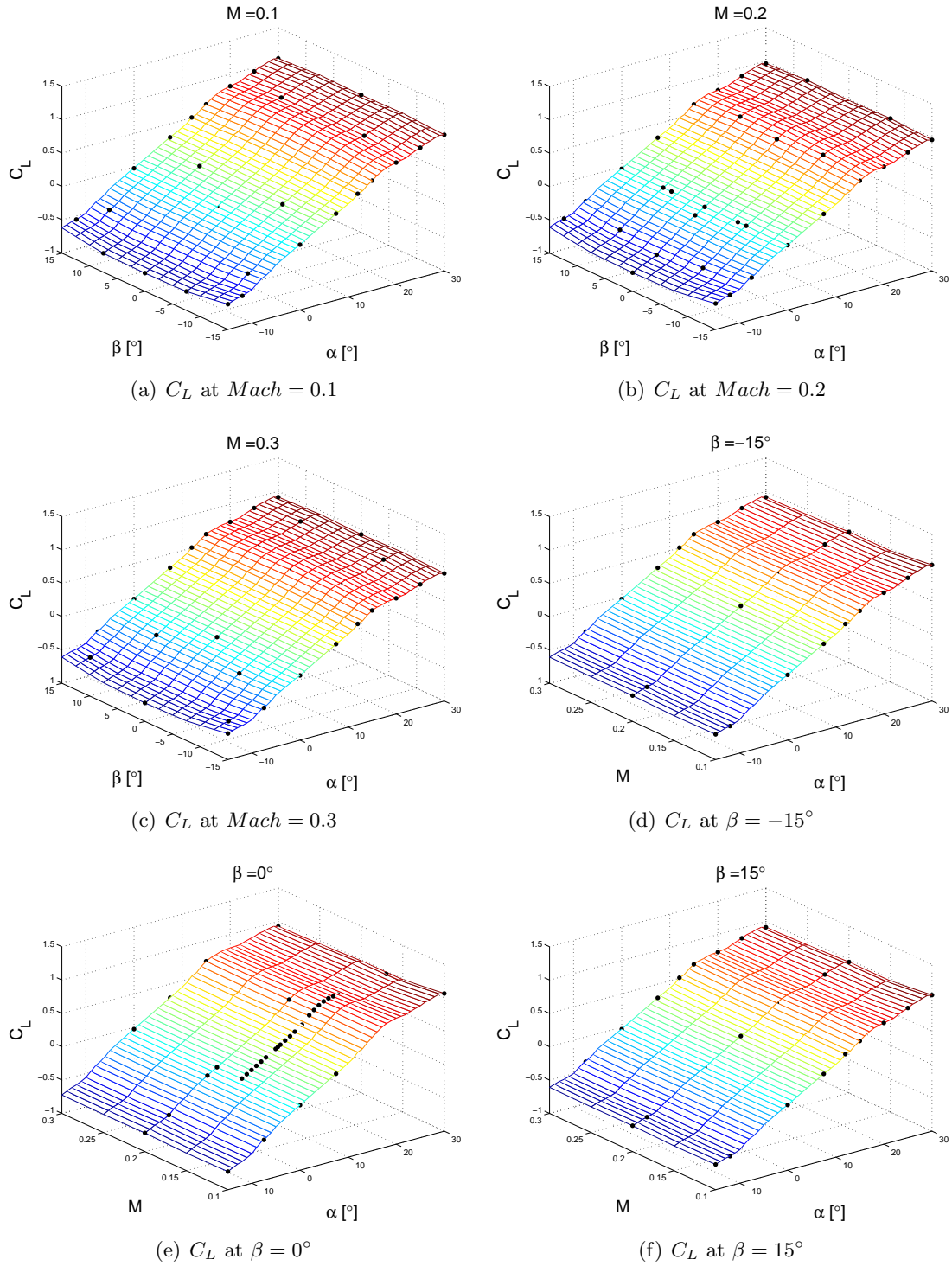
Figure 5.7: α with β and $Mach$ sweeps for the lift coefficient.

Beyond the $-5° < \alpha < 15°$ range the tables exhibit a force reaching ±0.05 at the highest Mach number and angle of attack. From Fig. 5.9 (d), (e) and (f) this increasing Mach number effect becomes clear.

(a) C_D at $Mach = 0.1$

(b) C_D at $Mach = 0.2$

(c) C_D at $Mach = 0.3$

(d) C_D at $\beta = -15°$

(e) C_D at $\beta = 0°$

(f) C_D at $\beta = 15°$
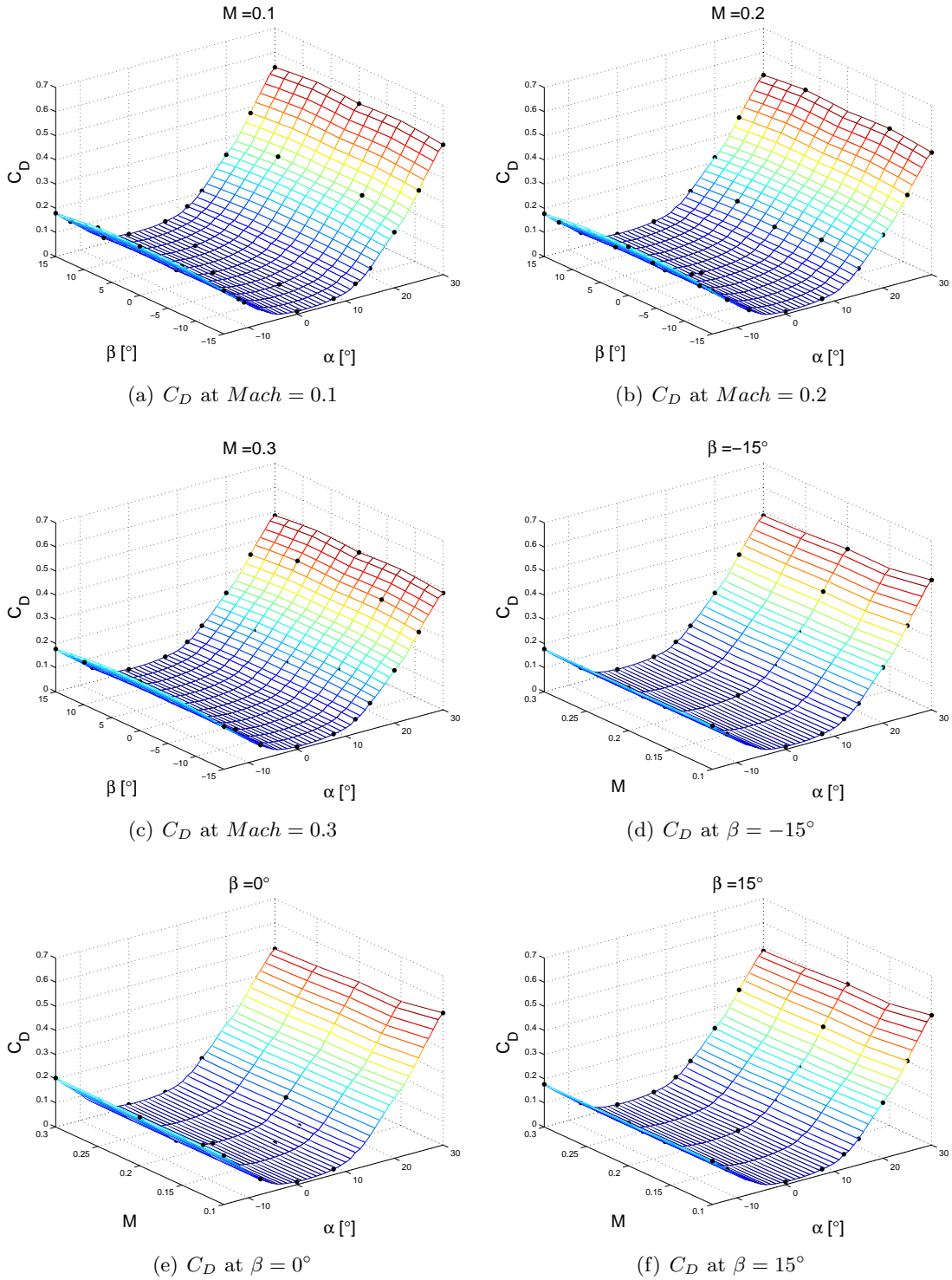
Figure 5.8: α with β and $Mach$ sweeps for the drag coefficient.

Figures 5.10, 5.12 and 5.13 show the moments about the three axes. Figure 5.10 shows a decreasing trend in pitching moment coefficient as seen in Fig. 5.2 (a). The dip at 15° angle of attack is seen to become weaker as the sideslip angle increases as seen
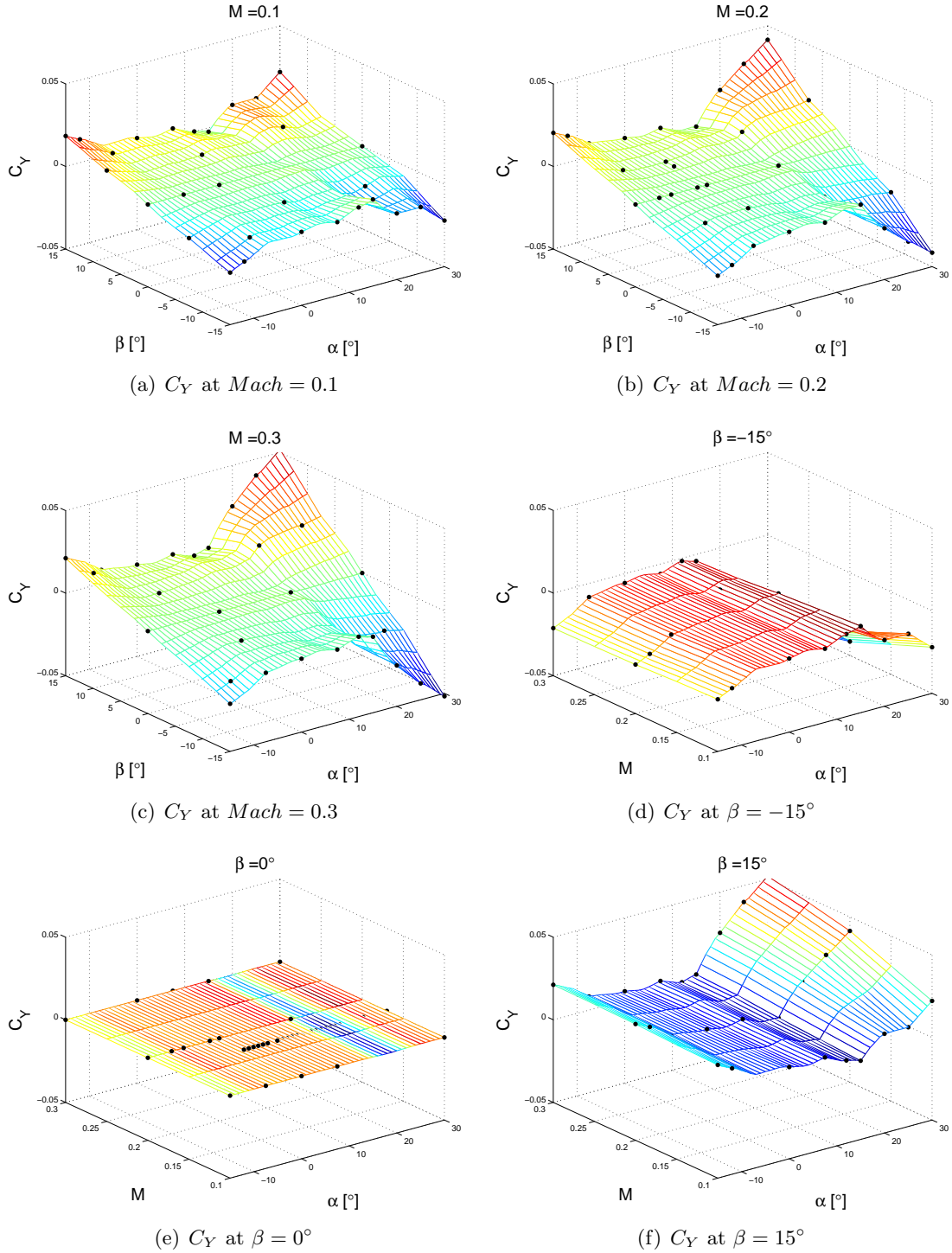
Figure 5.9: α with β and $Mach$ sweeps for the side force coefficient.

from Fig. 5.10 (a), (b) and (c). Figure 5.10 (d), (e) and (f) show only small changes in C_m due to variations in Mach number. The C_p distribution at the bottom of this dip, $\alpha = 15°$, at two different sideslip angles is shown in Fig. 5.11. The symmetrical case in (a) shows the vortical structures after they have separated from the leading edge in

the middle part of the wing. The $\beta = 15°$ case shown in (b) displays one side of the aircraft with a strong suction aft of the MRP and the other side with vortex breakdown forward of it. This lateral difference in suction tends to balance the moments in the longitudinal direction.

The rolling moment shown in Fig. 5.12 shows the expected behaviour throughout the angle of attack range. Looking at the surface plot on Fig. 5.12 (a), at $\beta = 15°$ for angles of attack below 0° a negative rolling moment is present and a positive moment for positive angles of incidence. As a symmetrical behaviour is assumed, the opposite happens at $\beta = -15°$. Figure 5.12 (d) and (f) show the first noticeable Mach number effects, although only at the highest angles of attack where the C_l is seen to increase with increasing Mach number.

Small yawing moments are seen to be present in the range of $-10° < \alpha > 15°$ at different angles of sideslip. Beyond these angles, the yawing moment is seen to increase significantly with no noticeable Mach number influence.

The $[M, \alpha, \delta_{ail}]$ table characteristics are shown in Figs. 5.14, 5.15 and 5.16. The first of these shows the rolling moment caused by the deflection of the ailerons from 0° to $\pm 15°$. The variation across the range of δ_{ail} is seen to be linear. Mach number is seen to have a small effect towards the limits of the deflections. Overall the control effectiveness remains constant across most of the angle of attack range, with the exception of $\alpha = 15°$ where a small perturbation is present.

The cross-coupling effect on the yawing moment is shown in Fig. 5.15. From (a), (b) and (c), it can be seen that at low angles there is no cross-coupling across the δ_{ail} range. As the incidence angle is increased or decreased, the effect on the yawing moment becomes noticeable, with values up to 0.025.

It can be seen from Fig. 5.16 that the effect of the aileron deflections on the rest of the forces and moments is negligible, with the exception of C_Y at $\alpha = 30°$ and a small oscillation in the pitching moment throughout α.

5.3   Damping Derivatives

In addition to the basic tables, which only describe the aerodynamics of the static aircraft, increments due to dynamic effects were predicted. Several methods to evaluate these increments, referred to as dynamic or damping derivatives, have been studied in the past with no definitive approach for the nonlinear aerodynamic regions [84]. With this in mind, two methods are used in this section to obtain the longitudinal dynamic derivatives of SACCON.

The influence of the pitch dynamic effects on the forces and moments on SACCON were determined by forcing oscillatory motions at a range of conditions. For these to be valid for flight dynamics purposes, the rotations were performed about the centre of gravity. A range of calculations were performed for different angles of attack and

(a) C_m at $Mach = 0.1$

(b) C_m at $Mach = 0.2$

(c) C_m at $Mach = 0.3$

(d) C_m at $\beta = -15°$

(e) C_m at $\beta = 0°$

(f) C_m at $\beta = 15°$
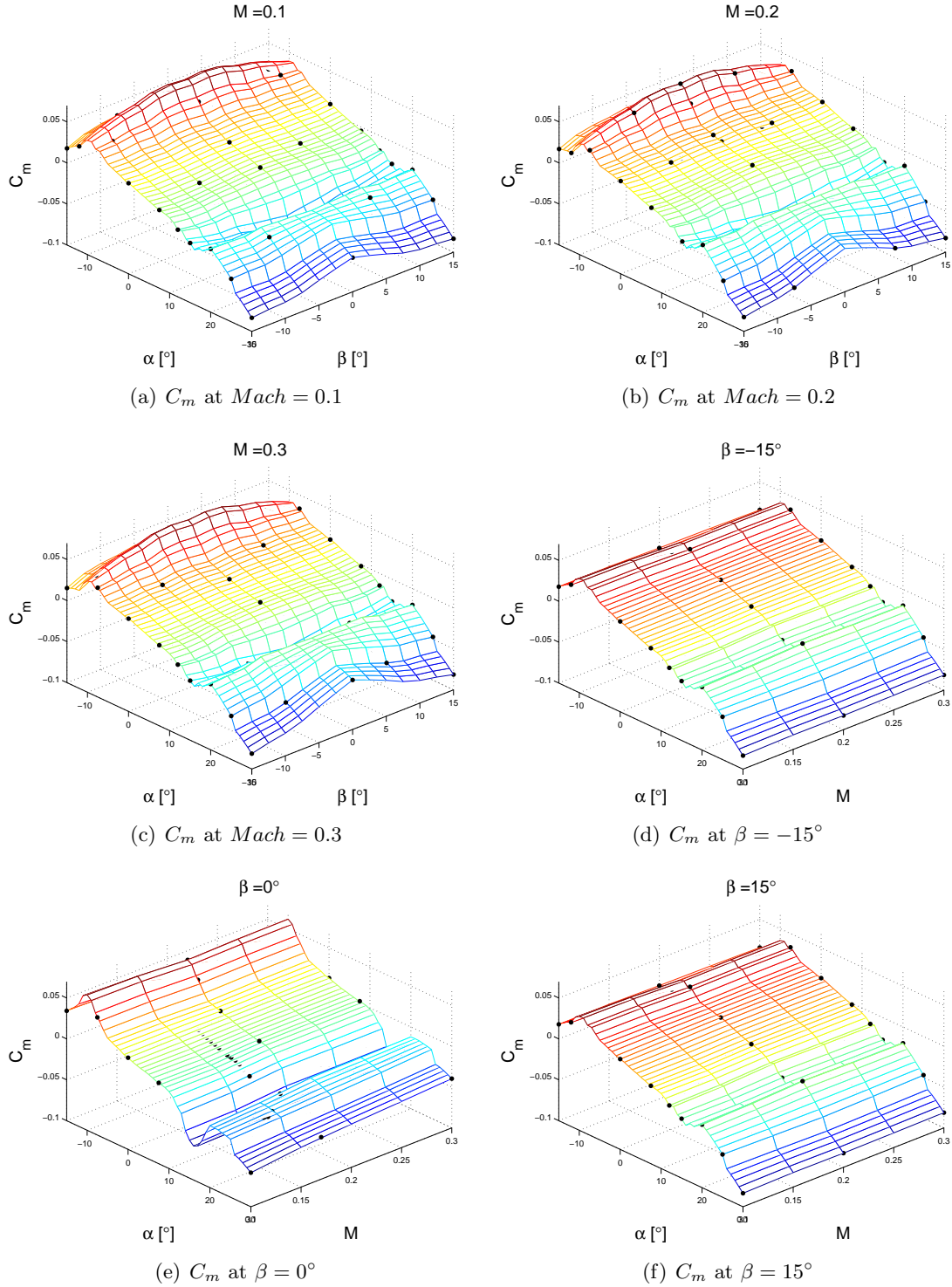
Figure 5.10: α with β and $Mach$ sweeps for the pitching moment coefficient.

frequencies. These are summarised in Table 5.4. All the cases computed correspond to the SLE model in pitch mode. The effect of amplitude was not investigated and a constant value of $A = 5°$ was used. The nondimensional frequency was calculated

(a) $\beta = 0°$ (b) $\beta = 15°$
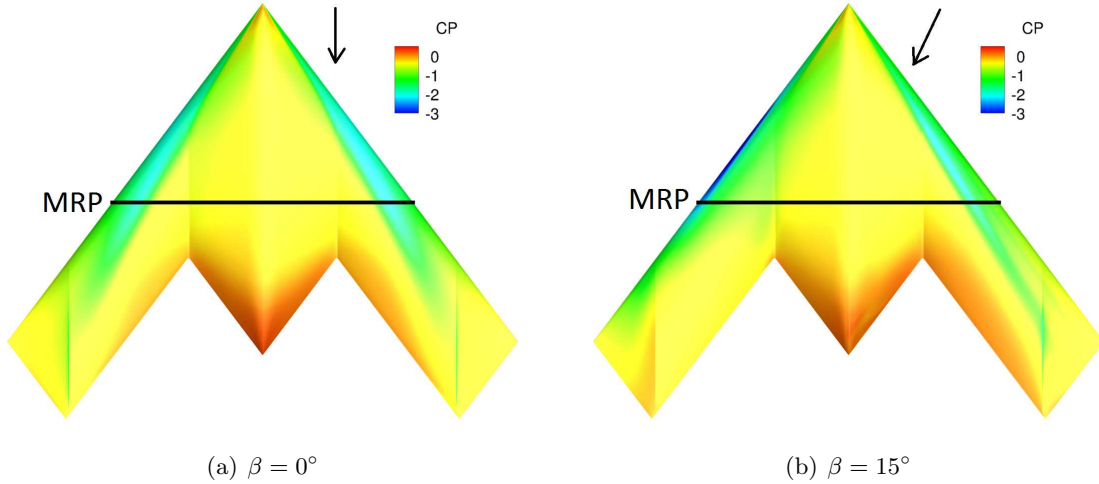
Figure 5.11: C_p distribution at different sideslip angles.

in the same manner as was done for the dynamic validation cases. The resulting nondimensional time, $\hat{t}$, and total nondimensional time per oscillation, T, are also given.

Table 5.4: Dynamic cases validated for SACCON.

Configuration	Mode	α_0 [°]	f [Hz]	A [°]	M	Re [·10^6]	k	$\hat{t}$	T
SLE	pitch	0	1	5	0.3	1.93	0.015	0.43	$215.2\hat{t}$
SLE	pitch	0	3	5	0.3	1.93	0.044	0.14	$71.7\hat{t}$
SLE	pitch	5	1	5	0.3	1.93	0.015	0.43	$215.2\hat{t}$
SLE	pitch	5	3	5	0.3	1.93	0.044	0.14	$71.7\hat{t}$
SLE	pitch	10	1	5	0.3	1.93	0.015	0.43	$215.2\hat{t}$
SLE	pitch	10	3	5	0.3	1.93	0.044	0.14	$71.7\hat{t}$
SLE	pitch	15	1	5	0.3	1.93	0.015	0.43	$215.2\hat{t}$
SLE	pitch	15	3	5	0.3	1.93	0.044	0.14	$71.7\hat{t}$
SLE	pitch	20	1	5	0.3	1.93	0.015	0.43	$215.2\hat{t}$
SLE	pitch	20	3	5	0.3	1.93	0.044	0.14	$71.7\hat{t}$

The longitudinal force and moment data from these cases are shown in Fig. 5.17. Frequencies of $1Hz$ and $3Hz$ are shown in blue and red, respectively. Steady state computations are also plotted as black squares. As was shown from the validation work described previously in this thesis, small dynamic effects are present below $14°$ angle of attack. Beyond this incidence angle, noticeable spreads can be seen as the difference between the static and dynamic predictions increases. At $20°$ mean angle of attack, the lower frequency predictions show a more non-linear behaviour than the higher ones. This is attributed to the flow transients having more time to settle to the new state, thus allowing more variation in the forces and moments. Both the C_L

(a) C_l at $Mach = 0.1$

(b) C_l at $Mach = 0.2$

(c) C_l at $Mach = 0.3$

(d) C_l at $\beta = -15°$

(e) C_l at $\beta = 0°$

(f) C_l at $\beta = 15°$
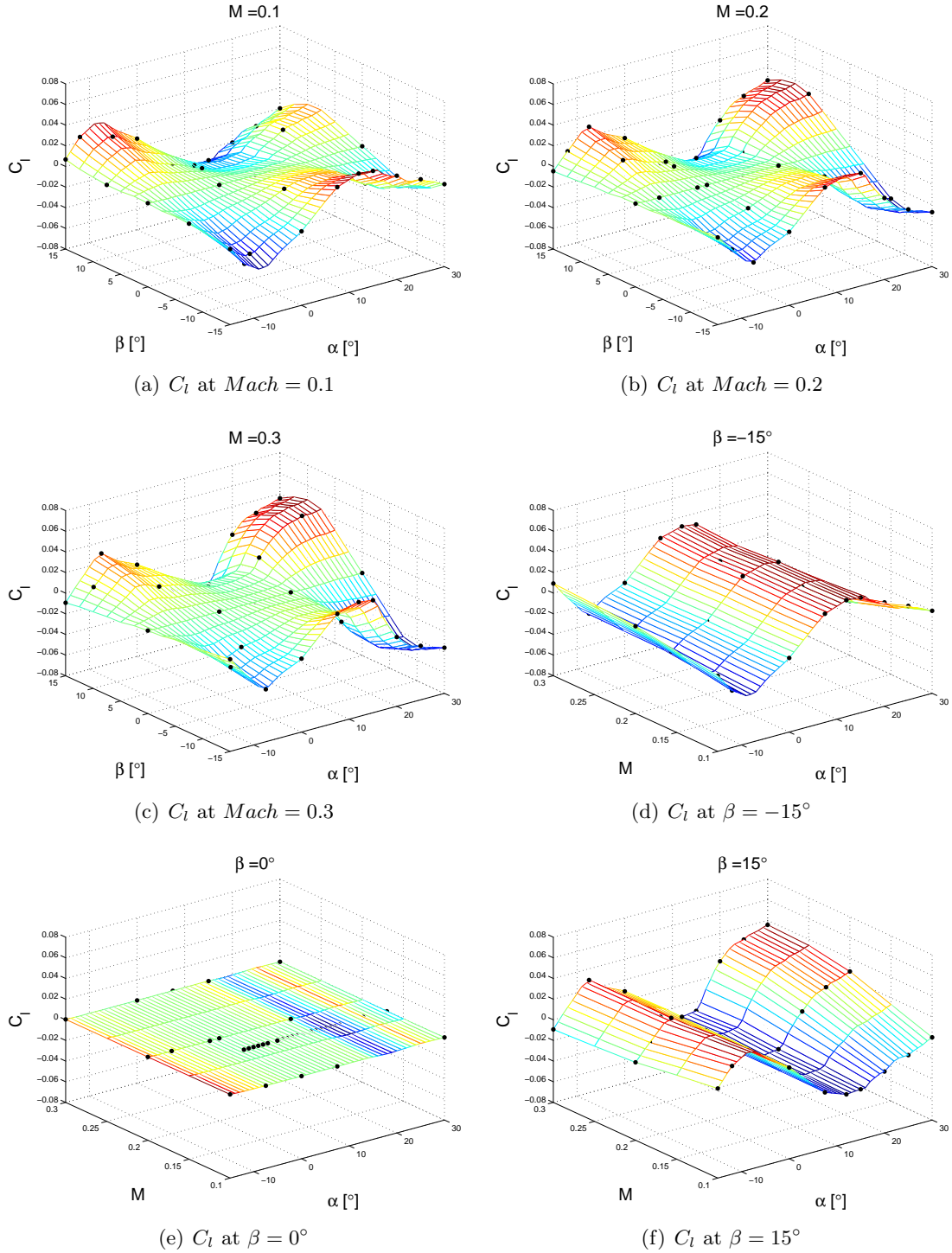
Figure 5.12: α with β and $Mach$ sweeps for the rolling moment coefficient.

and C_m loops rotate in an anticlockwise fashion. Although difficult to see, the C_D plot shows a crossover point at approximately the mean angle of attack value for each loop. For this reason the approaches for determining dynamic derivatives used in this study would be of little validity for this particular aerodynamic characteristic.

(a) C_n at $Mach = 0.1$

(b) C_n at $Mach = 0.2$

(c) C_n at $Mach = 0.3$

(d) C_n at $\beta = -15°$

(e) C_n at $\beta = 0°$

(f) C_n at $\beta = 15°$
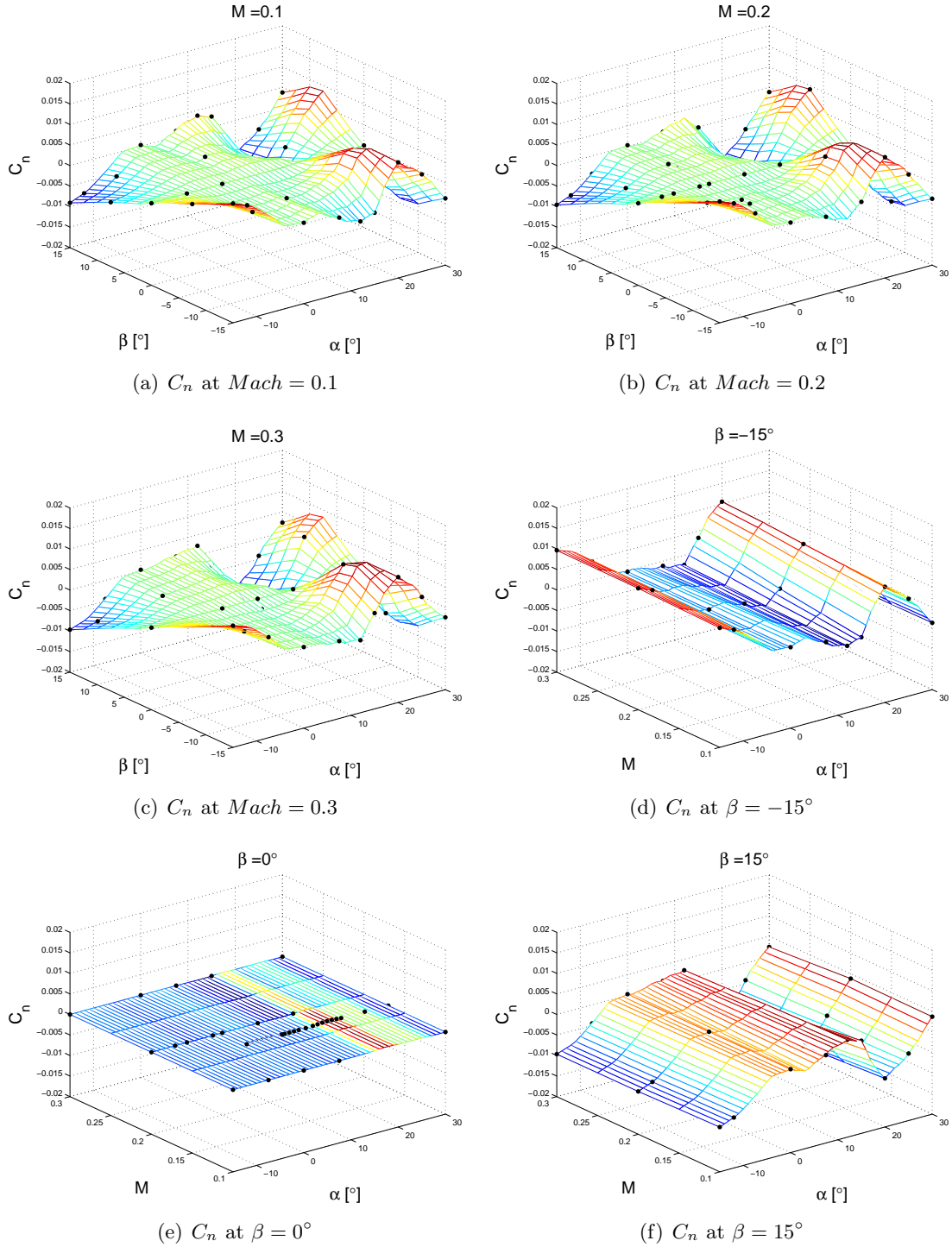
Figure 5.13: α with β and $Mach$ sweeps for the yawing moment coefficient.

When the loops cross the nominal angle of attack value, the rotational acceleration is known to be zero and the pitch rates are maximum or minimum. Here, the dynamic term is purely dependent on the body and velocity vector rotation rates, C_{j_q} and $C_{j_{\dot{\alpha}}}$,

(a) C_l at $Mach = 0.1$

(b) C_l at $Mach = 0.2$

(c) C_l at $Mach = 0.3$

(d) C_l at $\beta = -15°$

(e) C_l at $\beta = 0°$

(f) C_l at $\beta = 15°$
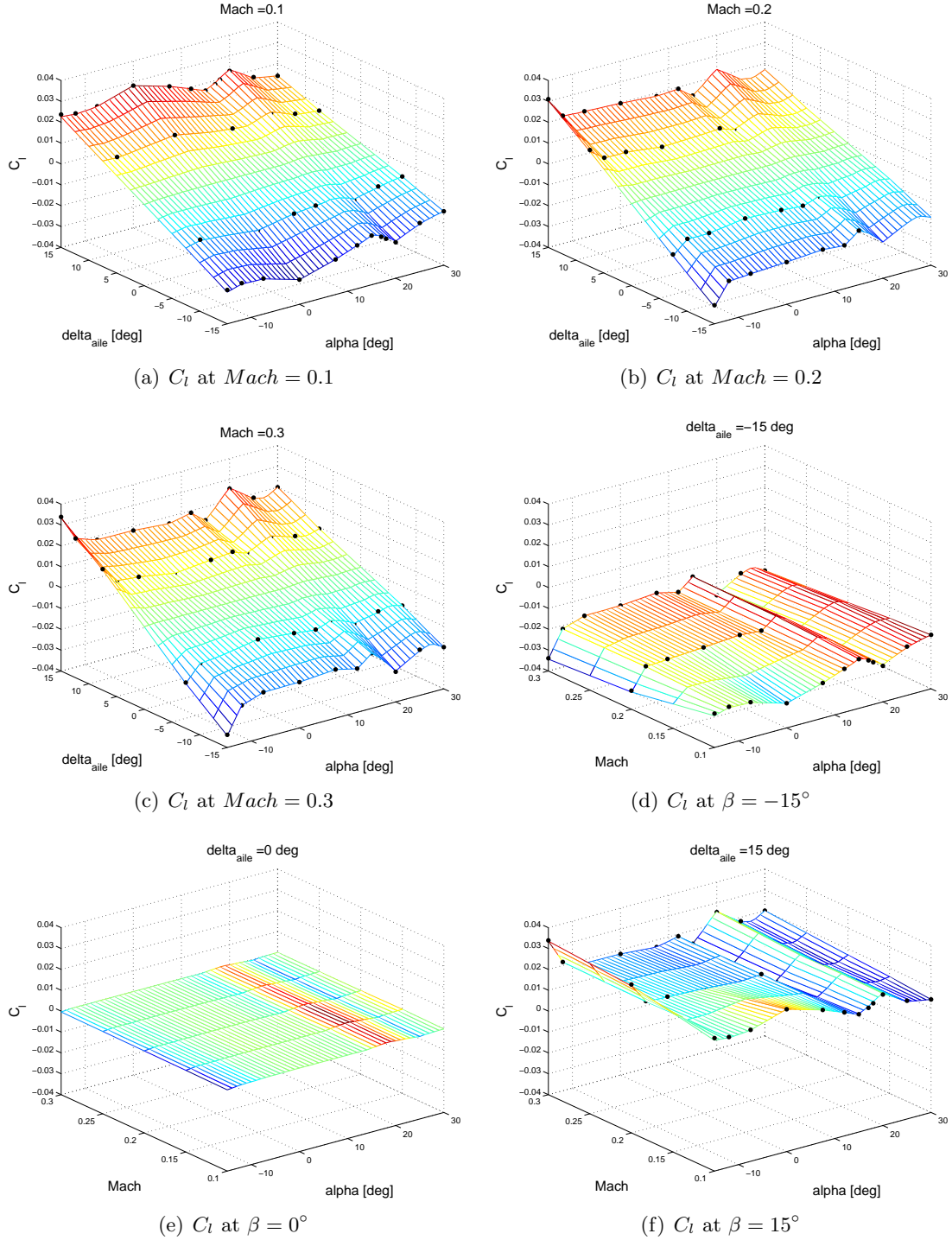
Figure 5.14: Aileron effectiveness for the range of α with β and $Mach$ sweeps for the rolling moment coefficient.

respectively. A combined pitching dynamic derivative can then be derived as,

$$\bar{C}_{j_q} = C_{j_q} + C_{j_{\dot{\alpha}}} \tag{5.1}$$

By identifying these points in the motion, a classic single point method [85] can be used

(a) C_n at $Mach = 0.1$

(b) C_n at $Mach = 0.2$

(c) C_n at $Mach = 0.3$

(d) C_n at $\beta = -15°$

(e) C_n at $\beta = 0°$

(f) C_n at $\beta = 15°$
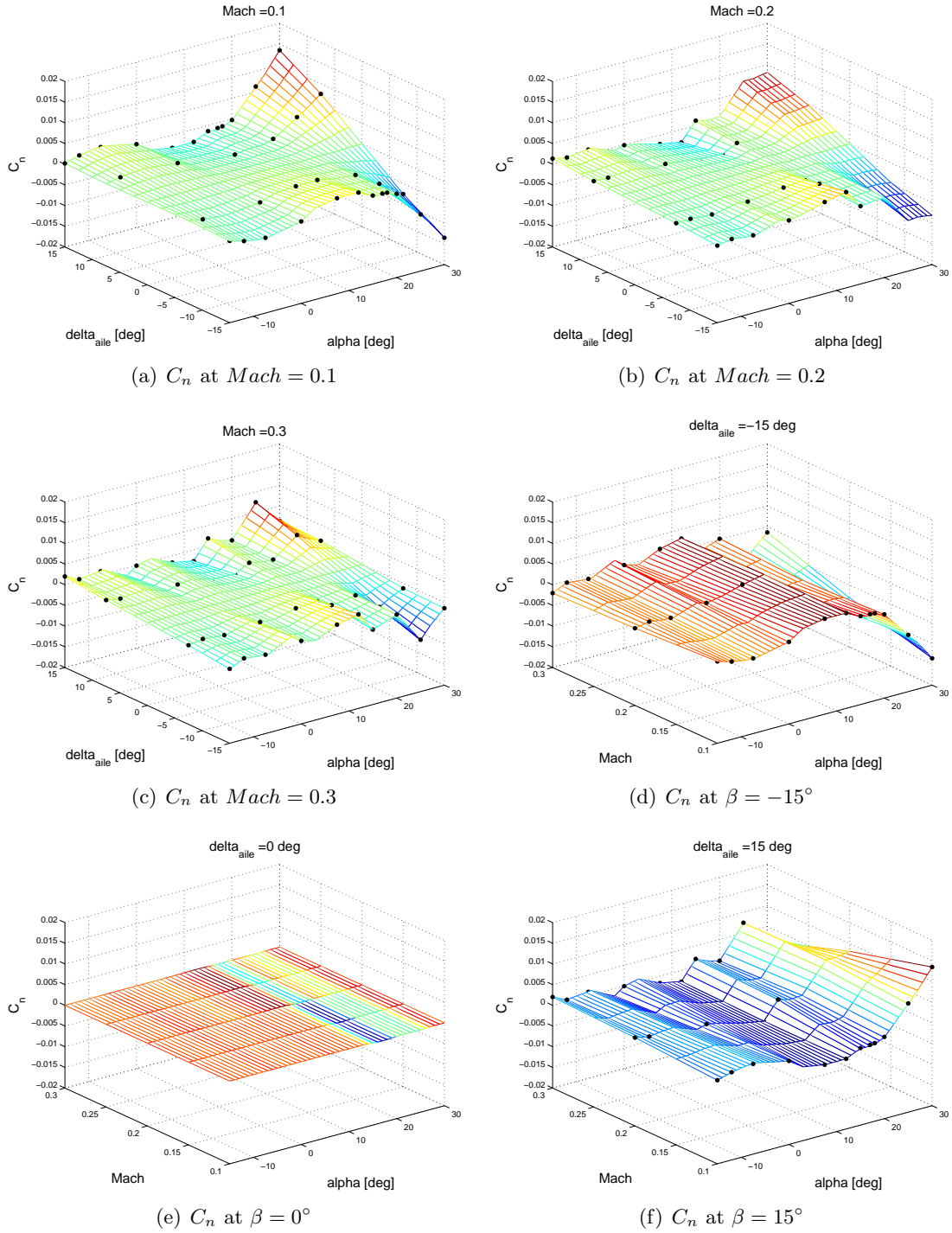
Figure 5.15: Aileron effectiveness for the range of α with β and $Mach$ sweeps for the yawing moment coefficient.

to extract the combined dynamic derivatives from the oscillation data. The difference between the coefficients at maximum and minimum rates of rotation are divided by the normalised maximum and minimum rates of rotation in radians per second, as shown

(a) C_L at $Mach = 0.1$

(b) C_D at $Mach = 0.2$

(c) C_Y at $Mach = 0.3$

(d) C_m at $Mach = 0.3$
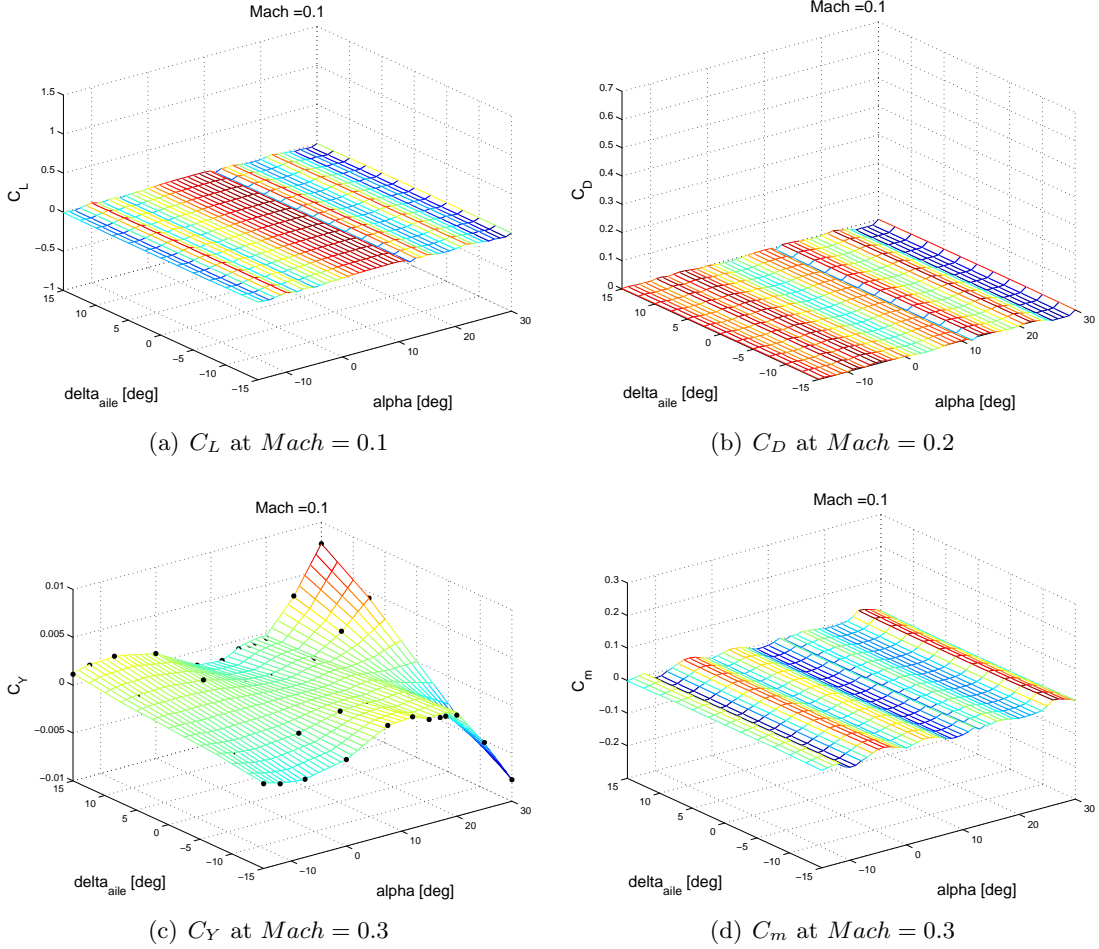
Figure 5.16: Effect of aileron on aircraft forces and pitching moment coefficients for the range of α and $Mach$.

in the following,

$$\bar{C}_{j_q} = \frac{C_{j_{q_{max}}} - C_{j_{q_{min}}}}{\frac{c_{ref}}{2V_{ft}}(q_{max} - q_{min})} \tag{5.2}$$

This is shown in Fig. 5.18 where the minimum and maximum values of q are marked with two red circles.

The results for $j = L$ and m are shown in Fig. 5.19. Here, the lift and pitching moment dynamic characteristics were obtained at two different frequencies. The blue circles correspond to the $1Hz$ frequency of oscillation and the red circles to the $3Hz$, which correspond to the nondimensional values of $k = 0.015$ and $k = 0.044$, respectively. The lift values remain on the positive side whereas the pitching moment ones remain negative throughout the positive range of angles of attack meaning the aircraft is dynamically stable. Negligible frequency effects can be seen at low angles of attack both in C_{L_q} and C_{m_q} whereas beyond $15°$ some differences can be seen, with greater values for the lower frequency at $20°$. It is worthy of note that the static computations

87

(a) C_L

(b) C_D

(c) C_m
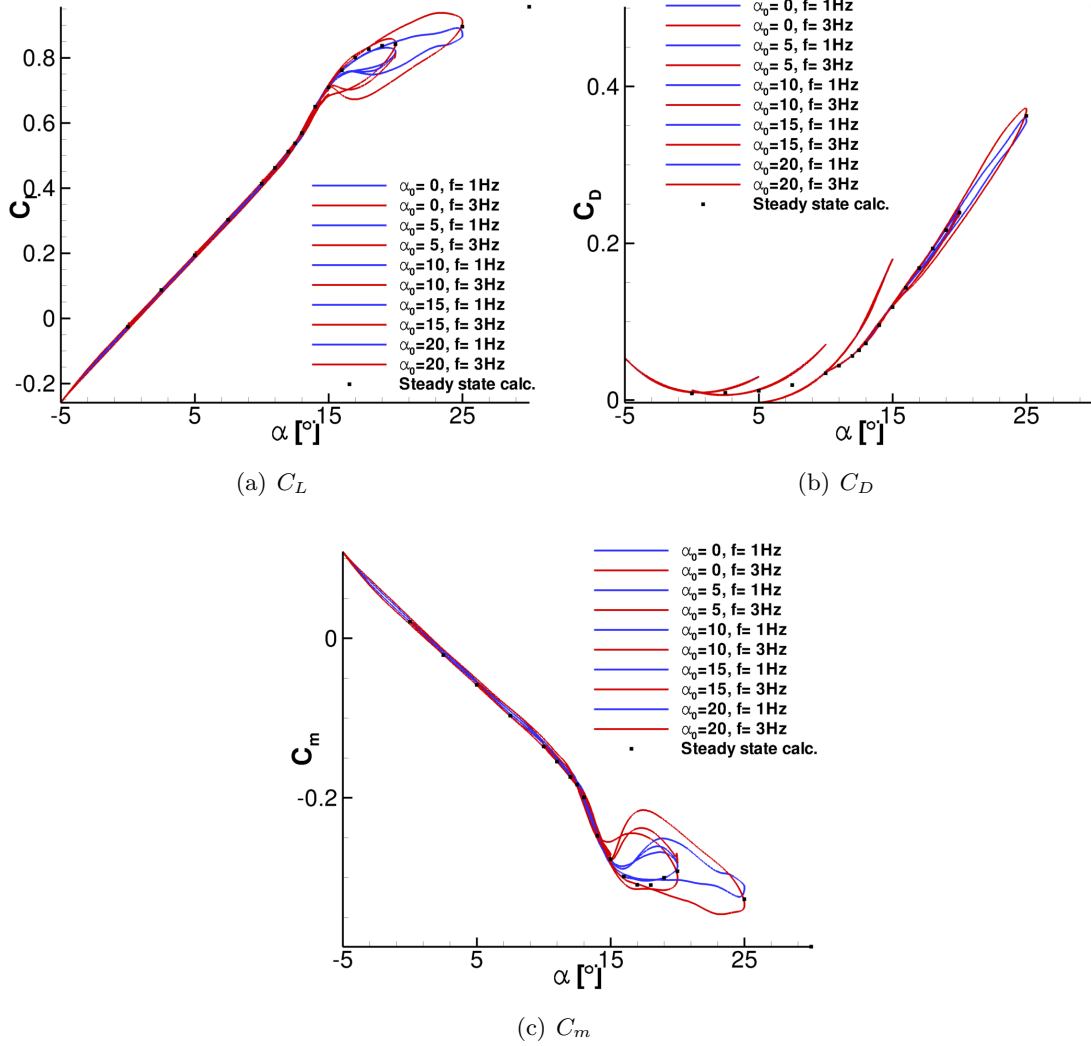
Figure 5.17: Time-accurate CFD predictions of the longitudinal force and moment coefficients.

agree very well with the downstroke values of the motion predictions, suggesting that the strong hysteresis effects happen when the model is performing a pitch up motion.

A second method of extracting damping derivatives was used for this set of data which was based on a least squares method [86]. Here, the aerodynamic coefficients are assumed to be linear functions of angle of attack, α, pitching angular velocity, q, and rates, $\dot{\alpha}$ and $\dot{q}$ as shown,

$$\Delta C_j = C_{j_\alpha}\Delta\alpha + \frac{L}{U_\infty}C_{j_{\dot{\alpha}}}\dot{\alpha} + \frac{L}{U_\infty}C_{j_q}q + (\frac{L}{U_\infty})^2 C_{j_{\dot{q}}}\dot{q} \qquad (5.3)$$

which can be reduced to:

$$\Delta C_j = \alpha_A \bar{C}_{j\alpha}sin(\omega t) + \alpha_A k \bar{C}_{jq}cos(\omega t) \qquad (5.4)$$

where $\bar{C}_{j\alpha}$ and $\bar{C}_{jq}$ correspond to the in-phase and out-of-phase components of ΔC_j,

(a) C_L (b) C_m
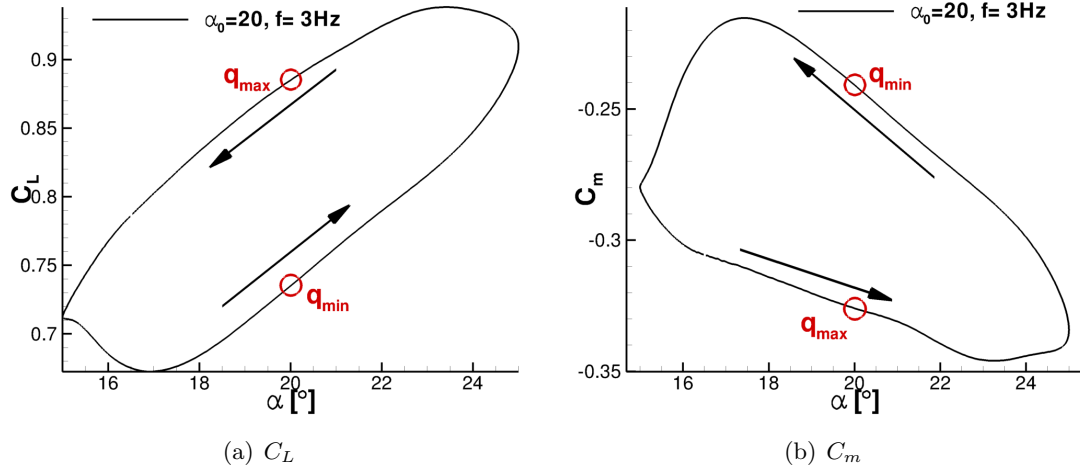
Figure 5.18: Minimum and maximum rotation rate points in the C_L and C_m loops.

respectively. It is clear from this assumption that the validity of this method is limited to the linear region of the forces and moments. This regression-based approach was used to analyse the time-histories of the longitudinal forces and moments. New loops can be reconstructed based on this method and the results are shown in Figs. 5.20 and 5.21. The black lines represent the reconstructed loops based on the extracted coefficients from the red simulated predictions. The dashed pattern is used for the $3Hz$ frequency and the solid for the $1Hz$. As expected, a perfect agreement occurs at mean angles of attack of $0°$ and $5°$. Small discrepancies start to occur at $10°$ mean angle of attack, where plots are seen to cross over at approximately $12°$. At $\alpha_0 = 15°$ and $20°$ the method breaks down with elliptically-shaped loops which do not represent the irregular shapes of the CFD predictions.

(a) C_{L_q} (b) C_{m_q}
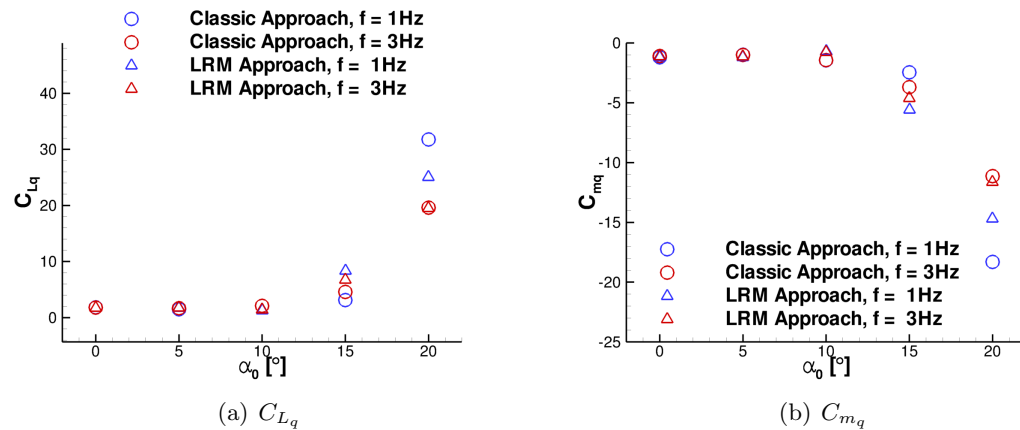
Figure 5.19: Dynamic derivative predictions using two different methods.

(a) $\alpha_0 = 0°$

(b) $\alpha_0 = 5°$

(c) $\alpha_0 = 10°$

(d) $\alpha_0 = 15°$

(e) $\alpha_0 = 20°$
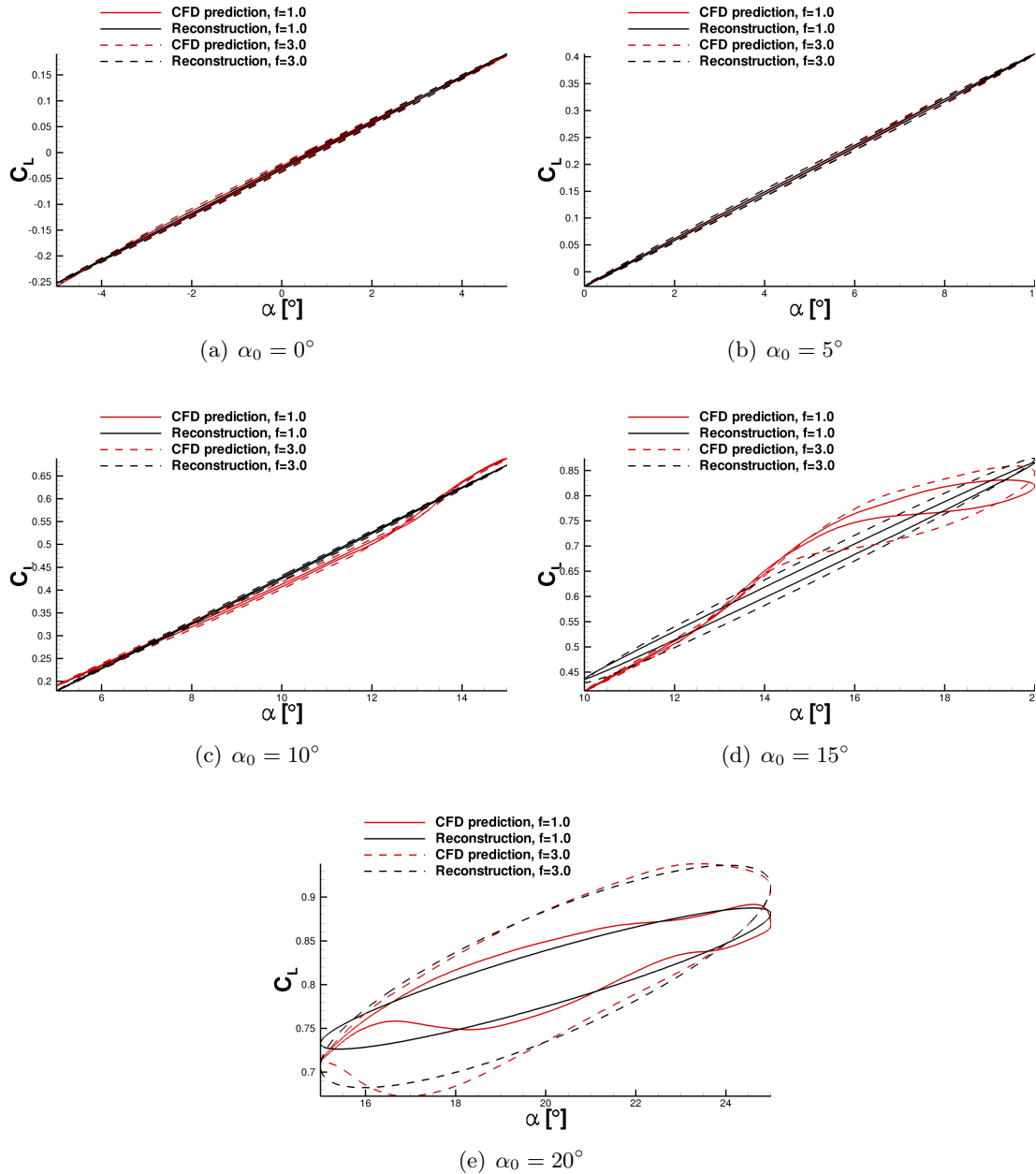
Figure 5.20: Normal force coefficient predictions using a linear regression model compared to the time-accurate CFD predictions.

Figure 5.19 shows the damping derivatives extracted using this linear regression model (LRM) by means of triangular blue and red symbols for the different frequencies. These are in good agreement with the predictions using the classic approach, particularly in the linear part. At mean incidence angles of $15°$ and $20°$ some scatter develops. The advantage these simple methods offer is the reduced size of the data sets in order to reproduce dynamic effects. Effectively three values are stored for each coefficient and mean angle of attack. The classic approach predictions are used in the
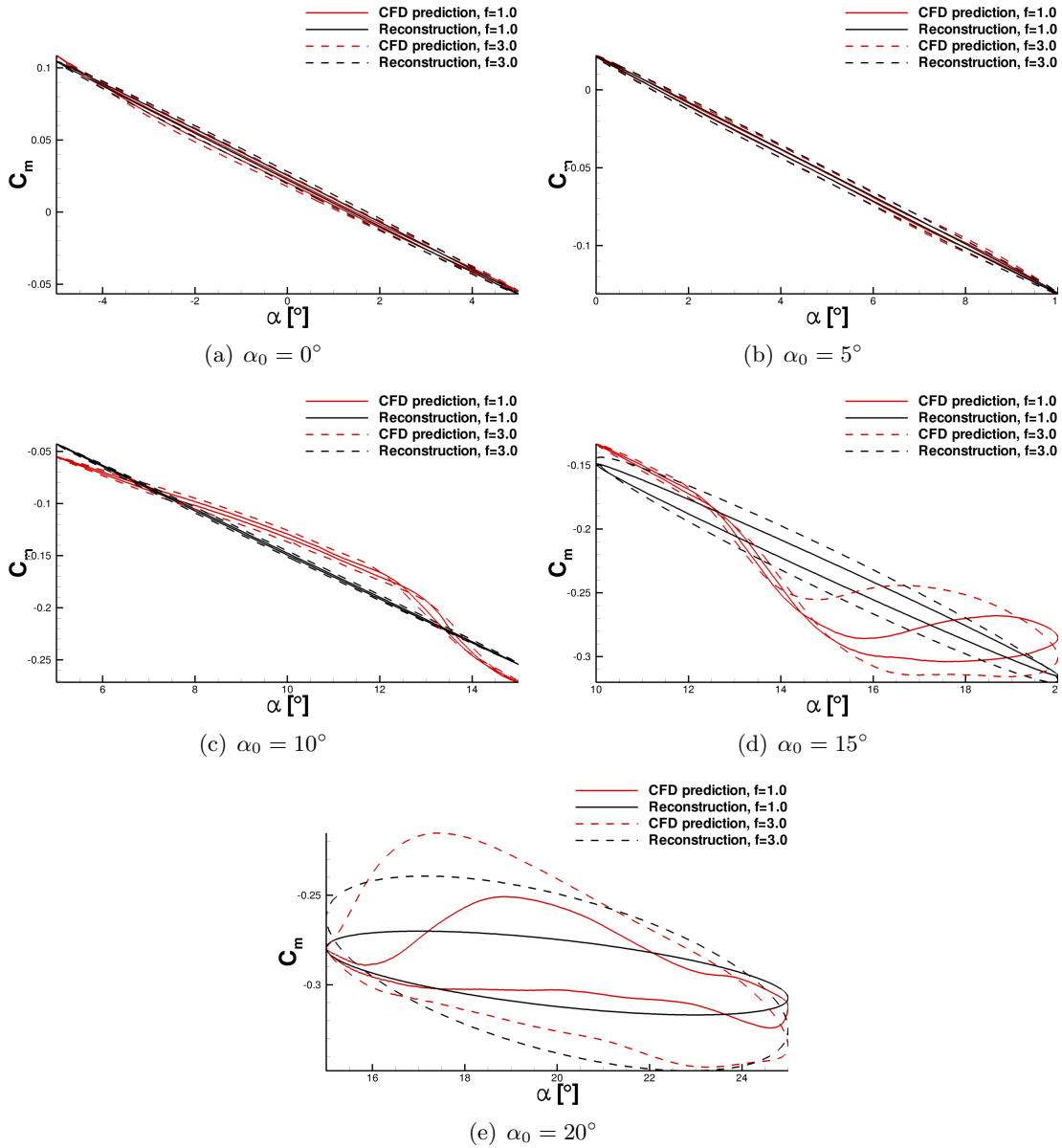
Figure 5.21: Pitching moment coefficient predictions using a linear regression model compared to the time-accurate CFD predictions.

manoeuvre prediction code using linear interpolation between the data points.

5.4 Manoeuvres

A method has been used which calculates time optimal manoeuvres through a combination of flight dynamics theory and aerodynamic data tables implemented in an iterative optimisation process. This has been implemented in a Matlab program which can be run overnight on a desktop machine for the most demanding cases. At the core of this calculation is a commercial code called DIDO [75] which solves the optimisation

problem based on a guess of the final time. The time optimal manoeuvres have been used to replay the motion using time-accurate PMB simulations to assess the limitations in the tabular aerodynamic model. The results from which will be discussed in the next chapter.

The solution to the optimal control problem is obtained using a pseudospectral or direct collocation approach. The problem is rewritten as a finite-dimensional parameter optimisation problem and then solved using a non-linear programming (NLP) technique [30, 31, 32]. It is defined to determine the state-control pair $\{\mathbf{x}(\cdot), \mathbf{u}(\cdot)\}$, and event initial and final times, t_0 and t_f, respectively, that minimise the Bolza cost function,

$$J[\mathbf{x}(\cdot), \mathbf{u}(\cdot), t_0, t_f] = E(\mathbf{x}(t_0), \mathbf{x}(t_f), t_0, t_f) + \int_{t_0}^{t_f} F(\mathbf{x}(t), \mathbf{u}(t), t)dt \qquad (5.5)$$

where E is the endpoint cost and F is the running cost. A set of constraints are defined in terms of the maximum and minimum values of the states and controls. These define a limiting box with the lower and upper boundaries for the states and controls,

$$\mathbf{x}^L < \mathbf{x}(t) < \mathbf{x}^U \qquad (5.6)$$

$$\mathbf{u}^L < \mathbf{u}(t) < \mathbf{u}^U \qquad (5.7)$$

A dynamic function, $\dot{\mathbf{x}}(\cdot)$, is also defined. This is the differential equation or set of equations with respect to time that relate the control parameters to the state parameters,

$$\dot{\mathbf{x}}(\cdot) = f(\mathbf{x}(t), \mathbf{u}(t), t) \qquad (5.8)$$

An iterative process is used to find a set of control parameters that will result in a set of states within the specified boundaries for the minimum possible time. The process finishes when these conditions are satisfied or a maximum number of iterations has been reached. After this, three types of solution may be reached, namely optimal, feasible or not converged. In the first case, a state-control pair has been found for the minimum possible time. In the second case, a realistic solution has been found in the sense that the states and controls remain within the boundaries but not necessarily in the least possible time. In the third case a converged solution could not be reached which could be due to poor problem definition.

The distribution of the time steps in the time domain is obtained using a Legendre-Gauss-Lobatto approach [87]. Path upper and lower limits can be defined to gain control over the states and controls available at each time step. Furthermore, it is possible to define an initial guess based on the results from a previous calculation made with coarser time stepping to accelerate the simulation. This technique has been proven to have a significant influence on simulation time [28]. Defining the problem using aircraft flight dynamics laws allowed for optimal manoeuvre flight path predictions to be made using this method.
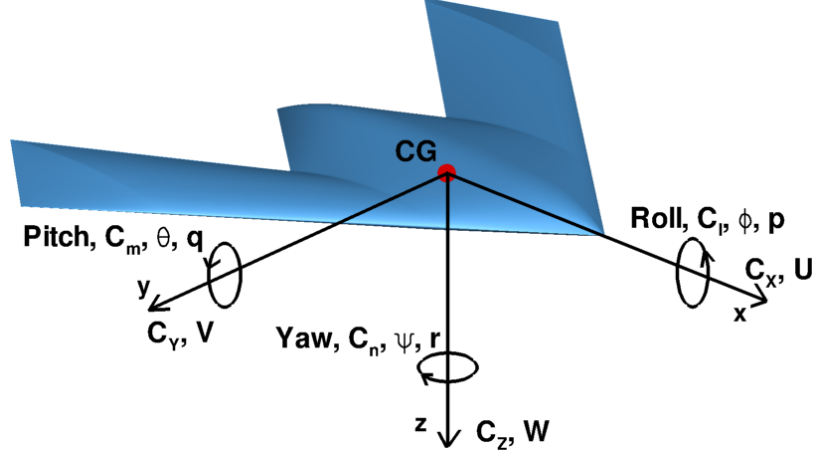
Figure 5.22: Motion variables notation.

The notation for aircraft motions is shown in Fig. 5.22. Here, a positive displacement is represented by the forward direction, towards the starboard and downward. A positive bank is given by a starboard wing down, a positive pitch by a nose up and a positive yaw by nose towards the starboard wing. This convention is used in this study. To start off, the state and control matrices for the SACCON model were defined,

$$\mathbf{x}(\cdot) = \left\{ \begin{array}{cccccccccccc} x & y & z & V_\infty & \alpha & \beta & \hat{p} & \hat{q} & \hat{r} & \phi & \theta & \psi \end{array} \right\} \tag{5.9}$$

$$\mathbf{u}(\cdot) = \left\{ \begin{array}{cccc} \eta_\theta & \delta_{ail} & \eta_\psi & \eta_T \end{array} \right\} \tag{5.10}$$

Here x, y and z are the position in three dimensional Cartesian axes, V_∞ is the freestream velocity, α and β are the angles of attack and sideslip, respectively, $\hat{p}$, $\hat{q}$ and $\hat{r}$ are the rates of roll, pitch and yaw, respectively and ϕ, θ and ψ are the roll, pitch and yaw angles, respectively. The controls δ_{ail}, η_θ and η_ψ correspond to the angular deflections of the aileron and pitch and yaw thrust vector, respectively, η_T is the amount of thrust relative to the maximum available. As mentioned before, each one of these variables is constrained by upper and lower limits throughout any given manoeuvre. These boundaries are useful to force the aircraft to perform the manoeuvre in a certain way which is realistic. A set of expressions based on the equations of motion, as written by Cook [88], are used as dynamic functions. Here, the relation between the control and state changes is established. These are defined in terms of the time derivative of each state variable, a full derivation of which can be found in Appendix A. Here, we state the equation for the force along the x-axis,

$$m(\dot{U} - rV + qW) = X_a + X_c + X_g + X_p + X_d \tag{5.11}$$

where X is the force along the x-axis and U, V and W are the velocities along the x, y and z axes in the body frame of reference. The subscripts a, c, g, p and d represent

the forces due to aerodynamic, control devices, gravitational, power and disturbance or atmospheric effects. For the problem in hand, the aerodynamic term is provided by the look-up tables of static and dynamic characteristics, $[M, \alpha, \beta]$ and $[\alpha, q]$ respectively, described in Sections 3.2 and 5.3, respectively.

$$X_a = \frac{\rho V_\infty^2 S(C_{X_{static}} + C_{X_{dynamic}})}{2} \tag{5.12}$$

The aerodynamic control term is given by the $[M, \alpha, \delta_{ail}]$ table in a similar manner,

$$X_c = \frac{\rho V_\infty^2 S C_{X_{\delta_{ail}}}}{2} \tag{5.13}$$

The power term is given by a specified maximum thrust, T, in the aircraft model. This was implemented along with the throttle control variable, η. The thrust vectoring control is applied by including η_θ and η_ψ terms in the control vector and including the effects of the deflections in the power force and moment terms. Gravitational force terms are also included in the equations. For the purpose of this study no disturbance forces were included.

The objective is to find a set of controls $\mathbf{u}(\cdot)$ that will minimise the cost function using these motion laws, minimising the time in which the manoeuvre is performed. The output from this iterative process is a history of states and control deflections required to achieve the motion.

This software attempts to obtain a solution that is time optimal. This means that the history of output states and controls yields the specified manoeuvre in the minimum possible time. Previous models with more effective control configurations have shown optimality for relatively simple manoeuvres, such as trim and three degrees of freedom pullups. In the case of SACCON, manoeuvre predictions yielded feasible solutions as opposed to optimum. This means that the solution could not be assured to be optimal in time but the state and control histories were within the boundaries of the model capabilities. For the purpose of this study, focus was put on achieving realistic manoeuvres which represent those that can be achieved by similar configurations in real operational scenarios.

The output information can be used in two ways to determine the forces and moments on the aircraft during the motion. One option is to simply feed these back into the look-up tables of aerodynamic data. A second approach is to use the time history of the manoeuvre as an input to the unsteady CFD solver.

The importance of this is to solve the flow in time steps small enough to highlight dynamic effects in the integral forces and moments. High frequency unsteady flow behaviour is thought to have a secondary influence on the overall forces and moments and therefore is not the focus of these simulations. As a rule, it was attempted to keep changes in attitude angles to a maximum of 1° per time step to ensure the motion was replayed accurately. Therefore, for slow manoeuvres with low rates of attitude change

the time step can be relatively large. As the agility levels increase, the required time step size decreases. Spline interpolation between the original timesteps is carried out for the replay state and control variables. The motion is replayed by forcing the translations and rotations on the grid model through the time domain. This is a computationally costly method but it accounts for hysteresis and cross-dependancy effects in the flow.

Each manoeuvre calculation using DIDO takes from 0.5 to 6 processor hours. The cost of each manoeuvre replay using CFD ranges from 750 to 830 processor hours, as shown in Table 5.5. Comparing these numbers with those shown in Table 5.3, it can be seen that the computational cost of running a DIDO simulation is negligible compared to that of the aerodynamic tables. The cost of each of the replay simulations is comparable to those of the tabular entries but for the total number of manoeuvres simulated, six, the overall cost was relatively low.

Table 5.5: Cost of manoeuvre generation and replay.

Simulation	Cost per simulation [processor-hour]	Cost for all simulations [processor-hour]
DIDO	$0.5 - 6$	$3 - 36$
Replay	$750 - 830$	$4500 - 4980$

5.5 Discrepancies

The comparison of the results from CFD and tabular sources allows the assessment of the latter for different types of manoeuvres. There are several possible sources of discrepancy between the two methods. In this case, the time-accurate CFD model is the highest fidelity source and is used as the reference for the validation of the tables.

To make the generation of the tabular model a feasible task based on CFD samples, this is split into a range of three-dimensional tables which considerably reduces the overall number of table entries. Thus, entries depend on three parameters, namely, Mach, α and a third variable. Therefore, the dependence of these third variables on each other is not accounted for, e.g. the effect of β on δ_{ail}. Due to this simplification, the model lacks dependencies which are thought to have relatively low impact in the overall forces and moments.

As mentioned before, a number of samples are used to populate these tables using a Kriging interpolator. For large flight envelopes, a high sample resolution beyond the stall angle of attack is required to recreate all the non-linearities in the aerodynamic characteristics. In most cases the main features in the flow are captured in the tables but some fidelity can be lost. This could in some cases be a source of disagreement with replay predictions for manoeuvres operating in the post-stall region.

An increment to the static tables is made by adding dynamic derivative terms. These are in general dependent on frequency of oscillation, angle of attack, amplitude and Mach number. High fidelity modeling of the dependency on each one of these variables is a computationally costly task and it is not apparent how to represent these parameters in terms of the history of the aircraft states. A range of SACCON dynamic derivatives was predicted using RANS calculations and sinusoidal motions of 1Hz and 3Hz at different mean angles of attack, α_0. In this study Mach number dependence is not considered because it is not thought to have an important effect on these predictions as the SACCON model operates up to $M = 0.3$.

Accurate dynamic derivatives implemented in the tables are expected to give a better prediction than the static tables alone. Although in the non-linear region of the flight envelope, this is at post-stall angles of attack, unusually shaped hysteresis loops may occur. In some cases the upper and lower paths may crossover which would lead to inappropriate predictions from the dynamic derivatives. For this reason, it is the manoeuvres with high angles of attack and high time rates of rotation which will pose the biggest challenge to the tabular model predictive capabilities.

Hysteresis is a potential source of discrepancies between the tables and the replay integral data. This is due to the fact that the static tables do not include information about previous states of the aircraft. The unsteady flow effects are thought to be of less importance as these are expected to have a smaller influence in the overall flight dynamics behaviour of the aircraft. None the less, aircraft at very high angles of attack may exhibit strong fluctuations in aerodynamic characteristics. In these cases, this source of disagreement may need to be considered.

Chapter 6

Replay and Interpretation

To investigate the limits of the tabular model validity, a range of manoeuvres was simulated. These were designed to investigate the performance of the tabular method throughout the flight envelope by benchmarking the load predictions against RANS time-accurate forced-motion replays. Although most of the validation work was concerned with longitudinal aircraft characteristics, a full, six DoF tabular model was generated. This was done with the simulation of agile manoeuvres at the extreme regions of the flight envelope in mind. The manoeuvres simulated in this chapter are illustrated in Fig. 6.1. Here, a pull-up, an Immelmann turn, a $90°$ turn and a lazy eight manoeuvre are shown. A detailed description of the motion of the aircraft throught each one of these manoeuvres is provided further in the chapter.

6.1 Trim

Initially, the manoeuvre prediction software described in Section 5.4 was used to determine the trim states of SACCON. Two cases were simulated, one with thrust vectoring and another without. Table 6.1 shows the results from both of these using standard atmospheric conditions at $305m$ ($1000ft$) above sea level. The first row shows the data for the case without thrust vectoring and the second with vectoring, as can be seen from the values of η_θ and η_ψ. The freestream velocity is given in SI units and remains between $75\frac{m}{s}$ and $85\frac{m}{s}$ for both cases. The angle of attack is $7.3°$ in the case with no vectoring, as would be expected since the aerodynamic pitching moment becomes zero at around this angle of attack as was seen in Section 5.1 for the chosen CG position. For the case with control vector deflection, this was increased to $9°$ as the increase in thrust and pitch down vector require a given amount of aerodynamic pitching moment to balance the aircraft in the longitudinal axis. The thrust setting is shown in terms of the proportion of available power, thus ranging from 0 to 1. The lateral parameters such as sideslip angle, β, and lateral control, η_ψ and δ_{ail}, were zero, as was expected since the model was generated assuming geometrical symmetry. Both of these predictions obtained the trim states at pitch angles of approximately $7°$ to $8°$. The rates
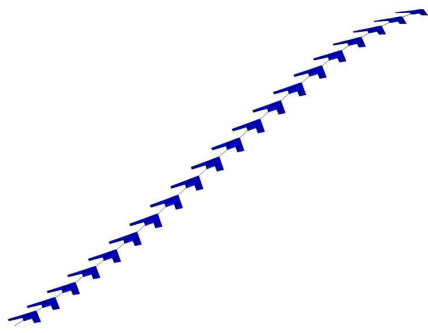
(a) Pull-up.
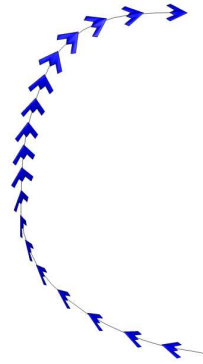
(b) Immelmann Turn.
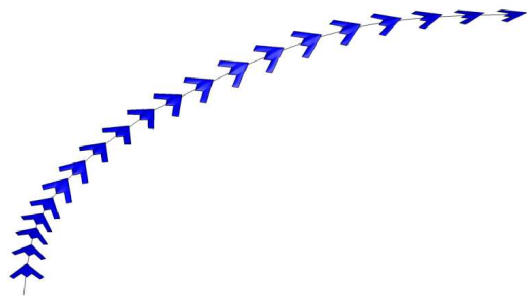
(c) 90° Turn.
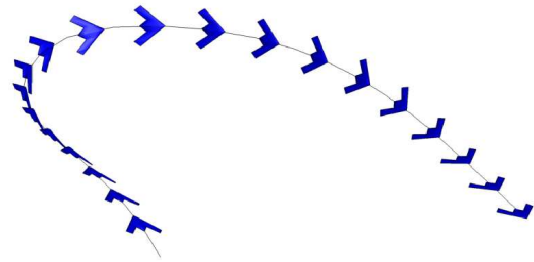
(d) Lazy Eight.

Figure 6.1: SACCON manoeuvre trajectories.

of rotation were negligible during these computations as would be expected while the aircraft is trimmed.

Table 6.1: Example trim states for SACCON.

$V_\infty \ \frac{m}{s}$	α_{trim} [°]	β_{trim} [°]	θ [°]	η_T	η_θ [°]	η_ψ [°]	δ_{ail} [°]
79.2	7.3	0	7.0	0.5	0.0	0	0
84.7	9.0	0	7.7	0.78	-10.0	0	0
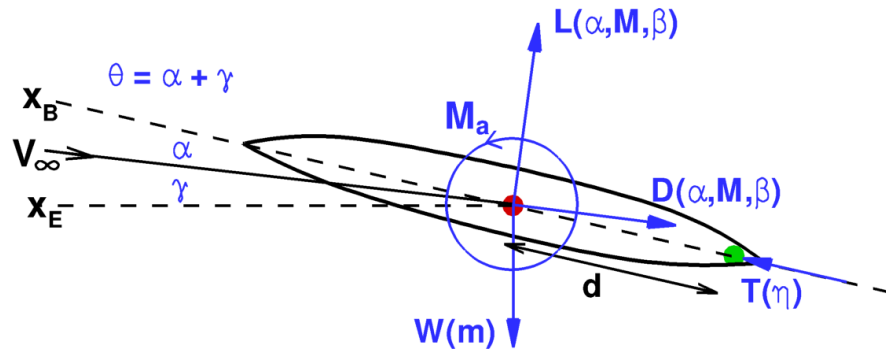
(a) No thrust vectoring applied.
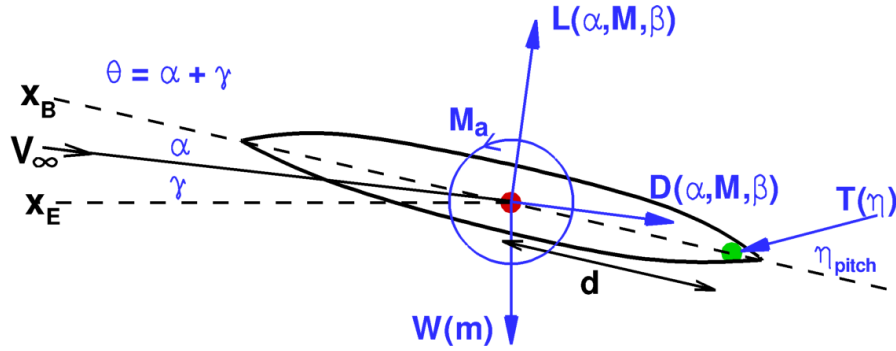
(b) With thrust vectoring.

Figure 6.2: Implemented SACCON model trim states.

The dynamics of the implemented SACCON model presented a challenge due to the applied thrust vectoring technique. Figure 6.2 shows a longitudinal free body diagram of the forces and moments for each type of trim case, where x_E and x_B represent the earth and body fixed Cartesian axes, respectively, W_a is the weight of the aircraft acting on the CG, m is the mass and γ the flight path angle. For the trim conditions to be satisfied a linear and rotational unaccelerated condition needs to be satisfied. This means that the forces and moments need to be balanced in each axes. From Fig. 6.2

the longitudinal equations with respect to the earth axes can be demonstrated to be

$$\underbrace{Lcos(\gamma)}_{\mathbf{L}(\alpha,\theta,\mathbf{M},\beta)} - \underbrace{Dsin(\gamma)}_{\mathbf{D}(\alpha,\theta,\mathbf{M},\beta)} - \underbrace{W_a}_{\mathbf{W_a}(\mathbf{m})} + \underbrace{Tsin(\theta + \eta_\theta)}_{\mathbf{T}(\theta,\eta,\eta_\theta)} = 0 \tag{6.1}$$

$$\underbrace{Tcos(\theta + \eta_\theta)}_{\mathbf{T}(\theta,\eta,\eta_\theta)} - \underbrace{Lsin(\gamma)}_{\mathbf{L}(\alpha,\theta,\mathbf{M},\beta)} - \underbrace{Dcos(\gamma)}_{\mathbf{D}(\alpha,\theta,\mathbf{M},\beta)} = 0 \tag{6.2}$$

$$\underbrace{Tdsin(\eta_\theta)}_{\mathbf{M_{TV}}(\theta,\mathbf{d},\eta,\eta_\theta)} - \underbrace{M_a}_{\mathbf{M_a}(\alpha,\mathbf{M},\beta)} = 0 \tag{6.3}$$

where d is the distance between the centre of gravity and the point about which the thrust actuates. Equations 6.1, 6.2 and 6.3 can be generalised and expressed in the following form

$$L(\alpha, \theta, M, \beta) - D(\alpha, \theta, M, \beta) - W_a(m) + T(\theta, \eta, \eta_\theta) = 0 \tag{6.4}$$

$$T(\theta, \eta, \eta_\theta) - L(\alpha, \theta, M, \beta) - D(\alpha, \theta, M, \beta) = 0 \tag{6.5}$$

$$M_{TV}(d, \eta, \eta_\theta) - M_a(\alpha, M, \beta) = 0 \tag{6.6}$$

where M_a and M_{TV} denote the aerodynamic pitching moment and that due to thrust vectoring. It can be seen that the thrust term influences all three equations and is always dependent on η and η_θ. The trim equations for a conventional aircraft with a wing and tail configuration are shown below

$$L_W(\alpha, \theta, M, \beta) - D_W(\alpha, \theta, M, \beta) + L_{TP}(\alpha, \theta, M, \beta, \delta_{ele})$$
$$- D_{TP}(\alpha, \theta, M, \beta, \delta_{ele}) - W_a(m) + T(\theta, \eta) = 0 \tag{6.7}$$

$$T(\theta, \eta, \eta_\theta) - L_W(\alpha, \theta, M, \beta) - D_W(\alpha, \theta, M, \beta)$$
$$- L_{TP}(\alpha, \theta, M, \beta, \delta_{ele}) - D_{TP}(d, \alpha, \theta, M, \beta, \delta_{ele}) = 0 \tag{6.8}$$

$$M_W(\alpha, M, \beta) + M_{TP}(d, \alpha, M, \beta, \delta_{ele}) = 0 \tag{6.9}$$

Here, some extra terms can be found due to the influence of the wing and tail plane, subscripts "W" and "TP", respectively. The variable d here corresponds to the distance from the the CG to the centre of pressure of the tail plane. An advantage of the conventional design over the SACCON model is the relatively large values of d, which provides increased elevator effectiveness. But what is most important for the purpose of finding trim states is the decoupled effects of T, L_{TP} and D_{TP}. Where the thrust term can be used to balance the force equations 6.7 and 6.8, since the tail plane forces have a small effect in these axes. This way the tail plane terms can be used primarily to control the pitching moments as shown in equation 6.9. This decoupled control system allowed for optimum manouevres to be computed more effectively and with more freedom than for SACCON as seen in Refs. [89, 74]. The coupled effect of the thrust term on all axes of the longitudinal stability equations created a very sensitive system with fewer trim states than conventional aircraft. Nonetheless, the aim of this study was to obtain realistic aircraft motions with the current flight dynamics model. The results are shown in this chapter.

6.2 Pull-up
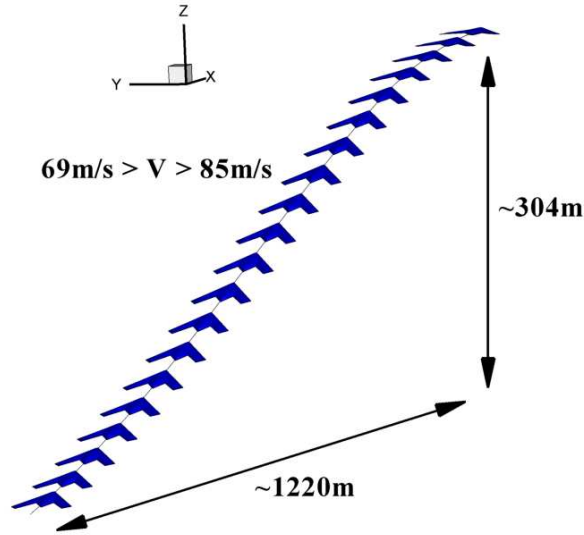
Figure 6.3: SACCON pull-up trajectory.

A slow pull-up was predicted where the aircraft had to change altitude from approximately $1525m$ to $1820m$ in $15s$, depicted in Fig. 6.3. The manoeuvre consists of an increase in aircraft altitude by pitching the aircraft up, and then down again. It was performed at low angles of attack and sideslip, below $\pm4°$, shown in Fig. 6.4 (a). The maximum rate of pitching rotation was $\pm10°/s$ with negligible lateral activity. This manoeuvre was computed initially with a slightly different setting of the CG as was previously described. In this case, the location was set at $x = 0.4m$ from the apex, corresponding to the dimensions of the wind tunnel model. Thus, causing a lower angle of attack trim condition, at approximately $1°$, as well as larger pitching moments. Later on it was discovered that this configuration was too stable to perform high angle of attack manoeuvres and therefore the CG position was shifted backward. The initial increase in pitching moment, q, allows the aircraft to pitch up to increase altitude, whereas the negative q towards the end causes the aircraft to pitch down again towards the trim state, shown in Fig. 6.4 (b). As a result of this, the pitch angle, θ is seen to vary during the manoeuvre between $0°$ and $20°$, Fig. 6.4 (c). To achieve the motion, the thrust vector is rotated from $15°$ at trim to $-15°$ while piching up. Towards the end of the manoeuvre it switches again, as shown in Fig. 6.4 (d).

The aerodynamic forces and moments produced during the manoeuvre were predicted using the tables and the time-accurate calculation. A comparison from the two sources can be seen in Fig. 6.5. The blue squares represent the static tabular predictions, the black circles the tables incremented using dynamic derivatives, the red lines

(a) α & β

(b) p, q and r

(c) ϕ, θ and ψ

(d) η_θ
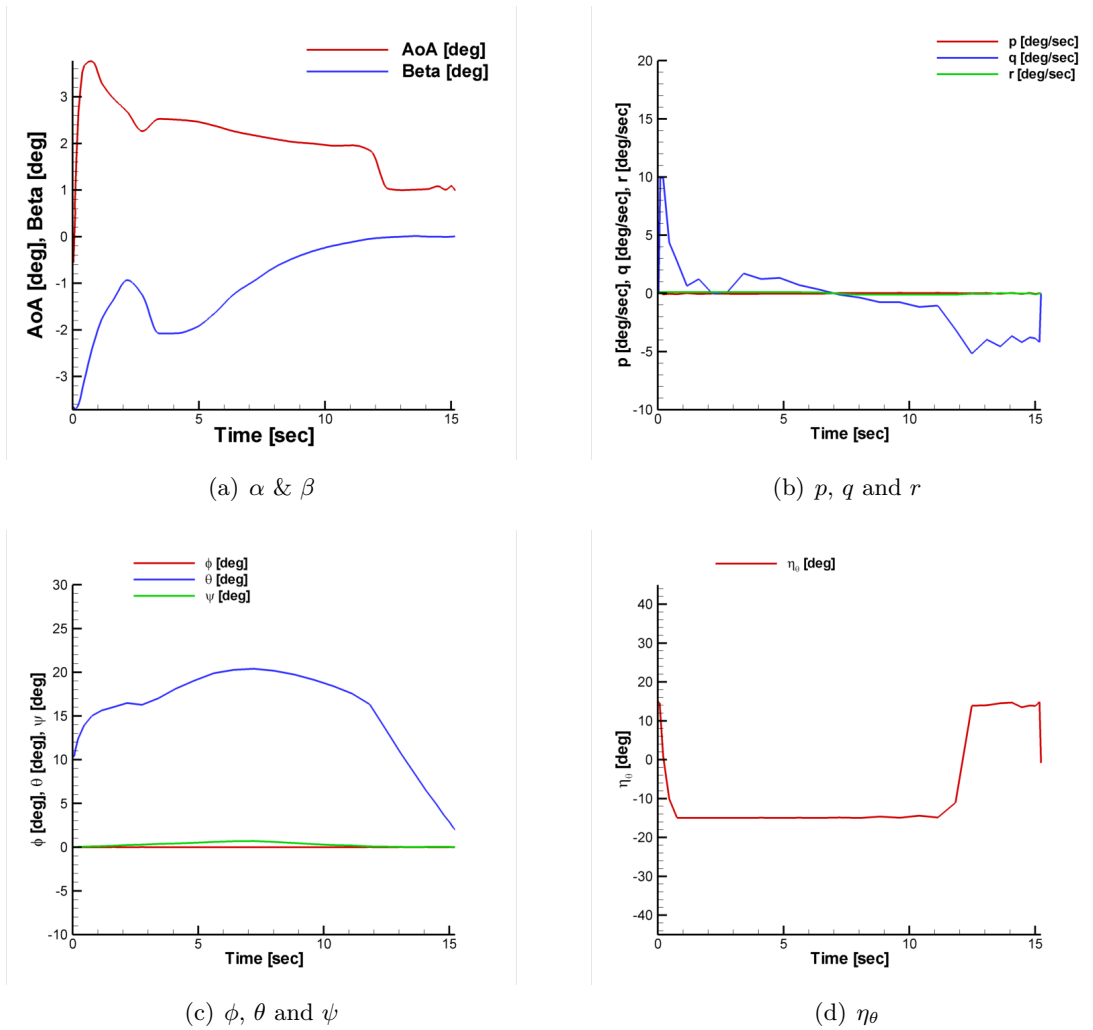
Figure 6.4: SACCON motion during a slow pull-up.

are the replay results and the green squares are steady state calculations performed at different points during the manoeuvre. This format is adopted from here on in this chapter.

Overall the agreement between the tables and the time-accurate predictions is good. Some discrepancies can be seen in the middle part of the manoeuvre for C_L, C_Y, C_l and C_n, although these are very small considering the scales at which these are plotted. For example, the maximum difference seen in C_L is approximately 0.011, which only represents 1.5% of the model's $C_{L_{max}}$. At first glance, the side force and yawing moment characteristics seem to be poorly represented in the tables since the trends shown in Fig. 6.5 (d) and (f) disagree. Although considering there is no vertical surfaces or direct aerodynamic control in these axes it is expected that small pressure distribution differences will trigger non-linear behaviour of small mangitudes, as seen in this manoeuvre. Also from these results it can be seen that the dynamic derivative increments are negligible for this particular manoeuvre, which is to be expected as q and $\dot{\alpha}$ remain very small during most of the manoeuvre. The steady state calculations were performed to directly assess the adequacy of the data fusion method used to populate the tables. The closer the static tables are to the steady state computations the better the data fusion approach. Overall the steady state calculations are in better agreement with the replayed results than with the tables themselves. This suggests that the small discrepancies between the tabular and the replay results are due more to fusion shortcomings than to dynamic effects during the manoeuvre. Nevertheless, the predictions from the tables are good within the region of low angles of attack and low attitude rates.

6.3   Immelman Turn

An Immelman turn was then simulated. In this manoeuvre the aircraft has to turn 180° in attitude by performing a half loop and levelling out the wings again at a higher altitude from the starting point, as shown in Fig. 6.6. Figure 6.7 (a) shows the changes in the attitude angles as it is performed. The angles ϕ, θ and ψ are shown in red, blue and green, respectively. After pitching the aircraft up to 90° a roll motion is started to level the wings at the top of the loop. In the meantime, the yaw angle steadily increases from 0° to 180° at the end of the manoeuvre. It should be noticed that no aircraft structural considerations were made when desiging this manoeuvre since the rolling motion is performed while the aircraft is still undergoing a high acceleration inside the loop. For this reason the rotation in ϕ would realistically be performed after θ had decreased again and ψ had reached 0°. Although, from the aerodynamic point of view, it was more interesting for the manoeuvre to be performed this way. Figure 6.7 (b) shows the time history of the angles of attack and sideslip. Both of these reach angles as high as 9°, although these are still conditions inside the linear flow region.
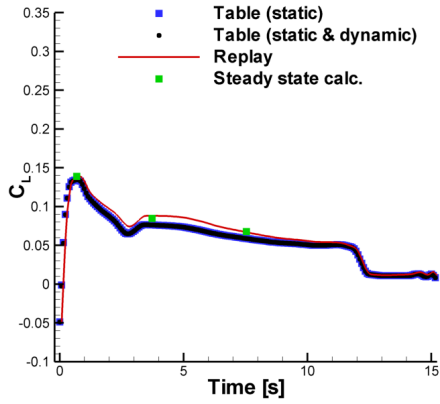
(a) C_L (b) C_D
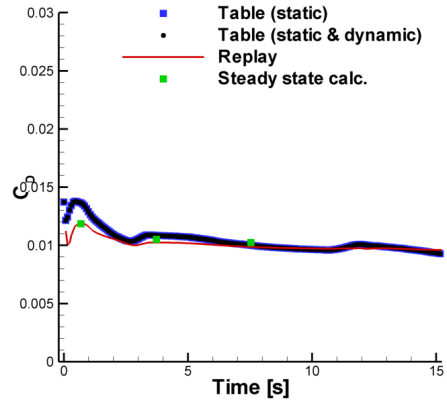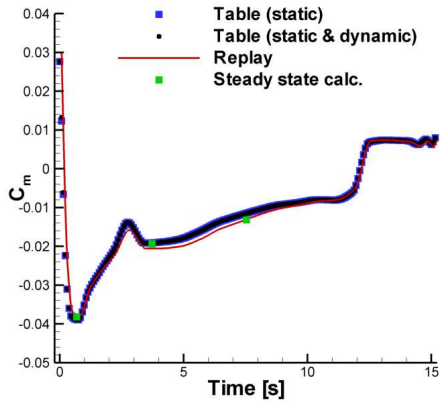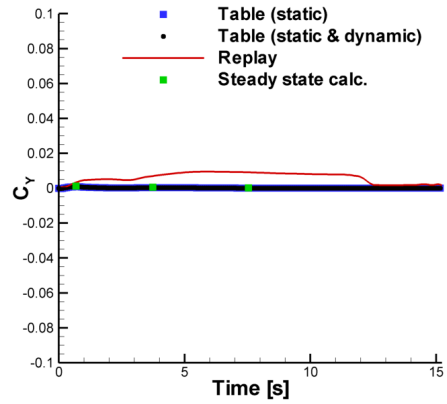
(c) C_m (d) C_Y
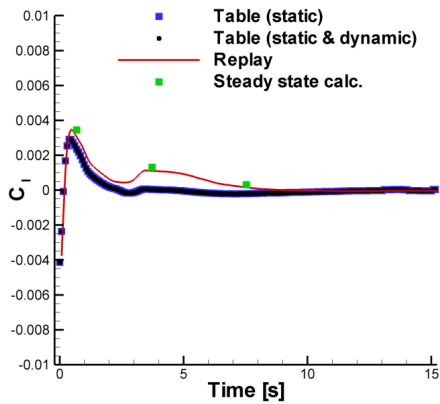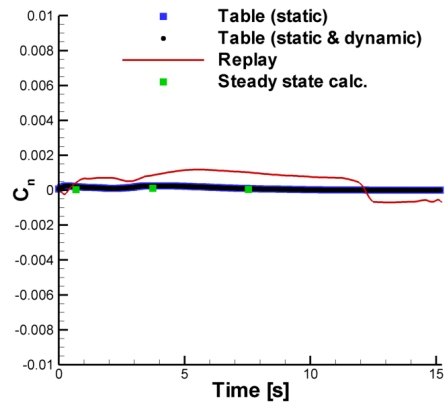
(e) C_l (f) C_n

Figure 6.5: SACCON forces and moments during a slow pull-up.

The rotational rates are limited to $\pm 10°/s$, as shown in Fig. 6.7 (c). Fig. 6.7 (d) shows how the thrust vector is deflected throughout the manoeuvre. The Immelmann turn represents a more complex manoeuvre than the pull-up where none of the aircraft states remain constant.
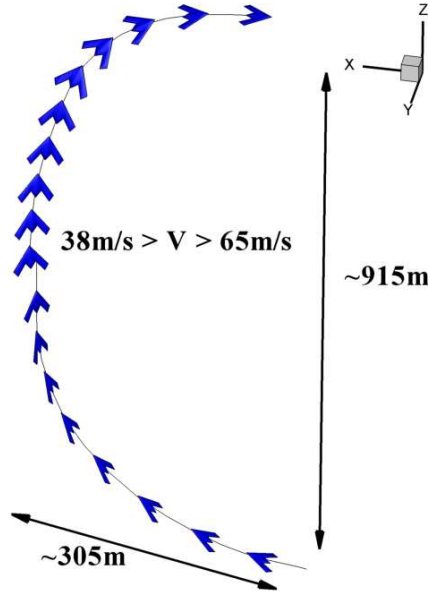
Figure 6.6: SACCON slow lazy eight trajectory.

The forces and moments predicted for this manoeuvre are shown in Fig. 6.8. The agreement between the two sets of results is again very good. Some discrepancies can be seen where sudden changes occur. This is likely to be a dynamic effect as opposed to a data fusion issue as was shown in the pull-up results.

As seen in the pull-up manoeuvre C_Y and C_n are predicted with different small scale trends. One way of looking at the magnitude of the history effects during the manoeuvre is by plotting the results against angle of attack. If a spread in the static tabular results is present this can only be due to the variation in sideslip angle. Spread in the replay beyond that seen from the tabular results is due to hysteresis. Figure 6.9 shows some presence of hysteresis during the Immelmann turn in the longitudinal characteristics. This is to be expected based on the experience from the dynamic derivatives results. Here some spread was seen at values of α_0 and $\dot{\alpha}$ similar to those experienced during the Immelman turn. The maximum spread in the lift, drag and pitching moment coefficients is relatively low, 0.03, 0.002 and 0.002, respectively. By inspecting the time histories of these characteristics in Fig. 6.8 it can be seen that the discrepancies between the tables and replay remain within these values for C_L, C_D and C_m. Although small, the first signs of hysteresis driven discrepancies are present for this manoeuvre which is performed at low to moderate angles of attack and low angular

(a) ϕ, θ and ψ

(b) α & β

(c) p,q and r

(d) η_θ
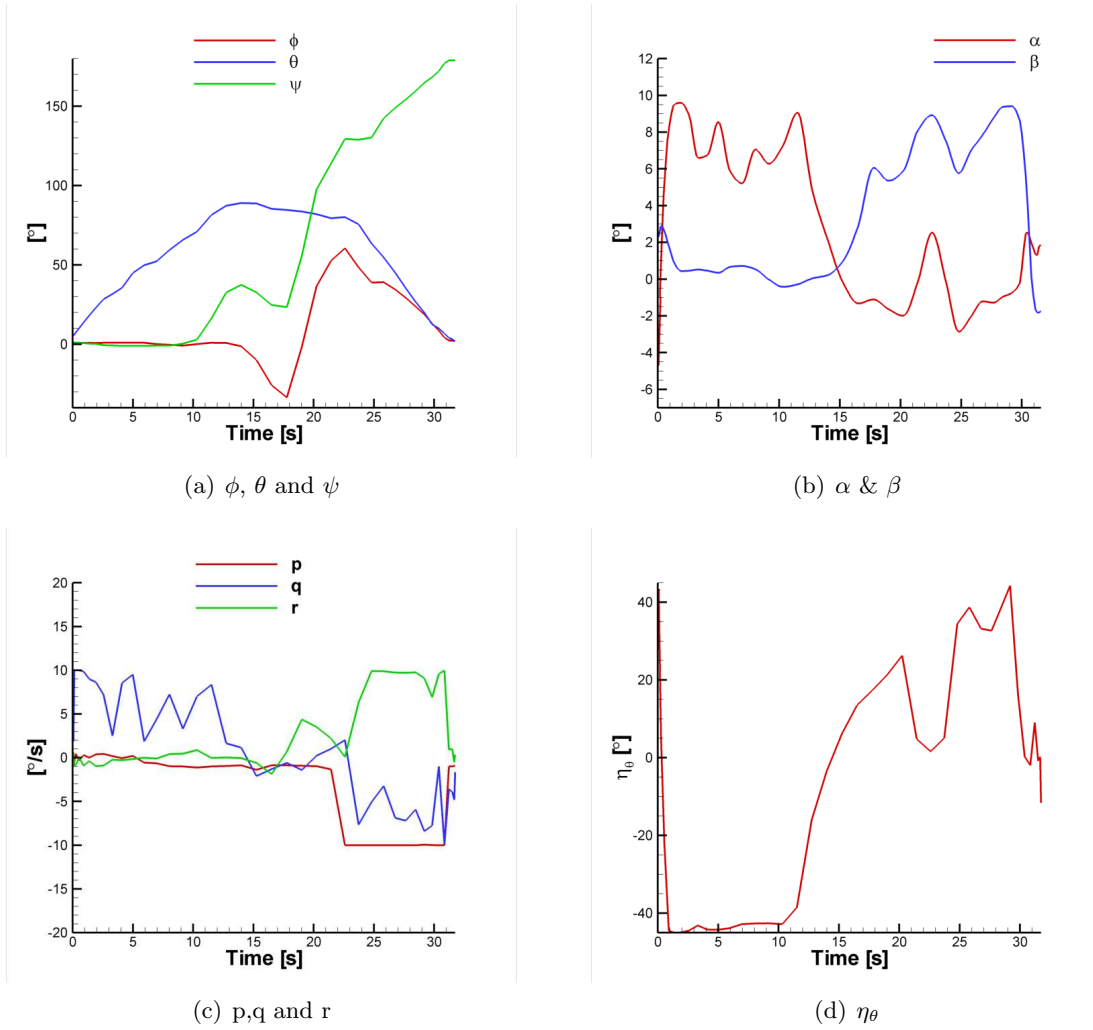
Figure 6.7: SACCON motion during an Immelmann turn.

(a) C_L

(b) C_D

(c) C_m

(d) C_Y

(e) C_l

(f) C_n
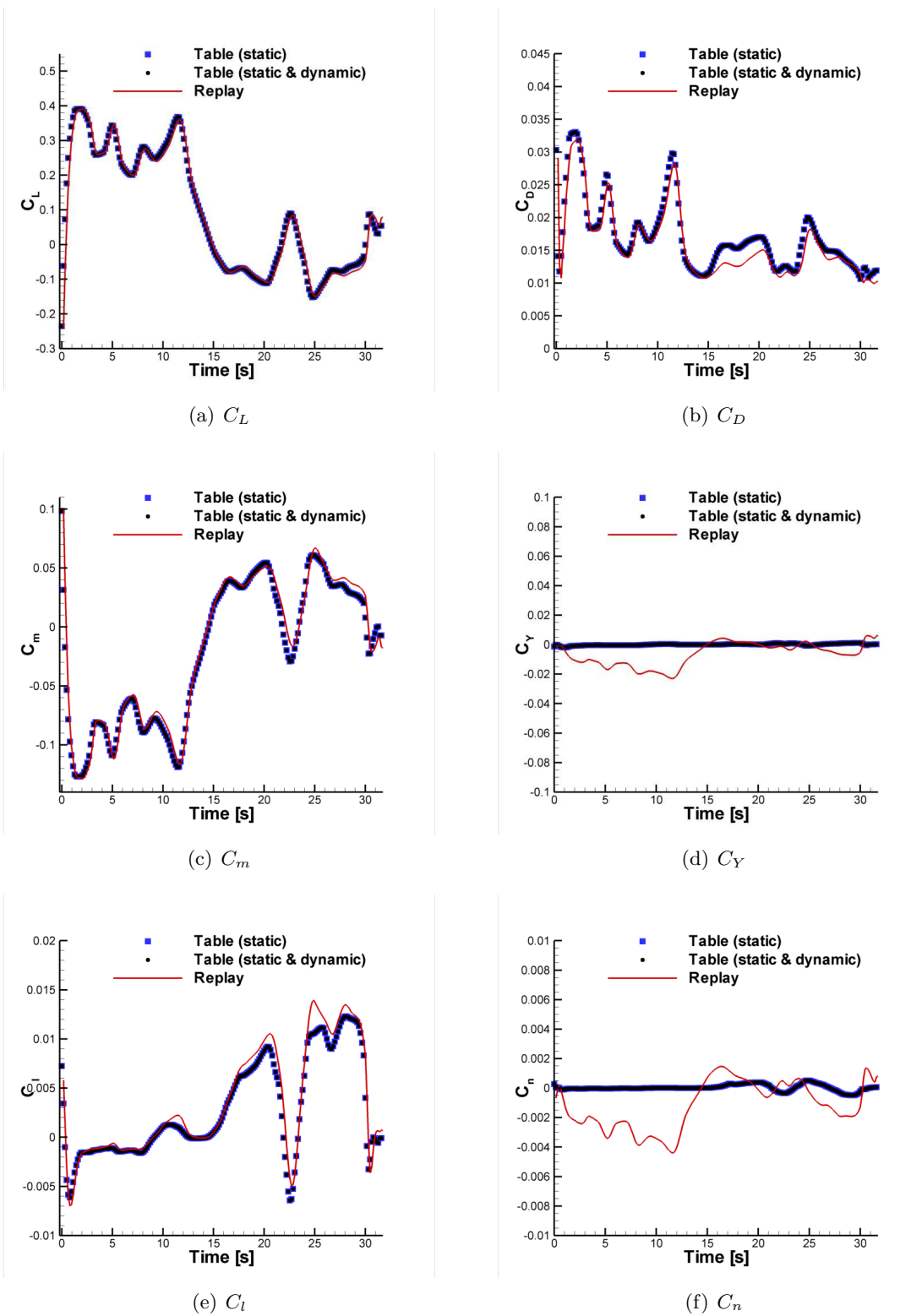
Figure 6.8: SACCON forces and moments during a slow Immelman turn.

velocities.

(a) C_L

(b) C_D

(c) C_m
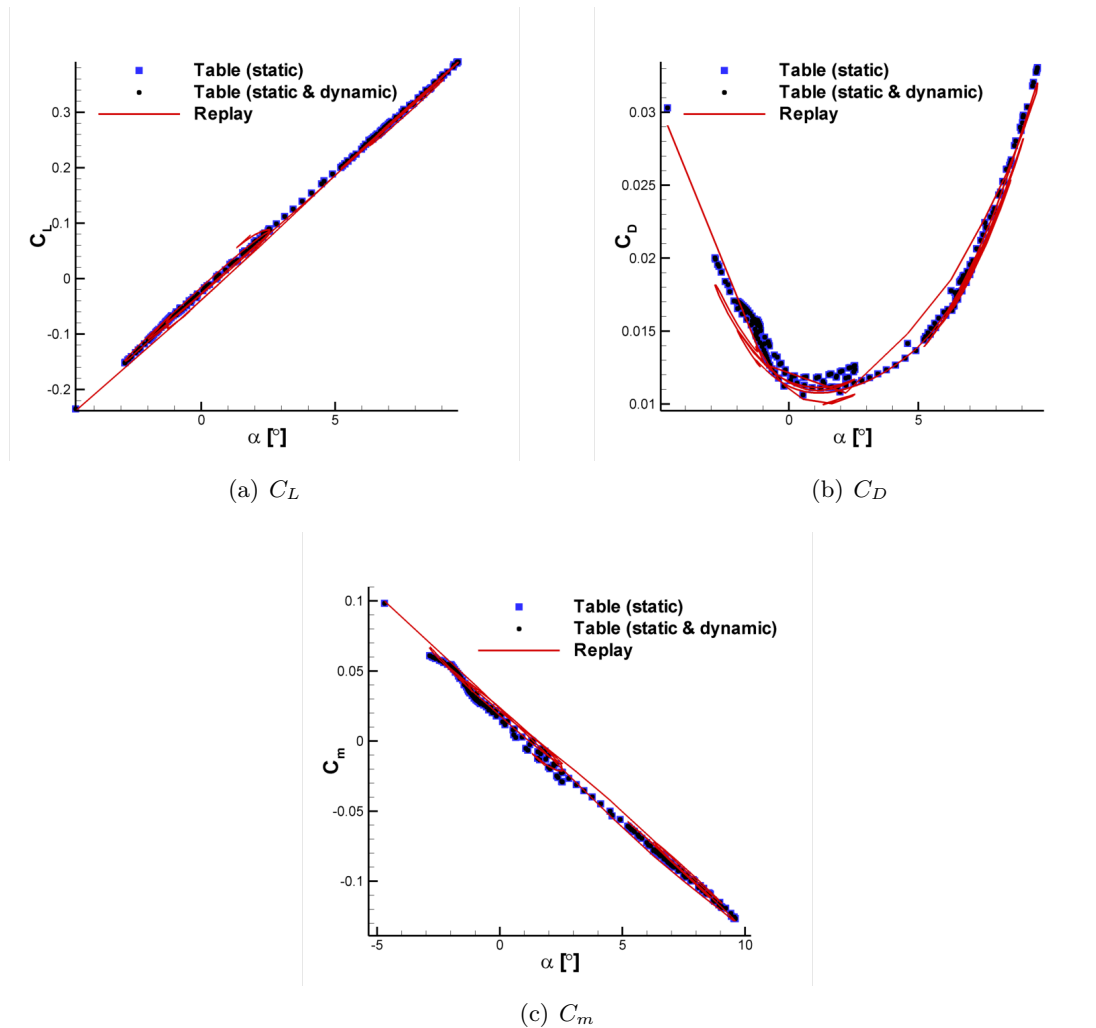
Figure 6.9: SACCON longitudinal forces and moments during a slow Immelman turn against angle of attack.

6.4 90° Turn

The next step in the assessment was to further increase the angle of attack and angular rates. For this, a 90° turn at high angle of attack was simulated. It was during the design of this manoeuvre that the position of the CG became an issue and it was decided to relocate it at $x = 0.55m$. This new location provides a marginally stable configuration allowing for more aggressive manoeuvres to be performed, as shown in Fig. 5.2 (a). During this manoeuvre the forward speed remains between $65m/s$ and $75m/s$ and the turn is performed within a $900m$ by $900m$ square with a small increase in altitude of approximately $100m$, as shown in Fig. 6.10. This increase in altitude is the consequence of a loose constraint in the z-axis and the fact that these were

feasible DIDO solutions as opposed to optimal. However, for the purpose of this study, this variation in altitude was not important. The aircraft is required to bank at an angle while increasing the angle of attack and sideslip. Figure 6.11 (a) shows how the attitude angle changes from $0°$ to $90°$ in 20 seconds while the bank and pitch angles reach $45°$ and $25°$ respectively. The angle of attack is seen to reach $20°$ twice during the manoeuvre while the aircraft is at high bank angles, as shown in Fig. 6.11 (b). This is to produce enough upward force to counteract the gravitational forces. The sideslip angle remains within the range of $-5° > \beta > 8°$. The rates were limited to $20°/s$ to allow comparison of tabular and replay results at high incidence angles with the influence from dynamic effects. The thrust vector longitudinal deflection is shown in Fig. 6.11 (c) where it is seen to reach minimum levels when the angle of attack is highest. This is mainly to counteract the strong aerodynamic pitching moment at those times during the motion.
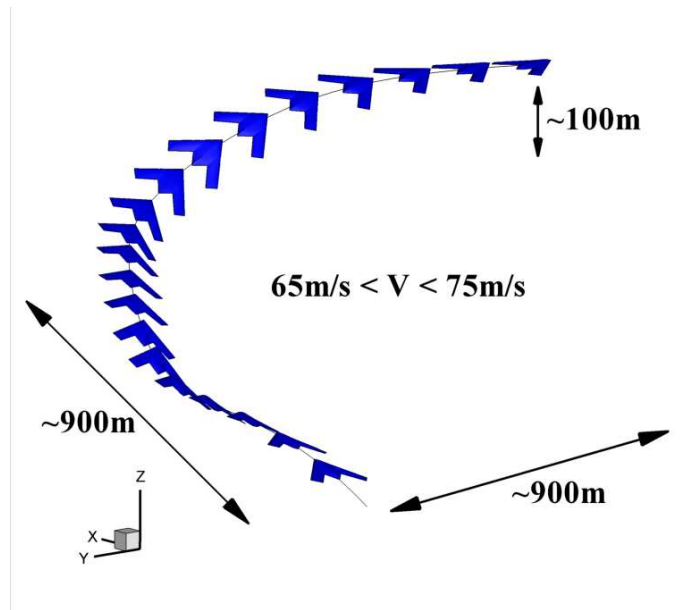
Figure 6.10: SACCON $90°$ turn trajectory.

As expected, the C_L and C_D coefficients shown in Fig. 6.12 (a) and (b) display very good agreement between the tables and the replay, even at the higher angles of attack. Small discrepancies occur at the points when the time rate of change of angle of attack, $\dot{\alpha}$, is highest, at approximately 6 and 13 seconds. Smaller discrepancies can be seen at 4.5, 11 and 12 seconds which coincides with small peaks in α. So for the longitudinal forces the shortcomings of the tabular model are present as the $\dot{\alpha}$ term increases.

The pitching moment coefficient shown in Fig. 6.12 (c) displays a large disparity between tabular and replay results. At approximately 6 and 13 seconds a rapid increase in α is seen which causes the large drop in all C_m predictions. The tabular results show

(a) ϕ, θ and ψ

(b) α & β

(c) η_θ
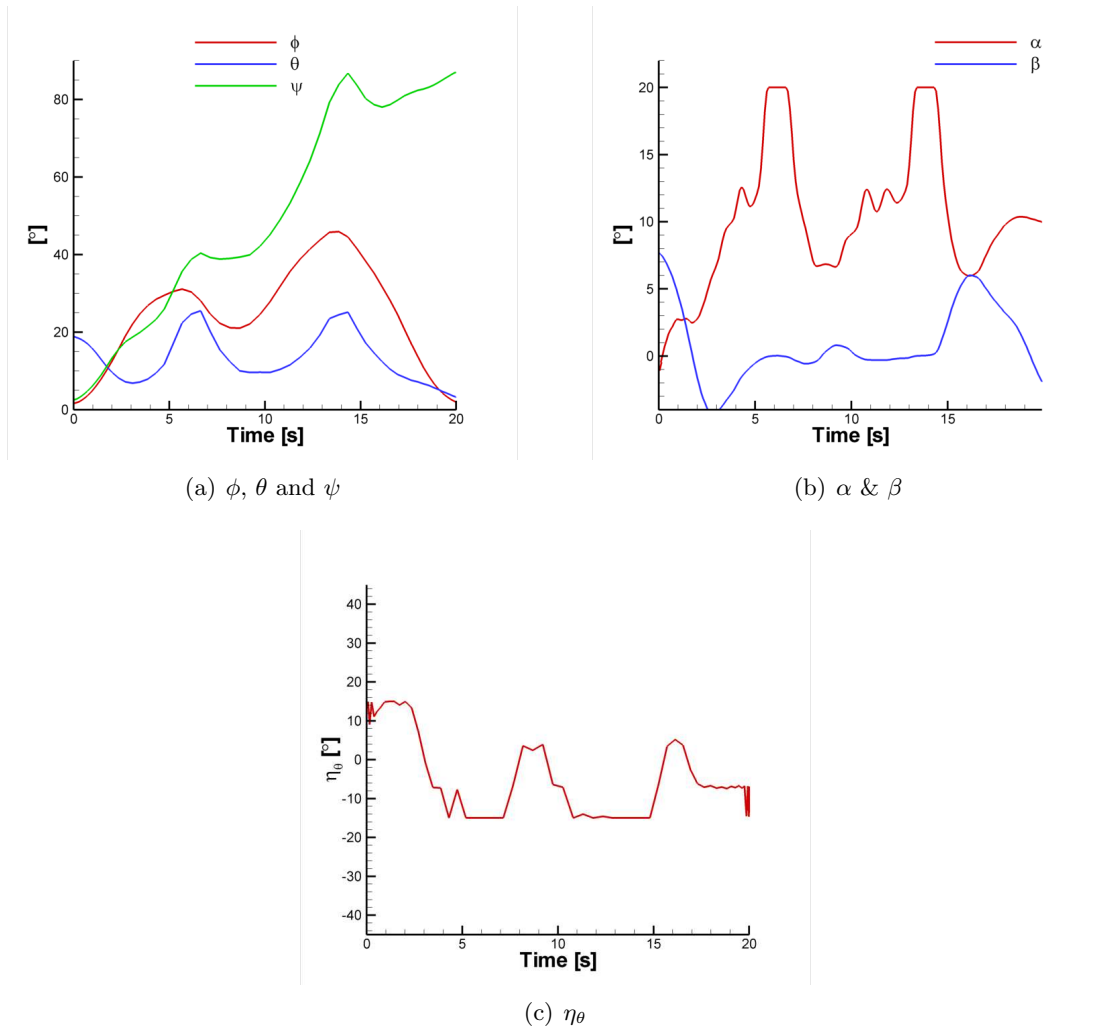
Figure 6.11: SACCON motion during a 90° turn.

(a) C_L

(b) C_D

(c) C_m
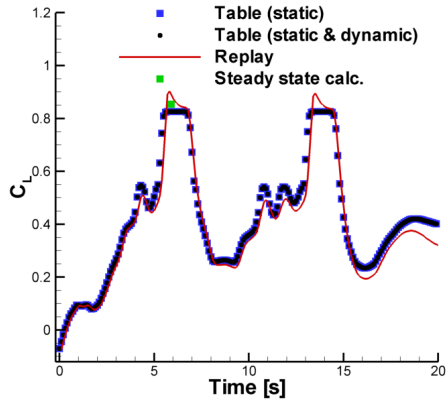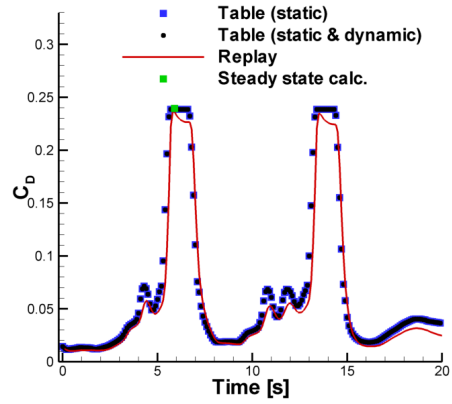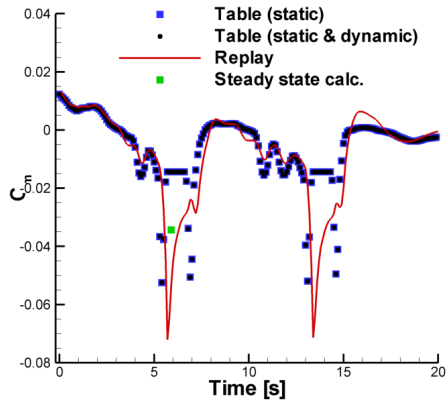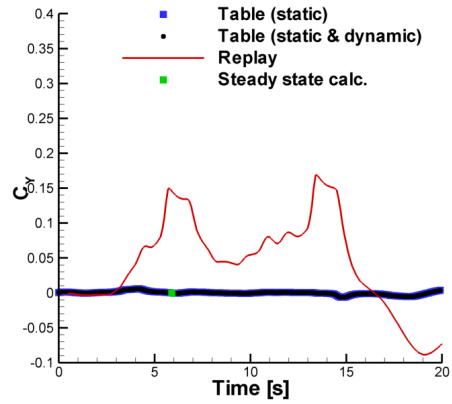
(d) C_Y
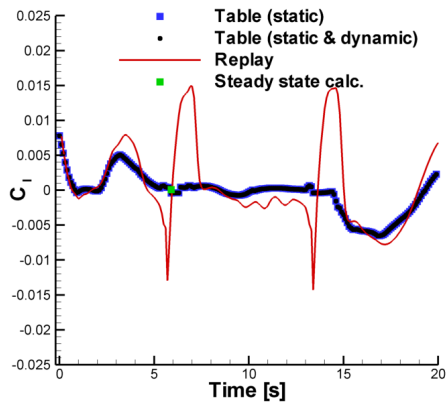
(e) C_l
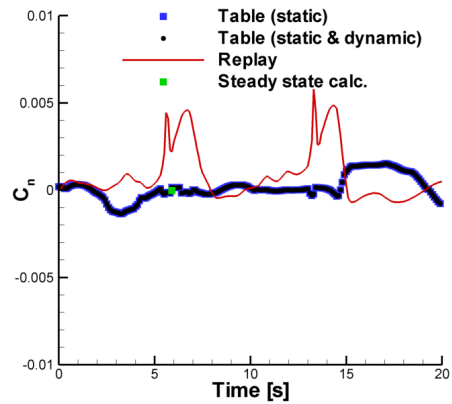
(f) C_n

Figure 6.12: SACCON forces and moments during a 90° turn.

a signal similar to a short pulse. This is because as the angle increases the C_m suffers the drop described in Chapter 4, after which, it recovers. The rapid change in α causes the pulse-like shape. The replay prediction on the other hand shows a delayed pulse which then takes a longer time to recover. The delay is the result of an induced flow which results in a lower effective angle of attack. The slow recovery is a result of the vortical transient flow which takes a noticeable period of time to settle. In fact, this seems to be longer than the time available before the angle of attack changes again, meaning the unsteady flow never reaches a steady state, instead the flow is dominated by transient flow effects.

In order to look at this vortical transient flow behaviour in more detail and quantify its effects on the lift and pitching moment coefficients, a simulation was run in the same manner as the replay manoeuvre with the exception that the state angles and velocities were frozen at 5.6 seconds. From this point on, the unsteady calculation was continued allowing the flow to settle over the required length of time. These results are shown in Fig. 6.13 plotted against the tabular predictions and a steady state calculation. The replay lift coefficient shows an exponential decay trend causing a change in lift coefficient of 0.052. This change in C_L due to vortex transient effects is denominated as ΔC_{L_3}. The difference seen between the steady state calculation and the static table prediction is due to data fusion errors and accounts for a change in lift coefficient of $\Delta C_{L_1} = 0.028$. Another error is due to the difference in flow topology obtained from an unsteady and a steady state simulation, as seen from the term ΔC_{L_2} in Fig. 6.13 (a) causing a difference of 0.013. Finally, the dynamic derivatives account for a correction of 0.002 from the basic tables. This transient flow regime at such high angles of attack has an even more important effect on the pitching moment, with $\Delta C_{m_3} = 0.039$ over a period of one second. This large difference, approximately double the steady state prediction, is due to the induced angle and the mentioned delay. There is also an error due to data fusion of $\Delta C_{m_1} = 0.016$. The agreement between the steady state calculation and the replay settled C_m characteristic is very good. This is surprising as C_m has shown to be significantly more sensitive than C_L to changes in flow topology.

The rolling moment coefficient shows disagreement where the peaks in α occur, at approximately $6s$ and $14s$, shown in Fig. 6.12 (e). At these moments in time, the roll rate is approximately $7°/s$, this combined with the angle of attack and pitch motion cause these peaks in C_l which the static tables are unable to predict. The yawing moment coefficient shown in Fig. 6.12 (f) is very small as expected from this type of configuration. Nonetheless, both C_Y and C_n display noticeable discrepancies between the two main prediction methods. A closer look at the pressure coefficient distribution is required to explain flow topology characteristics causing these differences. Figure 6.14 shows a snapshot of the replay at $6s$ (a) and the steady state solution (b) at the same conditions. Here, the C_p distribution over the SACCON wing is shown. In order

(a) C_L (b) C_m
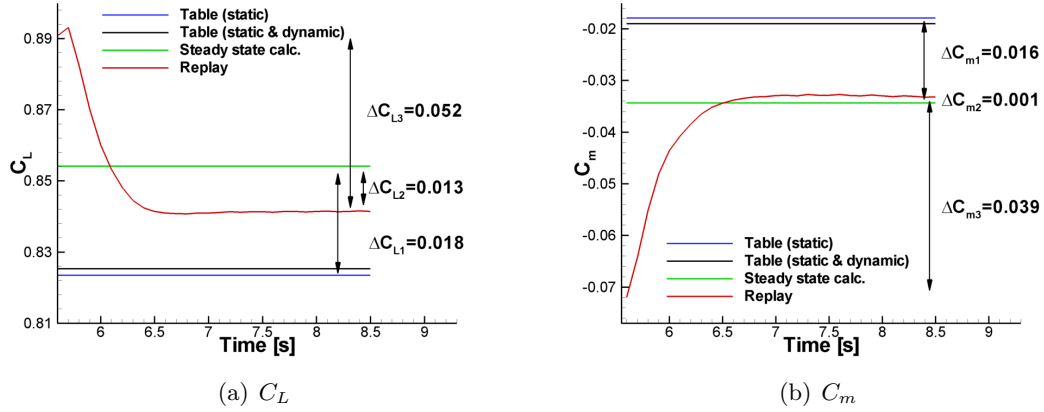
Figure 6.13: Transient flow effect on discrepancies during a 90° turn.

to highlight the differences between these flow topologies the ΔC_p distribution, Fig. 6.14 (c), was calculated as follows,

$$\Delta C_p = C_{p_{SS}} - C_{p_R} \tag{6.10}$$

where $C_{p_{SS}}$ and C_{p_R} are the pressure coefficient from the steady state and replay solutions, respectively. Therefore, the positive red colouring represents regions where the pressure is higher in the replay solution and vice versa. The maximum and minimum ΔC_p over the entire geometry reaches ±0.6. There is a clear asymmetry with greater differences in the flow over the port side, which explains the discrepancies in C_l, C_n and C_Y.

(a) Replay at t=6s   (b) Steady state at t=6s   (c) Difference at t=6s
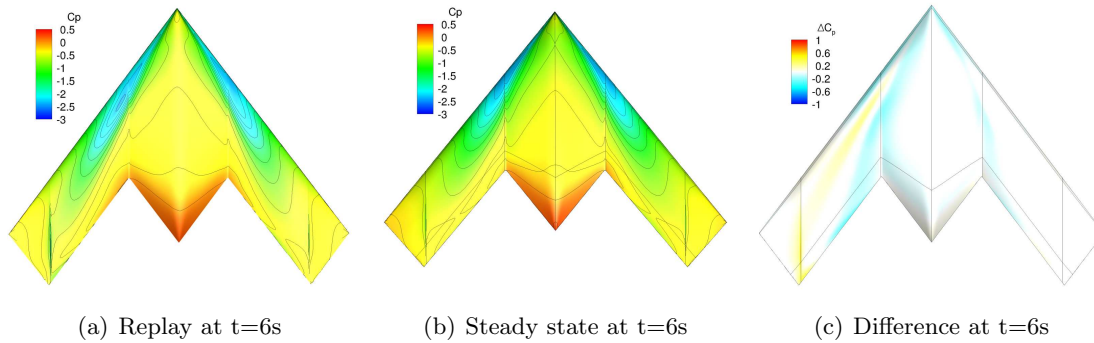
Figure 6.14: C_p and ΔC_p distributions at 6 seconds during the 90° turn.

Plotting C_L, C_D and C_m against angle of attack, as shown in Fig. 6.15, directly shows the extent to which hysteresis effects influence the overall longitudinal force and moment coeffiecients. The lift and drag coefficient show a spread of approximately 0.05 and 0.03, respectively, with a crossover at the high angles of attack. The pitching moment coefficient displays much larger hysteresis effects, up to 0.035 at 20° angle of

attack, which is very large taking into account that the range of C_m during this manoeuvre is $-0.07 < C_m < 0.02$. Here it is evident that history effects are predominant during the manoeuvre and that the tabular static predictions are not adequate under these conditions of high dynamics and angles of attack. The dynamic derivatives show a small increment from the static values, although these are neglible compared to the spread in the replay results. This highlights the inability of the damping derivatives to correct for flows at such high angles of attack.

(a) C_L

(b) C_D

(c) C_m
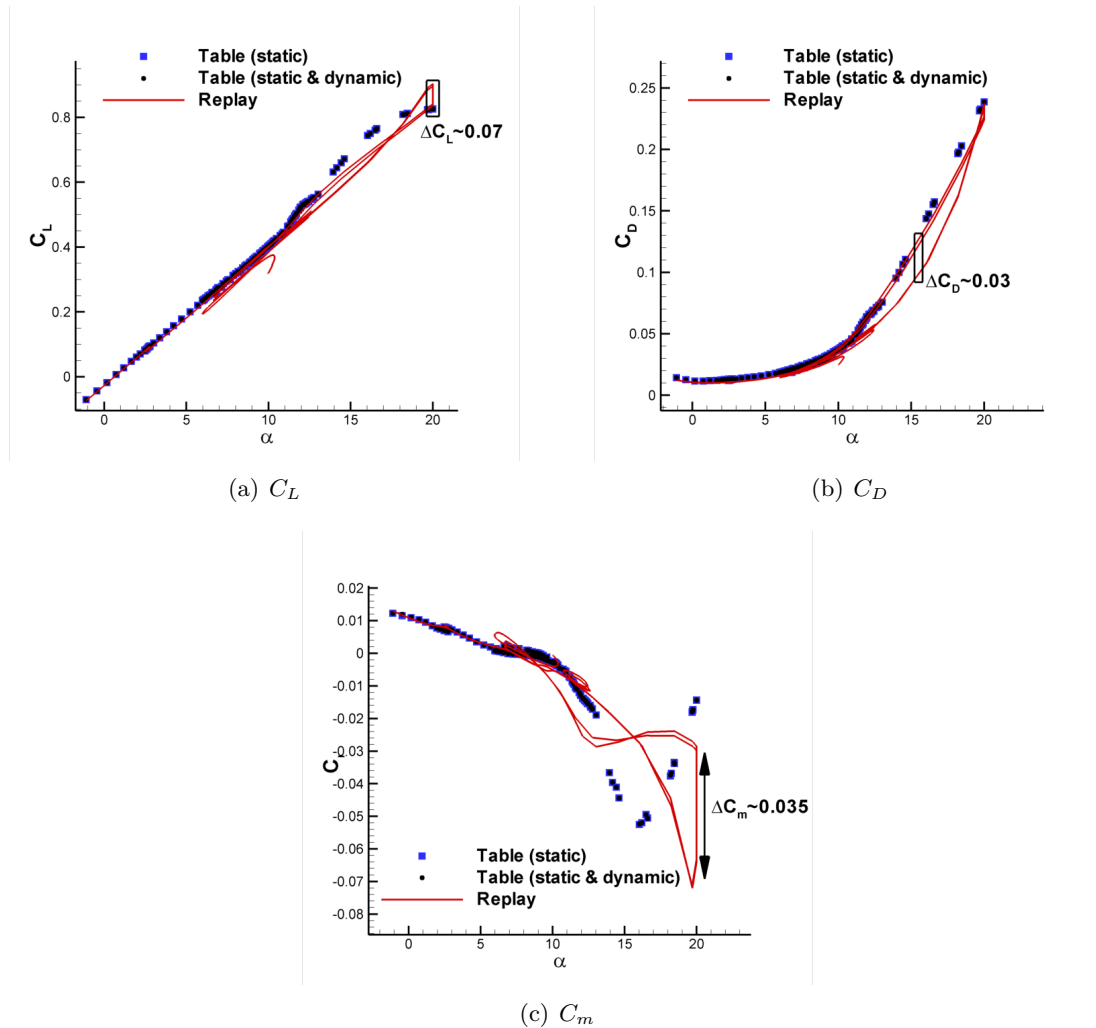
Figure 6.15: SACCON longitudinal forces and moments during a 90° turn against angle of attack.

6.5   Lazy Eight

A lazy eight manoeuvre was designed consisting of a 180° turn. This is performed by rolling and pitching the aircraft while gaining altitude and descending back to the starting height, as shown in Fig. 6.16.
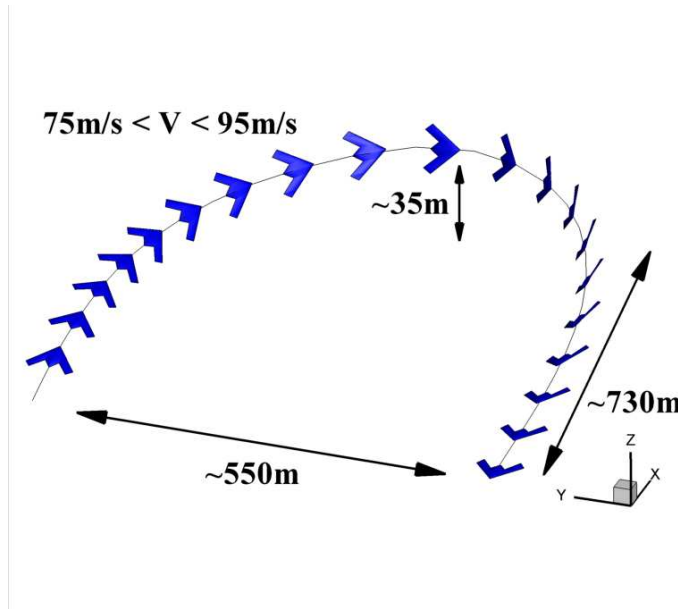
(a) Pull-up.

Figure 6.16: SACCON lazy eight trajectory.

Two lazy eight manoeuvres were simulated with different attitude rate constraints. First a slow manoeuvre was generated where the aircraft achieves the motion in 20 seconds with q reaching a maximum of $20°/s$. Then, a faster manoeuvre was obtained by allowing higher rates of change in attitude to be achieved, resulting in a reduction in the total time, in this case 15 seconds. Both of these manoeuvres are described in this section. Figure 6.17 shows the motion variables from both manoeuvres as they vary with time. The slow motion is denoted by the solid line while the fast one is shown with a dashed line. Similar trends can be seen in both of these except for the total time which yields the slightly more aggressive variations in the faster manoeuvre. Figure 6.17 (a) shows how the yaw angle changes from $0°$ to $180°$ while the roll angle reaches a maximum of $75°$ and $80°$ for the slow and fast manoeuvres respectively. The pitch angle oscillates between $20°$ and $0°$ in both cases. The most part of the manoeuvre is performed at an angle of attack of $12°$ at which vortex structures are known to develop. The sideslip angle remains approximately in the range between $-3°$ and $3°$, as shown in Fig. 6.17 (b). The rates of rotation are shown in Fig. 6.17 (c) with clear increases in all three components from the slow to the fast maneouvre. The slow version has a maximum q of $18°/s$ and p of $16°/s$ whereas the fast version reaches $25°/s$ and $23°/s$, respectively. The yaw rate, r, remains between $-5°/s$ and $10°/s$ for both cases. Figure 6.17 (d) shows the variation in the pitch angle of the thrust vector during the manoeuvre. Generally, the behaviour of this component is opposite to that of the angle of attack as it is used mainly to counteract the aerodynamic pitching moment at high

115

incidence angles.
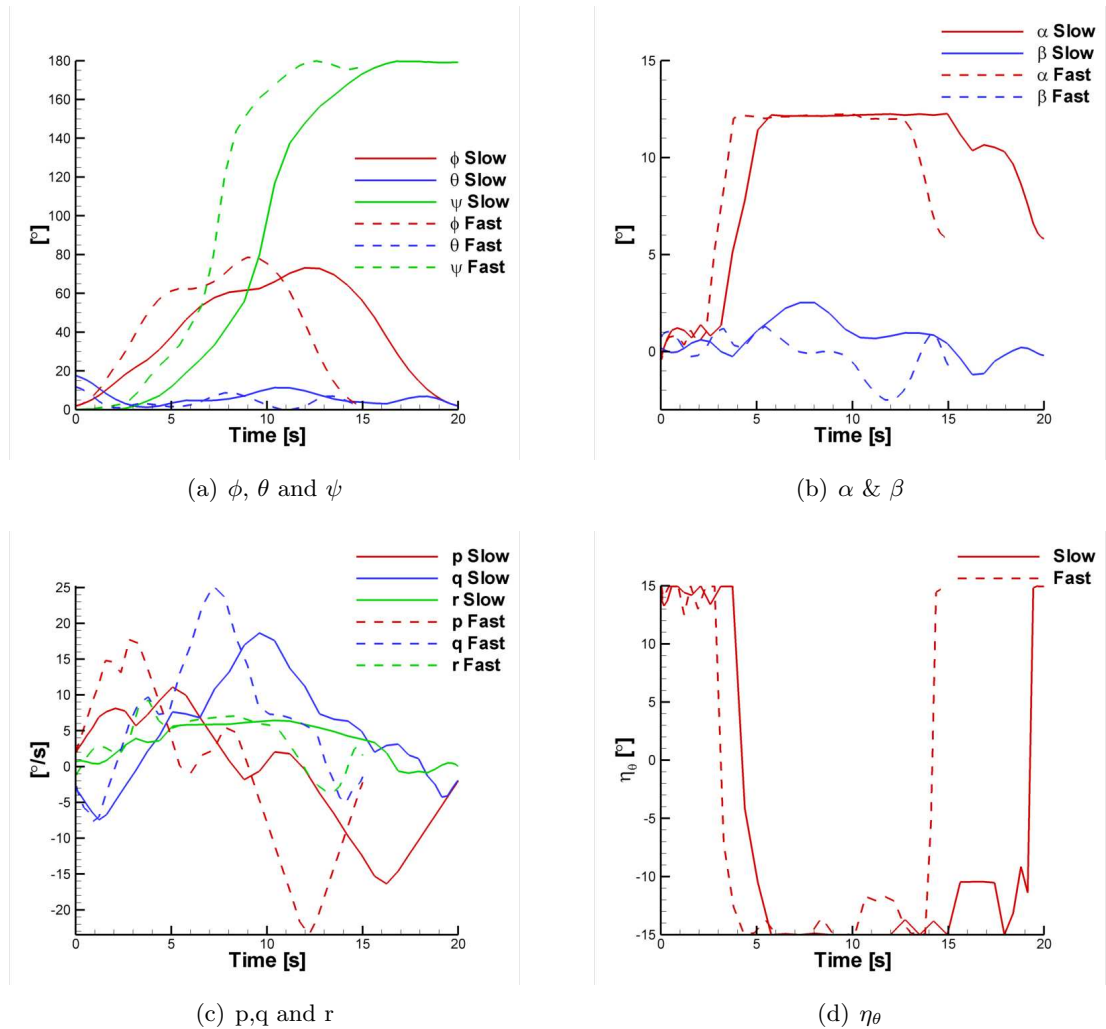
Figure 6.17: SACCON motion during both lazy eights.

Slow manoeuvre

Figure 6.18 shows the force and moment coefficients predicted using the tables, a CFD replay and three static steady state simulations at $12.9s$, $13.9s$ and $14.9s$. The C_L and C_D shown in Fig. 6.18 (a) and (b) display a good agreement up to 7 seconds into the manoeuvre, after which there is a decrease in both of these coefficients which is not captured by the tabular model. Similarly the roll, pitch and yaw moments in Fig. 6.18 (c), (e) and (f) show a similar trend. The steady state simulations agree well with the tabular results, with a difference of 0.008 and 0.003 in C_L and C_D, respectively. This corresponds to a 1.5% error in lift and 4.6% in drag coefficients arising from the table fusion. The largest difference between the tables and the replay in lift coefficient is approximately 0.122, resulting in 18.9% of the tabular prediction

at that point. For the drag this value is smaller, 0.016, although represents a larger percentage of the tabular prediction, 25.4%. The pitching moment coefficient displays similar discrepancies during the same periods of time. As was seen during less agressive manoeuvres, the lateral coefficients display a large disparity between tabular and replay predictions. As was noted in the 90° turn manoeuvre, the static steady state predictions agree well with the tables, which discards data fusion related errors. When the tables were generated, a certain level of confidence had been gained about the capability of the numerical models to predict aircraft longitudinal characteristics. With this in mind, lateral characteristics were also included in the tables to allow for more realistic manoeuvres to be predicted.

An identical analysis to the one carried out for the 90° turn is shown in Fig. 6.19. Here, the solutions from the static steady state calculations and the simulated replay are shown at 12.9s, 13.9s and 14.9s. It can be seen from the C_p distributions that a vortex is present which extends along the leading edge and detaches over the wing tip region, as expected from the results seen in Chapter 4. A barely noticeable asymmetry exists in all three cases due to the small sideslip angle, approximately 1°, present during this period. This becomes evident from the ΔC_p distribution. For all instances, a similar flow topology prediction is seen over the starboard wing. The port side, on the other hand, shows differences in the C_p distribution topology due to differences in the vortex trajectery. The unsteady replay solution predicts a vortex which remains closer to the leading edge. This difference in pressures between the two sides of the wing triggers the disparity between the lateral forces and moments.

One of the effects that is most relevant to this discussion is the loss of agreement in all force and moment coefficients starting at approximately 5.5s. From here up to 15s into the manoeuvre the incidence angle remains practically unchanged, 12.1° $< \alpha < 12.3°$, whereas the sideslip angle varies in the range of 0.5° $< \beta < 2.5°$. The ΔC_p distribution at different times over this time period was calculated as follows,

$$\Delta C_p = C_{p_{t_1}} - C_{p_{t_2}} \tag{6.11}$$

where t_1 and t_2 are selected time instants during the manoeuvre. Figure 6.20 shows the variation in angle of attack, red, and sideslip, blue, at the top of the figure and two ΔC_p distributions during the manoeuvre, 5.5$s - 10s$ and 10$s - 15s$ at the bottom. Here, a negative blue region means that there is an increase in pressure suction from t_1 to t_2, i.e. $-C_p$, and vice versa. In the first time period, shown at the bottom left corner of Fig. 6.20, the vortex over the port wing tip region moves toward the leading edge. On the starboard side the vortex at the tip moves inboards. Overall, the flow topology is changing towards a symmetric distribution as the sideslip angle becomes smaller. The image on the bottom right of Fig. 6.20 clearly shows an overall decrease in suction in the vortex region. This causes the disparity in the C_L, C_D and C_m between the tabular and replay results.

(a) C_L

(b) C_D

(c) C_m

(d) C_Y

(e) C_l

(f) C_n
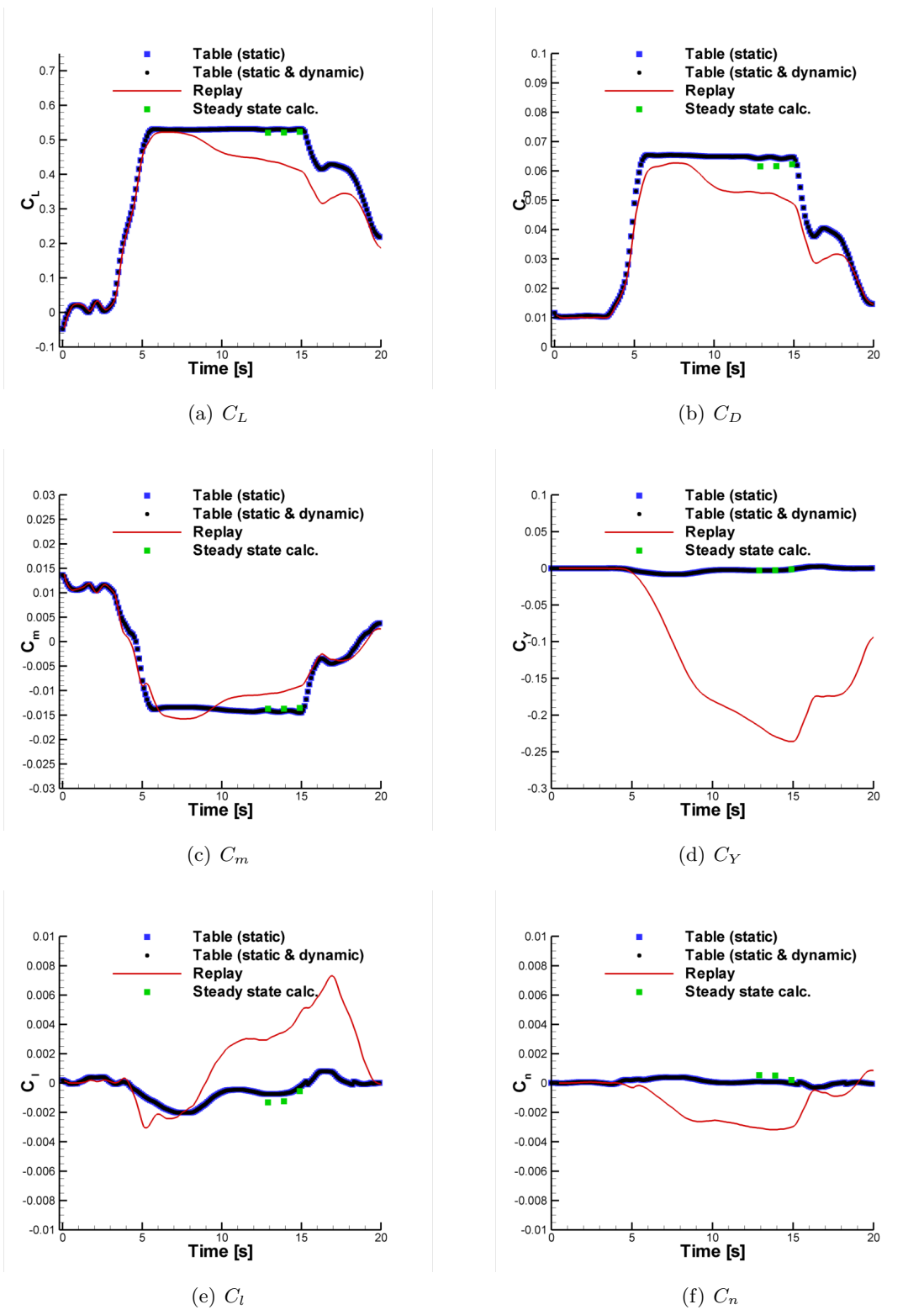
Figure 6.18: SACCON forces and moments during a slow lazy eight.

(a) Steady state at t=13s   (b) Replay at t=13s   (c) Difference at t=13s

(d) Steady state at t=14s   (e) Replay at t=14s   (f) Difference at t=14s

(g) Steady state at t=15s   (h) Replay at t=15s   (i) Difference at t=15s
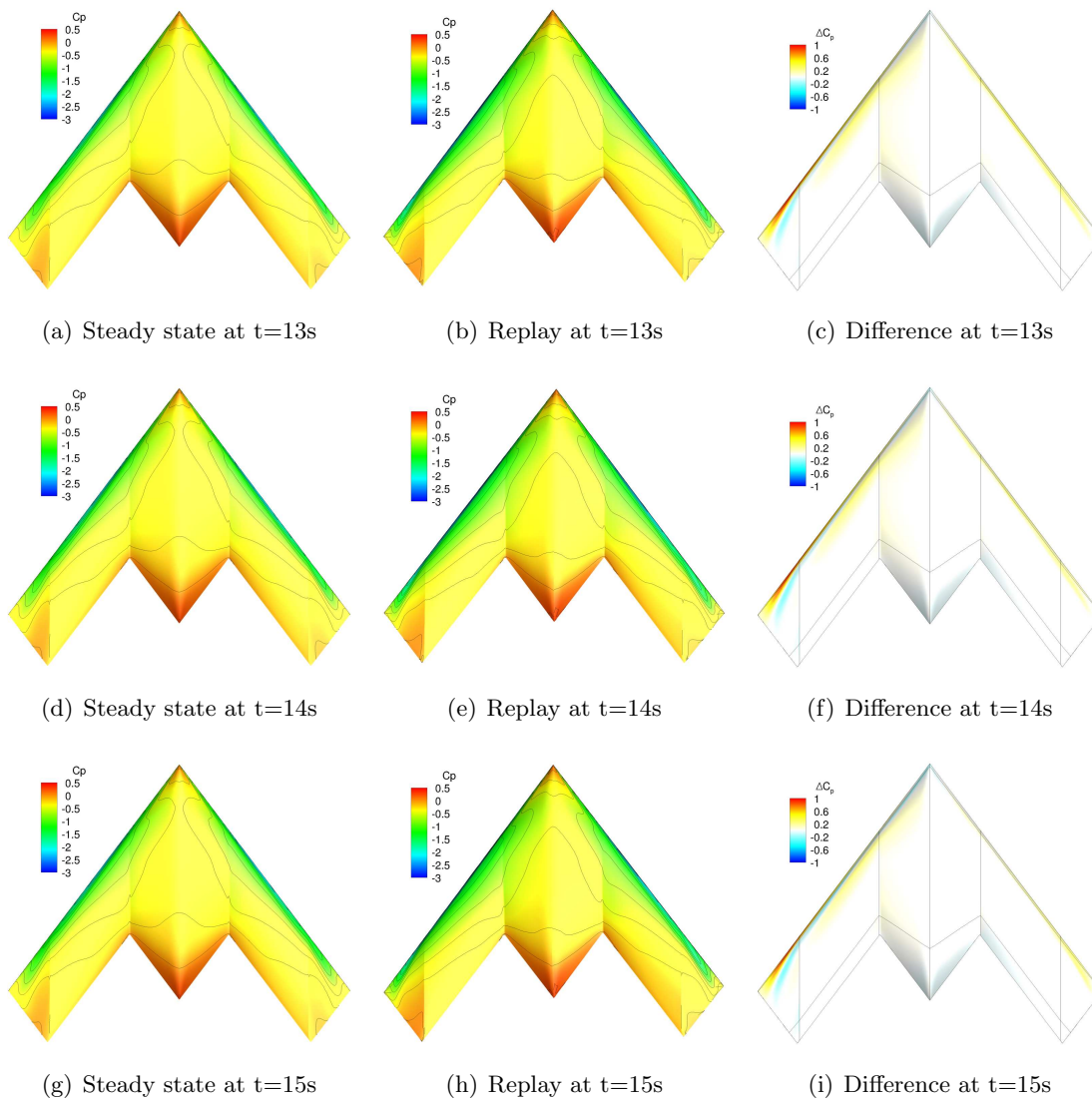
Figure 6.19: C_p and ΔC_p distributions at different times during the slow lazy eight.
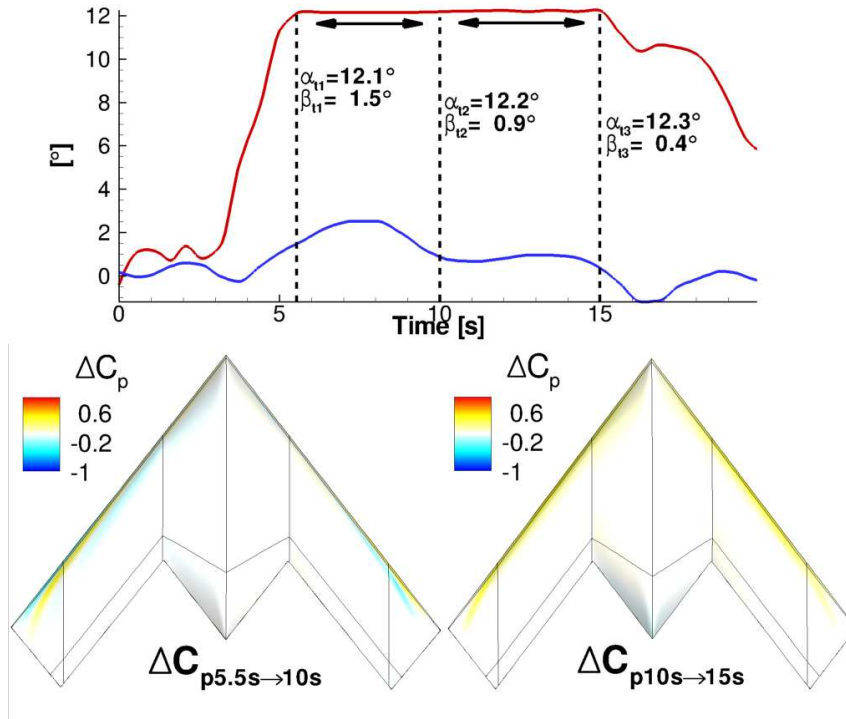
Figure 6.20: ΔC_p distributions over two periods during the slow lazy eight manoeuvre.

Looking at the spread in lift, drag and pitching moment coefficients it is obvious that less hysteresis is present in this manoeuvre compared to the $90°$ turn. This is due to the lower angles of attack reached during the manoeuvre as well as similar attitude rates. The maximum spread in C_L, C_D and C_m are 0.11, 0.014 and 0.007. This occurs from approximately $10°$ to $12°$ angle of attack, when the rate of change in angle of attack is highest, $\dot{\alpha} = 8°/s$.

Fast manoeuvre

The results obtained for the fast manoeuvre show a better agreement between the tables and the replay than the slow one. These are shown in Fig. 6.22. Also plotted on these graphs are the predictions using the tables incremented using dynamic derivatives and one steady state simulation at $t = 3.75s$ when the angle of attack is $12.0°$ and the sideslip angle is $0.4°$. The longitudinal characteristics show a good agreement between all sources, where the largest discrepancies between the replay and the tables represent 7.5%, 21.0% and 10.3% of the C_L, C_D and C_m, respectively. As seen throughout this study, the drag coefficient is the most challenging of logitudinal coefficients to predict using the tabular format. Similarly to the slower version of this manoeuvre, the lateral force component remains small and in agreement with the tabular predictions up to approximately 3 seconds from the start. Then the plot first reaches approximately

120

(a) C_L

(b) C_D

(c) C_m
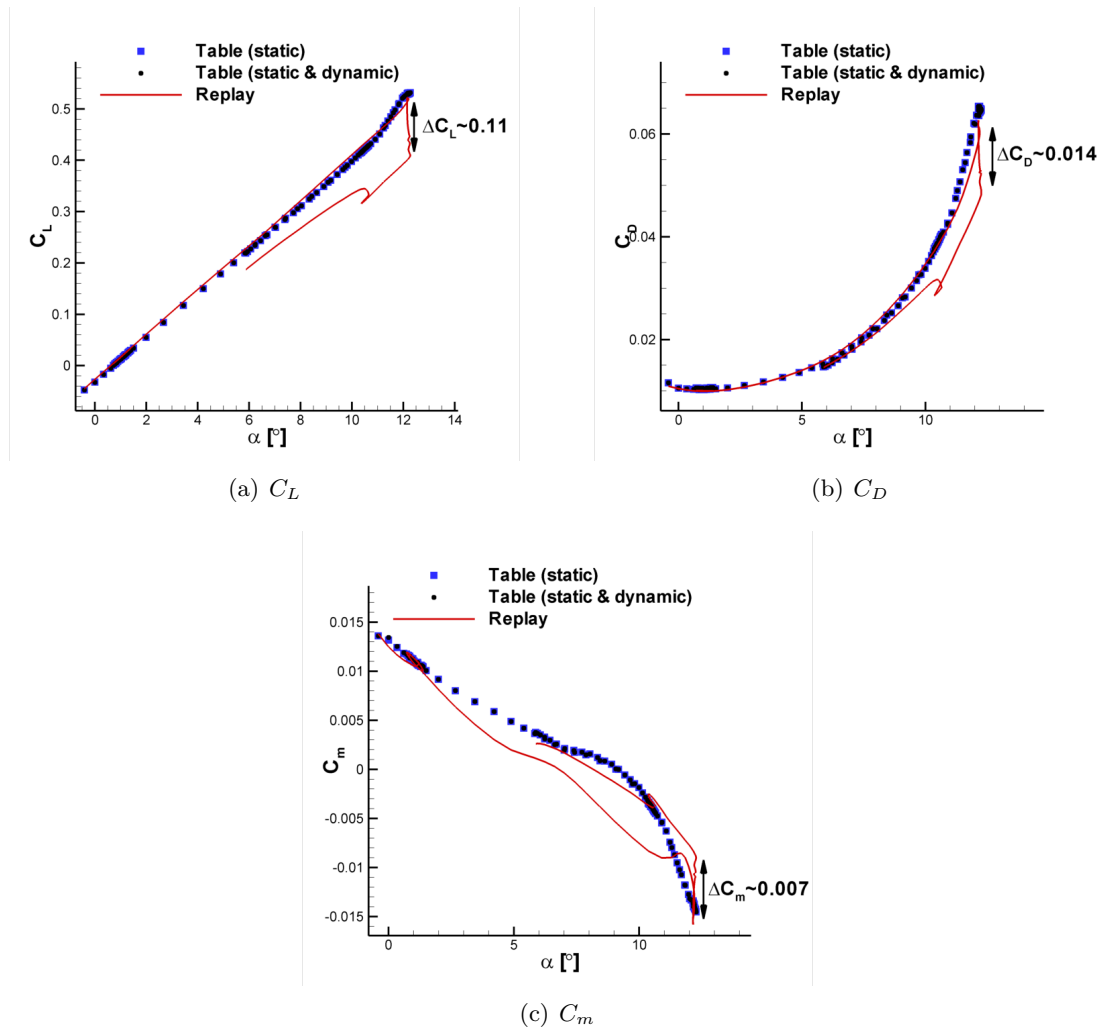
Figure 6.21: SACCON longitudinal forces and moments during a slow lazy eight against angle of attack.

−0.08. At $t = 10s$, C_Y starts to change again to reach 0.07. By inspecting Figs. 6.17 (a) and 6.22 (d), (e) and (f), a clear correlation between the sideslip angle and the lateral characteristics becomes evident. Both C_l and C_n remain very small within values of the order of 10^{-3}, and the agreement in these show a better performance from the tabular model.

The flow topology was analysed in the same manner as before. It can be seen from Fig. 6.23 that the C_p distribution at $t = 3.7s$ displays vortices extending along the leading edge, just before the vortex onset displacement occurs at $\alpha = 12.5°$. It is clear from these images that the apex vortex predicted at that moment in time during the replay has the characteristics of one which is at a lower angle of attack than the static steady state simulation. This is to be expected as the aircraft is in an upstroke motion from 0° to 12° angle of attack which induces a small decrease in incidence angle during the unsteady CFD simulation. Despite the predominantly positive yellow and red colouring in the vortex vicinity in Fig. 6.23 (c), the lift coefficient at this point is slightly higher for the steady state case. As described in Chapter 4, increasing the angle of attack yields an almost linear increase in the overall lift coefficient up to 18°.

The plots of C_L, C_D and C_m against angle of attack shown in Fig. 6.24 for the fast lazy eight manoeuvre show a smaller spread than the slower version of the manoeuvre. As seen from the dynamic derivative predictions from Section 5.3, the higher the frequency, and therefore the pitch and angle of attack time rates, the larger the hysteresis loops. In this case, the rates are slightly higher than those in the previous manoeuvre but the transient flow topology then has more time to settle producing a larger variation in the flow distribution. C_L has a maximum spread of 0.025, C_D of 0.004 and C_m of 0.005, which means a significant reduction in lift and drag coefficient discrepancy compared to the slower manoeuvre.

6.6 Summary

This chapter has looked at four different types of manoeuvres and benchmarked the aircraft load predictions from a look-up table method using time-accurate simulation predictions. The manoeuvres were designed to evaluate the performance of such methods in different regions of the flight envelope. The manoeuvres were presented starting from a simple three DoF motion at low angles of attack and low rates of angular rotation to 6 DoF manoeuvres at post stall angles of attack and high dynamic aerodynamic effects. Where possible, the differences between the time-accurate replay and the tabular predictions were quantified. The study focussed on the longitudinal characteristics and a summary of the tabular performance can be seen in Table 6.2. Here, each manoeuvre is specified on the left column along with the maximum angle of attack reached and pitch rate. The $\Delta_{max}C_j$ values correspond to the maximum discrepancy in C_j found throughout the manoeuvre between the tabular model and replay predictions. The

(a) C_L

(b) C_D

(c) C_m
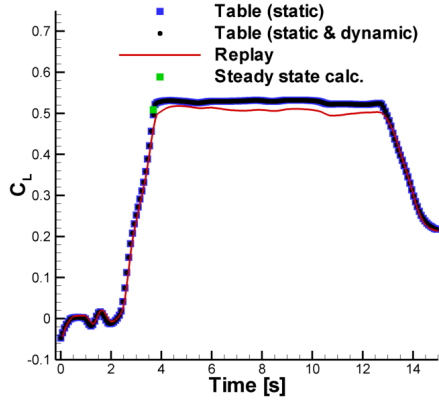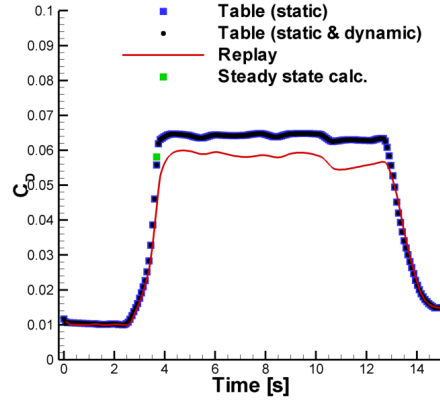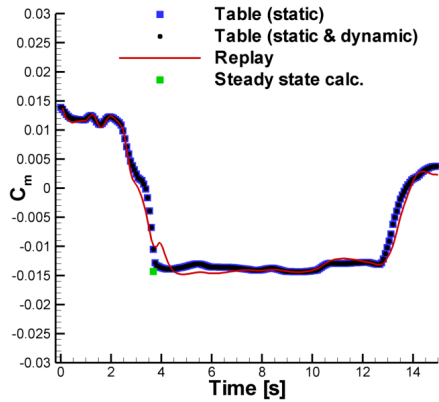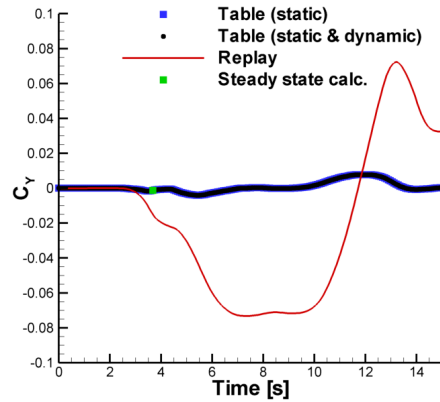
(d) C_Y
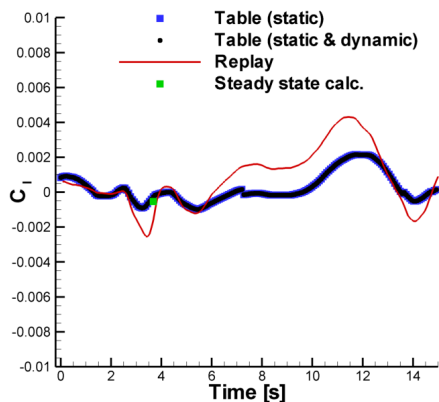
(e) C_l
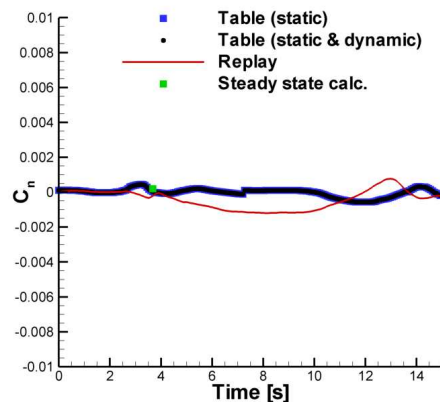
(f) C_n

Figure 6.22: SACCON forces and moments during a fast lazy eight.

(a) Steady state at t=3.7s   (b) Replay at t=3.7s   (c) Difference at t=3.7s
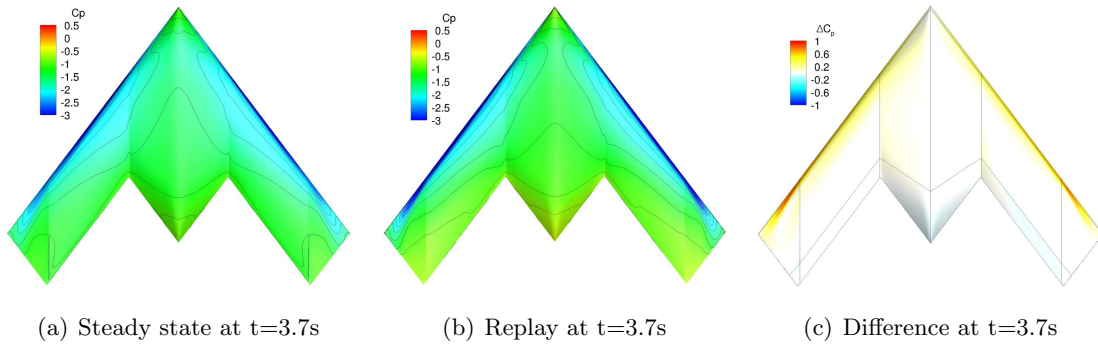
Figure 6.23: C_p and ΔC_p distributions at different times during the fast lazy eight.

(a) C_L

(b) C_D

(c) C_m
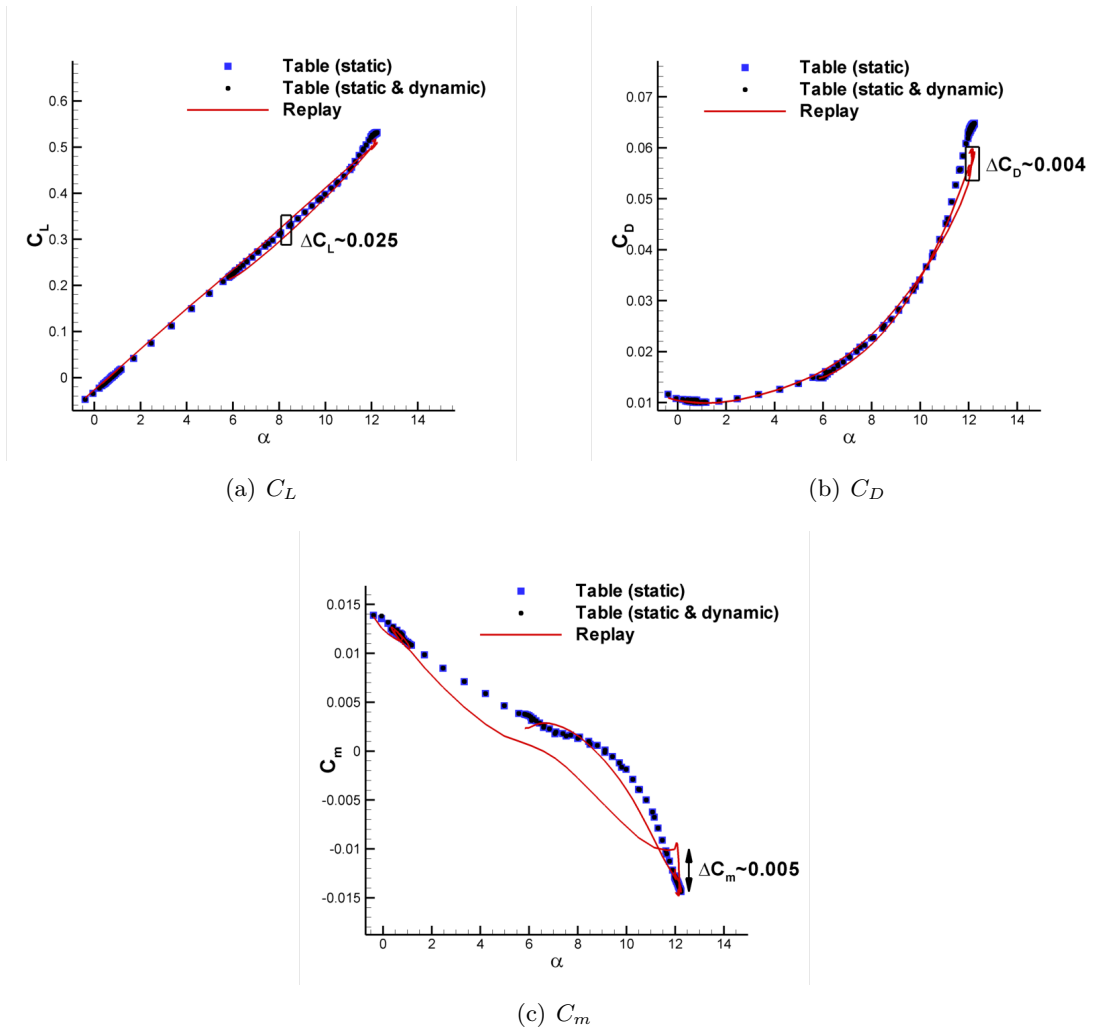
Figure 6.24: SACCON longitudinal forces and moments during a fast lazy eight against angle of attack.

values inside brackets represent the porcentages of each $\Delta_{max}C_j$ with respect to the value of C_j at 12.5° angle of attack. This is the angle at which linearity is broken and is used as a reference, where the normalising values are $C_L = 0.541$ and $C_D = 0.063$. For the pitching moment this has less meaning as the CG was different for the first two manoeuvres but the porcentages are shown nonetheless using $|C_{m_{0.4}}| = 0.183$ and $|C_{m_{0.55}}| = 0.015$. A set of ratings were awarded for the performance of the tables for each manoeuvre, namely good, adequate and poor. The first corresponded to a $\Delta_{max}C_j$ up to 10%, the second between 10% and 30% and the last to anything above 30%. These boundaries were set based on the performance observed during each of the manoeuvres and what was thought to be in need of improvement.

Table 6.2: Evaluation of manoeuvre longitudinal load predictions.

Manoeuvre	α_{max}	q	$\Delta_{max}C_L$	$\Delta_{max}C_D$	$\Delta_{max}C_m$	Model Performance
Pull-up	4°	$\pm 10°/s$	0.011 (2.0%)	0.002 (3.2%)	0.002 (1.1%)	Good
Immelmann Turn	9°	$\pm 10°/s$	0.018 (3.3%)	0.002 (3.2%)	0.016 (8.7%)	Good
90° Turn	20°	$\pm 20°/s$	0.078 (14.4%)	0.014 (22.2%)	0.054 (360%)	Poor
Lazy Eight (slow)	12°	$\pm 20°/s$	0.122 (22.6%)	0.016 (25.3%)	0.006 (40%)	Poor
Lazy Eight (fast)	12°	$\pm 25°/s$	0.037 (6.8%)	0.009 (14.3%)	0.004 (26.7%)	Adequate

Table 6.2 clearly shows how for the low angle of attack and rates of pitching moment below $\pm 10°/s$ the tables perform well. This gives confidence in the tabular model for predicting the aircraft loads during any manoeuvre performed within these boundaries. The force and moment coefficients were within 4% of the time-accurate solution whereas the moment was within 9%. The predictions of the manoeuvres performed up to angles of attack of 12° show poor and adequate performances. It would be expected that the faster version of the manoeuvre would yield worse predictions, but the truth is that these are considerably better. This might be due to transient effects having less time to settle and, hence, display a less non-linear behaviour. This is the same effect seen in the dynamic derivatives predictions, where the higher frequency oscillations showed more ellipse-like shapes. It is more likely that the sideslip angle sensitivity is causing these effects. As seen in Fig. 6.17 (b), the β behaviour is different for each lazy eight manoeuvre. As a matter of fact, the slow manoeuvre reaches higher angles of sideslip and for a longer period of time. This sideslip angle sensitivity may be the cause for such drops in longitudinal characteristic predictions performance. Furthermore, during the second half of the Immelman turn a high sideslip angle was achieved while the angle of attack remained low. It can be concluded that it is the medium to high angle of attack range with a given amount of sideslip which causes these discrepancies.

Discrepancies due to the data fusion process during the table generation were also assessed. The way to do so was to set steady state calculations to run at given points

during the manoeuvres. The predictions from these calculations were directly compared with the tables. The conclusion is that the tables were in good agreement with these calculations and that the data fusion was used efficiently. The discrepancies due to this remained within 5% of the reference value used for each aerodynamic characteristic.

The 90° manoeuvre, overall, saw the highest discrepancies, particularly in the pitching moment. When plotted against angle of attack, the large hysteresis loops were clearly seen. This showed a good example of a manoeuvre where hysteresis beyond stall angles of attack is causing the tabular models to breakdown. The dynamic derivatives where seen to be of little help in this region as the predicted q terms remained too small to trigger a large increment in C_m. Nonetheless, a better effort can be made using such increments based on aircraft dynamic predictions. In this study the most basic linear methods were implemented and used to populate a tabular model using a moderate amount of computational effort.

Significant discrepancies between the tabular and replay predictions have been seen in the lateral aerodynamic characteristics. In particular, C_Y demonstrates the greatest challenge for the tabular model. The rolling and yawing moment show a large sensitivity to sideslip angles during the replay simulations which were not seen from the tabular predictions or the steady state calculations at selected moments during the manoeuvres. The asymmetry in the flow was corroborated using C_p and ΔC_p distribution plots.

It is understood now that a good level of confidence in CFD prediction capability of the lateral static and dynamic behaviour is necessary to populate a full 6 DoF flight dynamics model. This may well be achieved following the same wind tunnel validation process carried out for the longitudinal characteristics. It could be argued that assessment could be improved using better benchmarking data. This could involve the use of CFD methods which include more physical theory, such as DES, wind tunnel experimentation using 6 DoF forced motion platforms or, ultimately, flight testing of a real aircraft. Since it does not seem like SACCON will be flying any time soon, further models based on real UCAV configurations could be implemented.

Chapter 7

Conclusions

A process by which CFD methods have been used ultimately to predict realistic manoeuvre trajectories and aircraft loads during the motion has been demonstrated and evaluated. The flow around the SACCON UCAV geometries has been computed and results validated against wind tunnel measurements. The model test case consisted of a 53° sweep delta wing with two different leading edge configurations, one that was sharp and another one which was partially round. It was found that this leading edge distribution was the main reason for highly non-linear flow topologies to occur at a range of angles of attack. The SLE model showed a vortex being generated at the apex and extending all along the leading edge. In the middle part of the wing, the geometry was thicker and the vortex became flatter with flow reattachment downstream. As the angle of attack was increased, the vortex began to peel from the leading edge starting from the tip. At an angle of attack of 13° the peeled vortex had travelled along the leading edge and a second structure of the same vorticity was noticed. This originated from a region close to the apex where the main vortex was split by the effect of the secondary vortex. This structure then changed rapidly as the angle was further increased with evidence of broken down flow moving upstream. Predictions on the RLE model displayed a different topology. In this case two distinct vortices coexisted over the SACCON top surface, one originating at the sharp apex and the other at the tip. These were first observed at angles of attack of 10°. The thick and round middle part of the wing allowed for the flow to remain attached up to angles of attack of 17° at which point the two vortices started to merge. Comparison with wind tunnel pressure tap measurements showed good agreement at low angles of attack and slight differences in vortex location at higher incidence angles, particularly for the RLE predictions. The SLE model yielded vortices which were easier to simulate because of the large adverse pressure gradients which were present at the sharp leading edge and fix the separation line along this edge. Rounded leading edges tend gradually to build up the adverse pressure gradient further downstream which eventually causes flow separation. Predicting the exact location of this separation line is numerically more challenging than

having it fixed, as in the SLE configuration. Hence, there was more confidence in the capability of the RANS models to predict the correct flow over the sharp configuration.

PIV measurements on the RLE model showed that a more complex vortical structure was present than that initially predicted by numerical methods, with small scale vortex structures noticed over the middle part of the wing. It also reinforced the idea that the cause for the disagreement in vortex locations is due to inadequate modelling of blunt leading edge separation. The inadequate flow separation prediction affects mainly the location of the vortices but not so much their strength for this particular case.

These two fundamentally different flow topologies yielded different body forces and moments which were compared against wind tunnel measurements. Breaks in linearity in lift were observed around 13° and 15° angle of attack for the SLE and RLE, respectively. The pitching moment showed a strong dip for both cases, with the RLE being sharper. This was due to sudden stall of the middle part of the wing, allowing the onset of the tip vortex structure to move upstream. The drag predictions showed very good agreement for both models. Sting mounting effects on the flow were found to be the cause for part of the disagreement in the integral data comparisons. Provided this, force predictions were in very good agreement with the measurements. As expected, the moments showed more sensitivity to both vortex flow behaviour and sting mounting effects.

Generally, steady state CFD prediction of the flow topology around the SLE model showed better agreement with the experimental measurements than those for the RLE. The main features in the forces and moments were well predicted and therefore, this configuration was chosen for the purpose of generating an aerodynamic tabular model for flight dynamics purposes. This was done in a manner which was efficient, in terms of computational costs, by reducing the size of the tabular model based on aerodynamic assumptions and a data interpolation technique. From a fully computed table to the final tabular model used a reduction from approximately 43 million processor hours to 32 thousand was achieved. These calculations were achieved in the UK HECToR supercomputers in a matter of weeks. Each CFD manoeuvre replay cost approximately 800 processor hours. In this study only six manoeuvres were calculated with a cost of approximately 5000 processor hours. This means that the most expensive process was the table generation. Although, considering the amount of manoeuvres that would need to be replayed during the design of an aircraft, it is the authors opinion that the cost of replaying these would greatly surpass that of the tables. Hence the importance of studying the validity of such prediction method. The cost of running optimal manoeuvres in DIDO was negligible considering the costs of the tables and replays.

The flight dynamics model consisted of aerodynamic tabular data merged using Kriging interpolation and a set of aircraft geometric approximations. These approxi-

mations were loosely based on the data available for a delta wing aircraft design, the YB-49. Two three-dimensional tables of aerodynamic data were generated. The first one acted as a baseline table consisting of the influence of angle of attack, Mach number and sideslip angle. The second acted as an increment to the aerodynamic characteristics due to control surface actuation. An optimisation software was used to predict realistic manoeuvre motions. The motions were used to test the capability of the tabular model for predicting aircraft loads within an extended flight envelope. These predictions were benchmarked against time-accurate RANS simulations with good agreement in the low dynamics and low angle of attack range. Higher rate of rotation and angles of attack showed important flow hysteresis effects taking place which the look-up tables were unable to predict. These effects were of particular importance in the pitching moment characteristics with spreads the in angle of attack domain twice as large as the static predictions in the case of the 90° turn manoeuvre. Dynamic derivatives were calculated in an attempt to correct for the deficiencies of the static tabular approach. These showed costly and inaccurate for angles of attack beyond stall. Furthermore, their effect on manoeuvre loads predictions were very small. Discrepancies due to data fusion during the table generation were proved very small demonstrating the validity of the method for this purpose.

Chapter 8

Future Work

It was discovered recently using DES simulations with sting mounting and wind tunnel walls that it was this combination which caused the discrepancies in the validation at low angles of attack. These calculations are costly in computational resources and manpower as new grids need to be generated for different flow angles. Nonetheless, an interesting future task would be to carry out at least one of these calculations at the conditions where the vortices are known to have some unsteadyness associated to it and evaluate the performance of the RANS methods in more detail. This would be a continuation from the PIV and RANS comparisons that were made in Chapter 4 where some disagreement in flow structure was observed.

When the tables were generated, a certain level of confidence had been gained about the capability of the numerical models to predict aircraft longitudinal characteristics. With this in mind, lateral characteristics were also included in the tables to allow for more realistic manoeuvres to be predicted. Validation of lateral characteristics was not carried out in this work although an extense amount of wind tunnel measurements is available. It would be interesting to evaluate the effect of the vortical structure behaviour on the lateral aerodynamic characteristics and damping derivatives. In particular at high angles of attack where important non-linearities in the longitudinal axes were seen to occur. This information could be used to update the tabular model and improve the loads predictions during the predicted manoeuvres.

As part of the follow-on RTO AVT work, several wind tunnel campaigns will look into the effect of control surface deflections using SACCON. This would be of great interest in order to make a detailed assessment of the adequacy of the mesh deformation scheme for such purposes. Further wind tunnel experiments will look at transonic flow effects using a rear-mounted, steel SACCON model. Initial results at high Mach numbers have shown flow topologies with little resemblance to those seen at low speeds.

On the flight dynamics aspect, future work will look at aircraft system identification using training manoeuvres and the already available data. It would be of great interest to evaluate the predictions from these methods and benchmarking them as it was done

for the tabular model. The estimation of the geometry characteristics could be replaced by actual aircraft parameters if a real test case became available in the future. This would avoid the need for CG position estimation. Although if this was not possible, a more in depth study of the effect of the CG on the aircraft dynamics could be made to avoid the need for its relocation for different manoeuvre simulations. An interesting study about aircraft motion prediction using SACCON is being carried out as part of a Garteur project, AG47. It would be interesting to compare free response predictions from the range of CFD groups involved with predictions from the tabular model presented in this work.

Ultimately the intention is to improve prediction methods for aircraft design purposes. With this in mind, what is of most interest is to know how accurate the models need to be for the purpose of aircraft design. A potential route would be to implement these CFD predicted models in a flight simulator using stability and control best practices to improve control law design. Flight dynamics assessments could be carried out for a range of models with identified levels of aerodynamic accuracy. This would give some idea about the importance of the accuracy of aerodynamic data.

Appendix A

Derivation and Implementation of the Equations of Motion

The non-linear equations of motion for a rigid symmetrical aircraft are used here to relate the state and control vectors. Here they are given in terms of the body fixed frame of reference,

$$m(\dot{U} - rV + qW) = X_a + X_c + X_g + X_p + X_d \tag{A.1}$$

$$m(\dot{V} - pW + rU) = Y_a + Y_c + Y_g + Y_p + Y_d \tag{A.2}$$

$$m(\dot{W} - qU + pV) = Z_a + Z_c + Z_g + Z_p + Z_d \tag{A.3}$$

$$I_x\dot{p} - (I_y - I_z)qr - I_{xz}(pq + \dot{r}) = L_a + L_c + L_g + L_p + L_d \tag{A.4}$$

$$I_y\dot{q} + (I_x - I_z)pr + I_{xz}(p^2 - r^2) = M_a + M_c + M_g + M_p + M_d \tag{A.5}$$

$$I_z\dot{r} - (I_x - I_y)pq + I_{xz}(qr - \dot{p}) = N_a + N_c + N_g + N_p + N_d \tag{A.6}$$

where X, Y and Z represent the forces in the forward, lateral and downward directions, respectively, and L, M and N the rolling, pitching and yawing moments, respectively. These equations represent the six DoF motion of the aircraft model from which the dynamic equations for the state $\{\mathbf{x}\}$ can be derived. But first, we focus on the right hand side of the equations stating the different forces and moments affecting the motion of the aircraft. These are divided into five terms, namely aerodynamic, a, gravitational, g, due to control devices, c, power, p and disturbance or athmospheric, g, such as gusts.

The non-linear equations of motion are layed out as described in [88, 91] for a rigid symmetric aircraft. The current form of the equations is very similar to the first derivation carried out by Bryan in 1911. We start with Newton's second law,

$$Force \quad = \quad \frac{d}{dt}(m\mathbf{v}) \tag{A.7}$$

Using a Cartesian frame of reference, with the origin located at the aircraft center of gravity, for the forces in the x, y and z directions we can rewrite this equation as

$$X = m(\dot{U} - rV + qW) \tag{A.8}$$

$$Y = m(\dot{V} - pW + rU) \tag{A.9}$$

$$Z = m(\dot{W} - qU + pV) \tag{A.10}$$

where the acceleration is made up by a linear and two rotary components. By realising the rotational form of Newton's second law of motion, we can write the generalised moment equations as

$$I_x\dot{p} - (I_y - I_z)qr + I_{xy}(pr - \dot{q}) - I_{xz}(pq + \dot{r}) + I_{yz}(r^2 - q^2) = L \tag{A.11}$$

$$I_y\dot{q} + (I_x - I_z)pr + I_{yz}(pq - \dot{r}) + I_{xz}(p^2 - r^2) - I_{xy}(qr + \dot{p}) = M \tag{A.12}$$

$$I_z\dot{r} - (I_x - I_y)pq - I_{yz}(pr + \dot{q}) + I_{xz}(qr - \dot{p}) - I_{xy}(q^2 - p^2) = N \tag{A.13}$$

These equations represent the motion of a generalised rigid body about the orthogonal axis through the c.g. For an aircraft, it may be assumed that the body is symmetric about the longitudinal plane Oxz and the mass is uniformly distributed. As a result $I_{xy} = I_{yz} = 0$ and equations A.11, A.12 and A.13 may be simplified as

$$I_x\dot{p} - (I_y - I_z)qr - I_{xz}(pq + \dot{r}) = L \tag{A.14}$$

$$I_y\dot{q} + (I_x - I_z)pr + I_{xz}(p^2 - r^2) = M \tag{A.15}$$

$$I_z\dot{r} - (I_x - I_y)pq + I_{xz}(qr - \dot{p}) = N \tag{A.16}$$

Due to the symmetry the Ixy term is much smaller than I_x, I_y and I_z.

The information is stored in wind axes whereas the equations are written in terms of body axis moments. The following transformation from wind to body axes is used [88, 91],

$$\left\{ \begin{array}{c} \phi \\ \theta \\ \psi \end{array} \right\} = \left[\begin{array}{ccc} cos(\alpha)cos(\beta) & -cos(\alpha)sin(\beta) & -sin(\alpha) \\ sin(\beta) & cos(\beta) & 0 \\ sin(\alpha)cos(\beta) & -sin(\alpha)sin(\beta) & cos(\alpha) \end{array} \right] \left\{ \begin{array}{c} \alpha \\ \beta \\ 0 \end{array} \right\} \tag{A.17}$$

Similarly, the velocity is converted from wind axes to the three components of body axis velocity,

$$\left\{ \begin{array}{c} U_b \\ V_b \\ W_b \end{array} \right\} = \left[\begin{array}{ccc} cos(\alpha)cos(\beta) & -cos(\alpha)sin(\beta) & -sin(\alpha) \\ sin(\beta) & cos(\beta) & 0 \\ sin(\alpha)cos(\beta) & -sin(\alpha)sin(\beta) & cos(\alpha) \end{array} \right] \left\{ \begin{array}{c} V_0 \\ 0 \\ 0 \end{array} \right\} \tag{A.18}$$

Since we are interested in the velocity with respect to the earth frame of reference, a further transformation of these velocities is required,

$$\mathbf{D} = \left[\begin{array}{ccc} cos(\psi)\,cos(\theta) & \begin{array}{c} cos(\psi)\,sin(\theta)\,sin(\phi) \\ -sin(\psi)\,cos(\theta) \end{array} & \begin{array}{c} cos(\psi)\,sin(\theta)\,cos(\phi) \\ +sin(\psi)\,cos(\theta) \end{array} \\ \\ sin(\psi)cos(\theta) & \begin{array}{c} sin(\psi)sin(\theta)sin(\phi) \\ +cos(\psi)cos(\theta) \end{array} & \begin{array}{c} sin(\psi)sin(\theta)cos(\phi) \\ -cos(\psi)sin(\phi) \end{array} \\ \\ -sin(\theta) & cos(\theta)sin(\phi) & cos(\theta)cos(\phi) \end{array} \right] \tag{A.19}$$

$$\left\{\begin{array}{c} \dot{x} \\ \dot{y} \\ \dot{z} \end{array}\right\} = \left\{\begin{array}{c} U_e \\ V_e \\ W_e \end{array}\right\} = \mathbf{D}\left\{\begin{array}{c} U_b \\ V_b \\ W_b \end{array}\right\} \tag{A.20}$$

Equation A.20 is the dynamic equation of $\dot{x}$, $\dot{y}$ and $\dot{z}$ as stated in the problem formulation. From equation A.1 we can rearrange to solve for the acceleration along the x-axis in the wind reference frame resulting in

$$(\dot{V}_0 - rV + qW) = \frac{X_a^w + X_c^w + X_g^w + X_p^w}{m} \tag{A.21}$$

$$\dot{V}_0 = \frac{\bar{q}SC_D}{m} + \frac{T\eta cos(\alpha + \eta_\theta)cos(\beta + \eta_\psi)}{m} + \\ g(cos\phi cos\theta sin\alpha cos\beta + sin\phi cos\theta sin\beta - sin\theta cos\alpha cos\beta) \tag{A.22}$$

where

$$\bar{q} = \frac{\rho V_0^2}{2} \tag{A.23}$$

The change in angle of attack and sideslip are defined as follows,

$$\dot{\alpha} = -\frac{\bar{q}SC_L}{mV cos\beta} + q - tan\beta(pcos\alpha + rsin\alpha) \\ + \frac{g}{V(cos\beta cos\phi cos\theta cos\alpha + sin\theta sin\alpha)} - \frac{T\eta sin(\alpha + \delta_{pitch})cos\eta_\psi}{mV cos\beta} \tag{A.24}$$

$$\dot{\beta} = -\frac{\bar{q}SC_Y}{mV} + psin\alpha - rcos\alpha + \frac{g}{V(cos\alpha sin\beta sin\theta + cos\beta sin\phi cos\theta - sin\alpha sin\beta cos\phi cos\theta} \\ - \frac{T\eta cos(\alpha + \eta_\theta)sin\beta + \eta_\psi mV}{mV_0} \tag{A.25}$$

For the derivation of the roll rate derivative we start from equation A.4.

$$I_x\dot{p} - (I_y - I_z)qr - I_{xz}(pq + \dot{r}) = L_a + L_c + L_g + L_p + L_d \tag{A.26}$$

$$\dot{p} = -\frac{1}{\tau}\left(I_{xz}(I_{xx} - I_{yy} + I_{zz})pq - (I_{zz}(I_{zz} - I_{yy}) + I_{xz}^2)qr + I_{zz}\bar{q}SbC_l \\ + I_{xz}\left(\bar{q}SbC_n + T\eta sin\eta_\psi cos\eta_\theta(1.068 - l_{thrust})\frac{13}{0.769}\right)\right) \tag{A.27}$$

Similarly, the pitching moment coefficient is derived by rearranging equation A.5 as follows,

$$\dot{q} = \frac{1}{I_y}\left((I_x - I_z)pr - I_{xz}(p^2 - r^2) + M_a + M_c + M_g + M_p + M_d\right) \tag{A.28}$$

where

$$M_{a,c} = \bar{q}ScC_m \tag{A.29}$$

$$M_p = T\eta sin(\eta_\theta)cos(\eta_\psi)l_{thrust} \tag{A.30}$$

$$M_g = 0 \tag{A.31}$$

Substituting equations A.29, A.30 and A.31 into A.28 the following expression for $\dot{q}$ is obtained,

$$\dot{q} = -\frac{1}{I_{yy}}\left((I_{zz} - I_{xx})pr - I_{xz}p^2r^2 + \bar{q}ScC_m - T\eta cos\eta_\psi sin\eta_\theta(1.068 - l_{thrust})\frac{13}{0.769}\right) \tag{A.32}$$

For the yaw rate derivative the following is done,

$$\dot{r} = \frac{1}{I_z}\left((I_x - I_y)pq - I_{xz}(qr - \dot{p}) + N_a + N_c + N_g + N_p + N_d\right) \tag{A.33}$$

$$\dot{r} = -\frac{1}{\tau}\left(\left((I_{xx} - I_{yy})I_{xx} + I_{xz}^2\right)pq - I_{xz}(I_{xx} - I_{yy} + I_{zz})qr - I_{xz}\bar{q}SbC_l\right.$$
$$\left.I_{xx}(\bar{q}SbC_n + T\eta sin\delta_{yaw}cos\delta_{pitch}(1.068 - 0.4)\frac{13}{0.769})\right) \tag{A.34}$$

Finally the rotational velocities are stated as follows,

$$\dot{\phi} = p + qsin(\phi)tan(\theta) + rcos(\phi)tan(\theta) \tag{A.35}$$

$$\dot{\theta} = qcos(\phi) + rsin(\phi) \tag{A.36}$$

$$\dot{\psi} = \frac{qsin(\phi) + rcos(\phi)}{cos(\theta)} \tag{A.37}$$

Appendix B

Replay of Manoeuvres using PMB

The manner in which the calculations are performed for steady state and replay simulations are described in this section. The steady state computations used throughout this thesis for the purpose of validation, generating the tabular aerodynamic model and obtaining steady state solutions at given points during a manoeuvre are described first. Figure B.1 shows the SACCON geometry generated from the grid file. For the steady state case the body axes, x_b, y_b and z_b, remain aligned with the global axes shown in the background. Instead, the inflow velocity vector is rotated accordinlgy. A converged solution is obtained within 5000 implicit iterations and the wind and body axes aerodynamic characteristics are determined.
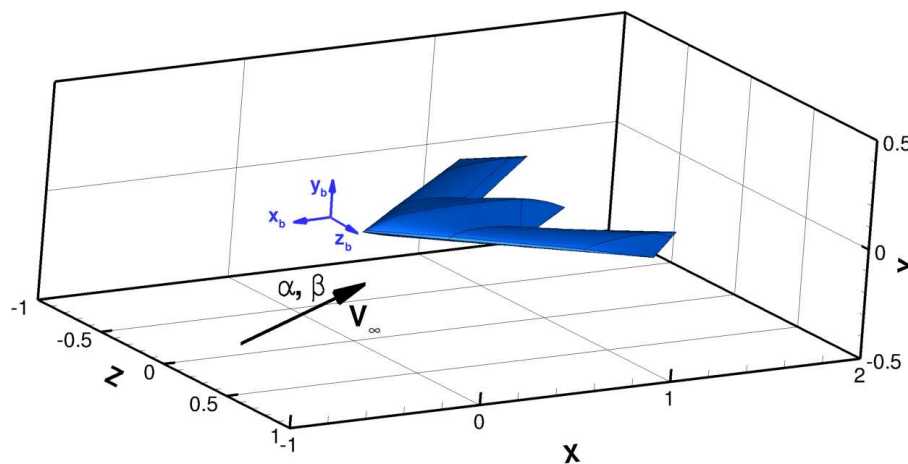
(a) Steady state setup.

Figure B.1: Definition of the conditions for steady state computations using PMB.

To replay the manoeuvres through the time-accurate PMB a motion needs to be forced on the grid. To do this, an input file needs to be defined specifying the nondimensional time and state variables at each timestep. The initial timestep, denoted as

t_0, is used to converge a steady state simulation. After this, the motion begins by rotating and displacing the grid at each timestep and converging the solution using pseudo-timestepping. The replay finishes when the last timestep is completed. Figure B.2 shows three timesteps during a manoeuvre replay, at t_0, t_1 and t_2. Figure B.2 (a) shows the conditions at t_0. Here the inflow velocity is kept aligned with the global x-axis and the grid is rotated by the angles α_0 and β_0. At this timestep the time rates of translation or rotation are zero and a steady state calculation is performed. At t_1 in Fig. B.2 (b), the angles of attack and sideslip have changed to α_1 and β_1 and the time rates of rotation, $\dot{\alpha}$ and $\dot{\beta}$ are specified. A translation in the global x-axis, Δx_1, calculated based on the wind velocity, is also specified along with changes to the freestream velocity V. Similarly, at t_2 in Fig. B.2 (c) the discplacement and velocity have reversed direction, in this case a the velocity has increased. Notice that a forward displacement corresponds to a negative change in x as the positive axis points in the wind direction. Hence, negative changes in velocity require positive displacements in the input file.

The information used to generate the input file is obtained from the state vector predicted by the manoeuvre simulation code. The freestream velocity and wind angles are extracted, V_∞, α and β. Here it is shown again for clarity,

$$\mathbf{x}(\cdot) = \left\{\begin{array}{cccccccccccc} x & y & z & V_\infty & \alpha & \beta & p & q & r & \phi & \theta & \psi \end{array}\right\} \tag{B.1}$$

The input file for PMB is composed of the nondimensional time and the three cartesian axes rotations and translations and their time derivatives as shown,

$$\left\{\begin{array}{cccccccccccc} \hat{t}_i & \phi_i & \theta_i & \psi_i & x_i & y_i & z_i & \dot{\phi}_i & \dot{\theta}_i & \dot{\psi}_i & \dot{x}_i & \dot{y}_i & \dot{z}_i \end{array}\right\} \tag{B.2}$$

where the subscript i denotes input file variables. The input file variables are used to rotate and displace the grid as appropriate throughout the time domain. The time history of the two angles is then used to determine their time derivatives. The following function is used for $\dot{\alpha}$,

$$\dot{\alpha} = \frac{\alpha_n - \alpha_{n-1}}{t_n - t_{n-1}} \tag{B.3}$$

This is done similarly for $\dot{\beta}$. Changes in the aircraft velocity vector are inputted as increments from the initial value. The freestream velocity information is also used to determine the displacement in the x-axis, $\dot{x}$, using the following function,

$$\dot{x} = (t_n - t_{n-1})\frac{V_{\infty_n} + V_{\infty_{n-1}}}{2} \tag{B.4}$$
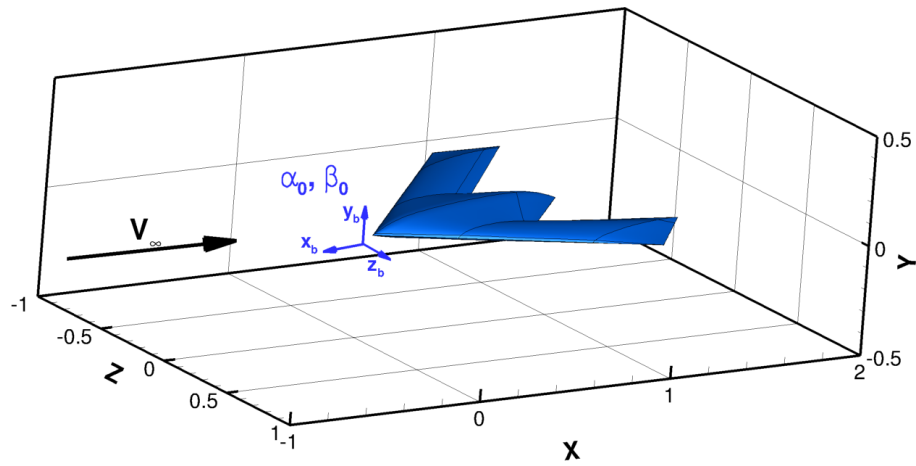
(a) Step 0, steady state solution.
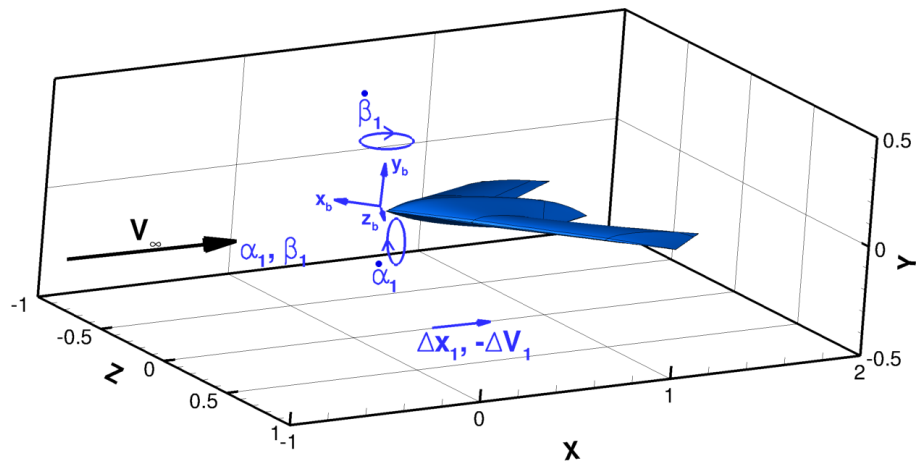
(b) Step 1.
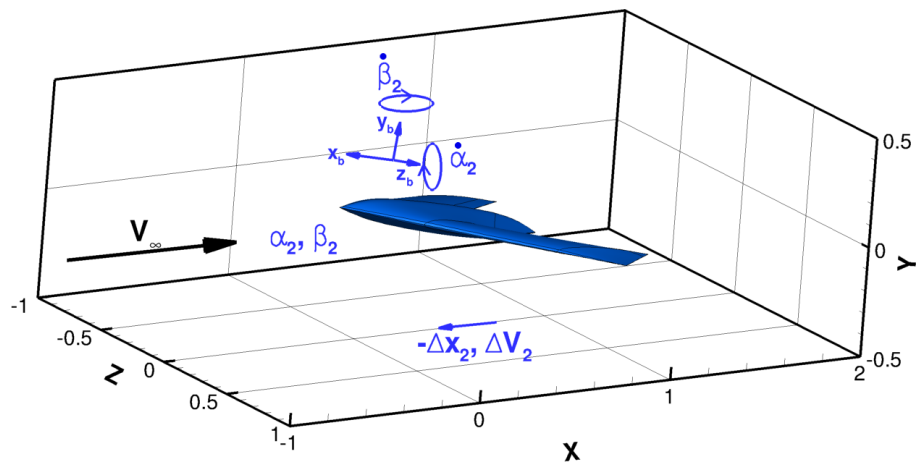
(c) Step 2.

Figure B.2: Step by step definition of the manoeuvre time-accurate PMB replay.

Bibliography

[1] Johnson FT, Edward NT and Jong Yu N. Thirty years of development and application of CFD at Boeing Commercial Airplanes, Seattle. *Computers & Fluids*, 34:1115-1151, 2005. DOI:10.1016/J.COMPFLUID.2004.06.005

[2] Statistical Summary of Commercial Jet Airplanes Summary, Worldwide Operations 1959 - 2010. Aviation Safety, Boeing Commercial Airplanes, June 2011. P.O. Box 3707 M/C 07-32, Seattle, Washington 98124-2207, U.S.A. http://www.boeing.com/news/techissues/pdf/statsum.pdf

[3] CAT Magazine, *The Journal for Civil Aviation Training*, 2:24-27, 2011. ISSN 0960-9024.

[4] Armada Compendium Drones, *Armada International*, 2-10, 2011. http://www.armada.ch/php/compendium.php.

[5] Gursul I, Gordnier R and Visbal M. Unsteady Aerodynamics of Nonslender Delta Wings. *Progress in Aerospace Sciences*, 41:515-557, 2005. doi:10.1016.

[6] Anderson JD. Fundamentals of Aerodynamics. *McGraw-Hill International 2nd Edition*, 1991.

[7] L. Schiavetta, Evaluation of URANS and DES Predictions of Vortical Flows over Slender Delta Wings, PhD theses submitted at the University of Glasgow, 2007.

[8] Yaniktepe B and Rockwell D. Flow Structure on a Delta Wing of Low Sweep Angle. *AIAA Journal*, 42(3):513-523, 2004.

[9] Taylor GS and Gursul I. Buffeting Flows over a Low-Sweep Delta Wing. *AIAA Journal*, 42(9):1737-1745, September 2004.

[10] Ol MV and Gharib M. Leading-Edge Vortex Structure of Nonslender Delta wings at Low Reynolds Number, *AIAA Journal*, 41(1):16-26, January 2003.

[11] Woods M. I., An Investigation of Buffet Over Low-Observable Planforms, PhD Thesis, University of Bath, 1999.

[12] Gursul I, Vortex flows on UAVs: Issues and Challenges, *The Aeronautical Journal*, Paper 2877, 597-610, December 2004.

[13] Gad-el-Hak M. and Blackwelder R. F., The Discrete Vortices from a Delta Wing. Technical Note, AIAA Journal, 23(6):961-2, 1985.

[14] Miau JJ, Kuo KT, Liu WH, Hsieh SJ and Chou JH. Flow Developments Above 50-Deg Sweep Delta Wings with Different Leading-Edge Profiles. *Journal of Aircraft*, 32(4):787-794, July-August 1995.

[15] Gordnier RE, Visbal MR, Gursul I and Wang Z. Computational and Experimental Investigation of a Nonslender Delta Wing. *AIAA Journal*, 47(8):1811-1825, August 2009.

[16] Bergmann A, Huebner A and Loeser T. Experimental and numerical research on the aerodynamics of unsteady moving aircraft. *Progress in Aerospace Sciences*, 44:121-137, 2008.

[17] Rein M, Gebhard H, Schutte A, Bergmann A and Loser T. Ground-Based Simulation of Complex Maneuvers of a Delta-Wing Aircraft. *Journal of Aircraft*, 45(1):286-291, 2008.

[18] Ericsson LE, Beyers ME. Wind-Tunnel Aerodynamics in Rotary Tests of Combat Aircraft Models. *Journal of Aircraft*, 35(4):521-528, 1998.

[19] Knight D, Longo J, Drikakis D, Gaitonde D, Lani A, Nompelis I, Reimann B and Walpot, Assessment of CFD capability for prediction of hypersonic shock interactions, *Progress in Aerospace Sciences*, 4849:826, 2012.

[20] Schiavetta LA, Boelens OJ, Crippa S, Cummings RM, Fritz W and Badcock KJ. Shock Effects on Delta Wing Vortex Breakdown. *Journal of Aircraft*, 46(3):903-914, 2009.

[21] Lawson SJ and Barakos GN. Evaluation of DES for weapons bays in UCAVs. *Aerospace Science and Technology*, 14:397-414, 2010.

[22] Boelens O, Badcock KJ, Elmilgui A, Abdol-Hamid KS and Massey SJ. Comparison of Measured and Block Structured Simulation Results for the F-16XL Aircraft. *Journal of Aircraft*, 46(2):377-384, 2009.

[23] Antoniadis AF, Drikakis D, Zhong B, Barakos G, Steijl R, Biava M, Vigevano L, Brocklehurst A, Boelens O, Dietz M, Embacher M and Khier W. Assessment of CFD methods against experimental flow measurements for helicopter flows. *Aerospace Science and Technology*, 10.1016/j.ast.2011.09.003.

[24] Marques S, Badcock KJ, Gooden JHM, Gates S and Maybury W. Validation study for prediction of iced aerofoil aerodynamics. *Aeronautical Journal*, 114(1152):103-111, 2010.

[25] Kruger WR. A multi-body approach for modelling manoeuvring aeroelastic aircraft during preliminary design. *Proceedings of the Institution of Mechanical Engineers, Part G: Journal of Aerospace Engineering*, 222(6):887-894, 2008. DOI:10.1243/09544100JAERO264

[26] Costello M and Sahu J. Using computational fluid dynamic/rigid body dynamic results to generate aerodynamic models for projectile flight simulation. *Proceedings of the Institution of Mechanical Engineers, Part G: Journal of Aerospace Engineering*, 222(7):1067-1079, 2008. DOI:10.1243/09544100JAERO304

[27] Koyuncu E, Ure NK and Inalhan G. Integration of Path/Maneuver Planning in Complex Environments for Agile Maneuvering UCAVs. *Journal Intell & Robotic Systems*, 57(1-4):143-170, 2010. DOI: 10.1007/s10846-009-9367-1.

[28] Basset G, Xu Y and Yakimenko OA. Computing Short-Time Aircraft Maneuvers Using Direct Methods. *Journal of Computer and Systems Sciences International*, 49(3):481-513, 2010. DOI: 10.1134/S1064230710030159.

[29] Benson DA, Huntington GT, Thorvaldsen, et al. Direct Trajectory Optimisation and Costate Estimation via An Orthogonal Collocation Method. *Journal of Guidance, Control and Dynamics*, 29(6):1435-1440, 2006.

[30] Fahroo F and Ross IM. Costate Estimation by a Legendre Pseudospectral Method. *Journal of Guidance, Control and Dynamics*, 27(3):270-277, 2001.

[31] Fahroo F and Ross IM. Direct Trajectory Optimization by Chebyshev Pseudospectral Method. *Journal of Guidance, Control and Dynamics*, 25(1):160-166, 2002.

[32] Ross IM and Fahroo F. Pseudospectral Knotting Methods for Solving Nonsmooth Optimal Control Problems. *Journal of Guidance, Control and Dynamics*, 27(3):397-405, 2004.

[33] Pontryagin LS, Boltyanskii V, Gamkrelidze R, et al. The Mathematical Theory of Optimal Processes. Pergamon, New York, 1964.

[34] Yakimenko OA. Direct Methods for Rapid Prototyping of Near-Optimal Aircraft Trajectories. *Journal of Guidance, Control and Dynamics*, 23(5):865-875, 2000.

[35] Kang W and Bedrossian N, Pseudospectral Optimal Control Theory Makes Debut Flight, Saves NASA $1M in Under Three Hours, *SIAM News*, 40(7), September 2007.

[36] Sekhavat P, Fleming A and Ross IM, Time-Optimal Nonlinear Feedback Control for the NPSAT1 Spacecraft, *Proceedings of the IEEE/ASME International Conference on Advanced Intelligent Mechatronics* TC1-02, USA, 843-850, July 2005.

[37] McFarland D, Near Real-Time Closed-Loop Optimal Control Feedback for Spacecraft Attitude Maneuvers, Master Thesis, Air Force Institute of Technology, Wright-Patterson Air Force Base, Ohio, 2009.

[38] Shaffer PJ, Ross IM, Oppenheimer MW and Doman DB, Optimal Trajectory Reconfiguration and Retargeting for a Reusable Launch Vehicle, *AIAA Guidance, Navigation, and Control Conference and Exhibit*, AIAA Paper 2005-6148, August 2005.

[39] Teleke S, Baran ME and Huang AQ, Optimal Control of Battery Energy Storage for Wind Farm Dispatching, *IEEE Transactions on Energy Conversion*, 25(3):787-794, 2010.

[40] Zhu Q and Lin HS, Comparing Ordinary Kriging and Regression Kriging for Soil Properties in Contrasting Landscapes, *Pedosphere*, 20(5):594-606, 2010. ISSN 1002-0160/CN 32-1315/P

[41] Paiva R, Carvalho A, Crawford C and Suleman A, Comparison of Surrogate Models in a Multidisciplinary Optimization Framework for Wing Design, *AIAA Journal*, 48(5):p995-1006, 2010.

[42] Huanga Z, Wang C, Chena J and Tian H, Optimal design of aeroengine turbine disc based on kriging surrogate models, *Computers & Structures*, 89(12):27-37, 2011. DOI: 10.1016/j.compstruc.2010.07.010

[43] Timme S, Marques S and Badcock KJ, Transonic Aeroelastic Stability Analysis Using a KrigingBased Schur Complement Formulation, *AIAA Journal*, 49(6):1202-1213, 2011.

[44] McDaniel DR, Cummings RM, Bergeron K, Morton SA and Dean JP. Comparisons of computational fluid dynamics solutions of static and manoeuvring fighter aircraft with flight test data. *Proceedings of the Institution of Mechanical Engineers, Part G: Journal of Aerospace Engineering*, 223:323-340, 2008.

[45] Jategaonkar RV. Flight Vehicle System Identification. Progress in Astronautics and Aeronautics, First Edition, 2006.

[46] Lawson SJ, High Performance Computing for High-Fidelity Multi-Disciplinary Analysis of Weapons Bays, PhD thesis, University of Liverpool, 2009.

[47] Barakos GN, Study of Unsteady Aerodynamic Phenomena Using Advanced Turbulence Closures, PhD thesis, University of Manchester Institute of Science and Technology, April 1999.

[48] Wilcox DC. Turbulence Modelling for CFD. DCW Industries Inc., 3rd Edition, La Cañada, CA, 2006.

[49] Brandsma FJ, Kok JC, Dol HS, Elsenaar A, Leading edge vortex flow computations and comparison with DNW-HST wind tunnel data. *Proceedings of the NATO RTO/AVT Symposium on Vortex Flows and High Angle of Attack*, NATO RTO/AVT, 2001.

[50] Menter FR. Zonal Two Equation k-ω Turbulence Models for Aerodynamic Flows. *24th AIAA Fluid Dynamics Conference*, AIAA Paper 93-2906, July 1993.

[51] Badcock KJ, Richards BE and Woodgate MA. Elements of computational fluid dynamics on block structured grids using implicit solvers. *Progress in Aerospace Sciences*, 36:351-392, 2000.

[52] ANSYS Inc. ANSYS ICEM CFD. http://www.ansys.com, February, 2008.

[53] Van Leer B, Towards the Ultimate Conservative Difference Scheme. V. A Second-Order Sequel to Godunov's Method. *Journal of Computational Physics*, 32:101-136, 1979.

[54] Jameson A, Time dependent calculations using multigrid, with applications to unsteady flows past airfoils and wings, *Proceedings of the 10th AIAA Computational Fluid Dynamics Conference*, AIAA Paper 1991-1596, June 1991.

[55] Rampurawala AM, Aeroelastic Analysis of Aircraft with Control Surfaces Using CFD. PhD thesis, University of Liverpool, 2006.

[56] Rampurawala AM and Badcock KJ. Evaluation of a Simplified Grid Treatment for Oscillating Trailing-Edge Control Surfaces. *Journal of Aircraft*, 44(4):1177-1188. DOI: 10.2514/1.24623.

[57] Da Ronch A, McFarlane C, Beaverstock C, Oppelstrup J, Zhang M and Rizzi A. Benchmarking CEASIOM Software to Predict Flight Control and Flying Qualities of the B-747. *Proceedings of the 27th International Congress of the Aeronautical Sciences*, 2010.

[58] Rizzi A. Modeling and Simulating Aircraft Stability and Control - The SimSAC Project. *Proceedings of the AIAA Guidance, Navigation, and Control Conference 2010*. AIAA Paper 2010-8238.

[59] Williams JE, Vukelich SR. The USAF Stability and Control Digital DATCOM. McDonnell Douglas Astronautics Company - St Louis Division 1979. AFFDL-TR-79-3032.

[60] Ghoreyshi M, Badcock KJ and Woodgate MA. Accelerating the Numerical Generation of Aerodynamic Models for Flight Simulation. *Journal of Aircraft*, 46(3):972-980, 2009. DOI: 10.2514/1.39626.

[61] Nielsen HB, DACE, A Matlab Kriging Toolbox. www2.imm.dtu.dk/ hbn

[62] Loeser T, Vicroy D and Schuette A. SACCON Static Wind Tunnel Tests at DNW-NWB and 14ftx22ft NASA LaRC. *28th AIAA Applied Aerodynamics Conference*, AIAA Paper 2010-4393, June 2010.

[63] Vicroy D and Loeser T. SACCON Dynamic Wind Tunnel Tests at DNW- NWB and 14x22 NASA LaRC. *28th AIAA Applied Aerodynamics Conference*, AIAA Paper 2010-4394, June 2010.

[64] Gilliot A. Static and Dynamic SACCON PIV Tests - Part I: Forward Flowfield. *28th AIAA Applied Aerodynamics Conference*, AIAA Paper 2010-4395, June 2010.

[65] Konrath R, Roosenboom E, Schroder A, Pallek D and Otter D. Static and Dynamic SACCON PIV Tests - Part II: Aft Flow Field. *28th AIAA Applied Aerodynamics Conference*, AIAA Paper 2010-4396, June 2010.

[66] Eckert E, Hegen GH and Kuhn W, DNW's method to correct for support and wall interference effects on low speed measurements with a large propeller powered transport aircraft model, *Proceedings of the 25th International Congress of the Aeronautical Sciences*, Hamburg, Germany, 2006.

[67] Boerstoel JW, Kassies A, Kok JC and Spekreijse SP. ENFLOW, a Full-Functionality System of CFD Codes for Industrial Euler/Navier-Stokes Flow Computations. NLR TP 96286U, NLR, Amsterdam, 1996.

[68] Huber K., Numerical Investigation of the Aerodynamic Properties of a Flying Wing Configuration, Master Thesis, Royal Institute of Technology, June 2010.

[69] Frink N. Strategy for Dynamic CFD Simulation on SACCON Configuration. *28th AIAA Applied Aerodynamics Conference*, AIAA Paper 2010-4559, June 2010.

[70] Tecplot 360, Release 2011, http://www.tecplot.com.

[71] Schuette A, Hummel D and Hitzel S. Numerical and Experimental Analyses of the Vortical Flow Around the SACCON Configuration. *28th AIAA Applied Aerodynamics Conference*, AIAA-2010-4690, June 2010.

146

[72] Le Roy J. SACCON CFD Static and Dynamic Derivatives Using elsA. *28th AIAA Applied Aerodynamics Conference*, AIAA Paper 2010-4562, June 2010.

[73] Jirasek A., Cummings R., Computation and Evaluation of Dynamic Derivatives Using CFD. *Proceedings of the 29th AIAA Applied Aerodynamics Conference 2011.* AIAA-2011-3965.

[74] Vallespin D, Badcock KJ, Da Ronch A, White MD, Perfect P and Ghoreyshi M, Computational Fluid Dynamics Framework for Aerodynamic Model Assessment, *Accepted in the Journal of Progress in Aerospace Sciences*, 2011.

[75] DIDO version 7.3, Elissar Global, PO Box 1365, Monterey, CA93942, US, www.elissarglobal.com.

[76] Osterhuber R. FCS Requirements for Combat Aircraft - Lessons Learned for Future Designs, *Proceedings of the NATO RTO AVT-189 Specialists Meeting*, Portsmouth, 2011.

[77] Saephan S, van Dam CP. Determination of Wing-Only Aircraft Tumbling Characteristics Through Computational Fluid Dynamics. *Journal of Aircraft*, 45(3):1044-1053, 2008. DOI: 10.2514/1.33730.

[78] Boeing Company website, http://www.boeing.com/history/boeing/x45_jucas.html

[79] National Museum of the US Air Force, http://www.nationalmuseum.af.mil/factsheets/factsheet.asp?i

[80] Boeing media release, http://www.boeing.com/bds/mediakit/2010/afa/pdf/bkgd_phantomray_0210.

[81] GE Aviation website, http://www.geae.com/engines/military/f404/f404-102.html

[82] Northrop Grumman X-47B UCAS Data Sheet, http://www.as.northropgrumman.com/products/nucasx47b/assets/UCAS-D_DataSheet_final.pdf.

[83] Ghoreyshi M, Badcock KJ, Da Ronch A, Marques S, Swift A, Ames N. Framework for Establishing the Limits of Tabular Aerodynamic Models for Flight Dynamics Analysis. *Journal of Aircraft*, 48(1):42-55, 2011.

[84] Da Ronch A, Vallespin D, Ghoreyshi M, Badcock KJ. Computation and Evaluation of Dynamic Derivatives Using CFD. *Proceedings of the 28th AIAA Applied Aerodynamics Conference* AIAA Paper 2010-4817, 2010.

[85] Vicroy D, Loeser T and Schuette A. SACCON Dynamic Wind Tunnel Tests at DNW- NWB and 14x22 NASA LaRC. *NATO RTO AVT-161 Technical Report*, October 2011.

[86] Da Ronch A, Badcock KJ, Ghoreyshi M, Woodgate MA, Görtz S, Widhalm M and Dwight RP. Linear Frequency Domain and Harmonic Balance Predictions of Dynamic Derivatives. *Proceedings of the 28th AIAA Applied Aerodynamics Conference*, AIAA Paper 2010-4699, 2010.

[87] Ross IM, Fahroo F. User's Manual for DIDO 2002: A MATLAB Application Package for Dynamic Optimization. 2002 NPS Technical Report, Dept. of Aeronautics and Astronautics, Naval Postgraduate School, Monterey, CA, AA-02-002.

[88] Cook MV. Flight Dynamics Principles, Elsevier, Second Edition, London, 2007.

[89] Ghoreyshi M, Vallespin D, Da Ronch A, Badcock KJ, Vos J, Hitzel S. Simulation of Aircraft Manoeuvres Based on Computational Fluid Dynamics. *Proceedings of the Guidance, Navigation and Control Conference*, AIAA Paper 2010-8239, 2010.

[90] Vallespin D, Da Ronch A, Badcock KJ and Boelens O. Validation of Vortical Flow Predictions for a UCAV Wind Tunnel Model. *Proceedings of the 28th AIAA Applied Aerodynamics Conference*, AIAA Paper 2010-4560, 2010.

[91] Stevens BL, Lewis FL. Aircraft Control and Simulation. Wiley, New York, 1992.